



UNIVERSITY OF  
BIRMINGHAM

# MICROMILLING OF HARDENED (62 HRC) AISI D2 COLD WORK TOOL STEEL

by

**JURI BIN SAEDON**

A thesis submitted to  
The University of Birmingham  
for the degree of  
**DOCTOR OF PHILOSOPHY**

School of Mechanical Engineering  
College of Engineering and Physical Sciences  
The University of Birmingham  
October 2011

UNIVERSITY OF  
BIRMINGHAM

**University of Birmingham Research Archive**

**e-theses repository**

This unpublished thesis/dissertation is copyright of the author and/or third parties. The intellectual property rights of the author or third parties in respect of this work are as defined by The Copyright Designs and Patents Act 1988 or as modified by any successor legislation.

Any use made of information contained in this thesis/dissertation must be in accordance with that legislation and must be properly acknowledged. Further distribution or reproduction in any format is prohibited without the permission of the copyright holder.

## SYNOPSIS

Following an extensive literature survey on key aspects relating to microscale machining including operational advantages/ challenges, machine tools, tooling, cutting mechanisms, five main phases of experimental work were undertaken to evaluate the micromilling of hardened AISI D2 (62HRC bulk) cold work tool steel. Phase 1 involved the evaluation of a range of commercial micro endmill products (0.5mm diameter) to ascertain the level of tool quality (as supplied), in terms of diameter variations, cutting edge sharpness, surface conditions and geometrical accuracies. The majority of the micro end mills supplied exhibited significant defects, irrespective of tool manufacturer. The nature of flaws typically involved poorly defined cutting edges, heavy surface grind marks and deficiencies in coating quality. Work in Phase 2 proceeded to determine the limitation of a commercial high speed machine tool intended for microscale machining (60,000rpm spindle speed with linear motor capability), particularly in terms of z-axis errors induced by spindle thermal growth. This entailed a series of experiments to indentify the extent of depth of cut deviations due to lab ambient temperature variations, machine warm up and cool down cycles, as well as durations of cutting operations. The effectiveness of the spindle cooling system and integrated error compensation algorithms were assessed with subsequent modifications incorporated to improve accuracy/reduce spindle growth. Machine tool accuracy was improved via modification of spindle acceleration/deceleration rates and manipulation of control algorithms, with consequent effects on the rate of thermal loading and cooling. Here, maximum spindle length variation was reduced by ~50% (8 $\mu$ m) at 60,000rpm. Mainstream investigations into microslot milling of high carbon, high chromium hardened AISI D2 cold work tool steel using 0.5mm diameter coated (TiAlN) tungsten carbide end mills, were carried out in Phase 3 tests. Performance was assessed in terms of tool life/tool wear, surface roughness, cutting forces, burr formation, slot geometry accuracy and workpiece surface integrity. Due to a lack of information and standards available, preliminary trials (Phase 3A) were conducted to gain an initial understanding of tool wear and surface roughness progression against length cut and to identify a suitable tool life criterion for micromilling experiments. The various tool wear

mechanisms/modes observed are also discussed. Based on the results obtained, a cut length of 520mm was defined as the end of test criterion in subsequent testing. The influence of operating parameters (cutting speed, feed rate and depth of cut) on tool life, surface roughness, burr width and cutting forces was investigated in Phase 3B using a full factorial experiment design. The cutting parameter levels were selected based on current best practice from the literature as well as those recommended by the tool manufacturer. Pre-machining of workpiece samples however produced a slightly softened layer of 55HRC to a depth of  $\sim 60\mu\text{m}$ . Analysis of results included main effects plots and calculation of percentage contribution ratios (PCR's) for each of the primary variable factors, their interactions were evaluated using analysis of variance (ANOVA). In terms of surface integrity, no evidence of major surface damage such as microcracks, un-tempered/over-tempered martensite, phase transformations or white layer formation was detected in any of the specimens analysed. No discernible deformation of the material grain structure beneath the machined surface was observed. This was mainly attributed to the comparatively low levels of mechanical force and temperatures generated during the micro milling operation. The test array (from Phase 3B) was further extended in Phase 4 work to allow for the implementation of Response Surface Methodology (RSM) analysis in order to develop first and second order models for the prediction of tool life and surface roughness response. The results showed that average percentage error between the predicted and experimental value for both models was less than 4%. Dual-response (cutting speed and feed rate) contour plots of metal removal rate and tool life/surface roughness were generated from the respective model equations. These maps were further developed to select the proper combination of cutting speed and feed per tooth in order to determine maximum possible tool life/surface roughness at specific metal removal rates. Phase 5 of the project assessed the impact of coatings and tool geometry (chip breaker feature) on tool life and workpiece surface roughness. It was found that coated micro end mills led to a 10 fold increase in cut length over uncoated tools and a greater resistance to cutting forces (60% higher at the point of tool failure). The presence of the chip breaker resulted in a lower tool wear rate during the initial stage of machining (up to  $\sim 600\text{mm}$  cut length), although cutting forces were marginally higher. Tool life however was  $\sim 30\%$  longer with the standard/plain geometry end mills as opposed to the chip breaker cutters.

## ACKNOWLEDGMENTS

First of all, I would like to express my deepest gratitude to my supervisors Dr. Sein Leung Soo (Lecturer and Head of the Machining Research Group) and Mr. David Aspinwall (Reader in Advanced Manufacturing Technology), both in the School of Mechanical Engineering, University of Birmingham for their academic supervision, guidance and encouragement over the course of the research.

Thanks also go to Mrs. Elaine Aspinwall for her generous time and help relating to experimental design and statistical analysis techniques.

I would like to acknowledge the support from Universiti Teknologi MARA, and The Ministry of Higher Education, Malaysia for providing the opportunity, time and scholarship which enabled this research to be carried out.

Special thanks go to Mr. Adrian Barnacle from Mitsubishi Materials Corporation (MMC) Hardmetal, UK for providing micro tools used in the experimental work as well as technical comment / support.

My sincere gratitude and appreciation to Mr. Richard Fasham, Mr. Andy Loat and Mr. Alan Saywell, Technical Engineers within the School of Mechanical Engineering for their invaluable assistance with the experimental work and preparation of workpiece material. Valuable discussions and support from members of the Machining Research Group, School of Mechanical Engineering over the period of the project is gratefully acknowledged.

I would also like to express my heartfelt gratitude to my family (Norasmah Ahmad, Afifah Zakiyyah, Azib Azamuddin and Ahmad Aiman) for their understanding and support in providing endless encouragement and motivation.

Lastly, I would like to thank my friends Dr. Richard Hood, Mr. Azman Yahaya and colleagues for all their assistance and support.

# TABLE OF CONTENTS

<b>SYNOPSIS</b> .....	<b>ii</b>
<b>ACKNOWLEDGMENTS</b> .....	<b>iv</b>
<b>LIST OF FIGURES</b> .....	<b>ix</b>
<b>LIST OF TABLES</b> .....	<b>xiii</b>
<b>Chapter 1 : INTRODUCTION</b> .....	<b>1</b>
<b>1.1 Background to the project</b> .....	<b>1</b>
<b>1.2 Aims and objectives</b> .....	<b>2</b>
<b>1.3 Project sponsors and collaborators</b> .....	<b>3</b>
<b>Chapter 2 : LITERATURE REVIEW</b> .....	<b>4</b>
<b>2.1 Micromilling</b> .....	<b>4</b>
2.1.1 Introduction .....	4
2.1.2 Challenges in micromilling .....	5
<b>2.2 Machine tools</b> .....	<b>6</b>
2.2.1 Commercial and research based machine systems.....	7
2.2.2 High speed spindle specifications .....	14
2.2.3 Thermal based machine tool errors .....	15
<b>2.3 Microtools</b> .....	<b>18</b>
2.3.1 Material, geometry and design .....	19
2.3.2 Coated and uncoated tooling .....	21
2.3.3 Tool quality and size accuracy .....	22
<b>2.4 Factors affecting cutting mechanisms in microscale machining</b> .....	<b>23</b>
2.4.1 Minimum chip thickness criterion and chip formation .....	23
2.4.2 Cutting edge radius effects .....	31
2.4.3 Influence of workpiece microstructure/grain size .....	33
<b>2.5 Overview of machinability research in micromilling</b> .....	<b>36</b>
2.5.1 Workpiece materials.....	36
2.5.2 Operating parameters .....	37
2.5.3 Performance measures and results .....	39
<b>2.6 Design of experiments</b> .....	<b>46</b>
2.6.1 Full and fractional factorial designs .....	46

2.6.2 Response surface methodology (RSM).....	46
2.6.3 Analysis of variance (ANOVA) technique .....	47
<b>Chapter 3 : EXPERIMENTAL WORK.....</b>	<b>48</b>
<b>3.1 Workpiece material .....</b>	<b>48</b>
<b>3.2 Tooling .....</b>	<b>49</b>
3.2.1 Micro end mills for Phase 1 work .....	49
3.2.2 Micro end mills for Phase 2 work .....	50
3.2.3 Micro end mills for Phase 3 and 4 experiments .....	50
3.2.4 Micro end mills for Phase 5 experiments .....	51
<b>3.3 Equipment .....</b>	<b>52</b>
3.3.1 Machine tool and experimental setup.....	52
3.3.2 Force measurement.....	54
3.3.3 Temperature measurement .....	55
3.3.4 Tool wear, burr width, workpiece/slot quality, microstructure and chip analysis.....	56
3.3.5 Workpiece surface roughness.....	57
3.3.6 Workpiece microhardness analysis .....	58
3.3.7 Residual stress analysis .....	58
3.3.8 Sample preparation.....	59
3.3.9 Statistical analysis .....	60
<b>3.4 Experimental design, procedure and test arrays .....</b>	<b>60</b>
3.4.1 Phase 1: Analysis of micro milling cutters.....	62
3.4.2 Phase 2: Investigation of machine spindle thermal growth errors .....	62
3.4.3 Phase 3A: Preliminary micromilling trials .....	64
3.4.4 Phase 3B: Influence of operating parameters.....	64
3.4.5 Phase 4: Optimisation of tool life and surface roughness .....	66
3.4.6 Phase 5: Effect of tool coating and tool geometry on tool life and surface roughness .....	68
<b>Chapter 4 : RESULTS AND DISCUSSION.....</b>	<b>70</b>
<b>4.1 Phase 1: Analysis of commercial micro milling cutters.....</b>	<b>70</b>
<b>4.2 Phase 2: Investigation of machine spindle growth errors .....</b>	<b>75</b>
<b>4.3 Phase 3A: Preliminary micromilling trials.....</b>	<b>81</b>
4.3.1 Evaluation of tool wear/reduction in tool diameter.....	81

4.3.2	Workpiece surface roughness assessment .....	85
4.3.3	Determination of end of test criterion .....	87
4.3.4	Microtool wear/failure modes .....	88
4.3.4.1	Coating delamination .....	88
4.3.4.2	Fracture of cutting edge .....	90
4.3.4.3	Abrasive wear .....	91
4.3.4.4	Workpiece material deposition .....	92
4.3.4.5	Tool breakage.....	94
<b>4.4</b>	<b>Phase 3B: Influence of operating parameters .....</b>	<b>94</b>
4.4.1	Tool life .....	94
4.4.2	Surface roughness.....	96
4.4.3	Burr formation.....	100
4.4.4	Cutting force.....	104
4.4.5	Slot quality/geometry .....	111
4.4.6	Cutting temperature.....	113
4.4.7	Microstructure .....	113
4.4.8	Microhardness .....	117
4.4.9	Residual stress .....	120
<b>4.5</b>	<b>Phase 4: Optimisation of tool life and surface roughness .....</b>	<b>121</b>
4.5.1	Tool life and material removal rate .....	121
4.5.2	First order model of tool life .....	122
4.5.2.1	Adequacy of the linear model .....	124
4.5.2.2	Utilisation of the first order tool life model .....	124
4.5.3	Second order model of tool life.....	126
4.5.3.1	Adequacy of the quadratic model .....	129
4.5.3.2	Utilisation of the second order tool life model .....	130
4.5.4	First order model of surface roughness .....	131
4.5.4.1	Adequacy of the linear model .....	133
4.5.4.2	Utilisation of the first order surface roughness model.....	133
4.5.5	Second order model of surface roughness.....	135
4.5.5.1	Adequacy of the quadratic model .....	137
4.5.5.2	Utilisation of the second order surface roughness model .....	138

<b>4.6 Phase 5: Effect of tool coating and geometry on tool life and surface roughness .....</b>	<b>139</b>
4.6.1 Influence of tool coating.....	139
4.6.1.1 Tool wear progression.....	139
4.6.1.2 3D surface topography.....	144
4.6.2 Effect of tool geometry.....	145
4.6.2.1 Tool wear progression.....	145
4.6.2.2 3D surface topography.....	149
<b>Chapter 5 : CONCLUSIONS.....</b>	<b>150</b>
<b>5.1 Literature review on micro-milling technologies .....</b>	<b>150</b>
<b>5.2 Experimental work .....</b>	<b>151</b>
5.2.1 Phase 1.....	151
5.2.2 Phase 2.....	151
5.2.3 Phase 3A.....	152
5.2.4 Phase 3B.....	152
5.2.5 Phase 4.....	155
5.2.6 Phase 5.....	156
<b>Chapter 6 : RECOMMENDATIONS FOR FUTURE WORK.....</b>	<b>158</b>
<b>REFERENCES.....</b>	<b>159</b>
<b>APPENDICES.....</b>	<b>172</b>
6.1.1 Appendix A: CNC programme.....	172
6.1.2 Appendix B: Spindle cool down cycles .....	175
6.1.3 Appendix C: Interaction Plots .....	178
6.1.4 Appendix D: Micrograph of slots machining using worn tools (Slot 26).....	181
6.1.5 Appendix E: Sample statistical calculations using Design Expert.....	182
6.1.6 Appendix F: List of publications.....	184

## LIST OF FIGURES

Figure 2.1: Examples of commercial ultra precision machine tools.....	9
Figure 2.2: Examples of meso-scale machine tools (mMT) and bench top systems, based in academic institutions .....	12
Figure 2.3: Thermal effect diagram [56] .....	17
Figure 2.4: Typical end mill tool geometry [80] .....	19
Figure 2.5: The relationship between various tool materials in relation with hardness .....	20
Figure 2.6: Measured surface topography [22].....	24
Figure 2.7: Experimental Y force (normal to the feed force) and the corresponding power spectrum at feed rate 0.25 $\mu$ m/tooth [102].....	27
Figure 2.8: Comparison of surface roughness Ra measurements with and without the minimum chip thickness effect [12]. .....	27
Figure 2.9: Comparison chip load/force relationship: (a) Pearlite (b) Ferrite [112].....	28
Figure 2.10: Chip formation relative to minimum chip thickness in microscale machining: based on [6] .....	29
Figure 2.11: Formation of a highly negative effective rake angle ahead of the rounded tool edge at the critical ratio $h/r_e=0.2625$ [1].....	29
Figure 2.12: Micromilling with minimum chip thickness effect: (a) – (c) first path, (d) – (f) following path: base on [17].....	30
Figure 2.13: Effect of cutting edge radius to chip thickness ratio: based on [9] .....	31
Figure 2.14: Plastic yielding zone at smaller (7.5 $\mu$ m) uncut chip thickness [115] .....	32
Figure 2.15: Relation between grain size and chip thickness for conventional cutting.....	33
Figure 2.16: Continuous chips (a-c) and Quasi-shear-extrusion chips (d-f), at different uncut chip thickness [125] .....	35
Figure 2.17: Micro milled surface by 0.2mm diameter ball end mil – material smeared behind the tool [21].....	41
Figure 2.18: Burr formation for 0.6mm diameter with rotational speed 30000rpm, feed 2 $\mu$ m/rev and depth of cut 0.3mm [44] .....	42
Figure 3.1: Workpiece material (a) Microstructure (b) Bulk hardness measurement .....	49
Figure 3.2: Example of machined test blocks.....	49
Figure 3.3: PCD end mills diameter 6mm .....	50
Figure 3.4: SEM picture of a new micro end mill .....	51
Figure 3.5: (a) No chip breaker with TiAlN coating (b) Chip breaker with TiAlN coating (c) Chip breaker no coating.....	52
Figure 3.6: Matsuura LX-1 machining centre .....	53
Figure 3.7: Experimental setup (a) Shrink fit tool holder and Hot Shot Jr heater (b) Renishaw NC-3 .....	53
Figure 3.8: (a) Matsuura LX-1 CNC machine tool - experiment setup.....	54
Figure 3.9: Force measurement (a) Kistler dynamometer type 9257A (b) Four channel Gould 6000s, charge amplifiers, and computer with Dynoware software.....	54
Figure 3.10: Micromilling temperature measurement set up.....	55
Figure 3.11: Workpiece emissivity setup .....	56
Figure 3.12: Method for measuring the slot width at several positions from slot base .....	57
Figure 3.13: Measurement equipments and tool (a) Leica DMLM microscope .....	57

Figure 3.14: Surface roughness measurement equipments: Taylor Hobson Form Talysurf 120L .....	58
Figure 3.15: Mitutoyo MVK-G3 hardness testing.....	58
Figure 3.16: Residual stress equipment .....	59
Figure 3.17: (a) ROBOFIL 200 electrical discharge wire machine (EDWM) (b) Buehler Epomet™ Bakelite mounting press (c) Buehler Alpha 2 grinder-polisher .....	59
Figure 3.18: Phase 2 setup (a) Schematic of the machine spindle (courtesy of Matsuura) (b) Machine control panel output measurement (c) Mitutoyo DTI (d) Renishaw OMP 40 .....	63
Figure 3.19: Central composite design for three factors.....	66
Figure 4.1: SEM micrographs of the end mills selected for this study.....	71
Figure 4.2: Microtool defects (a-b) Grinding marks. (c-d) Chipping/pitting of cutting edge .....	72
Figure 4.3: Broken cutting edge for different microtool .....	72
Figure 4.4: (a-b) Non uniform coating. (c-d) Coating droplets .....	73
Figure 4.5: Microtool diameter error .....	74
Figure 4.6: Microtool cutting edge radius .....	74
Figure 4.7: Average laboratory temperature in a day .....	75
Figure 4.8: Time versus average tool length deviation in a day (static spindle) .....	76
Figure 4.9: Time vs. temperature response curves during spindle warm up and cool down for various speeds at 17°C base temperature .....	77
Figure 4.10: Time vs. temperature response curves during spindle warm up and cool down at 30,000rpm for different base temperatures .....	77
Figure 4.11: Warming up and cooling down cycles when operating at 60,000rpm .....	78
Figure 4.12: z-axis length variation during cooling phase in cycle 4 with spindle stopped.....	79
Figure 4.13: The z-axis length variation during spindle operating at 60,000rpm .....	80
Figure 4.14: The z-axis length variation measured using NC3 when spindle operating at 30,000rpm, 40,000rpm, 50,000rpm and 60,000rpm. ....	80
Figure 4.15: Slot depths measured using the OMP 40 during machining of graphite following modification of spindle acceleration-deceleration rate .....	81
Figure 4.16: Microtool wear progression during micromilling .....	83
Figure 4.17: Correlation between tool diameter and slot width .....	84
Figure 4.18: Microtool wear progression .....	84
Figure 4.19: Cutting forces (a) new tool vs (b) worn tool .....	85
Figure 4.20: Slot surface roughness progression .....	86
Figure 4.21: 3D topography plots of surface (a) new tool (b) worn tool.....	86
Figure 4.22: Worn tool with adhered material.....	86
Figure 4.23: Cutting length versus surface roughness (Ra).....	87
Figure 4.24: Compilation of trials for various operating parameters .....	88
Figure 4.25: Delamination of the coating from (a) flank face (b) rake face (c) EDX analysis on site X.....	89
Figure 4.26: EDX area mapping of flank face.....	90
Figure 4.27: Fracture of cutting edge viewed from; (a) rake face (b) end flute (c) flank face .....	91

Figure 4.28: Abrasive wear (a) rake face (b) flank face and (c) end flute.....	91
Figure 4.29: Adhered material on tool; (a) rake face (b) flank face, .....	92
Figure 4.30: EDX of machined surface .....	92
Figure 4.31: EDX area mapping of slot machined surface.....	93
Figure 4.32: EDX spot analysis of microchip surface .....	93
Figure 4.33: Broken microtool.....	94
Figure 4.34: The cutting time versus reduction of tool diameter.....	95
Figure 4.35: Main effects plot, means for tool life .....	96
Figure 4.36: Mean surface roughness .....	97
Figure 4.37: Tool wear for Test 7 vs Test 8.....	97
Figure 4.38: 3D topography plot of surface in (a) Test 7 vs (b) Test 8 .....	98
Figure 4.39: Main effects plot, means for surface roughness .....	99
Figure 4.40: Effect of milling direction on burr formation.....	100
Figure 4.41: Burr widths after 520mm cut length .....	102
Figure 4.42: Mean burr width .....	103
Figure 4.43: Main effects plot, means for burr width .....	103
Figure 4.44: Mean static force at Slot 1- new tool.....	105
Figure 4.45: Mean static force at Slot 26 – worn tool .....	106
Figure 4.46: Comparison of static forces generated in Test 1 and Test 8 with new and worn tools .....	107
Figure 4.47: Micrographs of tool wear for low vs. high parameters .....	107
Figure 4.48: Main effects plot, means for $F_x$ worn tool – Slot 26 .....	108
Figure 4.49: Main effects plot, means for $F_y$ worn tool – Slot 26 .....	109
Figure 4.50: Main effects plot, means for $F_z$ worn tool– Slot 26 .....	110
Figure 4.51: Comparison of slot quality in Test 6 (a) New tool / Slot 1 (b) Worn tool / Slot 26 .....	111
Figure 4.52: Slot quality at different cut lengths for Test 1: (a) First slot (b) 100mm .....	112
Figure 4.53: Slot quality at different cut lengths for Test 8: (a) First slot (b) 100mm .....	112
Figure 4.54: Micromilling temperature measurement .....	113
Figure 4.55: Cross sectional micrograph of slots machined using new tools (Slot 1).....	114
Figure 4.56: Cross sectional micrograph of slots machined using worn tools (Slot 26) ...	115
Figure 4.57: Cross sectional (Y-Z plane) microstructure of a micromilled specimen from Test 8-Slot 26 (a) left side (b) right side (c) 3000x magnification of Section x .....	116
Figure 4.58: Cross sectional (X-Y plane) microstructure of a micromilled specimen from Test 8-Slot 26 (a) A-up milling side (b) B-down milling side .....	116
Figure 4.59: Cross sectional microstructure of a micromilled specimen from Test 8-Slot 26 (a) X-Z plane, C- cross section (parallel to feed direction) (b) Y-Z plane, D- cross section (perpendicular to feed direction) .....	117
Figure 4.60: Microhardness depth profiles of all tests compared to the bulk material – New tools .....	118
Figure 4.61: Microhardness depth profiles for face milling and bulk material .....	119
Figure 4.62: Combined microhardness depth profiles - worn tools .....	119
Figure 4.63: Microhardness depth profiles for Test 1 and Test 8 with new and worn tools.....	120
Figure 4.64: Surface residual stress .....	121

Figure 4.65: Tool life, volume removed and volume removal rate at test citation.....	122
Figure 4.66: First order tool life contours at 35 $\mu$ m doc.....	124
Figure 4.67: First order tool life contours and material removal rates .....	126
Figure 4.68: Comparison between experimental and predicted values for tool life.....	128
Figure 4.69: Second order tool life contours and material removal rates.....	131
Figure 4.70: First order surface roughness contours at 35 $\mu$ m depth of cut. ....	133
Figure 4.71: First order surface roughness contours and material removal rates.....	134
Figure 4.72: Comparison between experiment results, mathematical equation, prediction first and second order model for surface roughness .....	136
Figure 4.73: Second order surface roughness contours and material removal rates.....	138
Figure 4.74: SEM micrographs of uncoated tool wear progression. ....	140
Figure 4.75: SEM micrographs of coated tool with chip breaker wear progression. ....	141
Figure 4.76: Tool wear progression versus cutting length for uncoated and coated tools .....	142
Figure 4.77: Uncoated and coated microtool with cutting edge radius .....	143
Figure 4.78: Average cutting forces for uncoated and coated tool during Slot 1 .....	143
Figure 4.79: Average cutting forces for coated and uncoated tool at the point of tool failure.....	144
Figure 4.80: 3D surface topography plots when using new and worn tools.....	145
Figure 4.81: Coated micro end mill; (a) without chip breaker (b) with chip breaker.....	146
Figure 4.82: Tool wear progression versus cut length for different tool geometry .....	146
Figure 4.83: Wear progression of the coated tool without chip breaker geometry .....	147
Figure 4.84: Average cutting forces for tools with and without chip breaker during Slot 1.....	148
Figure 4.85: Average cutting forces for tools with and without chip breaker at the point of failure.....	148
Figure 4.86: 3D surface topography plots when using new and worn tools with and without chip breaker geometry .....	149

## LIST OF TABLES

Table 2.1: Main specifications of commercial ultraprecision machine tools .....	10
Table 2.2: Comparison between commercial, bench-top and research based micromilling systems .....	13
Table 2.3: Properties comparison between steel and ceramic balls bearing [47] .....	14
Table 2.4: Comparison between a typical conventional high speed spindle and ultra high-speed air bearing spindle.....	15
Table 2.5: Cutting tool material properties [80] .....	20
Table 2.6: Coating characteristics [81] .....	22
Table 2.7: Summary of key research publications relating to investigation of minimum chip thickness .....	26
Table 2.8 : Materials used in micromilling and associated applications .....	37
Table 2.9: Physical properties of AISI D2 [148] .....	37
Table 2.10: Cutting data for macro and micro flat end mills HRC : 45-52 HRC [80] .....	38
Table 2.11: Cutting parameters used in micromilling hardened steel by various researchers .....	38
Table 2.12: Description of workpiece surface integrity data sets [180] .....	45
Table 3.1: Microtool diameter and geometry used in Phase 1.....	50
Table 3.2: Micro tools for Phase 5.....	52
Table 3.3: Grinding, polishing and etching procedure for hardened AISI D2 steel .....	60
Table 3.4: Overview of experimental phases together with issues investigated.....	61
Table 3.5: Phase 3 Factors and levels .....	65
Table 3.6: Full factorial design matrix ( $L_8$ ) .....	65
Table 3.7: Phase 4 levels of independent variables .....	67
Table 3.8: Phase 4 design matrix using RSM ( $L_{18}$ ) .....	67
Table 4.1: ANOVA results for tool life .....	96
Table 4.2: ANOVA results for surface roughness.....	98
Table 4.3: ANOVA results for burr width.....	104
Table 4.4: ANOVA results for $F_x$ worn tool – Slot 26.....	108
Table 4.5: ANOVA results for $F_y$ worn tool – Slot 26 .....	109
Table 4.6: ANOVA results for $F_z$ worn tool – Slot 26 .....	110
Table 4.7: ANOVA results for tool life of linear model (based on $L_{12}$ ).....	123
Table 4.8: Percentage error of the tool life models.....	128
Table 4.9: Summary statistics of the tool life models (based on $L_{18}$ array) .....	129
Table 4.10: ANOVA results for tool life of quadratic model ( $L_{18}$ ) .....	130
Table 4.11: Linear model ANOVA results for surface roughness (based on $L_{12}$ ).....	132
Table 4.12: Percentage error of the surface roughness models .....	136
Table 4.13: Summary statistics of surface roughness models .....	137
Table 4.14: ANOVA results for surface roughness of quadratic model.....	137
Table 5.1: Summary of percentage contribution of each factor relative to response measures .....	154
Table 5.2: Summary of optimum cutting parameters with respect to response measures.....	155
Table 5.3: Summary of percentage contribution of each factor for cutting force components.....	155

## LIST OF NOMENCLATURE

$a_p$	:	Cutting depth ( $\mu\text{m}$ )
AE	:	Acoustic emission
AISI	:	American Iron and Steel Institute
Al	:	Aluminium
$\text{Al}_2\text{O}_3$	:	Aluminium oxide
ANOVA	:	Analysis of variance
BUE	:	Built up edge
CBN	:	Cubic boron nitride
Co	:	Cobalt
Cr	:	Chromium
CrTiAlN	:	Chromium titanium aluminium nitride
CVD	:	Chemical vapour deposition
d	:	Axial depth of cut ( $\mu\text{m}$ )
DTI	:	Digital touch indicator
EDWM	:	Electrical discharge wire machining
EDX	:	Energy-dispersive X-ray spectroscopy
EPSRC	:	Engineering and Physical Sciences Research Council
FEA	:	Finite element analysis
FEM	:	Finite element model
FIB	:	Focused ion beam
ft	:	Feed per tooth ( $\mu\text{m}/\text{tooth}$ )
$F_{\text{Res}}$	:	Resultant force (N)
$F_x$	:	Force in x direction (N)
$F_y$	:	Force in y direction (N)
$F_z$	:	Force in z direction (N)
h	:	Uncut chip thickness
$h_{\text{min}}$	:	Critical minimum chip thickness ( $\mu\text{m}$ )

HAZ	:	Heat affected zone
HK <sub>0.025</sub>	:	Knoop hardness (25gram load)
HRC	:	Hardness Rockwell C scale
HSK	:	Hollow shank kengel/tooling
HSM	:	High speed machining
HSS	:	High speed steel
IFM	:	Infinite focus microscope
IR	:	Infrared
l	:	Feed length
MEMS	:	Microelectromechanical systems
MMC	:	Mitsubishi Material Corporation
mMT	:	Meso-scale machine tool
Mn	:	Manganese
Mo	:	Molybdenum
MRR	:	Material removal rate
MTCVD	:	Medium-temperature chemical vapour deposition
N	:	Nitride
n <sub>f</sub>	:	Number of points used in the factorial design
OFHC	:	Oxygen free high thermal conductivity copper
PC	:	Personal computer
PCBN	:	Polycrystalline cubic boron nitride
PCR	:	Percentage contribution ratio
PDTE	:	Position dependent thermal errors
PITE	:	Position independent thermal errors
PMAC	:	Programmable multi-axis controller
PVD	:	Physical vapour deposition
R <sup>2</sup>	:	R-squared (coefficient of determination)
R <sup>2</sup> Adj	:	R-squared adjusted (adjusted coefficient of determination)
R <sup>2</sup> Pred	:	R-squared predicted (predicted coefficient of determination)
Ra	:	Average/mean surface roughness (µm)
RSM	:	Response surface methodology

Sa	:	Average surface roughness for 3D ( $\mu\text{m}$ )
SEM	:	Scanning electron microscopy
SI	:	Surface integrity
SMAC	:	Manufactures precision programmable electric actuators
$t_c$	:	Minimum chip thickness
TiAlN	:	Titanium aluminium nitride
TiC	:	Titanium carbide
TiCN	:	Titanium carbonitride
TiN	:	Titanium nitride
$V_c$	:	Cutting speed (m/min)
WC	:	Cemented tungsten carbide
WEDG	:	Wire electric discharge grinding
2D	:	Two-dimensional
3D	:	Three-dimensional
$\theta$	:	Rotation angle (degrees)
$\alpha$	:	Argument length.

# **Chapter 1: INTRODUCTION**

## **1.1 Background to the project**

Mechanical micromachining is becoming an important microfabrication technology due to the increasing demand for miniaturised products [1]. This has mainly been driven by the need for: (a) greater reduction in (component/assembly) size and weight; (b) better efficiency in energy consumption; and (c) increased portability in commercial and non-commercial applications. For small batch and prototype production, tool-based microscale cutting appears to be a more cost effective technique compared to alternative lithographic, etching and laser/energy beam based techniques [2]. While efficient volume manufacture is reliant on advances in rapid replication techniques such as micro-injection moulding, hot embossing etc., these processes in turn are dependent on the production of appropriate micro mould and die tooling, which encompass primarily ferrous/metallic based materials in order to meet specific geometric/feature requirements. Such components typically involve complex 3D surfaces with high aspect ratios that are not easily achievable using conventional micro manufacturing processes. Apart from dies/moulds, microscale components are prevalent in many applications including precision medical instruments, optical and electronics devices and automotive systems [3].

Micro high speed milling provides a viable and potentially preferable process route for the production of such micro/meso-scale mechanical components [4]. The flexibility and advantages provided including the ability to fabricate complex 3D structures, high material removal rates and capability for machining a wide variety of engineering materials, especially metallic alloys [5], has resulted in increased take-up in line with developments and the greater availability of carbide micro cutting tools (end mills, drills etc.) [6]. Additionally during micro milling it is possible to monitor the in-process quality of the component so that problems can be corrected during fabrication [6], a feature that is not available in MEMS.

Finally, micro milling can more cost effective than when employing MEMS technology as it does not require expensive setups such as the use of masks and a clean room environment.

Since the mid-1970's, the Machining Research Group at Birmingham, has been active in hard part machining research using conventional ceramic and PCBN tooling. Much of the work initially centred on both turning and face milling of hardened tool and bearing steels, however, in the early 1990's the research concentrated on high speed end/ball end milling of a wider range of hardened ferrous alloys (D2, D3, H13 etc.). The process eventually replaced much of the traditional die sink EDM application in the mould and die industry. Following the acquisition of a commercial mesoscale high speed machining centre and increased industrial interest, research commenced to evaluate the microscale milling of hardened AISI D2 steel, which is the focus of the work in this thesis.

## **1.2 Aims and objectives**

The overall aim of the project was to evaluate the machinability of hardened AISI D2 (62HRC) cold work tool steel using 0.5mm diameter carbide end mills and to assess the feasibility of microscale mechanical milling for the production of micro moulds and dies.

The specific objectives necessary to achieve the project aim were to;

1. Perform a comprehensive literature review to determine the current status of micro milling research and particularly in respect of hardened steel materials.
2. Evaluate the quality of 'off the shelf' commercial micro endmill tools produced by a range of manufacturers.
3. Quantify and minimise spindle thermal growth errors of the Matsuura LX-1 machine tool.
4. Investigate the influence of cutting speed, feed rate and depth of cut on tool life, surface roughness, burr width and cutting forces.
5. Determine cutting forces and cutting temperatures encountered under micromilling conditions.
6. Assess workpiece surface roughness and integrity including microstructure, microhardness, burr formation and the residual stress of micro milled surfaces.

7. Optimise tool life and surface roughness.
8. Determine the effect of tool coatings and geometry on tool life and workpiece surface roughness.
9. Identify tool wear mechanisms.

The thesis is organised into 6 main Chapters. Chapter 1 gives a brief introduction to the project including background to the work, research aims and objectives and industrial collaborators. Chapter 2 provides a detailed literature review focussing on operational advantages and challenges in microscale milling, machine tools, microtools, cutting mechanisms, related machinability research and design of experiment techniques. Chapter 3 details the experimental design process and test array as well as information on workpiece materials, machine tool, fixturing and equipment, cutting tools, analysis equipment and the statistical analysis procedure employed. Comprehensive results and discussion of the experimental trials are presented in Chapter 4. Finally Chapter 5 highlights the conclusions drawn from the research, while Chapter 6 provides suggestions for future work.

### **1.3 Project sponsors and collaborators**

The research studentship for the author together with additional financial support (bench fee of £6000) was provided by Universiti Teknologi MARA and the Malaysian Ministry of Higher Education. The project also benefitted from the collaboration of Mitsubishi Materials Corporation (MMC) Hardmetal UK Limited, which supplied the micro end mill tooling for the mainstream experiments together with associated technical support and staff time for attendance at formal project meetings. The principal contact and company details for MMC Hardmetal UK are given below.

Adrian Barnacle  
MMC Hardmetal UK, Ltd.  
Mitsubishi House,  
Galena Close,  
Amington Heights,  
Tamworth,  
B77 4AS, England.  
Tel: 01827 312312  
Email: [abarnacle@mitsubishicarbide.co.uk](mailto:abarnacle@mitsubishicarbide.co.uk)

## **Chapter 2: LITERATURE REVIEW**

### **2.1 Micromilling**

#### **2.1.1 Introduction**

The world market value for small scale/miniature commercial products based on micro electro mechanical systems (MEMS)/micro system technology (MST) has, according to Salomon [7], shown a yearly increase of 9% from approximately US\$ 36 billion in 2004 to US\$ 52 billion in 2009. The majority of products however are manufactured by what is commonly known as replication based processes, which are mainly confined to features with planar cross-sections and silicon based materials. Such limitations have therefore led to significant research activity over the past decade on mechanical micro milling, initially with ‘softer’ materials such as copper and aluminium but more recently involving hardened steels ranging from 45HRC – 58HRC [8, 9].

Micromilling is a term that is generally used to describe cutting processes which employ tools with diameters  $\leq 1$ mm. The basic kinematic movements such as rotation of the tool and translational feed motion of the tool through the workpiece are however similar to those in conventional milling. It is apparent from the literature that the current underlying science and technology of microscale mechanical machining is derived from down-scaling of conventional macroscale metal cutting theory. As the diameter of the tool is reduced however, the phenomenon of ‘size effect’ arises, which significantly affects aspects such as cutting forces, tool wear, and chip formation. Anticipated reasons for this are related to the ratio of undeformed chip thickness to cutting edge radius [9-11], and the microstructure of the workpiece material with respect to cutting parameters and tool dimensions [12]. These issues are discussed in greater detail in the following sections.

### **2.1.2 Challenges in micromilling**

There are several challenges in the implementation of micromilling that arise mainly from aspects such as miniaturisation of the cutting tools, the severe and often inconsistent nature of tool wear, inhomogeneity (non-uniformity) of the workpiece grain size, and machine tool errors/accuracy. As the tool diameter is reduced ( $< 1\text{mm}$ ), resistance to the relatively high stress levels is diminished [13], hence unpredictable tool life and premature failure are major problems [14]. The incidence of microtool failure can be further exacerbated by improper design of tool geometry (typically scaled down from macroscale cutters), tool manufacturing process defects, inappropriate substrate material and poor coating quality [15]. Furthermore, the use of unsuitable cutting conditions such as relatively large depths of cut often results in immediate breakage of the tool upon initial contact with the workpiece [9].

Tool wear progression in micromilling generally causes an increase in the cutting edge radius to uncut chip thickness ratio and promotes the incidence of burr formation [16-19]. The generation of burrs not only damages the normally delicate features on the workpiece [18] but may lead to rejection of the manufactured item due to the greater difficulties involved with burr removal operations for micro components [9]. Additionally, an increase in the cutting edge radius (as the tool wears) can alter the mechanics of tool-chip interaction leading to a high negative rake angle and ploughing (elastoplastic) effects, with the former resulting in a significant increase in the axial force [20], and the latter higher workpiece surface roughness levels [17, 21-23]. Details of cutting edge radius effects are further discussed in Section 2.4.2.

The investigation and quantification of wear in micro tools is still a considerable challenge due to limitations in conventional measurement techniques such as optical microscopy [24]. While methods such as scanning electron microscopy (SEM) can provide the necessary magnification and resolution (no depth of field problems etc.), the process is relatively time consuming and inefficient, particularly under experimental conditions where multiple measurements are required at frequent intervals. Apart from tool wear evaluation, the in process monitoring of micromilling operations is critical in order to maintain part tolerances and good surface quality [25], as micro end mills are prone to edge chipping and tool breakage. Online tool wear failure detection techniques using traditional force sensor dynamometry is however extremely difficult due to the magnitude of cutting forces involved in micromilling operations which can be  $< 1\text{N}$  and therefore masked/obscured by background noise.

Numerous researchers have suggested that the process of chip formation during micro cutting does not occur when the uncut chip thickness is smaller than a critical minimum chip thickness (the minimum chip thickness effect will be discussed in Section 2.4.1). Under such conditions, the workpiece material undergoes elastic deformation and ploughing rather than shearing which may cause cutting instabilities.

Unlike macroscale machining processes, the micromilling of multi-phase/heterogeneous materials is greatly influenced by the different grain size of the constituents within the workpiece. The stresses and hence forces encountered as the tool moves between the different workpiece metallurgical phases can vary significantly and cause higher levels of vibration, resulting in chatter or accelerated tool failure [9, 26]. The effects of microstructural grain size are further detailed in Section 2.4.3.

Machine tool errors also play a significant role in the effectiveness of micromilling operations. Common sources of such errors include poor machine design/manufacture, the process environment with respect to isolation/control of vibrational and thermal effects, together with inconsistency in job setup and operation etc. Facilities for accurate/repeatable tool/workpiece referencing is critical for avoiding errors in depth of cut or tool offset setting while tool run-out must be controlled to minimise out of balance forces. [27]. Thermal growth inherent in high speed spindles also presents a challenge which requires the implementation of powerful cooling systems and complex compensation techniques/strategies. Uriarte et al. [28] suggested that micromilling should ideally be carried out on precision machine tools having positional accuracies in the order of  $\pm 0.1\mu\text{m}$  due to the typical tolerances that are required in micro die manufacture, which is between 12 to  $25\mu\text{m}$  depending on their respective applications.

## **2.2 Machine tools**

Typically micromilling involves the use of high speed spindles with rotational speeds of up to  $\sim 160,000\text{rpm}$  but more realistically  $50,000 - 60,000\text{rpm}$  and tooling in the range  $50\mu\text{m}$  to  $1.0\text{mm}$  in diameter. The majority of the commercial micromilling machines however are sold with spindles capable of up to  $50,000\text{rpm}$ , due in part to microtool performance restrictions. For workpiece materials such as stainless steel or aerospace alloys including Ti and Ni alloys, the typical operating spindle speed may be substantially lower than  $10,000\text{rpm}$ . Consequently a more practical solution is a machine capable of using alternative/multiple spindles with one

able to operate at 500 – 50,000rpm and another designed for use at 60,000 - 90,000 or 100,000 – 160,000rpm. An example of a commercial general purpose machine is the Matsuura LX-1 which utilises a 60,000rpm spindle as standard but can be specified with an 80,000rpm unit.

Machine tool price is dependent on specification and additional requirements such as workpiece transfer hardware, number of controllable axes, workpiece probing, number of spindles, vibration isolation and other facilities such as miniature online camera and metrology systems. Such machines are available typically within the range of £150,000 - £400,000 [29] however a cheaper option would be the purchase of a retrofit high speed spindle with associated cooling and control equipment. Spindle systems rated at 60,000, 90,000 or 120,000rpm can be purchased off the shelf for £6,000 - £15,000 depending on the tooling mounting arrangements. Unfortunately, such systems are at best ad-hoc and can present problems in terms of location and fitting requirements, z-axis machine restrictions, axis float and automatic tool changing.

Currently there are broadly three categories of machine tools which are either commercial or research based prototype systems that have been employed for the micromilling of components and parts. These are reviewed in the following section and comprise;

- Conventional ultraprecision machine tools
- Microfactories/meso-scale machine tools (mMT)
- Bench-top ultraprecision machine tools

### **2.2.1 Commercial and research based machine systems**

Ultraprecision machining centres comprise three main sub-systems which are the mechanical structure, spindle - drive arrangement and control system. Most of the experimental research for micromilling has been conducted on either commercial ultraprecision machine tools or prototype systems which have been developed by researchers at universities/research organisations and are widely classified or referred to as meso-scale machine tools (mMT) or bench type machines. Conventional ultraprecision machine tools have several advantages such as superior rigidity for damping of vibrations and high resolution axes control using precision sensors and actuators [30]. Figure 2.1 shows examples of commercially available industrial precision machines with micromilling capability while Table 2.1 details the associated

product specifications. The data and information provides a good comparison of the design, limitations and characteristics of current state of the art commercial ultraprecision systems.

Conversely, Figure 2.2 shows a range of bespoke, laboratory scale meso-scale/bench type machine tools which have been reported in the literature. Such platforms generally utilise lower levels of energy, space and materials compared to their commercial counterparts leading to reduced costs for part fabrication. In addition, mMT systems have higher natural frequencies due to their smaller size and thus a wider range of spindle speeds can be employed without the risk of regenerative chatter. The disadvantages however are that mMT machines tend to have comparatively lower accuracy due to a lack of rigidity and poor resistance against base vibration [6, 31].

Recently, researchers from Brunel University in collaboration with UPL Ltd. developed a bench-top machining centre ( $\mu$ ltraMill) which aims to offer a good compromise between conventional ultraprecision machines and traditional mMT's [32]. The five-axis capable  $\mu$ ltraMill system which has been described as having features similar to commercial machines but with a smaller footprint, purports to fill the gap in the demand for the manufacturing 3D complex micro parts or features with nanometer surface finish. Table 2.2 shows a comparison of the keys characteristics of an ultraprecision machine, bench-top and mMT unit.



Nanotech 350UPL [33]



Makino Hyper2J [34]



Sodick AZ250L [35]



KERN micro [36]



Fanuc Robonano  $\alpha$ -0iB [37]



Kugler Micromaster 5X [38]



Matsuura LX-1 [39]

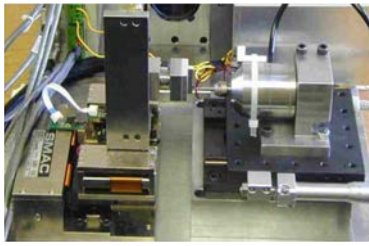
Figure 2.1: Examples of commercial ultra precision machine tools

Table 2.1: Main specifications of commercial ultraprecision machine tools

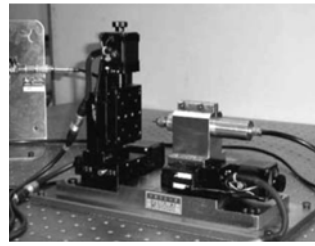
Commercial ultraprecision machine tools							
	Nanotech 350UPM [33]	HYPER2J [34]	Sodick AZ250L [35]	KERN Micro [36]	Robonano $\alpha$ -0iB [37]	Micromaster 5X [38]	Matsuura LX-1 [39]
Company	Moore Nanotech, US	Makino, Japan	Sodick, North America	KERN, Germany	Fanuc, Japan	Kugler, Germany	Matsuura, Japan
Configurations							
Machine size X/Y/Z (m $\times$ m $\times$ m)	1.9 / 1.9/ 2.1	N/A	N/A	2.5 /2.2 / 2.1	1.3 / 1.5 / 1.5	N/A	1.8/ 3.3/ 2.7
Table size (mm)	350X350	300X200	N/A	350X230	280 X 150	N/A	700X500
Axes type	Four axis configuration Three linear axes (X, Y and Z axis), rotary C axis	Three linear axes (X, Y and Z axis)	Two linear axes (X and Y axis)	Five-axes, X, Y and Z linear axes, two rotary axes (B and C axis)	Five-axes, X, Y, Z linear axes, two rotary axes (B and C axis)	Five-axes, X, Y and Z linear axes, two rotary axes (B and C axis)	Three linear axes (X, Y and Z axis)
Travel X/Y/Z (mm)		200/150/150	250/150/100		280/150/40	N/A	330/300/250
Travel B/C		N/A			360 <sup>0</sup> /360 <sup>0</sup>	N/A	N/A
Structure							
Base structure	Cast, epoxy/granite composite	Granite base	Cast iron	Polymer concrete	Cast iron base with concrete	Fine grained granite	Granite base
Column structure	Single	Single		C-frame structure		Single	Single
Vibration isolation	Air isolation system	Granite base for outstanding vibration isolation	N/A	N/A	Air and oil damper	Pneumatic vibration isolation	Granite base for outstanding vibration isolation

Continued

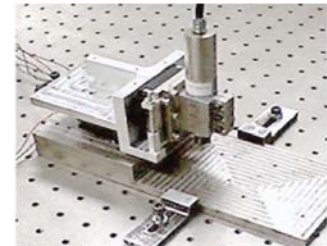
Commercial ultraprecision machine tools							
	Nanotech 350UPM [33]	HYPER2J [34]	Sodick AZ250L [35]	KERN Micro [36]	Robonano $\alpha$ -0iB [37]	Micromaster 5X [38]	Matsuura LX-1 [39]
Company	Moore Nanotech, US	Makino, Japan	Sodick, North America	KERN, Germany		Kugler, Germany	Matsuura, Japan
Control system							
Control system	Delta tau	Fanuc	N/A	Heidenhain	Fanuc	Multiprocessor path control	Fanuc 30i
Spindle							
Spindle type	Air bearing (liquid cooled)	Air bearing	Pneumatic static bearing	Air bearing (oil/air lubricated)	Air bearing	Air bearing	Ceramic bearing (oil/air cooled)
Speed range (rpm)	200–60,000	3000–170,000 40,000 standard	120,000 rpm (Max)	160,000 (Max)	20,000–100,000	100,000 (Max)	80,000 (Max) 60,000 standard
Power (kW)				0.5		N/A	4.5
Spindle motion accuracy	Axial: 50 nm Radial: 50 nm Table feed rate: 2000mm/min	N/A	50 nm	100 nm	100 nm	100 nm	N/A
Motion axes							
Motion axes type	Hydrostatic slides	N/A	Hydrostatic bearing	X, Y and Z (hydrostatic bearing) B axis (mechanical bearing) C axis (Aerostatic bearing)	Aerostatic bearing	X, Y and Z (hydrostatic bearing) B axis (mechanical bearing) C axis (Aerostatic bearing)	N/A



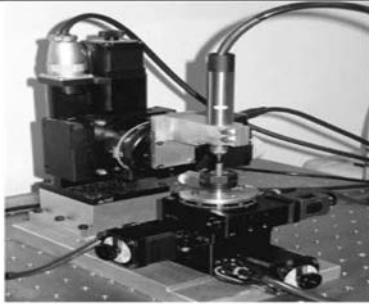
mMT – University of Illinois [40]



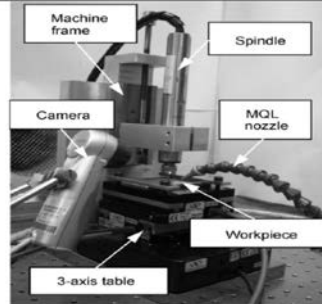
mMT – Shanghai Jiaotong University [41]



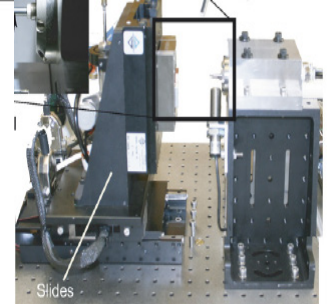
mMT – University of Michigan [42]



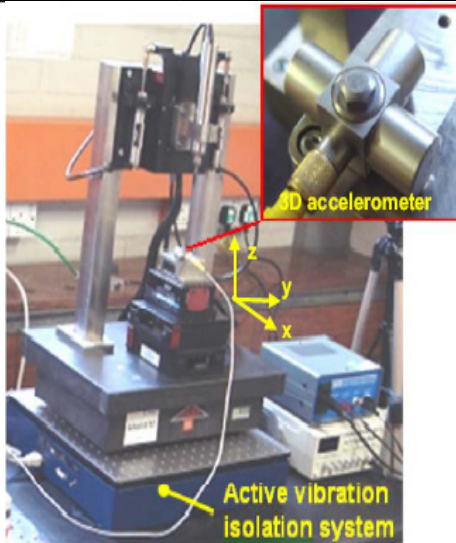
mMT – Seoul National University [43]



mMT-National Taiwan University [44]



mMT - Carnegie Mellon University [45]



mMT- University of Nottingham [46]



Bench-top UltraMill –Brunel University [32]

Figure 2.2: Examples of meso-scale machine tools (mMT) and bench top systems, based in academic institutions

Table 2.2: Comparison between commercial, bench-top and research based micromilling systems

	Commercial ultraprecision machine			Ultraprecision bench-top	Research base miniature machine tool		
Machine	Nanotech 350UPM	HYPER2J	KERN Micro	µltraMill	mMT	mMT-Lee	mMT-Vogler
Company/ University	Moore Nanotech, US	Makino, Japan	KERN, Germany	Brunel University and UPL Ltd.	SJTU, China	University of Michigan, USA	University of Illinois, USA
Overall Size – X/Y/Z (m/m/m)	1.91 m X 1.90 m X 2.13 m high	N/A	2.5 m X 2.2 m X 2.1 m high	1.1 m X 0.8 m X 2.1m high	165mm X 114mm X 250mm	150 X 70 X 140	250mm X 250 mm X 250 mm
Configurations	Four axis configuration Three linear axes (X, Y and Z axis), rotary C axis	Three linear axes (X, Y and Z axis)	Five-axes, X, Y and Z linear axes, two rotary axes (B and C axis)	Five-axes, X, Y and Z linear axes, two rotary axes (B and C axis)	Three precision linear stages	Three linear axes (X,Y, and Z axis)	Three linear axes (X, Y and Z axis)
Base structure	Cast, epoxy/granite composite	Granite base	Polymer concrete	Granite base	N/A	N/A	N/A
Vibration isolation	Air isolation system	Granite base	C-frame structure	Gantry frame	N/A	N/A	N/A
Control system	Delta tau	Fanuc	Heidenhain	Delta tau	PMAC	N/A	SMAC
Spindles	Air bearing	Air bearing	Air bearing	Aerostatic bearing	Air bearing	Air bearing	Air bearing
Speed range (rpm)	200–60,000	3000–170,000	160,000 (Max)	200,000	120,000	145,000	150,000
Spindle motion accuracy	<0.05µm	N/A	<0.1µm	< 1.0 µm	≤1µm	≤1µm	≤1µm

## 2.2.2 High speed spindle specifications

The characteristics of a machine tool spindle such as the power, rotational speed, stiffness, bearings, drive methods and thermal properties, have a huge impact on the overall machine tool performance and quality of the fabricated product. In general, there are four main types of spindles which are categorised according to their drive mechanism, namely belt-driven, gear-driven, direct drive and integrated drive spindles. Similarly, spindle motion is supported by bearings of various design/shape (taper, roller, angular etc.) and operating principle (magnetic, hydrostatic, hydrodynamic and aerostatic).

Bearings typically used in commercial machine tools are made from conventional steel although recently, hybrid-ceramic bearings have seen an increase in utilisation. Table 2.3 gives a comparison between the physical/mechanical properties of steel and ceramic ball bearings. The likely reasons for this shift include the superior performance (30% faster, 40% lower weight and 100% longer service life than steel balls) and lower level of friction coefficient of the ceramic based materials [47].

Table 2.3: Properties comparison between steel and ceramic balls bearing [47]

Properties (units)	Conventional steel bearing	Hybrid ceramic (Si <sub>3</sub> N <sub>4</sub> ) bearing
Young's modulus (GPa)	208.00	315.00
Hardness (Vickers, Rc)	60.00	78.00
Density (g/cm <sup>3</sup> )	7.80	3.20
Maximum usage temperature (°C)	120.00	800.00
Coefficient of expansion (10 <sup>-6</sup> /K)	11.50	3.20
Poisson's ratio	0.30	0.26
Thermal conductivity (W/mK)	45.00	35.00
Chemically inert	No	Yes
Electrically conductive	Yes	No
Magnetic	Yes	No

The majority of high speed machine tools are equipped with motorised spindles. A considerable amount of research has been conducted towards the development and continuous improvement of such spindles [48-50]. Abele et al. [51] in a recent keynote publication detailed the historical development, recent challenges and future trends of motorised spindle units. They suggested that future spindle technology will likely incorporate integrated sensor actuators for condition monitoring in order to better detect and correct deviations/errors during machining. Furthermore they also reviewed recent research

developments and modelling methods for the thermal and dynamic behaviour characterisation of spindles. Another notable innovation has been that by Borisavljevic et al. [52], who developed a novel integrated permanent magnet motor coupled with active magnetic bearings for driving a high speed micromilling spindle.

Conventional high speed spindles differ from ultra high-speed air bearing spindles (above 150,000rpm) typically used in meso-scale machine tools, see Table 2.4. The differences are not only due to their relative size and power consumption but also in maximum rotational speeds achievable and distribution of its power between cutting processes and that needed to overcome the friction of the spindle’s bearings. Whereas the majority of spindle power expended in macromachining is for cutting, only a small percentage of the spindle’s total energy is used to form the chip in micromilling [53]. The remainder is utilised to overcome the bearing inertia which generates a considerable amount of heat and contributes towards spindle growth and process inaccuracies. This however can be effectively counteracted in most cases by employing active cooling systems and implementing adaptive compensation algorithms based on recorded spindle deformation rates during operation.

Table 2.4: Comparison between a typical conventional high speed spindle and ultra high-speed air bearing spindle

	Conventional high speed spindle	Ultra high-speed air bearing spindle
Application/spindle manufacturer	Ultraprecision milling machine Matsuura LX-1	Meso-scale machine tool Nakanishi Xpeed1600
Spindle type	Motorised spindle	Air turbine spindle
Maximum output power (W)	4500	56
Maximum speed (rpm)	60,000	160,000
Bearing type	Ceramic bearing	Air static bearing
Diameter size (mm)	300	40
Weight (g)	N/A	520

### 2.2.3 Thermal based machine tool errors

Machine tool errors can broadly be classified as either quasi-static or dynamic [54]. Quasi-static errors (linear, angular, straightness, squareness) are geometric based discrepancies where the relative position between the tool and workpiece varies slowly over time and is typically related to the structure of the machined tool [55]. Sources of such errors include thermal effects, machine tool design and static loading. Conversely dynamic errors are caused by spindle motion run-out, controller limitations, vibrations of the machine structure and

deflection under inertial forces. These can generally be controlled by proper damping, rigid machine construction and employing appropriate operating conditions during cutting.

Bryan [56] estimated that quasi-static errors account for approximately 70% of the total positioning errors of a machine tool while Zhao et al. [57] found that the heat generated from high velocity tool spindles is the major contributor of thermal errors. Weck et al. [58] also highlighted that spindle growth in the axial direction can easily reach 100 $\mu$ m and in some cases, beyond this figure.

Thermally induced errors are highly time-variant and non linear, due to non-uniform temperature fluctuations in the machine structure [59], which compromise accuracy and dimensions of the part under fabrication [60]. Internal heat sources which can cause thermal deformations include the ball screw, bearings, nuts, axis drive motors, friction during cutting and the flow of the coolant/lubricating oil [61]. The effects from changing temperature distributions can be further classed as either position independent thermal errors (PITE) or position dependent thermal errors (PDTE) [62, 63]. PITE are a function of temperature but not the machine axis position and is affected by the rate of change of the PITE relative to the time taken to produce a part. Conversely, PDTE are influenced by both the axis position as well as temperature and can effectively alter the linear positioning of the machine. Each machine element will however have different thermal time constants which are likely to distort at different rates and magnitudes [63].

Figure 2.3 shows the various thermal effects present in machine tools which can be divided into six sources [56]: i) heat generated in the cutting process; ii) heat generated by the machine; iii) heating or cooling influenced by various cooling systems; iv) heating or cooling influenced by the room; v) the effect of people; and vi) thermal memory/history from any previous environment. Energy output from these sources can be transmitted through conduction, convection and radiation to create a uniform and non-uniform temperature field within the machine structure.

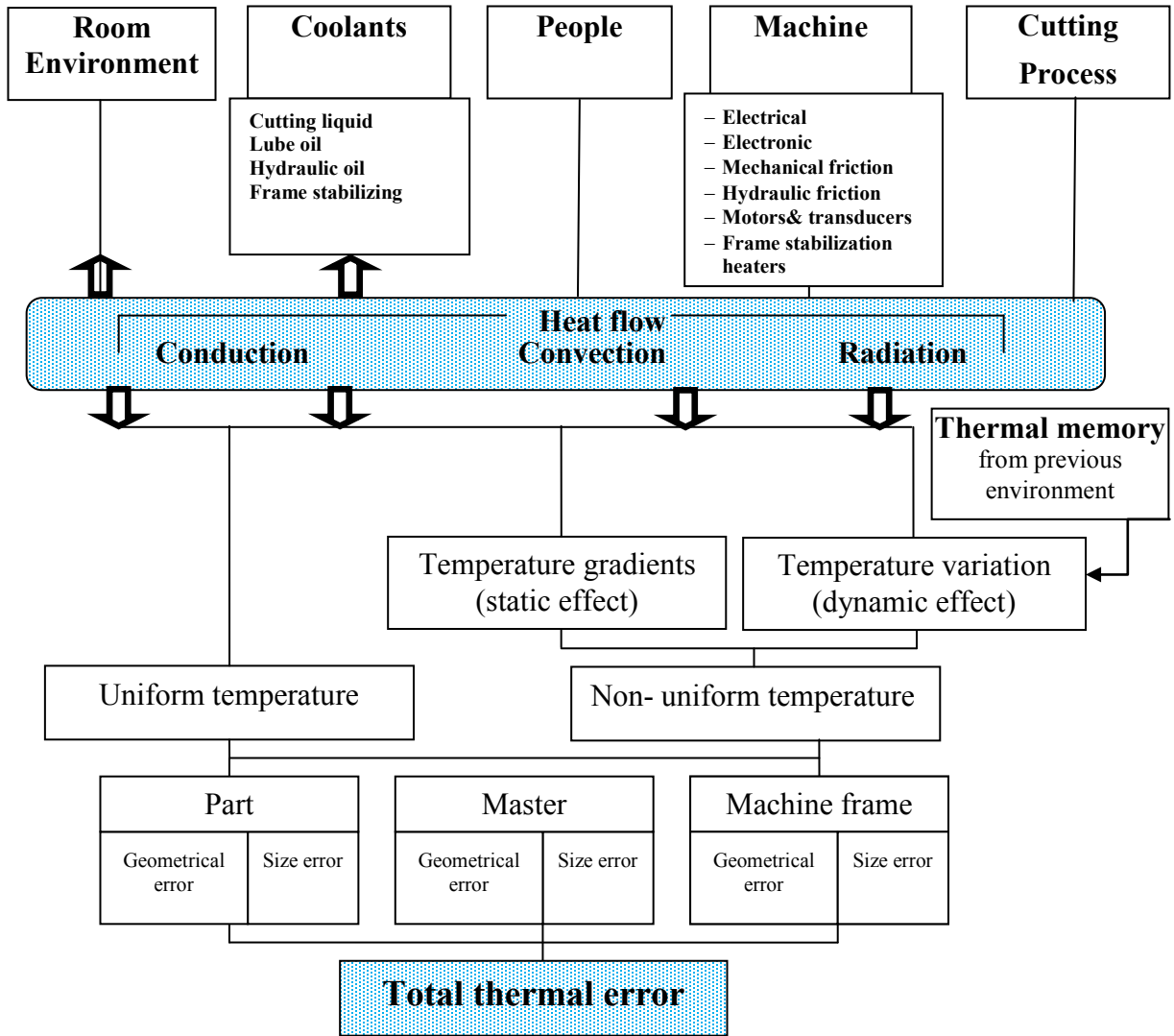


Figure 2.3: Thermal effect diagram [56]

Creighton et al. [53] proposed three primary means for counteracting thermal errors which can be categorised as elimination or avoidance, resistance and control, and compensation techniques. The first method aims to eliminate any change in dimension through symmetric design of the machine tool structure and has to be implemented during the design phase. The second approach looks to reduce and/or oppose any change in dimensions via the use of selected materials and components that generate very low amounts of heat in operation. Both of the aforementioned techniques however are only employed up to and during the build phase of the machine tool. Therefore dynamic compensation techniques are necessary to deal with interactive errors which arise during machining in order to preserve the quality and dimensional accuracy of produced parts. These can be applied to the machine tool either by direct or indirect measurement compensation methods [63]. With the former, drift displacements between the tool and workpiece are measured directly using an interferometer,

while for the latter a mathematical model is employed to calculate the displacement based on measurements taken (spindle speed and temperature) as the model inputs.

An extensive amount of work has been conducted towards formulating various compensation solutions in order to offset thermally based spindle displacement. A multitude of analytical/computational and experimental methodologies have been employed by various researchers and include dynamic simulation [57, 64], finite element method (FEM) [65], multi-variant regression analysis [66, 67], artificial neural network and direct displacement measuring systems [50]. Bissacco et al. [68] defined a procedure in developing spindle thermal growth calibration curves (recording the temperature using K-type thermocouples at which the tool length correction is performed) for optimal control of z-axis error in a high speed attachment spindle, while predicted results from a micromilling spindle thermal growth model developed by Creighton et al. [53] was found to agree closely with experimentally observed data. It was also reported that the model was successful in reducing spindle growth by up to 80% during laboratory based trials, which could be easily implemented in an industrial environment with minimal investment of time, material and personnel.

In general, the majority of work detailed in the literature has focussed on medium to large scale spindles. Further investigation is required on effective spindle growth compensation methods for miniaturised machine tools used in micromilling applications.

## **2.3 Microtools**

Current commercial micro endmills showed that the geometry of micro endmills is mainly derived from macro endmills, see Figure 2.4. Fabrication of micromilling cutters is a challenging task due to their relatively small size. Common defects associated with these tools are geometric deviations/irregularities and poor resolution/integrity of the cutting edges. Several researchers have investigated the manufacture of microtools, the processes used including focused ion beam (FIB) [69-71], wire electrical discharge grinding (WEDG) [72-74] and abrasive grinding processes [75-77]. Schmidt et al. [78] presented a comprehensive performance comparison between FIB, laser ablation, WEDG and grinding in the production of microscale cutting tools. They suggested that FIB offered superior tolerance control compared to the other methods but with lower material removal rates and at significantly greater cost. More recently Yan et al. [79] employed wire EDM operations to fabricate micro end mills with an error of  $< 1\mu\text{m}$  on geometrical features and roundness of cutting edges.

While some of the techniques discussed have been proven in a laboratory environment, the conventional mass production method for the manufacture of cemented carbide tools in industry is by mechanical grinding using diamond abrasives [75], giving a typical tolerance of  $\pm 10\mu\text{m}$  even for cutters as small as  $100\mu\text{m}$  diameter.

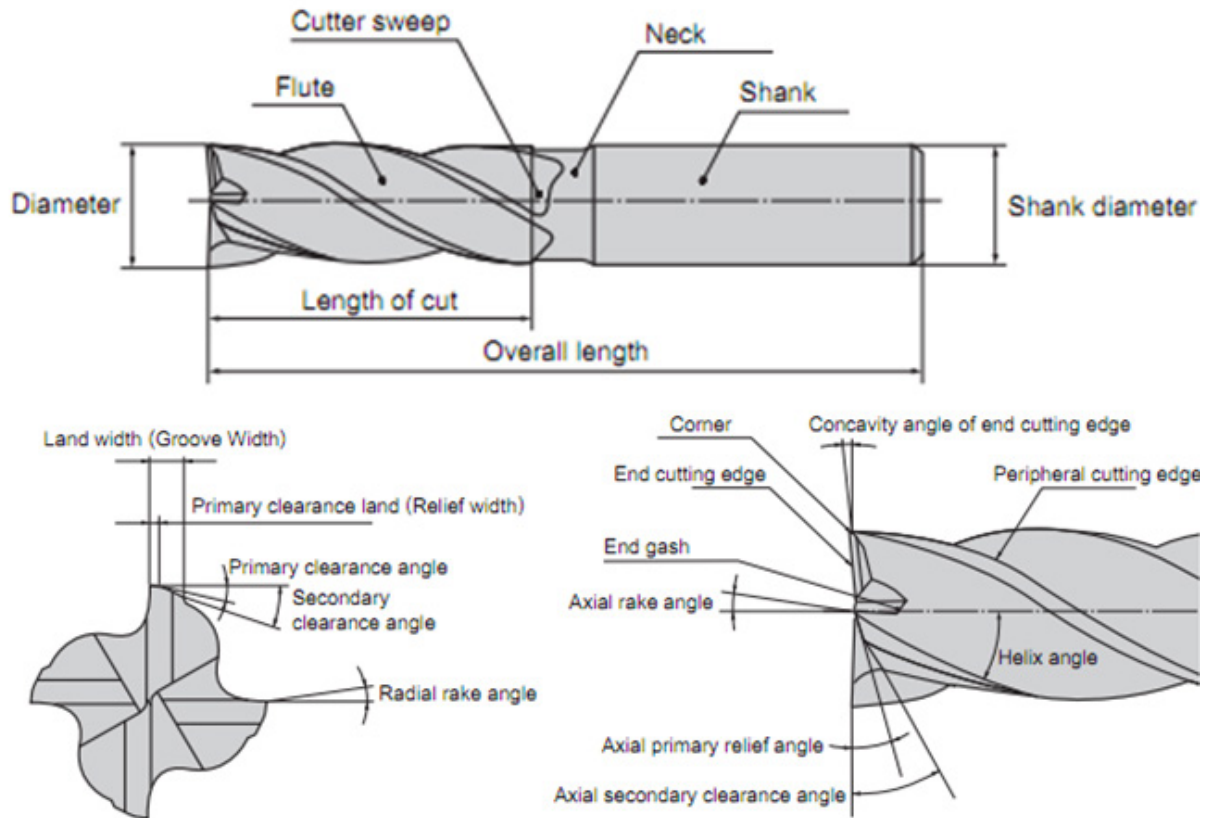


Figure 2.4: Typical end mill tool geometry [80]

### 2.3.1 Material, geometry and design

The main characteristics of cutting tool materials are hardness, toughness, wear resistance, chemical stability and fatigue resistance coupled with high compressive, tensile and shear strength [81, 82]. The three main groups of tool materials are high speed steel (HSS), cemented tungsten carbides (WC) and ceramic/super hard materials. This is in the order of decreasing toughness with HSS ( $18\text{MJ/m}^3$ ) being twice as tough as WC ( $10\text{MJ/m}^3$ ), and  $\sim 3$  times tougher than conventional ceramics ( $6.5\text{MJ/m}^3$ ) [83]. A comprehensive review of cutting tool materials and coating processes was reported by Byrne et al. [84]. Table 2.5 details selected mechanical/physical property values for a range of hard materials that are utilised in cutting tools while Figure 2.5 shows the relationship between the various cutting

tool materials in relation to their hardness and toughness. Carbide based materials possess the best balance of properties.

The hard tungsten carbide particles in cemented carbide tooling are held together by a metallic binder which is normally Co. The sintering temperature is typically above 1300°C [85]. Tungsten carbide is generally preferred for micromilling due to its favourable combination of hardness and strength over a broad temperature range [6]. Nevertheless, alternative materials such as cubic boron nitride (CBN) have been applied for the high speed milling of hardened steel and other difficult-to-cut materials.

Table 2.5: Cutting tool material properties [80]

Materials Type	Hardness (Hv)	Thermal Conductivity (W/m • K)	Thermal Expansion ( $\times 10^{-6}/K$ )*	Tool Terminology/Group
Diamond	>9000	2100	3.1	Diamond
c-BN	>4500	1300	4.7	Cubic Boron Nitride
Si <sub>3</sub> N <sub>4</sub>	1600	100	3.4	Ceramic
Al <sub>2</sub> O <sub>3</sub>	2100	29	7.8	Ceramic
TiC	3200	21	7.4	Cermet
TiN	2500	29	9.4	Cermet
TaC	1800	21	6.3	Cermet
WC	2100	121	5.2	Cermet

\*  $1W/m \cdot K = 2.39 \times 10^{-3} cal/cm \cdot s \cdot ^\circ C$

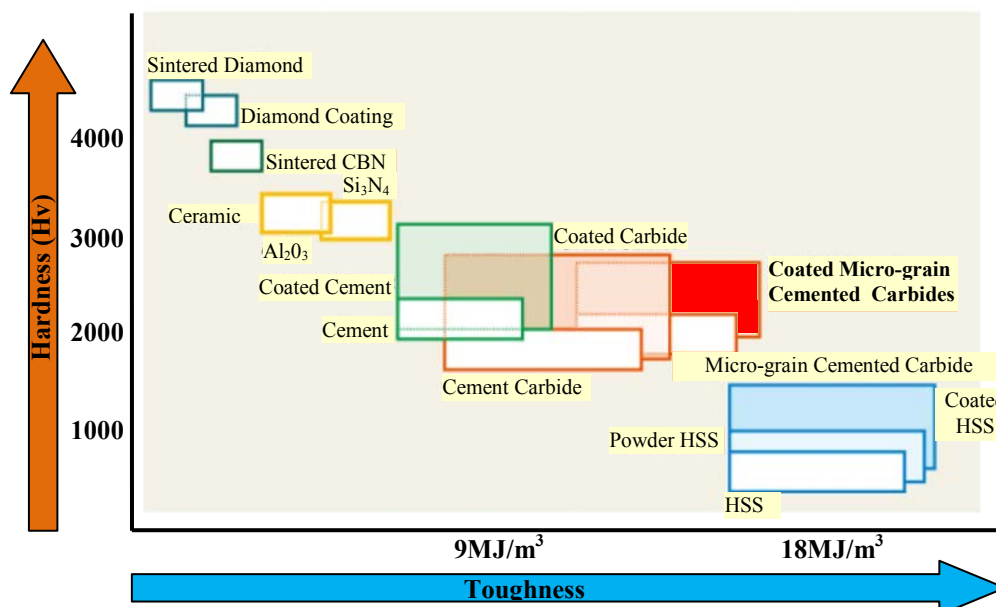


Figure 2.5: The relationship between various tool materials in relation with hardness and toughness [80].

Several studies relating to the influence of tool geometry when micromilling have been performed which have included the work of Fleicher et al. [86], Fang et al. [87], and Li et al. [88]. Fleicher et al. [86] micro milled brass with a single-edged tool in order to overcome relatively high manufacturing tolerances ( $\pm 10\mu\text{m}$ ) of current commercial micro tools. Their experimental results showed better process stability with a well defined contact condition. Fang et al. [87] attempted to investigate the determining factors leading to tool breakage through FEM simulation and experimental work. They concluded that microtool failure was principally due to the relative weakness of the cutter body and the fact that only a small portion of the tool tip was used in cutting. Furthermore, the ratio between tool run-out to diameter can be significantly higher in micromilling compared to conventional cutting. As a result, the force variations are significant. Li et al. [88] examined a range of commercial micro endmills and highlighted that their design and geometry were mainly derived from standard tooling. Based on their experimental observations, they concluded that current available products were not suitable for micro hard milling applications. With the aid of FEM, Li et al. [88] proposed that micro endmills should be fabricated with a negative rake angle in order to increase the strength of the cutting edge corner. Initial testing of the new design showed an improvement in tool life from 1.52m to 9.04m cut length when machining SAE H11 with a cutting speed of 47.1m/min, feed rate of 360mm/min and 0.07mm depth of cut.

### **2.3.2 Coated and uncoated tooling**

Approximately 80% of WC tooling currently supplied is coated. Coatings enhance the physical/mechanical properties of tools providing greater hardness and in some instances thermal conductivity, which improves the substrate material's resistance to chemical and abrasive wear [82, 89]. Other benefits are lower surface roughness which reduces the coefficient of friction compared to uncoated tools [89]. Coatings are reported to double the life and improve cutting performance of micro end mills [90], particularly when machining hardened tool steel. While TiAlN with an ultra fine grain size of  $< 0.5\mu\text{m}$  [82] is generally selected/preferred, other commonly employed coating materials include titanium nitride (TiN), titanium carbide (TiC), titanium carbonitride (TiCN), chromium nitride (CrN) and chromium titanium aluminium nitride (CrTiAlN), see Table 2.6 for associated properties.

Table 2.6: Coating characteristics [81]

Coating	Friction coefficient	Hardness (HV)	Roughness (nm)	Adhesion failure load (N)
TiN	0.46	2738	21	60
TiCN	0.16	3178	23	48
TiAlN	n/a	2949	30	40
CrN	0.31	n/a	12	60
CrTiAlN	0.31	3419	35	60

*\*All tools were PVD coated*

Generally, coating thicknesses typically varies in the range 2 – 10 $\mu$ m. The coating is applied on the substrate material either through chemical vapour deposition (CVD ~ 1000°C), physical vapour deposition (PVD ~ 500°C) or medium-temperature chemical vapour deposition (MTCVD ~ 700°C), the latter utilised particularly to improve transverse rupture strength [91]. The quality of coating deposition on microtools is critical in order to achieve the required workpiece surface finish and realise the advantages of coatings. Aramcharoen et al. [92] performed a comparative study to evaluate the influence of multilayer AlCrTiN coated and uncoated tools on machined surface topography. It was found that even after 1000mm length of cut, the coated tool gave a lower surface roughness due to its superior wear resistance compared to the uncoated tool. In subsequent research, Aramcharoen et al. [89] also studied the performance of hard and more complex coatings (TiN, CrN, TiCN, TiAlN and CrTiAlN) in relation to chipping and cutting edge radius wear when using 0.5mm diameter tools. The results suggested that TiN was the preferred coating when micro-milling AISI H13 (45HRC) in contrast to TiAlN or CrTiAlN products, which are favoured when using larger end mills. Anticipated reasons for this relate to the level of coating adhesion and the fact that oxidation performance was thought unlikely to be a significant factor.

### 2.3.3 Tool quality and size accuracy

The majority of published micromilling research have employed cutters with diameters in the range of 0.3mm – 1.0mm [9, 18, 92, 93]. As previously highlighted in Section 2.3, the main fabrication technique for micro tools is abrasive grinding, which limits the size of the cutting edge radius that can be generated, depending on the wheel grit and carbide grain size. The use of coatings further enlarges the edge radius, which can affect the overall tool profile. Experience has shown that the quality of microtools are highly inconsistent in terms of geometric tolerance with manufacturing process flaws such as adverse grinding marks and coating defects commonly appearing even within the same production batch. Similarly,

Aramcharoen and Mativenga [11] reported that approximately 60% of micro tools from any given batch were unacceptable due to chipping, cracking, incorrect geometry (rake angle etc.) or having a larger than specified cutting edge radius. Therefore the inspection of micro cutters is strongly recommended prior to commencement of machining. As reported in the literature, commercial microtools that are available 'off the shelf' are routinely quoted to have manufacturing tolerances (diameter) of  $\pm 10\mu\text{m}$  [78, 94, 95]. Kahnis and Weinert [96] measured the cutting edge radius using a confocal white light microscope and found it to be in the range of 1-2 $\mu\text{m}$  for uncoated and 6-7 $\mu\text{m}$  for coated tools. All measures were independent of the tool diameter. Weinert et al. [97] found that the cutting edge radius cannot be reduced by an equivalent ratio as the tool diameter due to the minimum grain size of cemented carbide (scaling effects). They suggested that the cutting edge radius is effectively larger for smaller diameter tools due to the grain size of cemented carbide and thickness of any applied coating.

## **2.4 Factors affecting cutting mechanisms in microscale machining**

Microscale machining is fundamentally different from macroscale cutting, not least in terms of the chip formation process, cutting force levels and operating conditions. There are several factors which distinguish the cutting mechanism in microscale machining including the minimum chip thickness criterion to enable chip formation, cutting edge radius effects together with microstructure and grain size of the workpiece material. These aspects are discussed in greater detail in the following sections.

### **2.4.1 Minimum chip thickness criterion and chip formation**

The minimum chip thickness value in an orthogonal cutting configuration can be defined as the smallest uncut chip thickness that can be removed from the workpiece for a given cutting edge radius under stable conditions [98]. A similar definition was proposed by Özel et al. [99] for micro slot milling, which was the minimum uncut chip thickness necessary for material shearing to occur at a given rotation angle. As the tool diameter and depths of cut become smaller in microscale machining, the ratio of the tool edge radius to the uncut chip thickness increases. At a critical value, surface ploughing dominates rather than conventional shearing/removal of the workpiece material. The uncut chip thickness under such conditions is referred to as the minimum chip thickness criterion, below which chip formation does not occur. The minimum chip thickness is typically a fraction of the cutting edge radius [100] and

strongly depends on the material properties where ductile materials tend to experience higher values [101]. The value of minimum chip thickness has a direct impact on surface roughness [12, 22], cutting forces [102] and process stability [103].

Ikawa et al. [98] postulated that the significance of the minimum chip thickness parameter was in determining whether stable chip formation/removal occurred when face turning electroplated copper with 5 $\mu$ m depth of cut using a diamond tool with an edge radius of 10nm. Weule et al.[22] identified the existence of the minimum chip thickness and its influence on achievable surface roughness when micromilling SAE1045 steel using tungsten carbide tools with a 5 $\mu$ m cutting edge radius. The topography of the machined surface was measured with a laser-based topography measuring device. A saw-tooth-like profile, see Figure 2.6 was observed which was attributed to the minimum chip thickness effect. They further estimated the minimum chip thickness to cutting edge radius ratio to be 0.293.

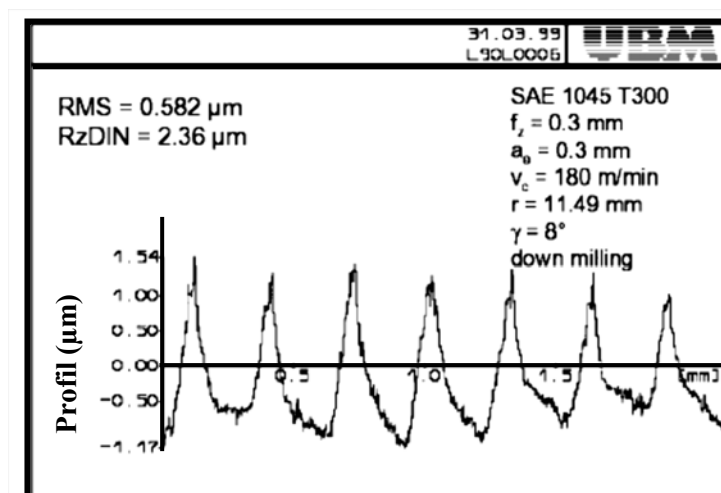


Figure 2.6: Measured surface topography [22]

Kim et al.[104] performed an experimental study to prove the existence of a minimum chip thickness value in micromilling brass, using 635 $\mu$ m micro end mills with feed rates range from 0.188 to 6 $\mu$ m/tooth. The collected chips were examined using SEM which was used to estimate the length, width and thickness of the chips. The chip volumes were then estimated using the trapezoidal numerical integration formula and compared with the nominal chip volume for different feed rates. It was found that for very small feed rates, the measured chip volume was much larger than the nominal chip volume, indicating that a chip was not formed with each pass of the cutting tooth. Further evidence was also obtained by examining the distance between feed marks on the machined surface. For a small feed per tooth, the distance

between feed marks was found to be much larger than the feed per tooth, which also indicated that chips did not necessarily form with each pass of the tool. Recently, Mian et al. [105] employed an acoustic emission technique in order to estimate the minimum chip thickness when micro machining a multi phase steel. The authors identified a relationship between chip formation and acoustic emission (AE) signals to determine the minimum chip thickness. They found the ratio between minimum chip thickness to cutting edge radius was in the range of 0.247 – 0.355 for AISI 1045 steel.

In terms of a modelling based approach, Kim et al. [106] developed a static model of chip formation incorporating the feed per tooth in order to study the chip formation in micromilling. The periodicity of cutting forces coupled with wavelet analysis was used as an indirect technique for estimating the minimum chip thickness which was found to be within the range of 11% – 40% of cutting edge radius. The authors also concluded that a local maximum of radial thrust force was present during the non-cutting regime as the feed per tooth was in the order of the minimum chip thickness. Son et al. [107] proposed an analytical model which takes into account the friction coefficient at the tool-workpiece interface to predict the minimum chip thickness during micro cutting, assuming continuous chip formation. The proposed model was used to determine the minimum chip thickness of brass, aluminium and oxygen free high thermal conductivity copper (OFHC), which was found to be within the range of 0.10 - 0.20 $\mu$ m. The model was validated by experimental square section grooving using a diamond tool (1mm width) and was found to match closely with the experimental results. Liu et al. [108] employed the Johnson-Cook model which incorporated the effects of thermal softening, strain hardening, cutting velocity (135 and 240 m/min) and tool edge radius (1 - 4 $\mu$ m) in order to predict the minimum chip thickness. In order to validate the proposed model, micromilling of AISI 1040 steel was performed using 508 $\mu$ m diameter end mills with a 100 $\mu$ m depth of cut. Both the experimental and simulated results were close, where the ratio between minimum chip thickness to cutting edge radius fell within the range of 0.2-0.4. Özel et al. [99] subsequently utilised the model by Liu et al. [108] in order to estimate the minimum chip thickness for a given tool edge radius (1, 3 and 5 $\mu$ m), feed per tooth (1.27, 2.54 and 5.08 $\mu$ m) and cutting speed (120, 240 and 360 m/min). The estimated minimum chip thickness to cutting edge radius ratio within the range of 0.3 – 0.36 for machining AISI 4340 steel was validated by the experiment. They also found that the chip formation angle (shear angle) for steel was smaller than aluminium due to the former's higher

modulus of elasticity, which limited elastic deformation and hence plastic flow commenced at a lower uncut chip thickness. Lai et al. [109] developed a finite element model which considered the size effect due to material behaviour, tool geometry, fracture characteristics and friction at the secondary shear zone in order to determine the minimum chip thickness. They proposed that the ratio of minimum chip thickness to cutting edge radius is 0.25 when microcutting OFHC.

Table 2.7, shows a summary of both experimental and modelling investigations by various researchers to determine the minimum chip thickness when micromachining. In general, the ratio between minimum chip thickness to cutting edge radius was between 0.1-0.45, depending on cutting conditions/operations.

Table 2.7: Summary of key research publications relating to investigation of minimum chip thickness

Authors	Tool diameter (mm)	Cutting edge radius ( $\mu\text{m}$ )	Ratio minimum chip thickness to tool edge radius	Year
Experiment				
Ikawa et al. [47]	N/A- Turning	N/A	0.10	1991
Yuan et al. [100]	N/A- Turning	0.3	0.25	1996
Weule et al. [22]	N/A- Turning	N/A	0.29	2001
Jaffery et al. [110]	0.5	1.0	0.40	2010
Mian et al. [105]	2.0	0.84	0.20	2010
Modelling				
Shimada et al. [101]	N/A- Turning	N/A	0.10	1993
Kim et al. [106]	0.6	3.0	0.11 – 0.40	2004
Vogler et al. [12]	0.5	2 - 5	0.20	2004
Son et al. [107]	N/A- Turning	0.5	0.10 – 0.20	2005
Liu et al. [108]	0.5	2.3	0.20 – 0.40	2006
Özel et al. [99]	N/A- Turning	5.0	0.36	2007
Lai et al. [109]	N/A- Turning	2.0	0.25	2008
Woon et al. [1]	N/A- Turning	8.0	0.26	2008
Sun et al. [111]	N/A- Turning	3.0	0.44	2009

Vogler et al. [102] experimentally studied the effects of varying feed per tooth on cutting forces in micromilling ductile iron using 500 $\mu\text{m}$  micro end mills with feed rates ranging from 0.25 to 3.0 $\mu\text{m}/\text{tooth}$ . The frequency spectrum of the force was found to contain a component that was a subharmonic of the tool passing frequency, at a feed rate less than the minimum chip thickness, as shown in Figure 2.7. This (subharmonic) frequency component was reflected in the time domain as a repeated pattern every  $n=3$  tooth passes (for case studied).

Because of the minimum chip thickness effect and when machining at a small feed rate ( $0.25\mu\text{m}/\text{tooth}$ ), the chip thickness accumulated and the force increased with each tool pass for  $n$  tooth passes until the chip thickness was greater than the minimum chip thickness. Vogler et al. [12] also formulated an analytical relationship between the cutting edge radius and workpiece microstructure of a single phase material in order to study the effect of minimum chip thickness on surface roughness. After determination of the minimum chip thickness to cutting edge radius ratio (from FE simulation) as being 0.2 and 0.3 for pearlite and ferrite respectively, the model was deployed to predict the surface profile of both materials. The authors identified the existence of an optimal feed rate ( $2\mu\text{m}/\text{tooth}$ ) in terms of surface roughness, due to a trade-off between the feed rate and the minimum chip thickness effect, as shown in Figure 2.8. They found a significant effect of minimum chip thickness on the surface roughness which was dominant at lower values of feed rate ( $0.25\mu\text{m}/\text{tooth}$ ) due to ploughing.

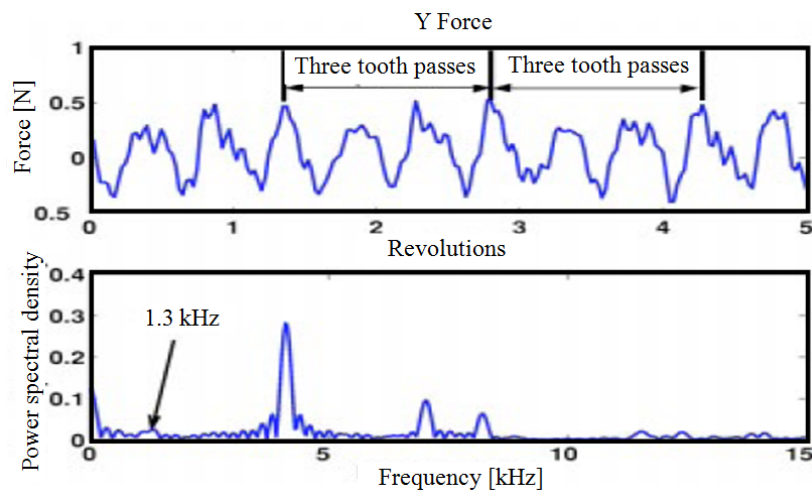


Figure 2.7: Experimental Y force (normal to the feed force) and the corresponding power spectrum at feed rate  $0.25\mu\text{m}/\text{tooth}$  [102]

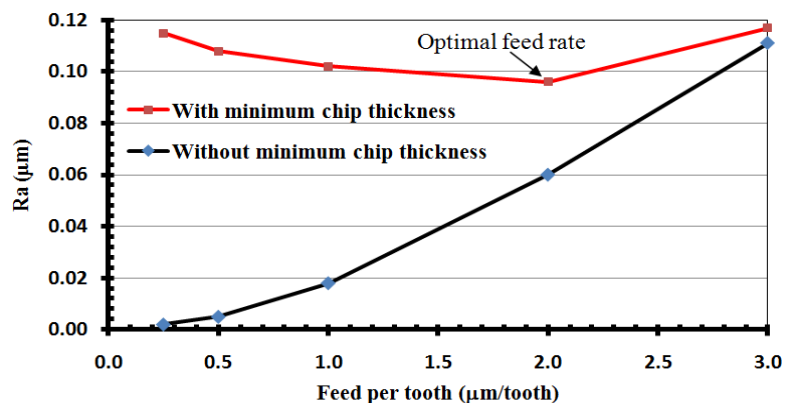


Figure 2.8: Comparison of surface roughness  $R_a$  measurements with and without the minimum chip thickness effect [12].

A dynamic model (cutting force) was devised by Jun et al. [103] in order to investigate the influence of minimum chip thickness and elastic recovery on micromilling stability over a range of feed rates (0.1 – 3.0  $\mu\text{m}/\text{tooth}$ ) for which the cutting mechanisms varied from ploughing to shearing. The model was validated against experimental results obtained following machining of pearlite and ferrite workpiece materials. Based on the recorded chip load and force data [112], the minimum chip thickness and thrust force levels for ferrite was higher than pearlite as shown in Figure 2.9. The increase in thrust force was due to a higher level of ploughing involved as a result of the greater ductility of ferrite. It was also observed that process instability/vibration was apparent at low feed rates and small axial depths of cut due to elastic recovery of the workpiece material during cutting. Biermann and Baschin [113] carried out micromilling trials on EN AW-2007 aluminium alloy using 1.0mm diameter tools with varying cutting edge radii (1.0 and 4.5 $\mu\text{m}$ ). They found that process/chatter stability in micromilling was heavily influenced by the cutting edge radius and minimum chip thickness. This aspect was reinforced by Dornfield et al. [10] who stressed the importance of selecting appropriate operating parameters (cutting speed, feed rate, doc etc) when cutting with small diameter tools.

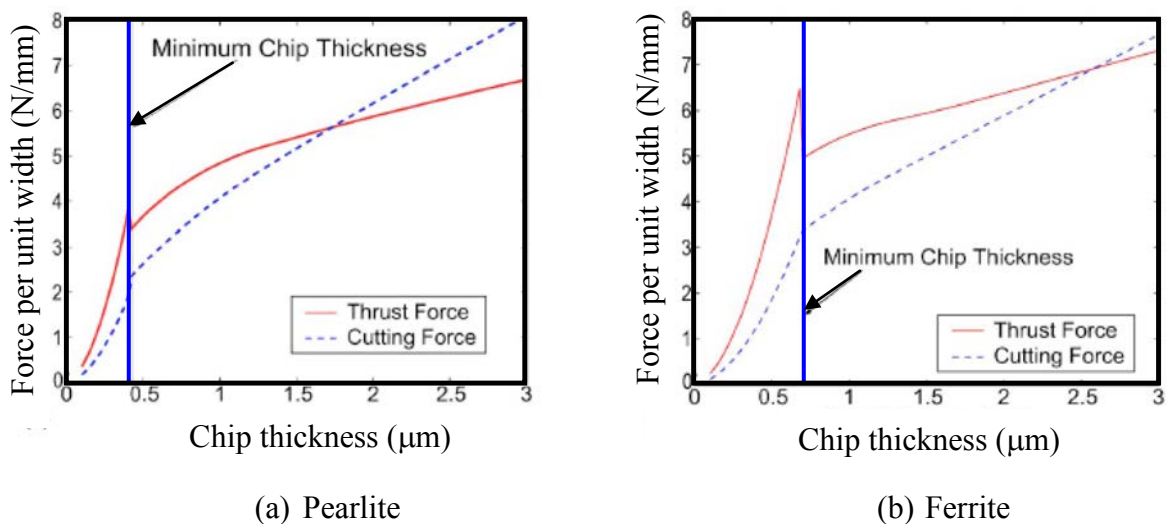


Figure 2.9: Comparison chip load/force relationship: (a) Pearlite (b) Ferrite [112]

Chae et al. [6] illustrated the three common chip formation mechanisms observed when micromachining as shown in Figure 2.10. In conditions where the specified uncut chip thickness,  $h$ , is smaller than the minimum chip thickness,  $h_{\min}$ , see Figure 2.10(a), the material is typically compressed and elastically deformed as the tool passes over the

workpiece. Therefore no material is removed from the surface in the shape of chips. As the uncut chip thickness approaches the critical chip thickness however, chips begin to form via shearing albeit with some elastic deformation still occurring, see Figure 2.10(b). As a result, the removed thickness of the workpiece is less than the desired depth of cut. When the uncut chip thickness increases beyond the minimum chip thickness value, the elastic deformation phenomena decreases significantly and chip formation proceeds in the conventional manner, see Figure 2.10(c). Woon et al. [1] also attempted to investigate the chip formation mechanism and corresponding workpiece stress when micro machining AISI 4340 steel using an Arbitrary Lagrangian-Eulerian (ALE) based FE model. It was shown that at the critical ratio (0.2625) of undeformed chip thickness to cutting edge radius, chips were formed through extrusion in the deformation zone along the rounded edge radius, as a result of a highly negative effective rake angle, see Figure 2.11. A small amount of material however was also pushed by the tool edge radius back onto the machined surface which led to residual compressive stresses.

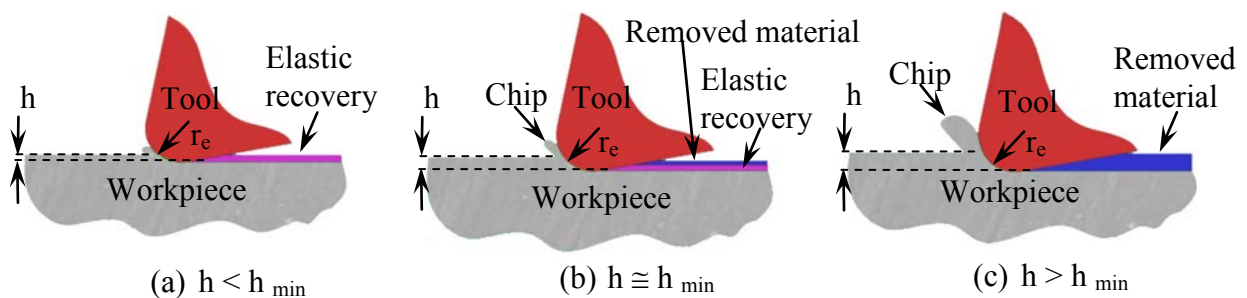


Figure 2.10: Chip formation relative to minimum chip thickness in microscale machining: based on [6]

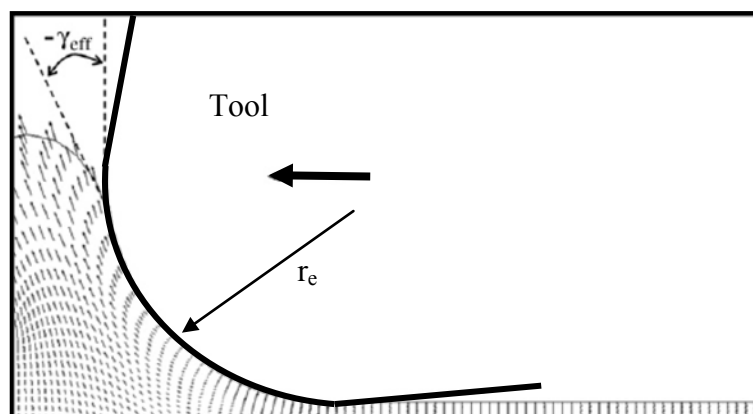


Figure 2.11: Formation of a highly negative effective rake angle ahead of the rounded tool edge at the critical ratio  $h/r_e=0.2625$  [1]

Filiz et al. [17] applied the minimum chip thickness concept to explain the cutting mechanism in micro slot milling. Here the term instantaneous uncut chip thickness, ( $h_{inst}$ ), was used to describe the changing chip size, which varies from zero at initial engagement, to a maximum value (equal to feed per tooth) at the centre of the slot and reduces back to zero at tool exit. Figure 2.12, illustrates the progression of material removal over a single revolution of a 2 fluted cutter. At the start of rotation of the first flute, no material is removed as the instantaneous uncut chip thickness is below the minimum chip thickness value, see Figure 2.12(a). As cutting proceeds,  $h_{inst} > h_{min}$  and the workpiece is sheared as shown in Figure 2.12(b). When the flute approaches the end of its contact length,  $h_{inst}$  drops below  $h_{min}$  leaving uncut material at both sides of the slot wall, see Figure 2.12(c). This essentially increases the instantaneous uncut chip thickness with respect to the following cutter flute which removes the residual material from the first flute, assuming that  $h_{inst}$  is greater than  $h_{min}$  at this point, see Figure 2.12(d). As cutting proceeds, again  $h_{inst} > h_{min}$  and the workpiece is sheared as shown in Figure 2.12(e), and the cutting regions are extended, see Figure 2.12(f). Where the feed per tooth is significantly less than the minimum chip thickness, a chip is only generated after several flute passes, once a sufficiently large uncut chip thickness has been accumulated [106, 114].

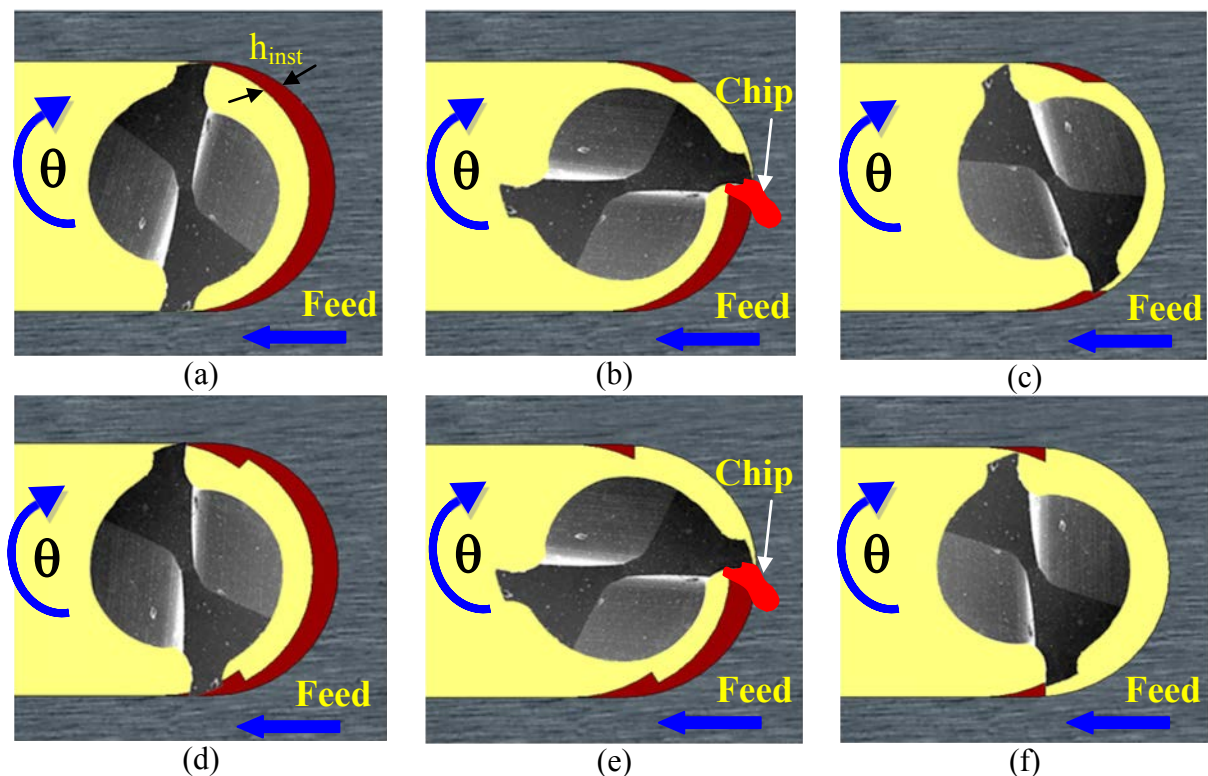


Figure 2.12: Micromilling with minimum chip thickness effect: (a) – (c) first path, (d) – (f) following path: base on [17]

## 2.4.2 Cutting edge radius effects

Figure 2.13 shows the effect of cutting edge radius on chip thickness ratio under macro and micro cutting conditions. In macrocutting, the cutting edge radius of carbide tools can be considered to be sharp as the uncut chip thickness is substantially larger than the cutting edge radius, see Figure 2.13(a). However, in microcutting, the uncut chip thickness is often smaller than the cutting edge radius and the chip forms in the area of the cutting edge radius, see Figure 2.13(b). As a result, a highly negative rake angle exists and the apparent relative bluntness of the tool increases the specific cutting forces.

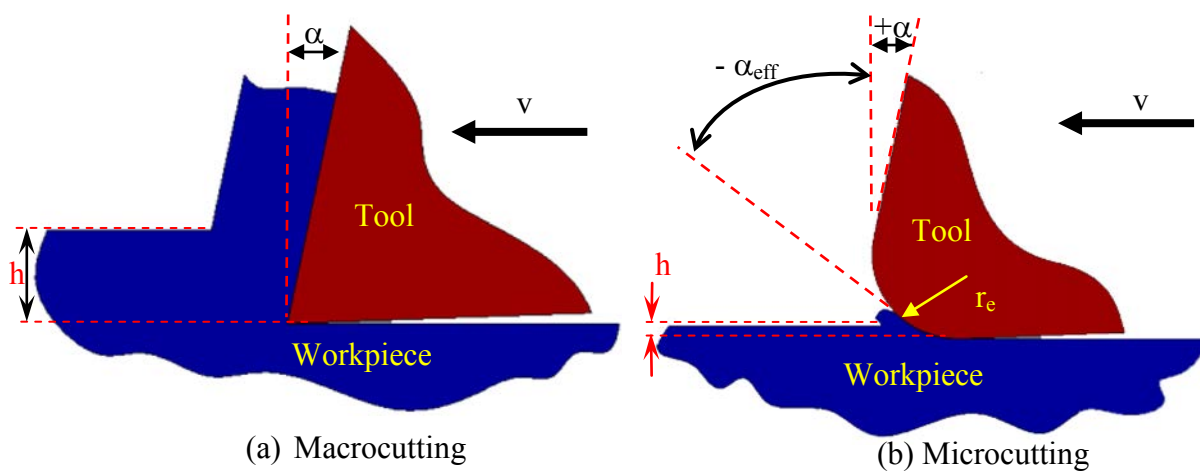


Figure 2.13: Effect of cutting edge radius to chip thickness ratio: based on [9]

The influence of cutting edge radius in micromachining has been studied by several researchers via both modelling and experimental methods. Liu and Melkote [115] identified the relationship between the cutting edge radius ( $d_1$  and  $d_2$ ) and characteristic length scale associated with the size effect in microcutting of steel through FEM analysis ( $V_c=200\text{m/min}$ ,  $d_1=7.5$  and  $d_2=75\mu\text{m}$ ). The authors showed that the plastic shear zone for a sharp tool was thinner ( $10\mu\text{m}$ ) compared to a radiused tool ( $110\mu\text{m}$ ) as shown in Figure 2.14. In addition the tool-chip contact length for the edge rounded tool was three times higher than the sharp tool. The size effect due to the cutting edge radius and small depth of cut altered the material flow pattern around the tool tip by expanding and widening the plastic shear zone, which led to higher energy dissipation due to the increased tool-chip contact length. Later work by Woon et al. [116], in modelling the frictional contact and flow stagnation phenomena under micro cutting conditions, revealed comparable conclusions. The characteristic behaviour of chip

formation in micromachining was also studied by correlating measured width, thickness and depth of plastic deformation in the shear zone relative to microtool sharpness [117].

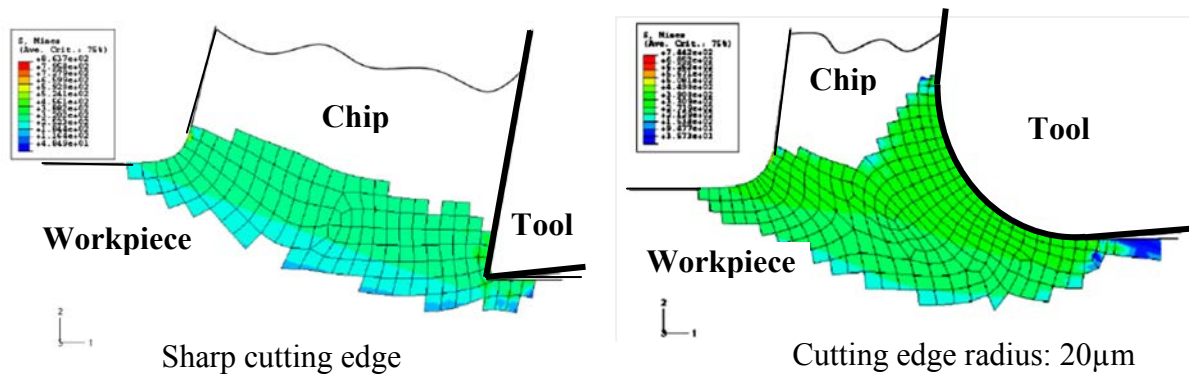


Figure 2.14: Plastic yielding zone at smaller ( $7.5\mu\text{m}$ ) uncut chip thickness [115]

Liang et al. [118] developed a 3D finite element model to evaluate the effect of varying cutting edge radii ( $4$ ,  $6$  and  $8\mu\text{m}$ ) on microburr formation. Results from both the simulation and experimental validation trials on Al2024-T6 showed large top-burr formation as a result of ploughing during cutting. A similar finding was reported by Mian et al. [119] when micromilling AISI 1045 medium carbon steel using  $800\mu\text{m}$  diameter flat end mills, where a larger cutting edge radius increased burr width for both up and down milling. Subsequent experiments on AISI 1005 low carbon steel also yielded comparable results [120].

Wyen and Wegener [121] presented experimental results following orthogonal cutting of Ti-6Al-4V with different cutting edge radii ( $10$ ,  $20$  and  $40\mu\text{m}$ ), cutting speeds ( $10$ ,  $30$  and  $110\text{m/min}$ ) and feeds ( $0.01$  and  $0.2\text{mm}$ ). Both tool edge radius and cutting speed had a significant influence on the calculated value of friction coefficient due to the existence of ploughing forces, which were observed even for idealised sharp tools.

The effect of tool edge radius (sharp,  $3$ ,  $5$  and  $7\mu\text{m}$ ) on cutting temperature when micro end milling an aluminium alloy was examined by Yang et al. [93] via a series of finite element simulations and experiments. While larger edge radii lead to an anticipated increase in cutting forces, the effective stress and mean cutting temperature decreased ( $\sim 16\%$ ), due to the heat being dissipated through the machined surface and flank face of the tool, rather than the chip.

### 2.4.3 Influence of workpiece microstructure/grain size

Another factor which has a significant effect on micromachining performance besides the minimum chip thickness and tool edge radius is workpiece material microstructure. This is especially true in dual-phase or multi-phase alloys [122], where the workpiece can no longer be treated as isotropic, with average material grain size being of a similar order to the feature size machined [10, 11, 119].

The typical minimum chip thickness (depth of cut) of several micrometers in micromachining essentially means that chip formation can occur within a few or even individual grains of the material microstructure, unlike macromilling, as shown in Figure 2.15. Bissacco et al. [9] carried out experimental work to investigate the relationship between grain size and chip thickness size-effect in microcutting. They concluded that when shear deformation occurs within a single grain, the stresses applied to the tool are dependent on individual grain orientations, which can cause high frequency fluctuations of cutting forces due to the inhomogeneous material microstructure.

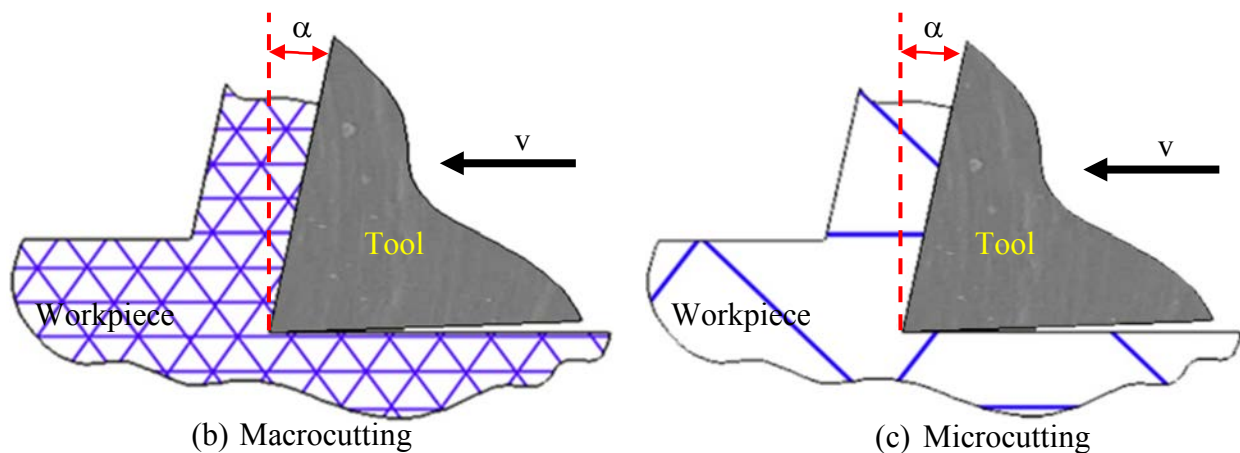


Figure 2.15: Relation between grain size and chip thickness for conventional cutting and microcutting: based on [9]

Considerable efforts have been made to characterise and simulate the effect of microstructure grain size during micromachining. Chuzoy et al. [123, 124] developed a FE model to describe the mechanism of microcutting in ductile cast iron. Large variations in the resulting chip shape (effect of phase boundaries) and cutting force were found due to the different phases in the material. Such effects often lead to higher levels of vibration and accelerated tool breakage. In a related study, Vogler et al. [26] developed a mechanistic model with microstructure mapping for the micro endmilling of inhomogeneous materials in order to

explain the kinematics of the machining process through cutting force signals. They showed that the frequency of force variation which exists in micromilling is primarily due to the material grain size effect. In subsequent work, Vogler et al. [102] introduced an enhanced multiphase material model of ductile iron which takes into account the cutting edge geometry and minimum chip thickness value, in order to predict the behaviour of forces in micromilling. In the case of multiphase iron, the greater ductility of the ferrite phase compared to pearlite leads to a higher tendency for ploughing in the former, causing instabilities in the force signatures obtained.

A surface generation model for both single and multiphase materials to predict surface roughness following microslotting was further developed by Vogler et al. [12] to investigate the influence of microstructure. The results indicated that for multiphase materials this was mainly influenced by the geometry of the tool (corner radius and end cutting edge angle), the minimum chip thickness criterion and burr formation at the grain boundary, whereas for single phase materials only the first two factors played a significant role. Additionally, frequency spectrum analysis revealed that an increase in surface roughness was due to 'interrupted chip formation' that occurs as the cutting edge moves between the different material phases. Similar observations were reported by Weule et al. [22], who indicated that variations in material properties from one grain to the next affected the machined surface produced.

Simoneau et al. [125] developed a FE model which takes into account the individual contributions of different grains (average 10 $\mu$ m Ferrite, 100 $\mu$ m Pearlite) and structures in order to simulate the microscale cutting process and chip formation phenomena in AISI 1045 steel. It was observed that continuous chips were formed only when the uncut chip thickness was greater than or equal to the average microstructure grain size. At lower uncut chip thicknesses, a transition to a quasi-shear-extrusion chip occurred as shown in Figure 2.16, which is comprised of alternating layers of pearlite and ferrite [125]. Similar observations were reported by Liu et al. [8], where the chip formation becomes interrupted (chip shape change) as the tool exits a phase at the grain boundary with burrs forming at these locations.

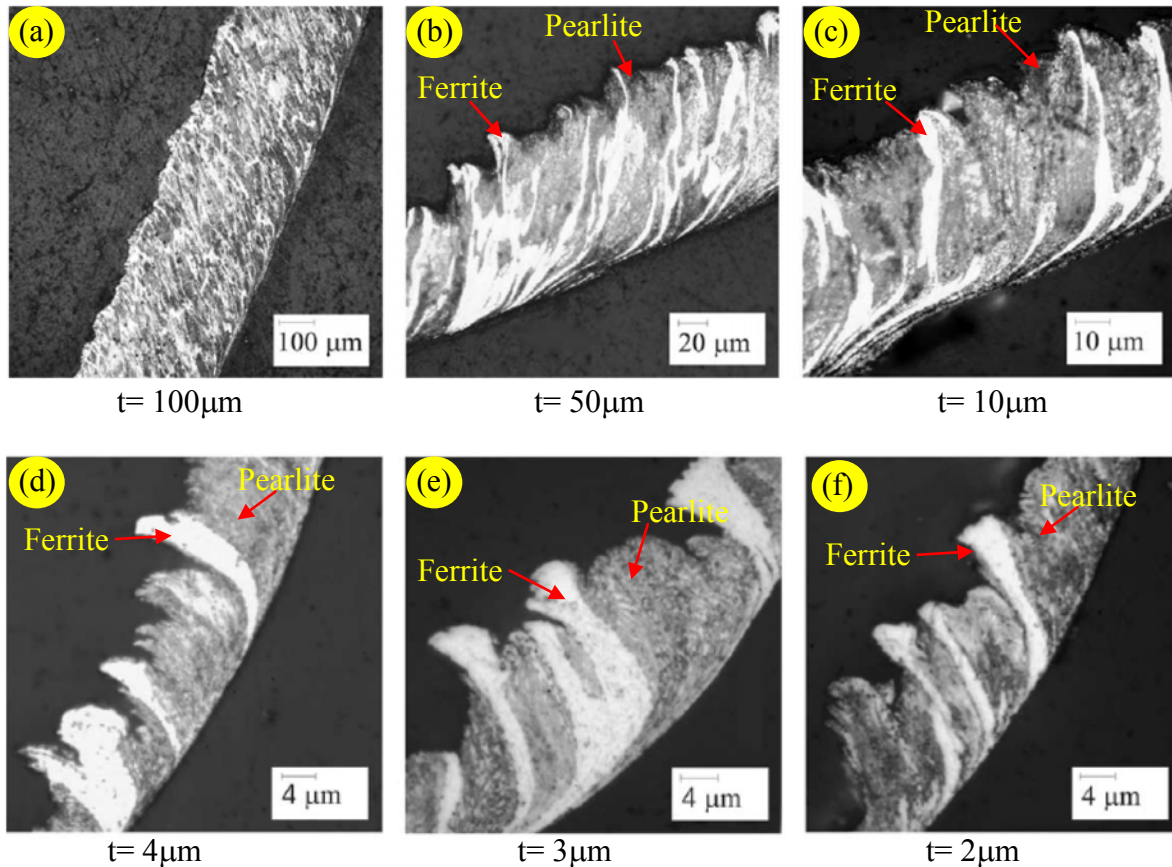


Figure 2.16: Continuous chips (a-c) and Quasi-shear-extrusion chips (d-f), at different uncut chip thickness [125]

In subsequent work by Simoneau et al. [126], the variation in plastic dissipation energy from individual grains during microcutting was used to show that the surface dimples which form are due to the dual phase structure of the workpiece material and always occur at a pearlite to ferrite grain boundary in AISI 1045 steel. The size of dimples on the machined steel surface could therefore only be effectively reduced by appropriate selection of the grain structure with respect to cutting parameters and specifically the uncut chip thickness. This agreed with Zhou and Ngoi [127], who recommended that microstructure based effects can be controlled through the use of super-fine grain material.

Experimental investigations were conducted by Wang et al. [128] to determine the effect of grain size when micromilling Al6061 aluminium alloy. They found that the minimum chip thickness and elastic recovery heights of each grain varied between phases due to the different physical characteristics (friction coefficient ( $\mu$ ) and elastic modulus ( $E$ )). As a result of the grain boundary effect between phases, the chips were always discontinuous. Popov et al. [129] similarly investigated the influence of varying grain size in a 5000 – series Al alloy

on the resulting surface roughness following micromilling. Their investigation showed that through a refinement in material microstructure from 100 - 200 $\mu\text{m}$  to 0.6 $\mu\text{m}$ , surface roughness was improved by more than three-fold (from Ra 0.51 to 0.13 $\mu\text{m}$ ), as a result of the reduction in grain size and anisotropic properties of the alloy. In contrast, Mian et al. [119] when examining the micromachining of a multiphase material AISI 1045 medium carbon steel with a relatively large grain size (10 $\mu\text{m}$ ), found that the resulting surface roughness was significantly lower (Ra=0.4 $\mu\text{m}$ ) than the grain size. Anticipated reasons for this relate to the possibility of grain polishing or fracture as an integral part of the mechanics of micromachining for coarse-grained materials.

## **2.5 Overview of machinability research in micromilling**

### **2.5.1 Workpiece materials**

Early research work (since ~1996) on micromilling using solid carbide tools, generally focused on cutting relatively soft materials like brass, copper, aluminium alloys and graphite. The main applications were for the production of miniature electrodes for EDM and brass tools for injection moulding processes. While such materials are less likely to cause frequent breakage of micro end mills, they are prone to rapid wear under the high loading cycles typically associated with replication based process such as hot embossing, injection moulding, and metal forming.

Since the middle of the last decade, several studies have been published relating to the micromilling of hardened steel materials for implementation with technologies for mass production of parts/components. Although properties such as high wear resistance and fatigue strength make hardened steels ideal for mould and die applications, they also present significant challenges in terms of microscale machinability [130, 131]. These include low/unpredictable tool life, poor surface quality (burning etc) and the propensity for sudden/catastrophic cutter failure [9, 11, 16]. More recently, the micromilling of advanced/exotic materials such as NiTi shape memory alloy, Ti alloys, silicon and glass have been investigated for potential use in the biomedical, microelectronic and aerospace industries, see Table 2.8.

As far as the author is aware, published data have only involved workpieces with hardness < 60HRC, hence one of the reasons for the current research to investigate the machinability of

hardened (~62HRC) AISI D2 cold work tool steel when micromilling with 0.5mm diameter tools. The material has a chemical composition of : 1.5% C; 11.5% Cr; 0.8% V; 0.75% Mo [132]. Key physical/mechanical properties of the material are detailed in Table 2.9.

Table 2.8 : Materials used in micromilling and associated applications

Materials	Earliest date	Applications	References
Graphite	1996	Mould for X-ray lithography mask	[133]
Polymethyl methacrylate (PMMA)	1997	Mould for X-ray lithography mask	[134]
Aluminium	1997	Prototype moulds	[14, 19, 135-138]
Copper	2001	Die and mould	[17, 109, 139-141]
Steel	2005	Die and mould	[3, 9, 22, 28, 142]
Tungsten-copper	2005	EDM electrode	[143]
NiTi	2007	Medical applications	[144, 145]
Silicon	2008	Microelectronics	[146]
Glass	2008	Medical application, microelectronics	[147]
Ti alloy	2010	Aerospace, biomedical	[110]

Table 2.9: Physical properties of AISI D2 [148]

Density	$7.70 \times 10^3 \text{ kg/m}^3$
Hardness, Rockwell C	62 HRC
Modulus of elasticity	210 GPa
Thermal expansion (20 °C)	$10.5 \times 10^{-6} \text{ }^\circ\text{C}^{-1}$
Specific heat capacity	461 J/kgK
Thermal conductivity	20 W/mK
Wear resistance	$2.2 \times 10^5 \text{ MN/mm}^2$
Toughness	$25 \text{ J/m}^3$
Machinability	Low

## 2.5.2 Operating parameters

As highlighted previously, micromilling essentially involves downscaling of the cutting tools used in conventional macroscale milling to sub-millimetre diameters. Table 2.10 shows a comparison between the manufacturers recommended cutting parameters for slot milling using a 16mm diameter tool and a 0.3mm diameter micro cutter on hardened steel workpiece material. The data was based on tools with identical tool geometry and coating [80]. While the ratio between the two tool diameters is 53.3, the rotational speed for the micro tool was only increased by a factor of ~33. This meant that the peripheral cutting speed under

‘conventional’ conditions was approximately 60% greater than when micromilling. The feed per tooth however was 16 times lower in line with tool diameter reduction. The most critical parameter with the highest differential ratio (160) was the axial depth of cut which is generally only 5µm or less for micromilling. Failure to accurately control the axial depth of cut can result in instant tool failure upon first contact with the workpiece [68]. Even considering the typical capabilities of ultra precision milling machines, local variations in chip load of more than 100% is not uncommon during micro cutting setup inaccuracies (workpiece position registration, tool length setting etc.) and machine tool errors (spindle thermal growth, rigidity etc.). According to Li et al. [16] there is currently no definitive reference which provides guidance on the appropriate selection of operating parameters when micromilling hardened steel. Researchers recommend values provided by the tool suppliers and machining best practice. Table 2.11 details examples of the different cutting parameters that have been employed by various researchers [11, 21, 28, 89, 149, 150].

Table 2.10: Cutting data for macro and micro flat end mills HRC: 45-52 HRC [80]

	Macro slot milling	Micro slot milling	
Cutting parameter	Conventional tool VC2MSD1600	Micro tool VC2MSD0030	Parameter ratio (conventional/micro)
Diameter (mm)	16	0.3	53.3
Rotational speed (rpm)	1200	40000	0.033
Feed per tooth (µm/tooth)	41.6	2.5	16.64
Feed rate (mm/min)	100	200	0.5
Axial depth of cut (µm)	800	5	160
Radial depth of cut (µm)	500	3	167
No. of teeth	2	2	
Cutting speed (m/min)	60.3	37.6	1.60

In terms of microslot production, higher cutting speeds have been reported to improve surface roughness [151], however spindle speed restrictions/limitations are a controlling factor. Conversely, feed rate rises generally lead to deterioration in surface quality, as do depth of cut due to the larger induced cutting forces and possible vibration/chatter effects. Another

factor that can have an influence on the machined surface quality is the tool condition where any irregular features on cutting edges due to tool manufacture may be transferred onto the machined workpiece surface during micromilling.

Table 2.11: Cutting parameters used in micromilling hardened steel by various researchers

References	Material	Tool diameter (μm)	Cutting speed (m/min)	Feed per tooth (μm/tooth)	Depth of cut (μm)
Aramcharoen et al. [89]	AISI H13 (45 HRC)	500.0	47.0	5.0	5.0
Aramcharoen and Mativenga [11]	AISI H13 (45 HRC)	900.0	85.0	0.2 - 3.6	50
Uriate et al. [28]	SAE H13 (50.3 HRC)	300.0	42.4	0.4	8.0
Klocke et al. [149]	X38CrMoV5-1 (53 HRC)	500.0	100.0 – 200.0	5.0 – 10.0	20.0
Li et al. [150]	SAE H11 (54 HRC)	500.0	15.7 – 56.5	2.0 – 9.0	30.0 – 100.0
Bissacco et al. [21]	Stainless steel (58 HRC)	600.0	30.0	9.0	83.3

### 2.5.3 Performance measures and results

A large portion of the current academic and industrial interest in micromachining stems from developments over the past 10-15 years [29]. Key review papers concerned with the mechanics of machining at the microscale level which identify the current state of the art together with future areas of research are those by Liu et al. [8], Dornfeld et al. [10], Chae et al. [6], Robinson et al. [24], Gowri et al. [27] and Miao et al. [122]. Other researchers have focused on process characteristics such as tool edge radius effects in relation to the undeformed chip thickness, workpiece grain size/microstructural effects and the mechanism of cutting with consequent effects of built up edge (BUE) formation. Work on cutting forces [152, 153], tool wear [154-156], workpiece surface roughness [139, 157], burr formation [44, 158] and cutting temperature [93, 99, 138, 159] has also been performed. Much of the information detailed in the review papers relates to micro-turning rather than micro-milling and there are notable knowledge gaps with respect to thermal measurement, workpiece integrity effects and modelling. Recent publications encompassing micro-milling include those by Liu et al. [23, 160], Li et al. [150], Aramcharoen and Mativenga [11] and Bissacco et al. [21]. The two papers by Liu et al. [23, 160] provide useful insight with respect to micro-fluidic device manufacture, particularly micro-channel side wall roughness while the

remaining three concentrate on the micro-milling of hardened steels and highlight challenges such as unpredictable tool life/premature tool failure and differences in process mechanisms compared to macroscale machining.

The most commonly used measures to evaluate the performance of micromilling processes can broadly be classified into two categories as either quality based or economic related criteria. The typical factors influencing the latter are machining time and production cost, providing the quality of the machined product is satisfactory/acceptable. Quality based measures on the other hand are related to aspects such as tool wear, tool life, form accuracy, workpiece surface quality and burr formation which have a significant effect on the quality of the machined surface. These are discussed later in this section.

The onset of cutting edge rounding is rapid, especially with square/flat cornered micro end mills and generally occurs soon after machining commences. This effect is more pronounced when cutting harder materials and results in radiusing of the interface between the bottom and side walls of the machined slot/features [137]. Following work in evaluating machine stiffness and process stability in micromachining, Uriarte et al. [28] showed that the main source of error in finish milling of microparts/features was due to tool deflection as a result of inappropriate operating conditions and tool wear. This was further reinforced in subsequent work involving milling of hardened AISI H13 steel (54HRC) with 0.3mm diameter square end mills [161], which highlighted tool wear extending past the cutting edge area. Five types of tool failure mechanisms were reported by Li et al. [150] including fracture of the cutting edge, abrasive wear, flank wear, tool breakage, and material deposition following machining of SAE H11 (56HRC) tool steel with 0.5mm diameter end mills. Fracture of the cutting edge radius was however the dominant mode which occurred during the early stages of machining. Aramcharoen et al. [3] similarly found that chipping/fracture of the cutting edge was prevalent when micromilling hardened steel AISI H13 (45HRC) with two fluted, 0.7mm diameter cutters. When employing ball nose end mills down to 0.2mm diameter on hardened steel (58HRC), Bissacco et al. [162] noted that the change in cutting edge profile due to wear increased the edge radius by a factor of 20, while the tool rake and clearance angles were no longer discernable even under high magnification microscopy. This led to a rise in process forces and significant tool deflection.

Surface finish is an important consideration which can influence the functional properties of microcomponents. In microscale machining, key factors that have been found to affect the machined surface roughness include minimum chip thickness value [8], cutting edge radius [23], workpiece material [12, 22], and operating feed rate [8]. The accumulation of plastically deformed material in the main ridges of the machined surface and smearing of workpiece material behind the tool are common place, particularly at large ratios of tool edge radius to underformed chip thickness [21], see Figure 2.17. Wang et al. [163] employed statistical experimental techniques (full factorial design) to examine the effect of tool diameter (0.2 – 1.0mm), spindle speed (60000 – 80000rpm), depth of cut (10 - 40 $\mu$ m) and feed rate (12 – 48mm/min) on surface roughness in micromilling of brass. Tool diameter was found (based on ANOVA) to be the most significant factor affecting surface roughness in micromilling as the intensity of tool vibration becomes lower when the stiffness of the cutter is high. Similarly, use of neural networks and Taguchi fractional factorial methods to study the effects of spindle speed (30000 – 50000rpm), feed rate (10 – 50mm/min) and axial depth of cut (10 - 30 $\mu$ m) on surface roughness, has been reported [164]. Here, the results suggest that surface roughness decreased with higher spindle speed but increased with larger magnitudes of feed rate and depth of cut.

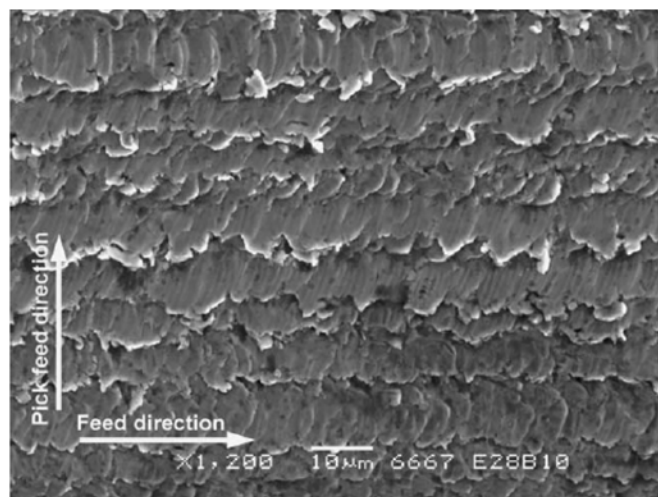


Figure 2.17: Micro milled surface by 0.2mm diameter ball end mil – material smeared behind the tool [21]

Burr formation is generally prevalent in microscale machining as a result of ploughing instead of shearing, particularly where the ratio of feed per tooth to cutting edge radius is less than 1 [165]. This was apparent when micromilling a range of different materials including

steel [44], brass [75], aluminium [166], copper [17] and titanium alloy [167]. The continued generation/presence of burrs remains a major obstacle against greater implementation/application of micromilling in industrial production [9], not least due to the significant difficulties associated with de-burring micro components. Developments aimed at preventing or significantly minimising burr formation should therefore be a priority [165] with allowable burr width size of  $<110\mu\text{m}$  [11]. The mechanism of burr formation in microscale machining has been proposed by several researchers as the result of interaction between the cutting edge radius and feed per tooth [17, 21, 165] where an effective negative rake angle is formed due to the cutting edge radius being larger in comparison to the undeformed chip thickness. Here, workpiece material ahead of the tool is typically pushed, bent and moved in the axial direction of the cutter resulting in a burr [165]. As mentioned previously, the condition is further exacerbated by rapid wear of tools. More recently, work by Li and Chou [44] in micromilling SKD 61 (38HRC) using 0.6mm diameter end mills suggests that an up milling mode gives smaller burrs in comparison to a down milling direction, see Figure 2.18. This is due to the effective direction of cutting force and stress on the material which is away from the up-milling side and towards the down-milling side, and explains the direction of the material deformation [168]. Similar results were also obtained by Schmidt and Tritschler [169], and Filiz et al. [17], when micromilling steel and copper respectively.

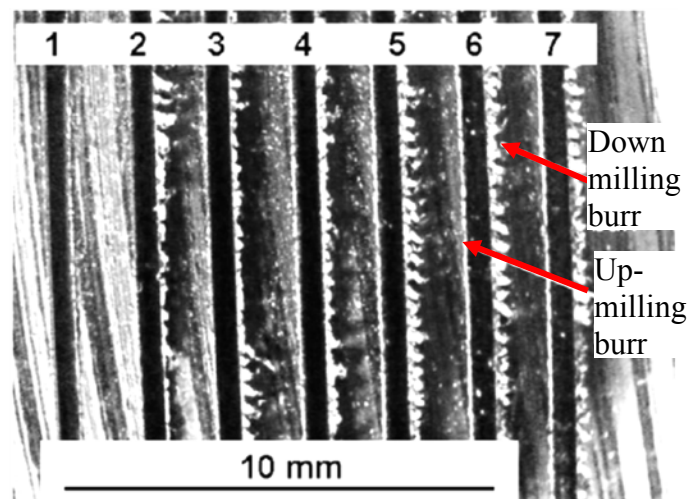


Figure 2.18: Burr formation for 0.6mm diameter with rotational speed 30000rpm, feed  $2\mu\text{m}/\text{rev}$  and depth of cut 0.3mm [44]

Cutting force is one of the key responses used with on-line tool monitoring in macro-cutting operations where gradual wear or catastrophic failure of the cutting tool can generally be

determined from the nature of force traces/data. However, this is somewhat more difficult under micromilling conditions as the relatively low force levels ( $< 1\text{N}$ ) can be obscured by the intrinsic background/machine noise signals. Extensive work has been performed involving the study of cutting forces and its prediction for micromachining operations. Cheng et al.[170] investigated the effect of depth of cut and feed per tooth at constant spindle speed on cutting forces in micromilling of annealed AISI D2 steel (25HRC) to verify the influence of the uncut chip thickness (function of feed per tooth) with respect to the tool edge radius. Kang et al. [19] developed an analytical model based on the undeformed chip thickness to predict cutting force which included the effects of cutting edge radius. This model was later improved by Malekian et al. [5] who considered the effects due to tool run-out, tool dynamics, ploughing and elastic recovery. A different approach was employed by Afazov et al. [152] who incorporated factors such as tool path trajectory and undeformed chip thickness in developing a FEM simulation to predict the cutting force in micromilling. The predicted and the measured forces when micromilling AISI 4340 with 0.5mm diameter showed the same trends and peak magnitudes. The significant challenges and issues relating to experimental measurement of cutting forces in micromilling was described by Bissacco et al. [171] following trials in machining aluminium. They suggested that highly specialised equipment (high sensitivity dynamometric platforms with several tens of kHz sampling frequency simultaneously on each sampled channel) and the ability for high positioning accuracy, control/compensation of machine tool thermal deformations etc. are critical, in order to discriminate between forces due to the tool workpiece interaction and measured signals from the machining system (background noise, vibration etc.) [171].

Temperatures generated in metal cutting are widely recognised as a major factor affecting aspects such as tool wear/life, surface quality, part dimensional accuracy and workpiece residual stress. Abukhshim et al. [172] critically reviewed the mechanisms/sources of heat generation and heat dissipation in high speed orthogonal machining mainly under macroscale machining conditions. It includes an overview of common temperature measurement techniques such as direct conduction (thermocouple/embedded thermocouple), indirect radiation (infrared camera) and metallographic based methods. However as with cutting forces, the measurement of temperature in microscale cutting processes poses significant challenges. Several studies involving micromilling have suggested that cutting temperatures (measured by infrared camera) are significantly lower compared to those in conventional

macromilling. Dhanorker and Özel [173] developed a finite element simulation in order to model the cutting temperature when micromilling. The predicted cutting zone temperatures were found to be around 50-60°C and 100-150°C when cutting Al2024-T6 aluminium and AISI 4340 (35HRC) steel respectively with a cutting speed of 80m/min and feed/tooth of 10µm, although no experimental trials were performed to validate the simulation. A similar result however was reported by Yang et al. [93] when modelling the micromilling of Al2024-T6 using an IR temperature measuring system. They concluded that the tool edge radius was a significant factor influencing the temperature distribution. Wissmiller and Pfefferkorn [159] characterised the heat transfer using an infrared thermal camera when micromilling Al-6061-T6 alloy and AISI 1018 steel with 0.3mm diameter end mills at feed rates of 700m/min and 200m/min respectively. The maximum temperatures were found to be approximately 92°C and 50°C for steel and aluminium respectively. Similarly, Mativenga et al. [174] reported that the maximum temperature observed was less than 100°C when micromilling AISI H13 (45HRC) steel with 0.7mm diameter flat micro end mills (spindle speed 20000rpm, feed rate 320mm/min and depth of cut 50µm). In contrast, Dewes et al. [175] reported that maximum interface temperature (tool/workpiece) observed was 390°C when face milling (macromilling) AISI H13 (52HRC) steel with 6mm diameter ball nose end mills (spindle speed 19194rpm, feed rate 7678mm/min and depth of cut 0.5mm). All measurements detailed were obtained using infrared thermography.

Workpiece surface integrity can be defined as the description and control of alterations produced in a surface layer during machining [176], which has a significant influence on the properties and service life of the final components. Defects or changes include the formation of microcracks, phase transformations development of tensile/compressive stresses, plastic deformation of the workpiece/microstructure as well as variations in the microhardness [177]. The main factors affecting the surface integrity of a machined component are typically related to mechanical loads, thermal gradients and phase transformation [178] present during the cutting process. High temperatures in particular can lead to detrimental effects such as part distortion, chemical reactions and subsequent absorption of foreign elements into the workpiece surface [179]. In the late 1960's, Kahles and Field [180] developed a procedure for surface integrity evaluation which suggests the type of data measures and analysis necessary, depending on the level of workpiece surface integrity knowledge required [180]. This was categorised into Minimum, Standard and Extended Surface Integrity (SI) Data Sets as

described in Table 2.12. The Minimum SI Data Set should always be considered first in surface screening tests as it is the least expensive. It essentially includes surface/subsurface metallographic information supplemented with microhardness and surface roughness measurements. For more critical applications, the Standard SI Data Set provides additional in-depth information such as residual stress and basic fatigue life, while the Extended SI Data Set encompasses further empirical data gathered from statistically designed fatigue experiments and yields data suitable for detailed product/system design [179]. There has been significant research on evaluating surface integrity effects due to machining particularly for advanced materials used in safety critical applications such as aerospace [181-184]. More recently, an extensive literature review relating to the influence of residual stress on surface integrity was presented by Guo et al. [185], while M'Saoubi et al. [186] critically discussed the impact of surface integrity on functional performance and life of machined products.

Table 2.12: Description of workpiece surface integrity data sets [180]

Surface integrity evaluation level	Technique/Method	
Minimum Surface Integrity Data Set	Surface finish	Roughness measurement SEM images
	Macrostructure (10X or less)	Macrocracks Surface defects Macroetch indications
	Microstructure (crosssection examination)	Microcracks Plastic deformation Phase transformations Intergranular attack Pits, tears, laps and protrusions Built-up edge Melted and deposited layers Selective etching
Standard Surface Integrity Data Set	Minimum Surface Integrity Data Set	
	Residual Stress and distortion	
	Stress corrosions tests	
	Fatigue tests	
Extended Surface Integrity Data Set	Standard Surface Integrity Data Set	
	Fatigue tests – statistical data to established design	
	Additional mechanical tests	Tensile
		Stress rupture
		Creep
		Crack propagation
Fracture toughness		

## **2.6 Design of experiments**

An experiment can be defined as a test or series of tests that manipulates the input variables within a process in order to observe and identify the reasons for changes in the output response [187]. To ensure that an experiment is conducted effectively, statistical experimental design is generally recommended where appropriate data can be recorded and statistically analysed for valid conclusions to be drawn. Ross [188] further describes the process of designing of experiments as a simultaneous evaluation of two or more factors for their ability to affect the output response or variability of a particular product or process characteristic.

### **2.6.1 Full and fractional factorial designs**

Experimental design can broadly be classified into two categories; full and fractional factorial. A full factorial experimental design is generally feasible when only a few factors and levels are to be investigated, otherwise the approach can lead to an excessive number of trials:  $n^k$ ; where  $n$  is the number of levels and  $k$  is the number of factors. Here the levels of one factor are evaluated against each level of every other factor and thus, this design arrangement provides for all possible effects and interactions to be assessed. Consequently, such an approach is widely used in factor screening experiments, although the scale of testing can be inefficient in typical engineering applications due to demands on time and resources. Under these circumstances, a fractional factorial experiment can be a more efficient/practical option, which only involves a portion of the total possible variable combinations but still enables an acceptable estimate of the main factor effects and some (if not all) of the interactions [188]. The Taguchi methodology is one such technique, which involves a family of standard fractional factorial Orthogonal Arrays (OA), with an emphasis on mean performance characteristics close to the target value rather than a value within certain specification limits [187]. However such an approach allows the calculation of relative influence of individual test variables in relation to the selected response measure (e.g. surface roughness, cutting forces, tool life etc.). Thus the Taguchi method is typically applied most efficiently at the early stages of process development.

### **2.6.2 Response surface methodology (RSM)**

Montgomery [187] defines response surface methodology (RSM) as a collection of mathematical and statistical techniques for determining the relationship between various

factors and corresponding output responses within the desired criteria. RSM is a useful procedure for developing, improving and optimising processes, which provides a global view of the system response within a given design space [187]. In most RSM based experiments, the form of the relationship between the output response and independent variables (factor) is unknown. Hence, the first step would be to identify a suitable approximation for the true functional relationship between the output response and set of independent variables. A low order polynomial as a function of the independent variables is initially specified. If the output response is well represented by a linear function of the variables, then the approximating equation is known as a first order model. If curvature is observed in the system, then a polynomial of a higher degree must be used, which translates to second or third order models etc. [187].

A significant number of researchers have employed RSM to design and analyse the results from experiments involving end milling [189-194], which has proven to be an efficient tool [195] not only to reduce the number of experiments (and hence time and costs), but also to provide reliable information on the main and interaction effects with respect to the parameters investigated [196].

### **2.6.3 Analysis of variance (ANOVA) technique**

Analysis of variance (ANOVA) is a powerful technique to interpret experimental data and subsequently make necessary decisions. Ross [188] defined ANOVA as a statistically based, objective decision making tool for detecting any differences in the average performance of groups of factors tested. A confirmation experiment, especially when a fractional factorial design has been applied, is used in order to validate the conclusions drawn from the analysis. In addition to ANOVA, other approaches such as observation, ranking, column effects and plotting methods can also be considered to support and enhance the analysis of data [188].

## Chapter 3: EXPERIMENTAL WORK

### 3.1 Workpiece material

The workpiece material employed in all tests was hardened AISI D2 cold work tool steel which had an average grain size of  $\sim 18\mu\text{m}$ . Key physical/mechanical properties of the material are detailed in Table 2.9 (see section 2.5.1), while Figure 3.1(a) shows a micrograph of the typical microstructure. The material was initially supplied in the form of large slabs measuring  $200\text{mm} \times 50\text{mm} \times 300\text{mm}$  (W×H×L), with a nominal bulk hardness of  $62 \pm 1$  HRC which was measured using a portable hardness tester, see Figure 3.1(b). A Charmilles ROBOFIL 200 electrical discharge wire machine (EDWM) was used to cut the workpiece material into smaller blocks of  $20\text{mm} \times 20\text{mm} \times 90\text{mm}$  (W×H×L) for testing, see Figure 3.2. All four surfaces of the workpiece blocks were subsequently ground to remove any surface defects as well as heat affected layers and to achieve squareness during workpiece setup in order to prevent any bias of the results. Following mounting on the machine worktable, the test surface of a new block was further machined using an 8.0mm diameter face milling cutter (product code VF-SD 8.0) prior to trial commencement, to ensure flatness as well as to provide a suitable machining reference. The face milling parameters used were  $V_c=100\text{m/min}$ ,  $f_t=7.5\mu\text{m/tooth}$  and  $d=100\mu\text{m}$  [80].

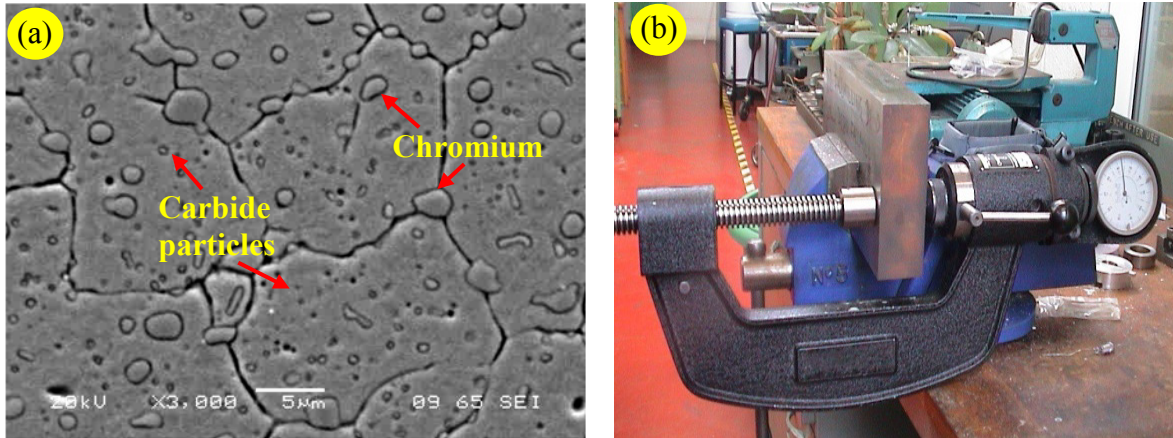


Figure 3.1: Workpiece material (a) Microstructure (b) Bulk hardness measurement



Figure 3.2: Example of machined test blocks

## 3.2 Tooling

### 3.2.1 Micro end mills for Phase 1 work

Eleven different micro end mill cutters from various manufacturers were purchased in order to evaluate their relative geometrical accuracy and coating quality in the as-supplied condition. The manufacturers selected provided a cross section of leading micromachining tooling. All tools had a nominal diameter of 0.5mm but varying cutter /edge geometry. Details of the tools are listed in Table 3.1.

Table 3.1: Microtool diameter and geometry used in Phase 1

	Manufacturer	Tool code	No of flutes
Tool 1	Iscar	Ec-A2005-007/02 C4M45	2 flute
Tool 2	Sandvik	R216.32-00530-AE05G	2 flute
Tool 3	Mitsubishi	MS2JSD0050	2 flute
Tool 4	Mitsubishi	VC2MSD0050	2 flute
Tool 5	Mitsubishi	VCMDSCD0050	4 flute
Tool 6	Mitsubishi	VCMDSCD0050	4 flute
Tool 7	Seco	905L005-MEGAT T	2 flute
Tool 8	Dixi	DIXI 7240 D0.50	2 flute
Tool 9	Fraisa	D5736050	2 flute
Tool 10	Dixi	DIXI 7520 XIDUR	2 flute
Tool 11	Dixi	DIXI 7240 D0.50	2 flute

\*Tool 5 and Tool 6 were from different batches

\*\*All tools coated with TiAlN

### 3.2.2 Micro end mills for Phase 2 work

Phase 2B encompassed evaluation of machine tool spindle growth during actual machining of graphite (operating at 60,000rpm) and involved dry cutting of test slots. The tests employed twin flute, 6 mm diameter PCD end mills (product code ITC-2111-6.0 PCD 2 FLT) with a cutting length and shank diameter of 8 and 6mm respectively, see Figure 3.3. The tools were purchased from Industrial Tooling Corporation (ITC), UK.



Figure 3.3: PCD end mills diameter 6mm

### 3.2.3 Micro end mills for Phase 3 and 4 experiments

Phase 3 and 4 trials employed 4-flute TiAlN coated  $\text{\O}0.5\text{mm}$  carbide end mills (product code VCMDSCD0050), with a cutting length of 1.0mm, shank diameter of 6mm, helix and rake angle of  $30^\circ$  and  $0^\circ$  respectively. The tools were supplied by Mitsubishi Materials Corporation (MMC) Hardmetal UK Ltd. Both TiN coated and negative rake angle cutters were not used in this work as it was not recommended by the industrial collaborator. All tools were inspected prior to use with the cutting edge radius measured using an SEM and typically found to vary from 5-7 $\mu\text{m}$ . A comparable result was obtained when a batch of 4

tools were evaluated using an Alicona Infinite Focus Microscope (IFM). In order to minimise quality variations, all tools were sourced from the same production batch and SEM pictures were taken before and after machining. Tool geometry and configuration were kept constant throughout the experiments, see Figure 3.4 which shows a sample SEM micrograph of a new microtool and associated feature geometry with typical rake and clearance angles  $0^\circ$  and  $12^\circ$  respectively [80].

The size selected (0.5mm) was small enough to exhibit the characteristics of the micromilling process while still being in line with the definition of micromachining proposed by Masuzawa and Tonshoff [197] and Liu et al. [8] which involves dimensions of the order of  $1\mu\text{m}$  to  $999\mu\text{m}$ .

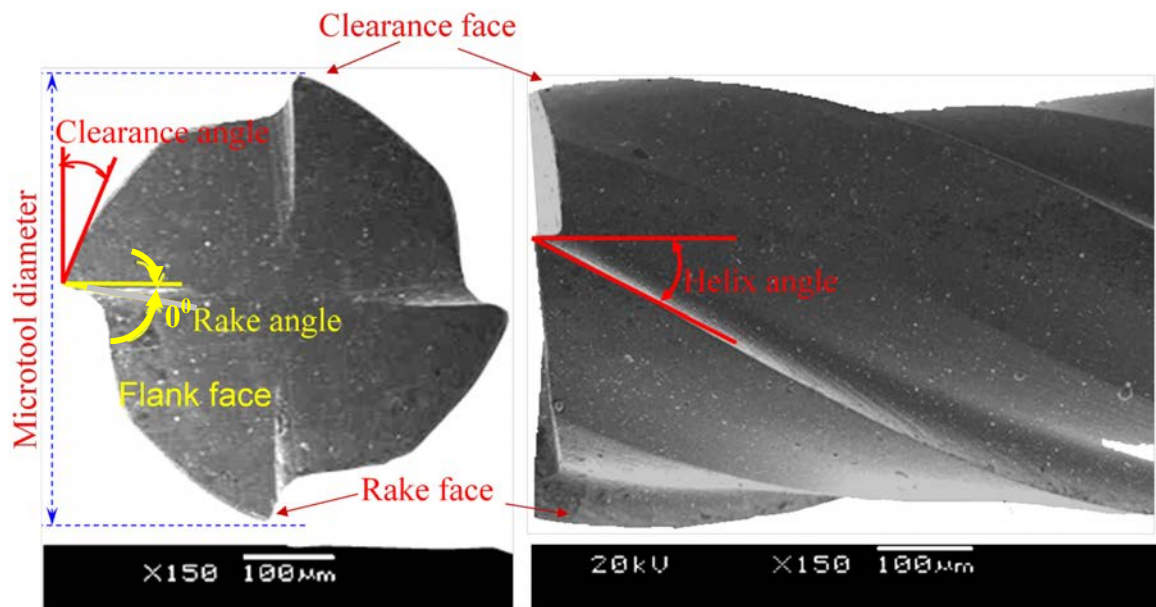


Figure 3.4: SEM picture of a new micro end mill

### 3.2.4 Micro end mills for Phase 5 experiments

Table 3.2 lists the microtools while Figure 3.5 show the SEM micrograph used in Phase 5 testing. This essentially involved evaluating the effect of a chip breaker feature with an approximately flat/concave ( $2\text{-}3\mu\text{m}$  trough at centre) face angled at  $\sim 20^\circ$  to the tool radial axis together with equivalent uncoated tooling. Standard (non-chip breaker) tools were ground with a comparatively large root radius between the cutting edge of the flute and the tool body. All other aspects of the tools (geometry, substrate material etc.) were identical

to that used in Phase 3 and 4 work. Similarly all cutters were inspected using the SEM upon receipt from MMC Hardmetal.

Table 3.2: Micro tools for Phase 5

	Specification number	Coating	Geometry
Microtool a*	VCMDSCD0050	TiAlN	No chip breaker
Microtool b	VCMDSCD0050	TiAlN	With chip breaker
Microtool c	CMSCD00550	Uncoated	With chip breaker

\*Used in Phase 3 and 4 experiments

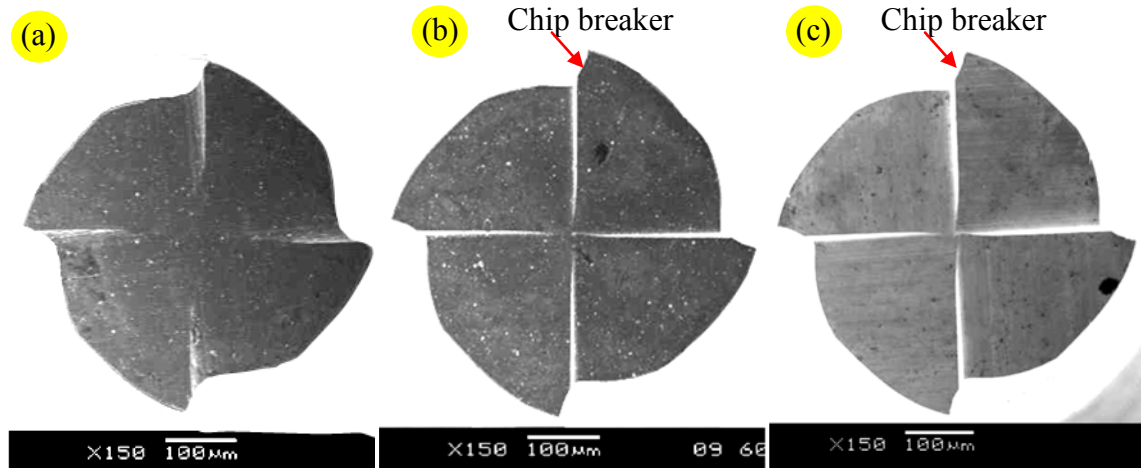


Figure 3.5: (a) No chip breaker with TiAlN coating (b) Chip breaker with TiAlN coating (c) Chip breaker no coating

### 3.3 Equipment

#### 3.3.1 Machine tool and experimental setup

All the experiments were performed on a linear motor, 3-axis, ultra high speed Matsuura LX-1 machining centre having an integrally oil cooled and compensated spindle with a maximum rotational speed of 60000rpm rated at 3kW. Visual inspection of the cutting process was facilitated using a miniature camera located within the machine tool enclosure connected to an external flat screen monitor, see Figure 3.6. On-machine measuring equipment include a Renishaw NC-3 non-contact laser tool setting unit and a Renishaw OMP 40 contact probe system for workpiece inspection. Microtools were held in MST Mizoguchi HSK shrink fit tool holders which were heated using a Hot Shot Jr. heater, see Figure 3.7(a), while tool length compensation was achieved using the NC-3 with a repeatability of  $\pm 0.15\mu\text{m}$ , see Figure 3.7(b). Tool overhang was maintained at 20mm while

tool run-out was measured (at tool shank) using a Mitutoyo dial indicator ( $1\mu\text{m}$  resolution), which did not exceed  $3\mu\text{m}$  in all tests.

Appropriate spindle warm up cycles of approximately 1 hour was initiated prior to the start of tests to minimise/eliminate effects from spindle thermal growth. Despite this and the associated machine compensation system algorithms, significant z-axis growth up to  $16\mu\text{m}$  was typically observed with knock-on effects relating to micromilling accuracy. This problem was therefore addressed in Phase 2 experimental work. All experiments were performed dry. In order to avoid ramping, the tool was initially positioned 20mm away from the workpiece and then slots milled with the full tool diameter engaged. The typical experimental setup is illustrated in Figure 3.8.

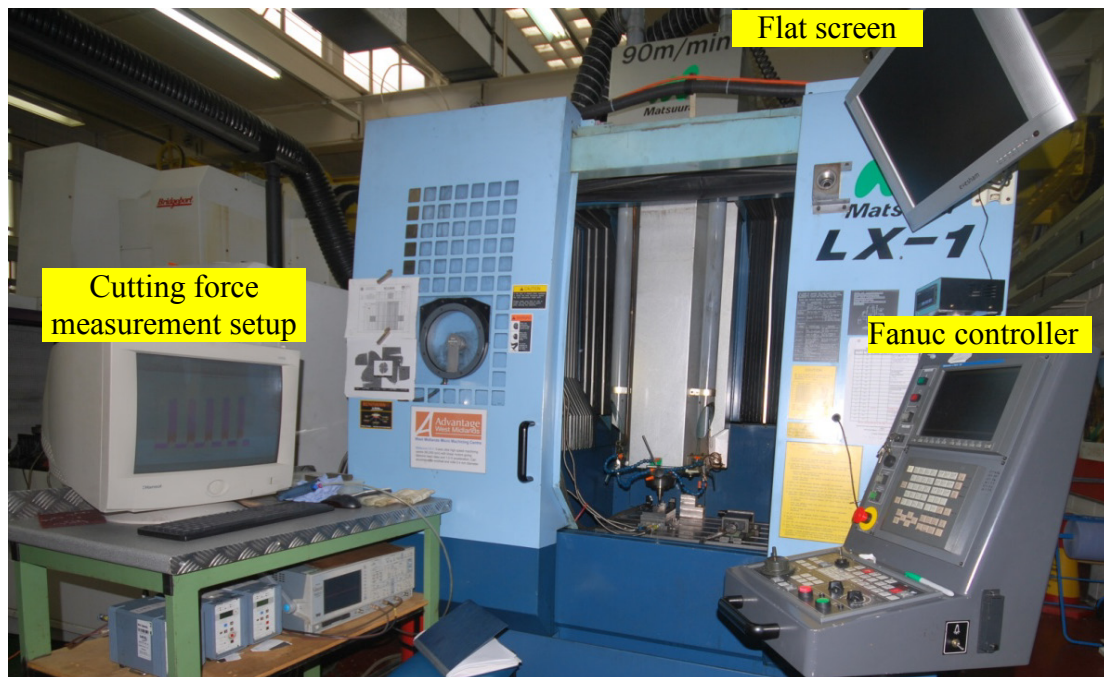


Figure 3.6: Matsuura LX-1 machining centre

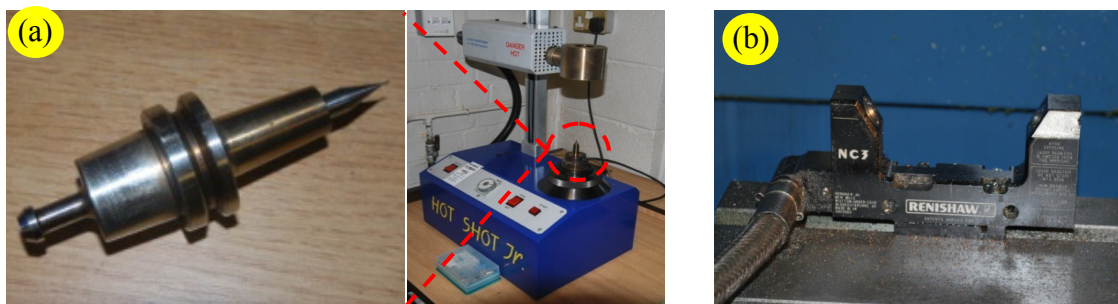


Figure 3.7: Experimental setup (a) Shrink fit tool holder and Hot Shot Jr heater (b) Renishaw NC-3

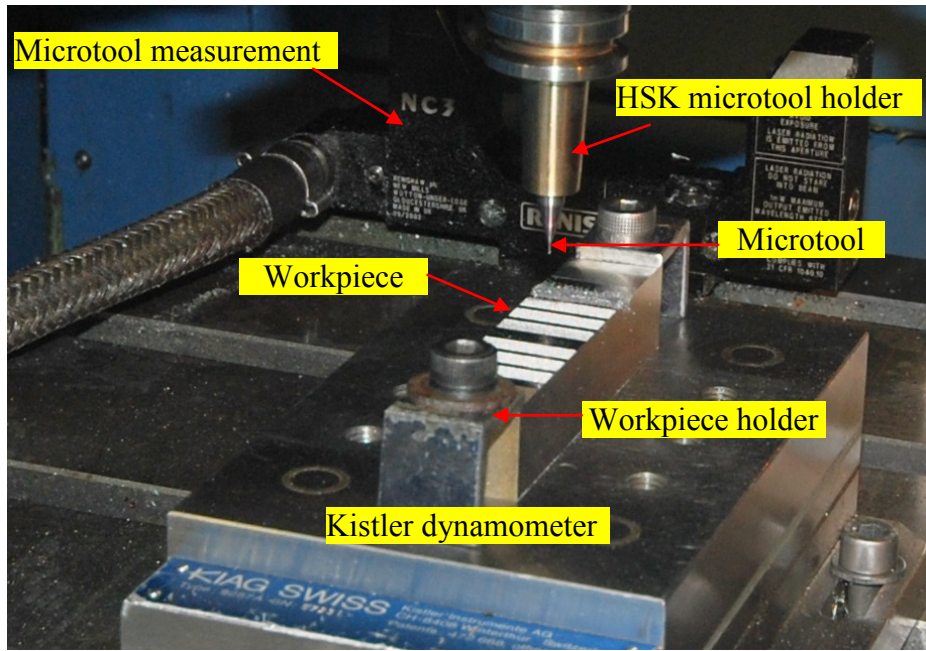


Figure 3.8: (a) Matsuura LX-1 CNC machine tool - experiment setup

### 3.3.2 Force measurement

Cutting forces (feed force  $-F_x$ , normal force  $-F_y$  and thrust force  $-F_z$ ) were measured using a Kistler 3-component piezoelectric platform dynamometer (type 9257A) with a resonant frequency of 2.3kHz and recommended operating frequency of  $< 760\text{Hz}$ . The dynamometer was connected to a series of charge amplifiers (Kistler 5011A) and a 4-channel Gould 6000 series oscilloscope (maximum sampling rate of 200Msamples/sec) linked to a PC running Kistler Dynaware software for signal analysis and output, see Figure 3.9. The system was also initially checked and calibrated using accurate weights.

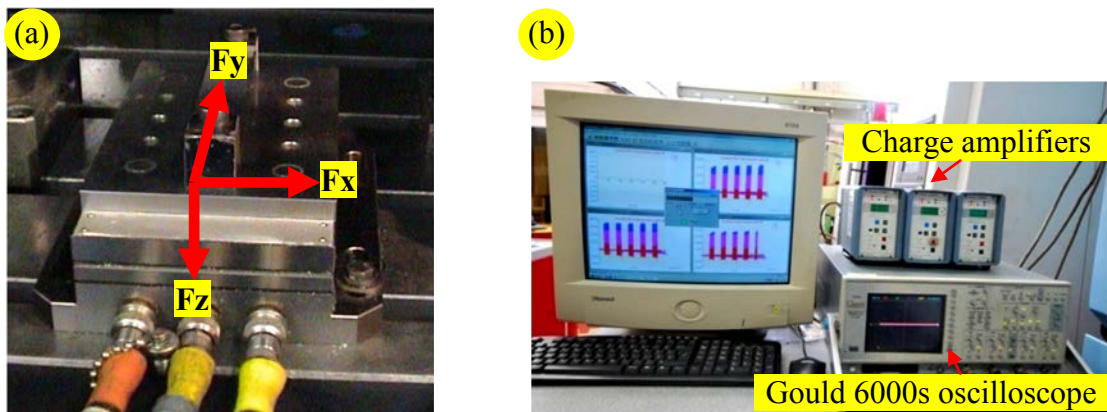


Figure 3.9: Force measurement (a) Kistler dynamometer type 9257A (b) Four channel Gould 6000s, charge amplifiers, and computer with Dynaware software.

### 3.3.3 Temperature measurement

A FLIR ThermoCAM SC640 infrared (IR) thermal imaging camera loaned from the EPSRC Engineering Equipment Pool was used for measuring cutting temperatures. The unit has a spectral band from  $8\mu\text{m}$  to  $14\mu\text{m}$  with a measurement range of  $-40^{\circ}\text{C}$  to  $2000^{\circ}\text{C}$  and a sensitivity of  $60\text{mK}$  at  $30^{\circ}\text{C}$ . The camera was capable of capturing real-time images at a speed of 30 frames per second with a resolution of  $640 \times 480$  pixels and was equipped with a built-in optical digital video system allowing data to be recorded and stored for subsequent evaluation. The camera was positioned at a distance approximately 300mm from the tool workpiece interface, see Figure 3.10. The information acquired was analysed using the ThermalCAM software installed on the accompanying PC.

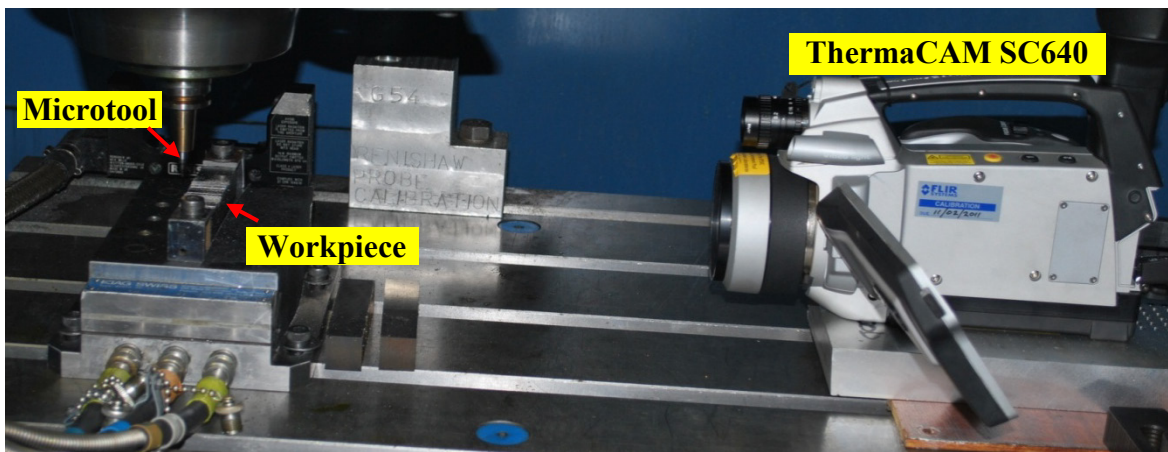


Figure 3.10: Micromilling temperature measurement set up

The emissivity of the AISI D2 material was determined by initially embedding an analogue thermocouple into a workpiece block via a pre-drilled hole which was connected to a data logger, see Figure 3.11. The specimen was then heated on an electrical hot plate to  $200^{\circ}\text{C}$  (approximate anticipated temperature during micromilling) for 30 minutes until the temperature of the block was uniform/stable. Information displayed on the data logger was subsequently used to calibrate the infrared thermal imaging system and determine the corresponding emissivity level. The average emissivity value (based on five measurements) of the hardened steel workpiece was found to be 0.81.

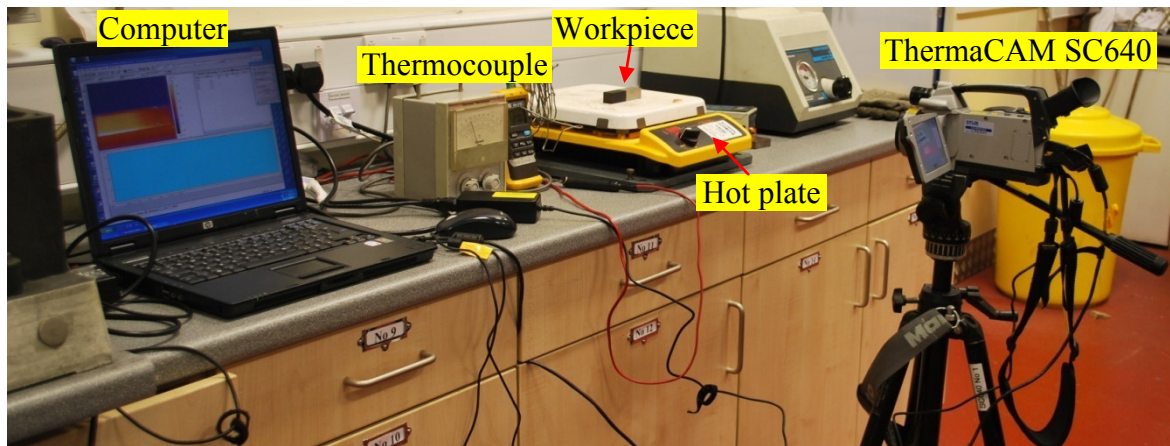


Figure 3.11: Workpiece emissivity setup

### 3.3.4 Tool wear, burr width, workpiece/slot quality, microstructure and chip analysis

Due to the difficulties associated with measurement of flank wear on micro cutters, the width of slot machined was taken as the measure of tool wear corresponding to cutter diameter reduction. The slot width was measured using an optical microscope viewed from the entry position at the mid height of the slot from the base, see example in Figure 3.12. Measurements of microslot widths were performed using a Leica DMLM optical microscope connected to a PC running Buehler Omnimet software, see Figure 3.13(a). New and worn micro end mills were analysed using a JEOL 6060 scanning electron microscope with Digimizer software version 3.0.6.0., see Figure 3.13(b), to evaluate cutting edge geometry, wear mechanisms, coating quality etc. A special jig was designed and fabricated in order to hold the microtools inside the SEM chamber, see Figure 3.13(c). In addition, the SEM was also utilised to investigate/measure aspects including burr width/size, machined slot quality, workpiece microstructure and tool wear mechanisms as well as elemental analysis through an integrated energy-dispersive X-ray spectroscopy (EDX) system.

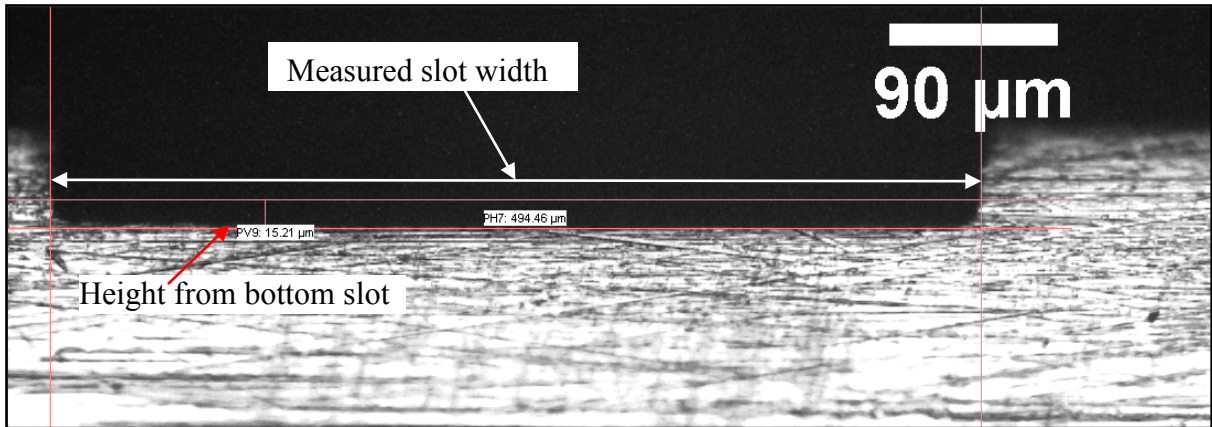


Figure 3.12: Method for measuring the slot width at several positions from slot base

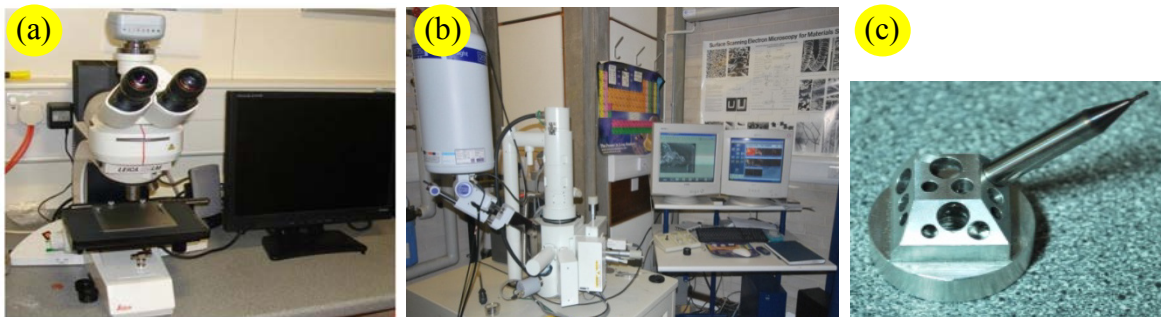


Figure 3.13: Measurement equipments and tool (a) Leica DMLM microscope (b) SEM -JEOL 6060 (c) Jig for microtool

### 3.3.5 Workpiece surface roughness

Both 2D and 3D surface roughness evaluation of the base of the micro slots were performed following Phase 3 and 4 testing. This was carried out using a Taylor Hobson Form Talysurf 120L with a vertical resolution of 10nm, a stylus angle of 60° and a stylus tip radius of 2μm, see Figure 3.14. For 2D line measurements, a 0.8mm cut-off and 4mm sample evaluation length was used. Each slot was measured at 3 locations (the middle and opposite ends of the slot) along the 20mm distance and averaged. In terms of 3D topographical plots, a 0.250 × 0.250mm<sup>2</sup> sampling area was used with the data analysed using Digital Surf Mountains Map Universal software.

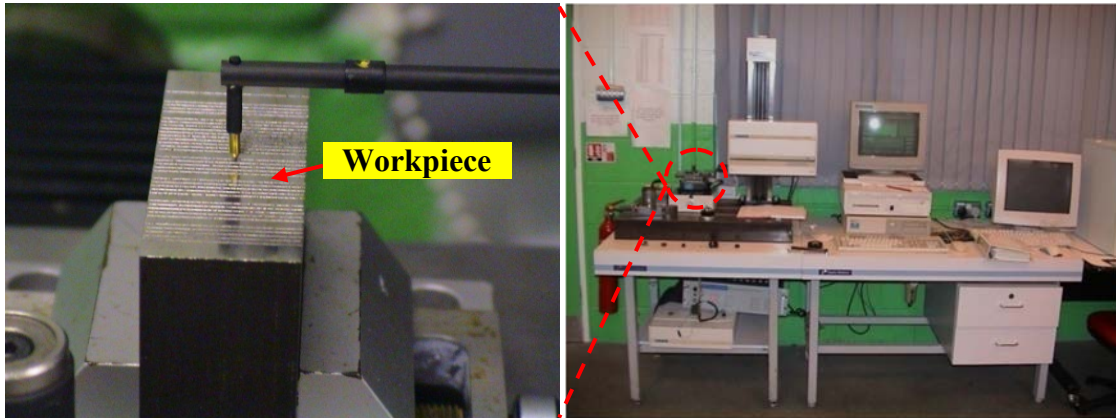


Figure 3.14: Surface roughness measurement equipments: Taylor Hobson Form Talysurf 120L

### 3.3.6 Workpiece microhardness analysis

Microhardness depth profile evaluation was undertaken on a Mitutoyo MVK-G3 testing unit equipped with 10X and 100X optics together with Knoop and Vickers indenters, see Figure 3.15. The former scale ( $HK_{0.025}$ ) was employed at a load of 25g and indentation duration of 15 seconds. Each hardness profile was obtained by taking measurements at appropriate depth intervals (average of 3 readings at each depth level) starting at  $5\mu\text{m}$  below the machined surface and extending up to  $1000\mu\text{m}$ .



Figure 3.15: Mitutoyo MVK-G3 hardness testing

### 3.3.7 Residual stress analysis

Limited residual stress measurements of the slot surfaces were carried out using a Rigaku Strainflex MSF-2M<sup>TM</sup> X-ray stress analyser (Bragg's diffraction theory) with a spot size of  $1.52\text{mm} \times 3.05\text{mm}$ , see Figure 3.16. It utilises a parallel beam method to calculate surface residual stress. Four different tilt angles ( $\psi$ ) were applied during the testing at each point:

$0^{\circ}$ ,  $30^{\circ}$ ,  $45^{\circ}$  and  $60^{\circ}$  with a H1733 (Cr) X-ray tube. Only surface readings were taken (as any residual stresses generated in micromilling were not expected to significantly affect the subsurface), with measurements repeated twice over a milled slot width of 5mm.



Figure 3.16: Residual stress equipment

### 3.3.8 Sample preparation

All slot cross sections for analysis (microstructure, microhardness, burr formation etc.) were cut using a Charmiles ROBOFIL 200 electrical discharge wire machine (EDWM), see Figure 3.17 (a), and subsequently hot mounted in a Buehler Epomet™ Bakelite mounting press, see Figure 3.17 (b). In order to remove any damage induced by the EDWM process, approximately  $300\mu\text{m}$  was ground and polished off the test samples using a Buehler Alpha 2 grinder-polisher, see Figure 3.17 (c). The specimens were subsequently etched with a 2% Nital solution to reveal the workpiece microstructure for investigation. The complete grinding, polishing and etching regime used for AISI D2 steel is detailed in Table 3.3.

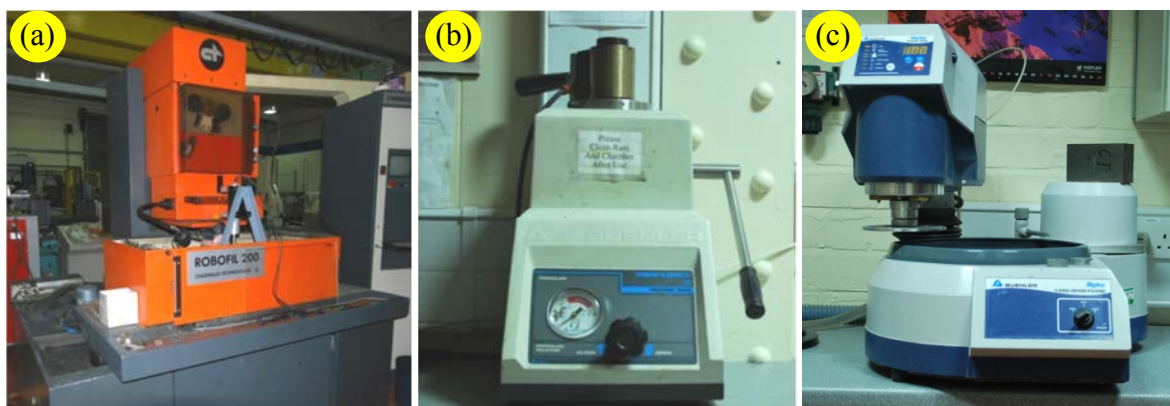


Figure 3.17: (a) ROBOFIL 200 electrical discharge wire machine (EDWM) (b) Buehler Epomet™ Bakelite mounting press (c) Buehler Alpha 2 grinder-polisher

Table 3.3: Grinding, polishing and etching procedure for hardened AISI D2 steel

Operation/Step	Force (N)	Time (min)	Rotation
SiC paper (120 grid)	6	Until plane	Complimentary
SiC paper (240 grid)	6	5.0	Complimentary
SiC paper (600 grid)	6	5.0	Complimentary
SiC paper (1200 grid)	6	5.0	Complimentary
Buelher Ultra-Pol polishing cloth with 9µm MetaDi Supreme diamond	6	5.0	Complimentary
Buelher Ultra-Pol polishing cloth with 3µm MetaDi Supreme diamond	6	3.0	Complimentary
Buelher Ultra-Pol polishing cloth with 0.06µm colloidal silica	6	2.0	Contra
Etched using 2% Nital solution for 40s			

### 3.3.9 Statistical analysis

Statistical analysis including the production of main effect plots, interaction plots and ANOVA tables was performed using Minitab version 15. In addition, the analysis of the mathematical models and response surface contour plots generated in Phase 4 testing were carried out using Design Expert software (version 6.0.5).

## 3.4 Experimental design, procedure and test arrays

As previously outlined, the experimental work was divided into five main phases. Due to scale and difficulties associated with fabrication of micro cutting tools, product quality has been known to be inconsistent, especially between different production batches and tool suppliers. Phase 1 involved a comparative assessment of a range of micro end mill cutters from different tool manufacturers in terms of geometric precision/tolerance (diameter, cutting edge radius etc.) and surface condition. The accuracy and limitations of a commercial meso-scale high speed machining centre (Matsuura LX-1) to be used for subsequent cutting experiments was then evaluated in Phase 2, particularly with respect to spindle thermal growth when operating at high rotational speeds. In Phase 3, the influence of operating parameters on the micro machinability of hardened AISI D2 steel was studied via a full factorial experimental design. Following results from Phase 3 work, further trials were performed to optimise tool life and workpiece surface roughness using Response Surface Methodology (RSM). Finally, the effect of coatings and chip breaker geometry in terms of tool wear/life was investigated in Phase 5 testing. An overview of the experimental work together with issues investigated in each phase are summarised in Table 3.4.

Table 3.4: Overview of experimental phases together with issues investigated

Experimental work				
Phase 1	Phase 2	Phase 3	Phase 4	Phase 5
Analysis of microtool	Investigation of machine tool behaviour and spindle thermal growth errors	Machinability testing - Influence of operating parameters - full factorial design	Machinability testing - Optimisation of tool life and surface roughness - RSM	Machinability testing - Effect of tool geometry and coating
<ul style="list-style-type: none"> <li>• Microtool geometry tolerances</li> <li>• Tool surface condition</li> </ul>	<ul style="list-style-type: none"> <li>• Thermal growth levels at different conditions in terms of;                             <ul style="list-style-type: none"> <li>- Spindle speeds</li> <li>- Base temperatures</li> </ul> </li> <li>• Machine repeatability;                             <ul style="list-style-type: none"> <li>- Warm up and cool down cycles</li> </ul> </li> </ul>	<ul style="list-style-type: none"> <li>• Tool life</li> <li>• Tool wear</li> <li>• Volume of metal removed</li> <li>• Cutting forces</li> <li>• 2D and 3D surface topography</li> <li>• Burr formation</li> <li>• Temperature measurement</li> <li>• Surface integrity;                             <ul style="list-style-type: none"> <li>- Microstructure</li> <li>- Microhardness</li> <li>- Residual stress</li> </ul> </li> </ul>	<ul style="list-style-type: none"> <li>• First and Second order models to predict;                             <ul style="list-style-type: none"> <li>- tool life</li> <li>- surface roughness</li> </ul> </li> <li>• Machinability maps                             <ul style="list-style-type: none"> <li>- tool life</li> <li>- surface roughness</li> </ul> </li> </ul>	<ul style="list-style-type: none"> <li>• Tool wear/life</li> <li>• Wear mechanisms</li> <li>• 3D surface roughness</li> </ul>

### **3.4.1 Phase 1: Analysis of micro milling cutters**

The main objective of this phase was to evaluate the typical quality of commercially available 0.5mm diameter micro endmills. Details of tools assessed were given in Section 3.2.1. All tools were initially cleaned in an ultrasonic bath of acetone to remove hydrocarbon or detergent based contaminants and any adhered particulates. Each cutter was then analysed using the SEM with measurements performed using Digimizer image analysis software.

### **3.4.2 Phase 2: Investigation of machine spindle thermal growth errors**

This phase was aimed at characterising and minimising spindle thermal growth errors on the commercial Matsuura LX-1 unit intended for micro/mesoscale machining operations. The work was divided into two sub-phases (2A and 2B). Phase 2A initially investigated the variation in the temperature of the laboratory in which the machine tool was located. This encompassed some 1100m<sup>3</sup> of space with high speed machining centres; creep feed grinding systems, CNC lathes etc. Due to the scale involved, environmental control is basic as with standard industrial facilities. Following on from this, the spindle temperature during machine warm-up and cool-down cycles (from cold) at rotational speeds of 30,000, 40,000, 50,000 and 60,000rpm was evaluated. Temperature values were recorded at specific time intervals from the spindles' own sensor output onto the control panel, with testing spread over a period of several days. Additionally, measurements were also taken with the machine baseline temperature (temperature of spindle prior to start of trial) varying between 15°C and 18°C. Measurements of spindle displacement/change in tool z-axis position during a spindle cooling cycle were in accordance with standards detailed in BS ISO 230-3:2007 [198], which followed a machine warm up sequence undertaken according to manufacturers' guidelines [199]. This therefore simulated normal operating practice such that any displacement was due to supplementary cooling during spindle down time and any thermal lag. In practice, displacement will depend on the spindle start-stop regime, rotational speed and with increasing periods of down time, greater z-axis error will occur. Figure 3.18(a) gives a schematic of the machine spindle arrangement and shows the ceramic bearings positions adjacent to where temperatures were monitored. Temperature output on the machine control panel, see Figure 3.18(b), reflected the variation associated with bearing 2 located near to the spindle nose. Phase 2B involved evaluation of spindle growth when operating at 60,000rpm with z-axis position measurements taken using a 'dummy tool' (blunt, flat ended carbide rod) and following a machining operation on graphite workpieces. Both contact and non-contact

techniques were employed to determine changes in z-axis length, involving a Mitutoyo dial test indicator (DTI) and Renishaw NC-3 laser tool setting unit respectively. Graphite workpieces (150mm × 110mm × 50mm block) were utilised to avoid problems with built-up edge (BUE) and tool wear during machining. The cutting tools were twin fluted 6mm diameter PCD end mills. The rationale for employing relatively large tools (instead of sub-millimeter cutters) was principally to facilitate measurement. With the dummy tool, a programme was written to incorporate spindle operation at 5 minute intervals with a 3 second measuring period during which the spindle was stopped. The dummy tool approached and contacted the digital touch indicator (DTI) using a step-down feed rate sequence, see Figure 3.18(c) for the general arrangement. The same methodology was adopted for non-contact measurement with the dummy tool ‘interrupting’ the beam from the NC-3 laser tool setting unit. Details of the CNC programme for both methods are given in Appendix A. Investigation of spindle growth during actual machining involved dry cutting of test slots using a feed rate of 50mm/min and depth of cut of 50µm, with the spindle bearing at a baseline/initial temperature of 18°C. The actual slot depth on the workpiece was measured using a Renishaw OMP 40 contact probe mounted in the spindle, see Figure 3.18(d). The average of 3 measurements at each assessment position on the slot (correlated with cutting time), was recorded graphically as a calibration curve.

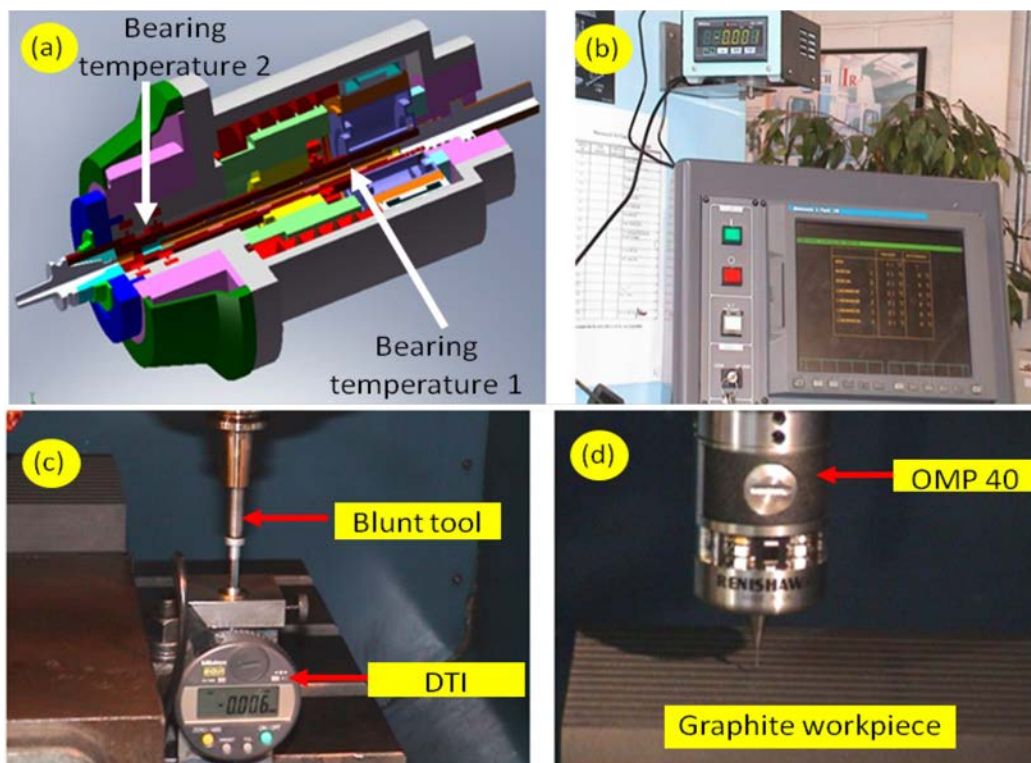


Figure 3.18: Phase 2 setup (a) Schematic of the machine spindle (courtesy of Matsuura) (b) Machine control panel output measurement (c) Mitutoyo DTI (d) Renishaw OMP 40

### **3.4.3 Phase 3A: Preliminary micromilling trials**

In Phase 3A, an initial set of exploratory tests were performed in order to gain preliminary insight of the key operating parameters involved in slot milling of hardened D2 steel and their effect on tool performance. Tests as far as possible were performed in accordance with ISO 8688-2: 1989 (Tool life testing in milling) standards [200]. The main variables investigated were cutting speed, feed per tooth and depth of cut, based on information gathered from the literature review. Tool life/end of test criterion is generally based on a specific level of cutter flank wear in conventional macro milling operations. The small dimensions of tools used in micromilling however, makes flank wear measurement extremely difficult using standard techniques (optical/tool makers microscope), notwithstanding the fact that chipping/catastrophic fracture is the dominant tool failure mode/mechanism. Therefore the change/reduction in tool diameter has been used by several researchers [17, 139] to quantify/characterise tool wear progression. This was adopted in the present work with the cutter diameter assumed to be approximately equivalent (further details in Section 4.3.1) to the width of slot machined. Each slot channel was measured after the completion of the trials using the Leica optical microscope and SEM. In terms of specific parameter levels, these were selected according to guidelines provided by the tool supplier [80], as well as recommendations from previous research work relating to micro machining of hardened steel [11, 16, 21, 28, 89, 149, 150]. A total of eleven trials were performed with cutting speed, feed per tooth and depth of cut ranging between  $V_c = 5 - 70\text{m/min}$ ,  $ft = 0.5 - 3.0\mu\text{m/tooth}$  and  $d = 1.0 - 70\mu\text{m}$  respectively. All trials were carried out to the point of tool fracture/failure. Results from this phase of work were used to determine appropriate baseline parameters and end of test criteria for subsequent mainstream trials.

### **3.4.4 Phase 3B: Influence of operating parameters**

Phase 3B was designed primarily to establish the influence of cutting speed, feed rate and depth of cut on tool life, slot quality, cutting forces, burr formation and associated workpiece surface integrity (microhardness, microstructure, surface roughness), when full immersion slot milling (0.5mm width) hardened AISI D2 cold work tool steel. Limited cutting temperature and surface residual stress assessment was also performed. Trials were conducted dry (without coolant or air blast) with the full tool diameter engaged and based on a full factorial experimental design (no replications) with variation of 3 factors each at 2 levels. The associated experimental details are given in Table 3.5 and Table 3.6 respectively.

Respective spindle rotational speed (RPM) was calculated based on nominal diameter 0.5mm (all tools assumed to be equivalent as they were supplied from the same batch), which was kept constant in all tests as reduction in tool diameter at the end of test criterion was typically less than 10%.

Tests were carried out in random order while the end of test criterion was 520mm length of cut (after 26 slots machined) based on results from Phase 3A. Each run was conducted with a new tool (cutting edge radius 5-7 $\mu$ m) and SEM pictures were taken before trial commencement and at the end of test to determine cutter conditions while slot width was measured with the optical microscope. Workpiece surface roughness (Ra) was measured at 3 locations on the final slot (slot 26) with the mean recorded for statistical analysis. Similarly, slot quality and burr widths (viewed from the top of the channel) were assessed following every experiment using SEM. Cutting forces ( $F_x$ ,  $F_y$  and  $F_z$  components) were investigated with tools in the new (slot 1) and worn (slot 26) condition. Results were subsequently evaluated using analysis of variance (ANOVA) to determine statistically significant factors and associated percentage contribution together with generation of main effects plots. This was performed using Minitab software (version 15.1.20.0).

Table 3.5: Phase 3 Factors and levels

Factors	Low	High
Cutting speed, $V_c$ (m/min)	20	50
Feed, $ft$ ( $\mu$ m/tooth)	1	2
Depth of cut, $d$ ( $\mu$ m)	15	55

Table 3.6: Full factorial design matrix ( $L_8$ )

Test No.	Factors and levels		
	$V_c$ (m/min)	$ft$ ( $\mu$ m/tooth)	$d$ ( $\mu$ m)
Test 1	20	1	15
Test 2	50	1	15
Test 3	20	2	15
Test 4	50	2	15
Test 5	20	1	55
Test 6	50	1	55
Test 7	20	2	55
Test 8	50	2	55

### 3.4.5 Phase 4: Optimisation of tool life and surface roughness

The experimental design employed in Phase 3 was extended in Phase 4 by employing RSM with a central composite design (CCD) to enable optimisation of tool life and slot surface roughness. This also allowed the formulation of first and second order models for the prediction of defined response outputs. Results from tests in Phase 3 were adopted to form the corner points/vertices (Test 1 – 8) of the CCD cube, while centre points (Test 9 - 12) based on 4 repeated trials were specified for development of first order (linear) models/relationships (based on  $L_{12}$  experimental design). As first order models are typically only valid/reliable over a narrow range of variables, the experimental matrix was further expanded with 6 axial points at 1.68 argument length ( $\alpha = (n_f)^{1/4}$ :  $\alpha$ - argument length,  $n_f$  – number of experiment) for correlation of variable factor responses to second order (quadratic) models ( $L_{18}$  experimental design), see Figure 3.19 and Table 3.7 for specific parameter levels. Experiments were performed in a random order with Table 3.8 showing the full test matrix of the RSM design. Further details of the RSM technique can be found in the reference by Montgomery [187].

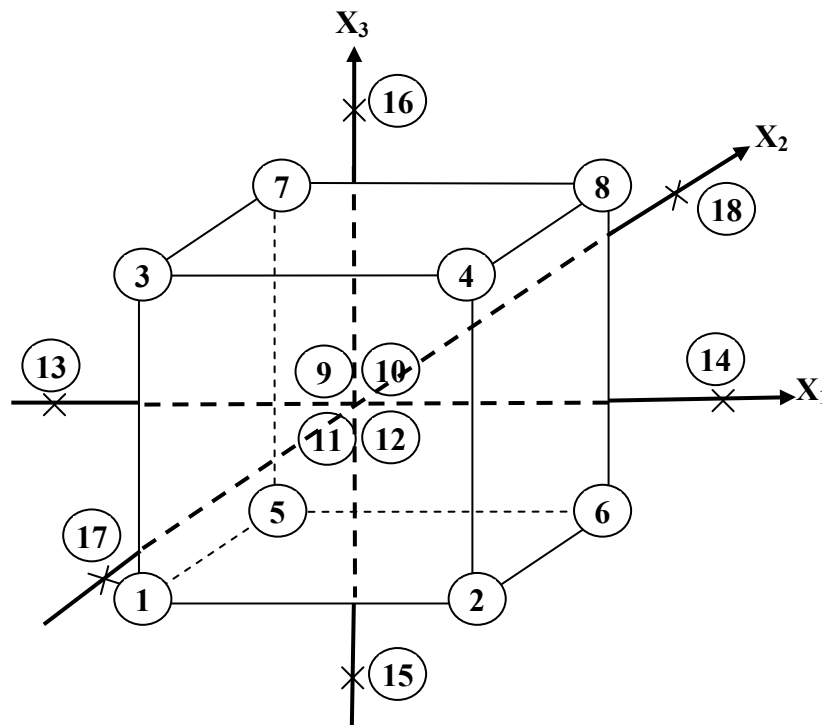


Figure 3.19: Central composite design for three factors

Table 3.7: Phase 4 levels of independent variables

	Lowest	Low	Centre	High	Highest
Coded	-1.68	-1.00	0.00	1.00	1.68
Cutting speed, $V_c$ (m/min)	9.77	20.00	35.00	50.00	60.23
Feed, $ft$ ( $\mu\text{m}/\text{tooth}$ )	0.66	1.00	1.50	2.00	2.34
Depth of cut, $d$ ( $\mu\text{m}$ )	1.36	15.00	35.00	55.00	68.64

Table 3.8: Phase 4 design matrix using RSM ( $L_{18}$ )

Test No.	Location in CCD	Independent parameters			Coded		
		$V_c$ (m/min)	$ft$ ( $\mu\text{m}/\text{tooth}$ )	$d$ ( $\mu\text{m}$ )	$x_1$	$x_2$	$x_3$
Test 1	Factorial	20.00	1.00	15.00	-1.00	-1.00	-1.00
Test 2	Factorial	50.00	1.00	15.00	1.00	-1.00	-1.00
Test 3	Factorial	20.00	2.00	15.00	-1.00	1.00	-1.00
Test 4	Factorial	50.00	2.00	15.00	1.00	1.00	-1.00
Test 5	Factorial	20.00	1.00	55.00	-1.00	-1.00	1.00
Test 6	Factorial	50.00	1.00	55.00	1.00	-1.00	1.00
Test 7	Factorial	20.00	2.00	55.00	-1.00	1.00	1.00
Test 8	Factorial	50.00	2.00	55.00	1.00	1.00	1.00
Test 9	Centre	35.00	1.50	35.00	0.00	0.00	0.00
Test 10	Centre	35.00	1.50	35.00	0.00	0.00	0.00
Test 11	Centre	35.00	1.50	35.00	0.00	0.00	0.00
Test 12	Centre	35.00	1.50	35.00	0.00	0.00	0.00
Test 13	Axial	9.77	1.50	35.00	-1.68	0.00	0.00
Test 14	Axial	60.23	1.50	35.00	1.68	0.00	0.00
Test 15	Axial	35.00	0.66	35.00	0.00	-1.68	0.00
Test 16	Axial	35.00	2.34	35.00	0.00	1.68	0.00
Test 17	Axial	35.00	1.50	1.36	0.00	0.00	-1.68
Test 18	Axial	35.00	1.50	68.64	0.00	0.00	1.68

The relationship between the response factor (tool life) and process independent variables can be represented by Equation 1 [187];

$$T = C(V_c^l, ft^m, d^n)\varepsilon \text{ -----Eq. 1}$$

where T is the tool life in minutes,  $V_c$ ,  $ft$ , and  $d$  are the cutting speed (m/min), feed per tooth ( $\mu\text{m}/\text{tooth}$ ), and depth of cut ( $\mu\text{m}$ ) respectively while  $C$ ,  $l$ ,  $m$ ,  $n$  are constants and  $\varepsilon$  is a random error. Eq. 1 can also be expressed in the following logarithmic form, see Equation 2;

$$\ln T = \ln C + l \ln V_c + m \ln ft + n \ln d + \ln \varepsilon \text{ -----Eq. 2}$$

A first-order linear model based on of Equation 2 can then be represented as shown in Equation 3;

$$\hat{y}_1 = y - \varepsilon = b_0x_0 + b_1x_1 + b_2x_2 + b_3x_3 \quad \text{-----Eq. 3}$$

where,  $\hat{y}_1$  is the estimated response based on the first-order equation and  $y$  is the measured tool life on a logarithmic scale;  $x_0 = 1$ , is a dummy variable;  $x_1, x_2, x_3$  are logarithmic transformations of cutting speed, feed per tooth and depth of cut respectively, while  $b_0, b_1, b_2, b_3$  are the parameters to be estimated.

The transformation equations for each of the independent variables are defined in Equations 4 to 6:

$$x_1 = \frac{\ln V - \ln 35}{\ln 50 - \ln 35}; \quad \text{-----Eq. 4}$$

$$x_2 = \frac{\ln ft - \ln 1.5}{\ln 2.0 - \ln 1.5}; \quad \text{-----Eq. 5}$$

$$x_3 = \frac{\ln d - \ln 35}{\ln 50 - \ln 35}; \quad \text{-----Eq. 6}$$

Following the formulation of the first order model, second order relationship can then be derived according to Equation 7;

$$\hat{y}_2 = y - \varepsilon = b_0x_0 + b_1x_1 + b_2x_2 + b_3x_3 + b_{11}x_1^2 + b_{22}x_2^2 + b_{33}x_3^2 + b_{12}x_1x_2 + b_{13}x_1x_3 + b_{23}x_2x_3 \quad \text{-----Eq. 7}$$

where,  $\hat{y}_2$  is the estimated response based on the second order models. In the second order response equation, the influence of single factors, quadratic terms and their interaction effects are all considered, and therefore are generally expected to provide more accurate predictions. A lack of fit test for the estimated coefficients was carried out using ANOVA to verify the models and model predictions were tested at the 5% significance level.

### **3.4.6 Phase 5: Effect of tool coating and tool geometry on tool life and surface roughness**

All previous phases of work utilised coated end mills, which is the industry standard for carbide based tools. Coatings however tend to increase the cutting edge radius and hence

reduce the effective sharpness of tools. This can therefore have a significant influence on the mechanics of cutting particularly under microscale machining conditions.

Phase 5 aimed to benchmark the performance of uncoated tools as well as coated end mills incorporating a chip breaker feature against conventional geometry, coated micro cutters. The only variable factors were either the presence of the coating or a chip breaker, with all other features remaining constant. All trials used the same cutting parameters; cutting speed of 50m/min, feed rate of  $1\mu\text{m}/\text{tooth}$  and a depth of cut of  $55\mu\text{m}$ . Comparisons were primarily assessed in terms of tool life, surface roughness/topography and cutting forces.

All trials were conducted to the point of tool breakage, each of which was replicated twice. Changes in microtool diameter/slot width after each pass were evaluated using SEM. Three dimensional (3D) topographical maps were plotted following the first (new tool) and last (failed tool) slots for every test to evaluate surface roughness. Additionally, the various tool failure mechanisms observed were assessed, with EDX measurements used to verify coating delamination and workpiece material adhesion.

## **Chapter 4: RESULTS AND DISCUSSION**

### **4.1 Phase 1: Analysis of commercial micro milling cutters**

There are numerous cutting tool manufacturers (such as Mitsubishi, Iscar, Sandvik, Fraisa, Seco, Union Carbide, etc.) that offer carbide micro end mills typically down to 100 $\mu\text{m}$  diameter as standard products, with even smaller cutters ( $\sim 60\mu\text{m}$  diameter) available for bespoke applications. The mass fabrication of such microtools usually involves abrasive grinding operations followed by a coating process such as physical vapour deposition (PVD). The nature and scale of the manufacturing process however can lead to significant difficulties in achieving or maintaining geometrical accuracy, tolerances and integrity, particularly between different production batches. Figure 4.1 details SEM micrographs of the end mills selected for this study, viewed from top face of the tool. Note that although Tool 5 and 6 had the same code/designation, there were differences in the tool geometry (with and without chip breaker). Additionally, only one of each tool was inspected and therefore cannot be assumed as representative of a complete batch. Defects were observed in all of the tools evaluated, at varying levels of severity. Common/obvious flaws included chipped/broken cutting edges and heavy grinding marks/scratches on the tool surfaces, see Figure 4.2. This could have been due to deficiencies in quality monitoring and limitations of the microtool fabrication process [10]. A number of the tools received also had broken cutting edges, see Figure 4.3, although whether this was due to the manufacturing process, could not be ascertained. A likely scenario is that the tools were damaged either as a result of collisions during cutter inspection or during transport/delivery due to inadequate packaging/handling. Coating quality in general was similarly poor, with defects such as non-uniform deposition of coated layer (particularly around the cutting edge radius), flaking of the coating and formation of droplets/bubbles on the surfaces of the tools, see Figure 4.4. Based on these observations, it is imperative that inspection and assessment of microtools is conducted prior to machining, in order to minimise errors and maintain consistent results.

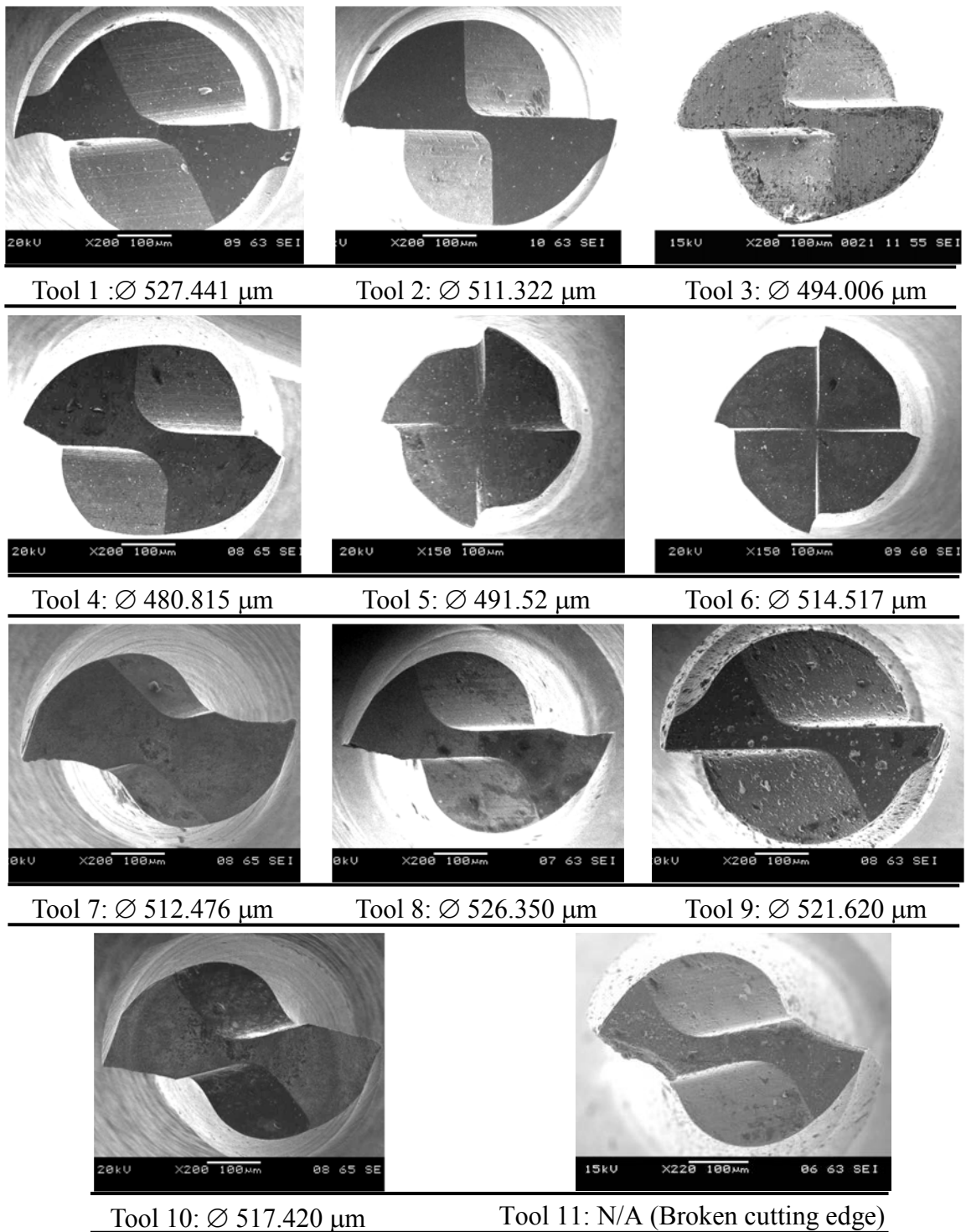


Figure 4.1: SEM micrographs of the end mills selected for this study

\*For details of each tool refer to Table 3.1

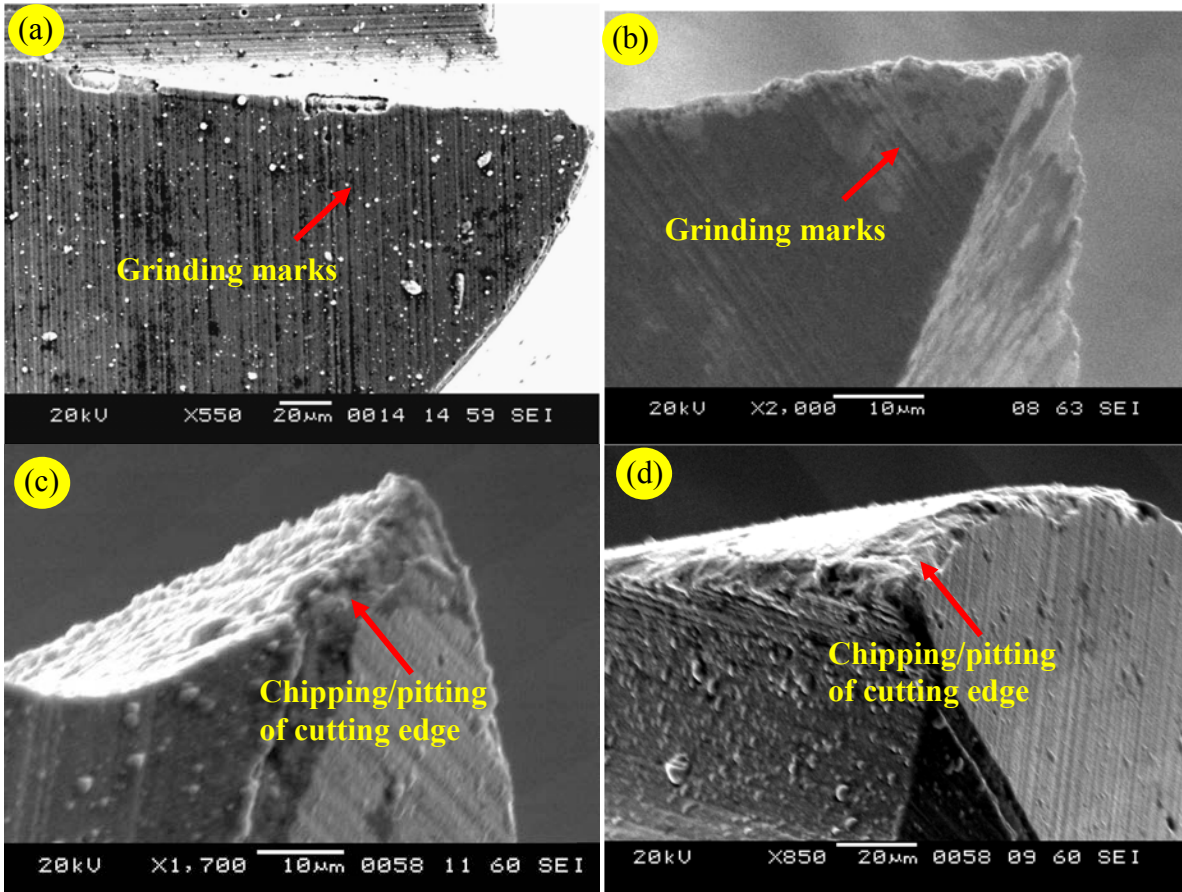


Figure 4.2: Microtool defects (a-b) Grinding marks. (c-d) Chipping/pitting of cutting edge

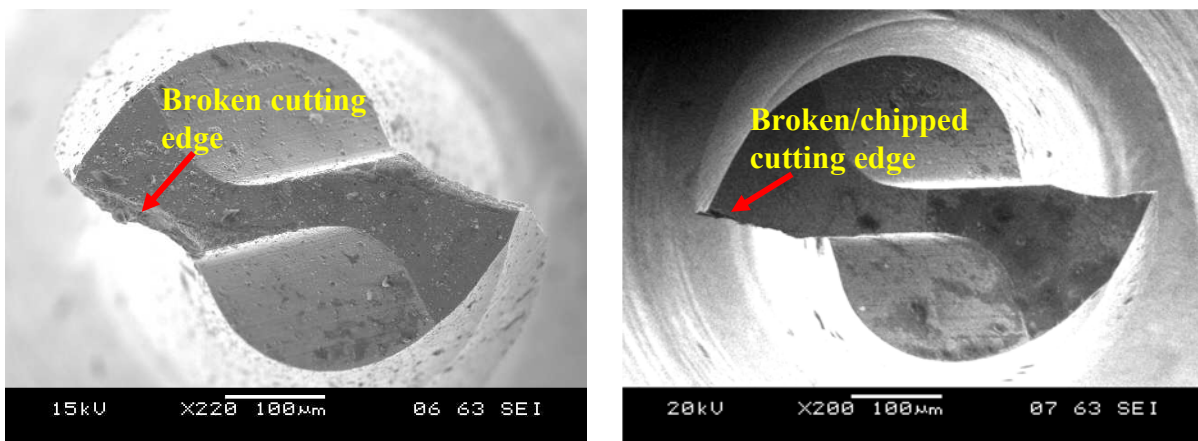


Figure 4.3: Broken cutting edge for different microtool

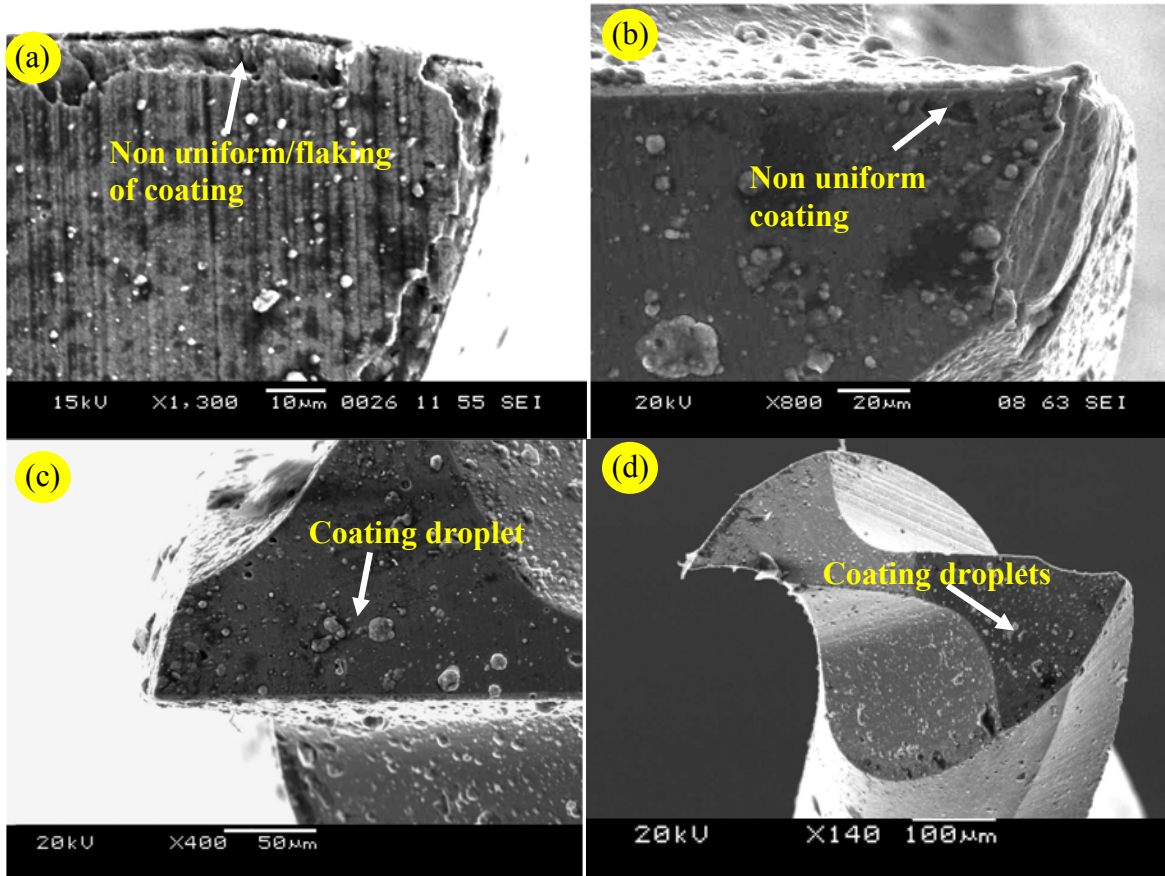


Figure 4.4: (a-b) Non uniform coating. (c-d) Coating droplets

Results from the microtool diameter analysis are detailed in Figure 4.5 (excluding Tool 11- which had a broken cutting edge). Three of the end mills were found to be undersized while the rest were oversized, with the deviation from the nominal diameter (0.5mm) ranging between  $5.9\mu\text{m}$  and  $27.4\mu\text{m}$  (1.2% to 5.5% in percentage terms). This appears to indicate considerable disparity in terms of manufacturing process capability and quality control between the different tool suppliers. In additions, the diametrical errors in 8 of 10 tools inspected were greater than  $10\mu\text{m}$ , which is larger than the typical value ( $\pm 10\mu\text{m}$ ) reported by several researchers in the literature [78, 94, 95].

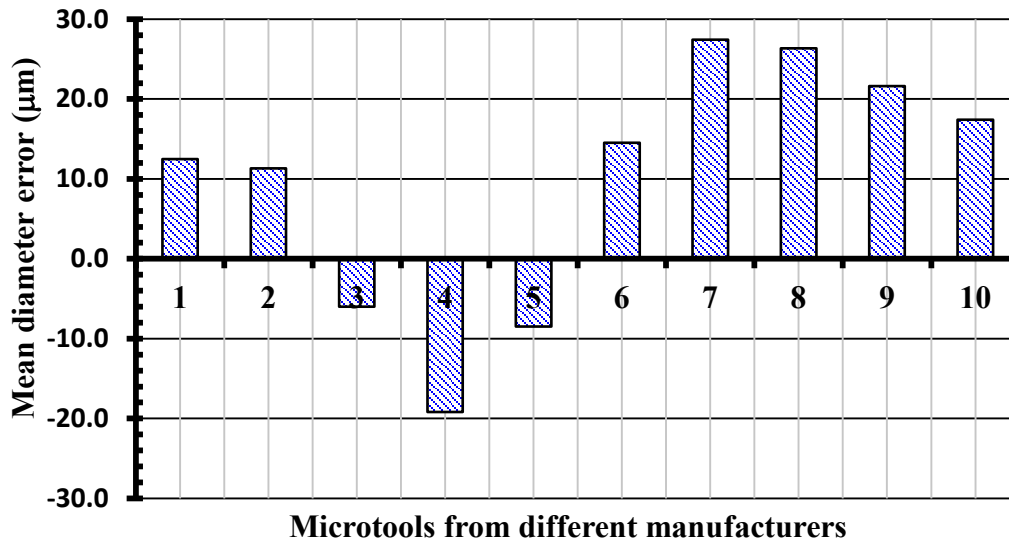


Figure 4.5: Microtool diameter error

*\*Mean diameter is average of 3 readings*

Figure 4.6 shows the measured cutting edge radius for the 10 tools. The variation in edge radius observed over the entire sample set ranged from 3.5µm for Tool 6 to 8.9µm with Tool 9. This suggests that significant differences in performance are likely as the minimum chip thickness criterion for each tool would be expected to vary for a given workpiece material-operating parameter combination.

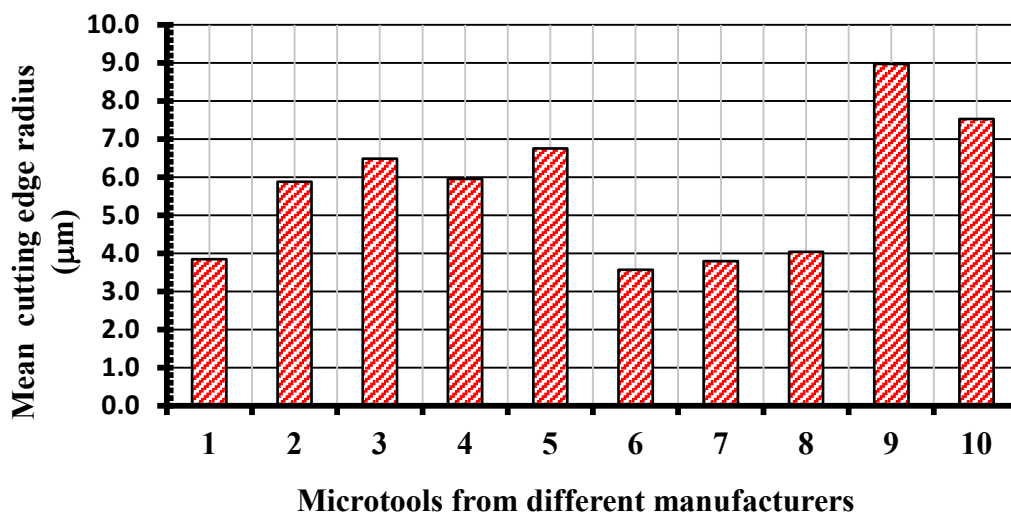


Figure 4.6: Microtool cutting edge radius

In order to minimise variations and ensure consistency in performance, it is advisable that tools are obtained from the same production batch whenever possible. However, Aramcharoen and Mativenga [4] reported that even within an individual batch, 60% of the cutters were unacceptable due the chipping, cracking, incorrect target rake angles or larger than specified cutting edge radii.

## 4.2 Phase 2: Investigation of machine spindle growth errors

Figure 4.7 shows the variation in average daily laboratory temperature (measured using a standard thermometer) from 0900 to 2000 assessed over a one week period, with the error bars showing the range of measurements (max-min) at each hour when readings were recorded. The temperature changed by approximately 3°C to 4°C on a typical day, however seasonal variations were not taken into account. Figure 4.8 shows the corresponding variation in average tool length due to the temperature change, measured without spindle rotation. The mean tool length growth was approximately 4.5µm as a consequence of machine tool flexure while the error bars details the maximum and minimum values obtained at each time over the week. The increasing trend of the temperature (and hence tool length) was mainly due to the rise in activities within the laboratory as the day progressed (other machines operating etc.) as well as the prevailing environment/weather conditions on the days measurements were performed.

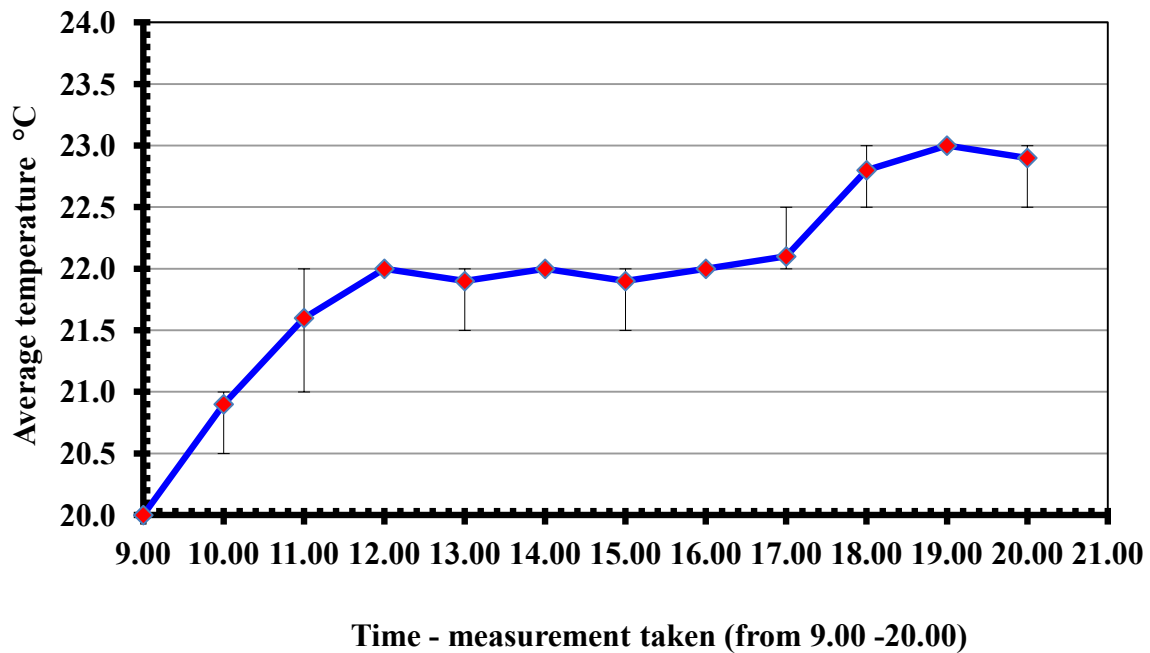


Figure 4.7: Average laboratory temperature in a day

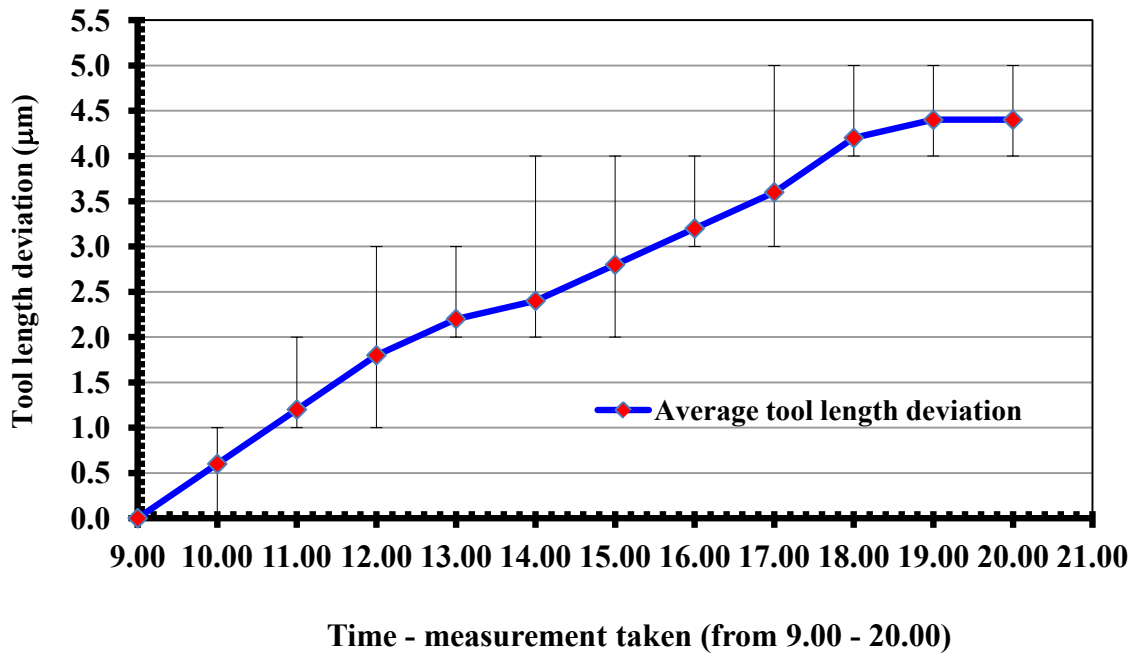


Figure 4.8: Time versus average tool length deviation in a day (static spindle)

Figure 4.9 shows the time-temperature response curves during spindle warm up and cool down at rotational speeds of 30,000rpm, 40,000rpm, 50,000rpm and 60,000rpm respectively (refer to Section 3.4.2 for measurement procedure). The spindle rotation was halted once the temperature for a given rotational speed was judged to have reached a plateau (10 minute duration removed from the graph). This was approximately after 4 minutes at 30,000rpm while for 60,000rpm it took 12 minutes. The plateau and corresponding rise in temperature varied depending on rotational speed, which was 23°C at 30,000rpm (6°C rise) but was up to 54°C (37°C rise) at 60,000rpm. Cool down time took about 2 to 3 times longer than warm up. Figure 4.10 details data for a fixed rotational speed of 30,000rpm and different baseline temperatures (ambient room temperature) experienced in the laboratory. During the experiment, spindle rotation was actuated once the sensor temperature (at bearing 2, see Figure 3.18(a)) had reached the pre-determined test value (15°C, 16°C, 17°C and 18°C). It can be seen that the rise in temperature for the different response curves was essentially the same at approximately 6/7 °C. As expected, the plateau region matches the majority of baseline (initial) temperatures. All the measurements were undertaken whilst the active cooling system was in operation. Without this, the temperature rise from ‘cold’ would have been substantially higher. In any event, the spindle was designed to shut down automatically should bearing 1 and 2 reach a defined temperature above the baseline value, however this was not reached in the current tests.

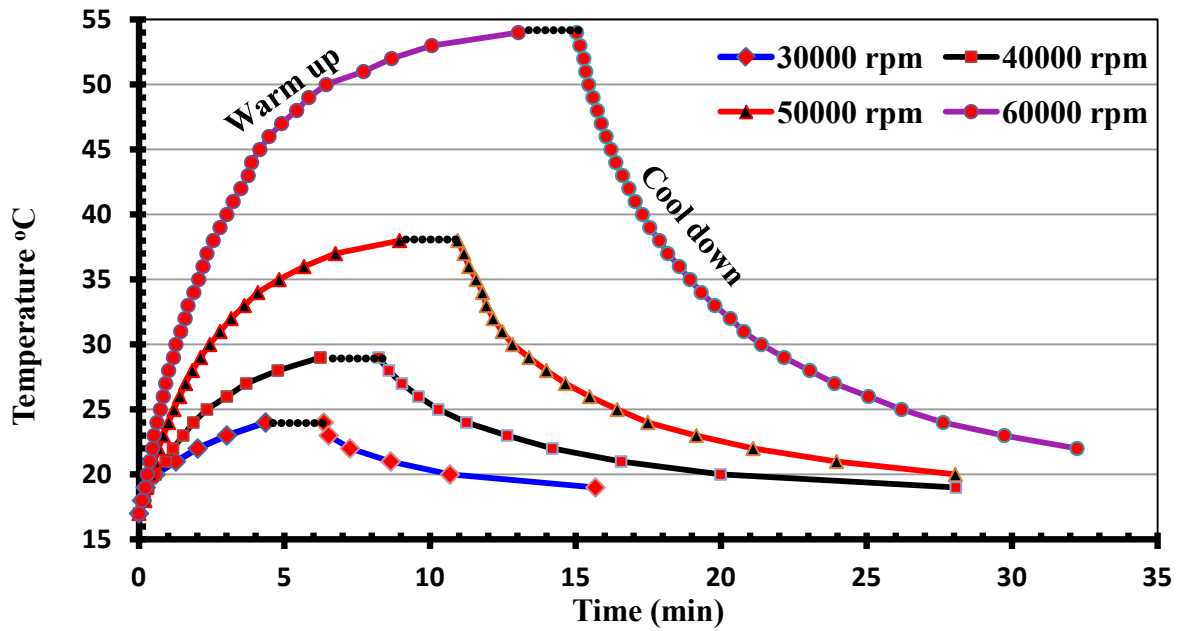


Figure 4.9: Time vs. temperature response curves during spindle warm up and cool down for various speeds at 17°C base temperature

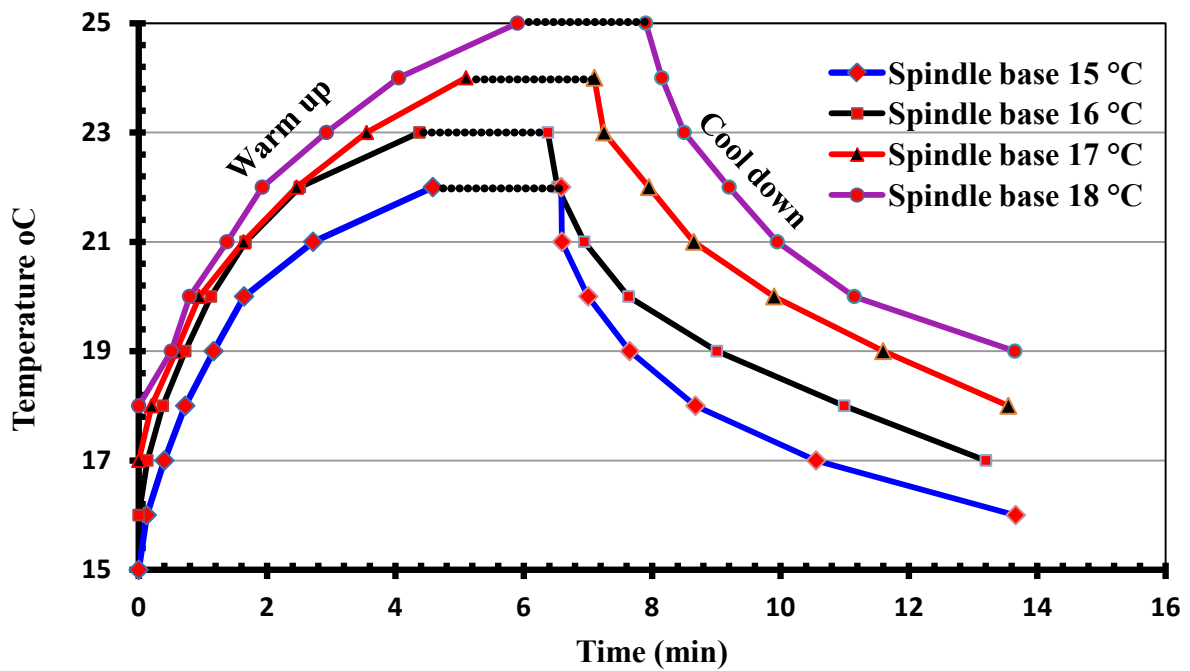


Figure 4.10: Time vs. temperature response curves during spindle warm up and cool down at 30,000rpm for different base temperatures

Figure 4.11 details multiple consecutive warming up and cooling down cycles when operating at 60,000rpm. It highlights the relative repeatability of the rate of spindle temperature rise and the effects of cooling truncation. Here, the period during which the

spindle is not rotating and therefore cooling is 10 minutes, which is arguably at the limit of operation before a further warming up cycle is necessary. This is evident in data for the associated spindle z-axis variation during the cooling phase for Cycle 4 shown in Figure 4.12. With the spindle stopped, the sensor adjacent to the spindle nose (bearing 2) shows a fall from approximately  $\sim 56^{\circ}\text{C}$  to  $\sim 31^{\circ}\text{C}$  over the 10 minute cooling period. In contrast, the z-axis experiences rapid ‘growth’ of  $\sim 16\ \mu\text{m}$  during the first  $\sim 3$  minutes before returning as expected to ‘zero’ after a further 7 minutes. The apparent lag in z-axis growth could be due in part to spindle thermal transfer by conduction to the machine head casing and x-axis bridge of the machine, which are not subject to active cooling. Results for the other cycles are given in Appendix B.

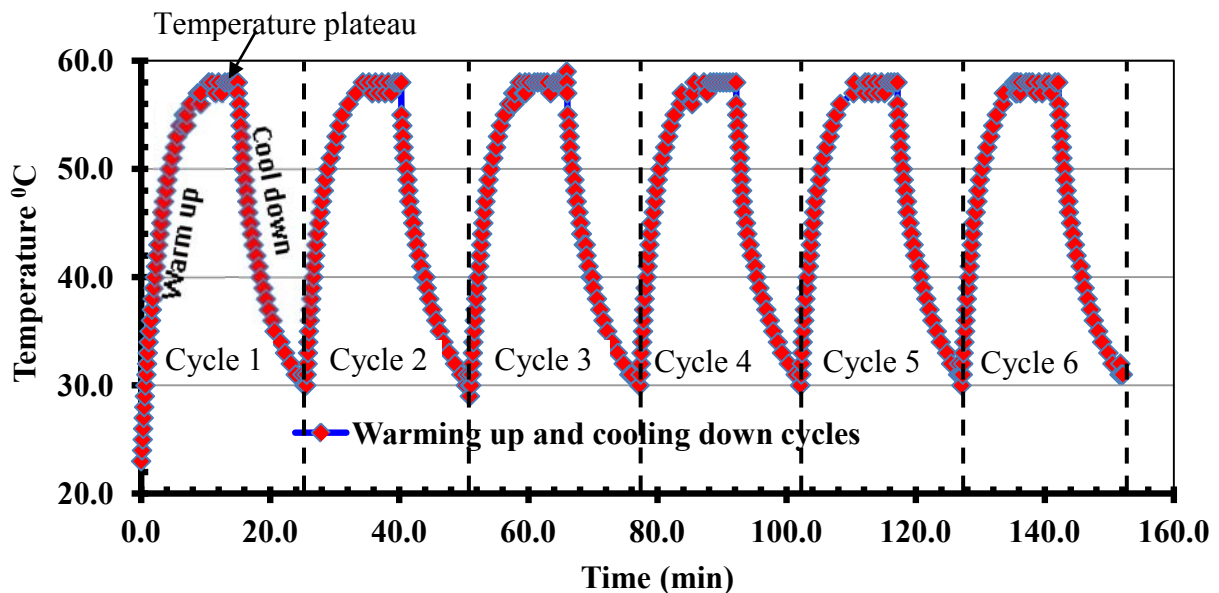


Figure 4.11: Warming up and cooling down cycles when operating at 60,000rpm

*\*Spindle cooling system and active z-axis compensation was employed throughout the tests*

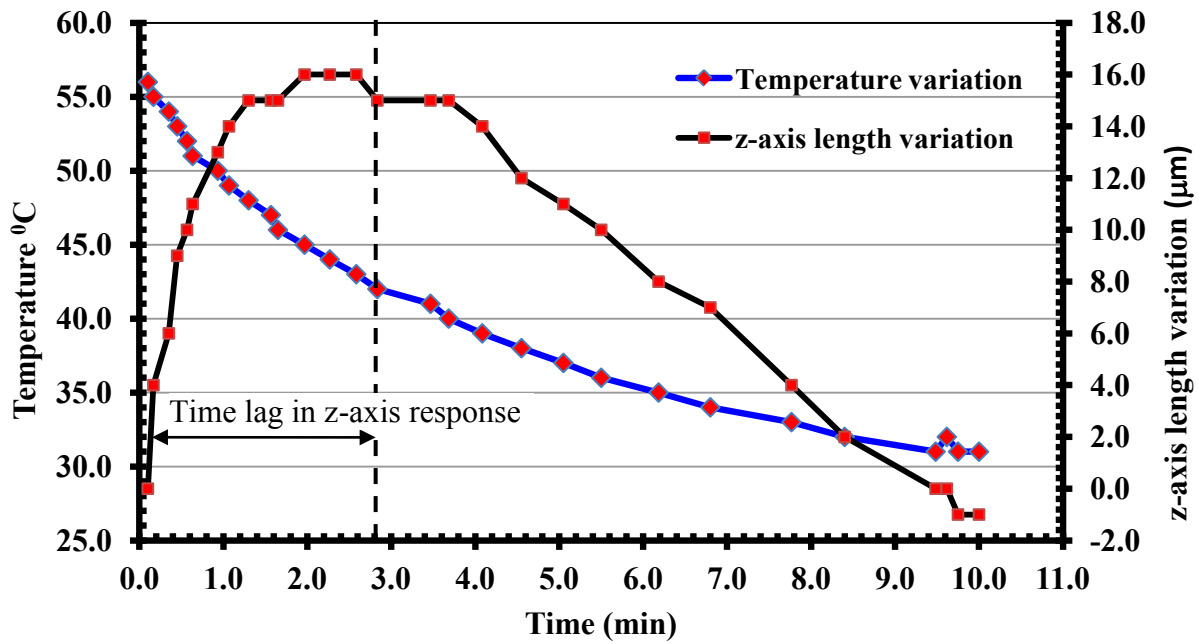


Figure 4.12: z-axis length variation during cooling phase in cycle 4 with spindle stopped

Figure 4.13 shows the z-axis length variation during spindle operation at 60,000rpm following a standard warm-up cycle. Here, spindle growth of approximately 15µm measured with both the DTI and NC3 systems was only attained after a longer period of operation (25 – 35 minutes rather than 15 minutes), although the reason for the apparent disparity in relation to results in Figure 4.12 is not clear. The only significant difference between the data in Figures 4.12 and 4.13 was that the former related to measurements with the spindle stationary for a prolonged period of 10 minutes (but cooling system still active as long as bearing temperature is above baseline/room temperature) as opposed to only 3 seconds during which measurement was made in the latter. Figure 4.14 shows the difference in z-axis length change measured using the NC3 with the spindle operating at 30,000rpm, 40,000rpm, 50,000rpm and 60,000rpm respectively. Greater variation was observed as the speed increased, which is in line with the results reported by Bissacco et al. [68] and Creighton et al. [53].

In order to minimise the apparent spindle length variation, changes were made to the acceleration and deceleration rates of the spindle (no effect on rotational speed during cutting). Due to commercial considerations, complete disclosure of the changes is prohibited however the modifications resulted in significantly reduced z-axis variation by approximately 50% (8µm). Figure 4.15 shows slot depths following the machining of graphite using a Ø6 mm PCD end mill. Tool wear was found to be negligible and therefore the deviation in

programmed slot depth (nominally 50 $\mu\text{m}$ ) reflects the variation in z-axis length due to thermal growth. The results show that z-axis growth was restricted to  $\sim 8\mu\text{m}$ , even after operating at 60,000rpm for  $\sim 40$  minutes. The modified spindle setting/configuration was therefore maintained and utilised for subsequent mainstream experimental testing.

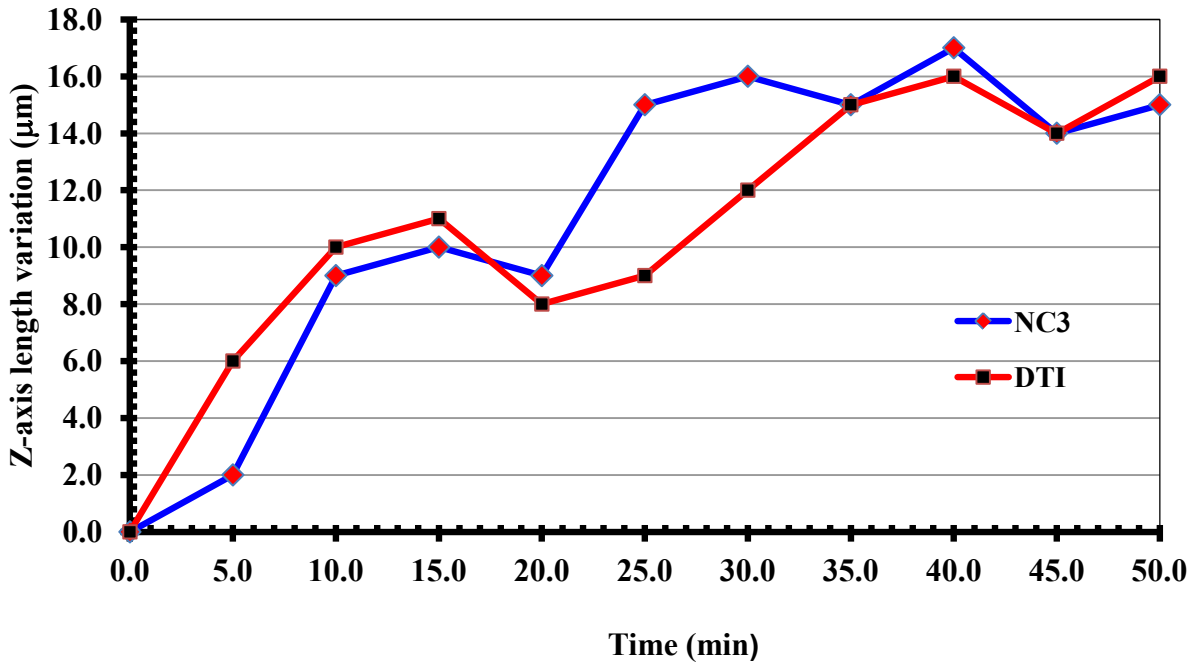


Figure 4.13: The z-axis length variation during spindle operating at 60,000rpm

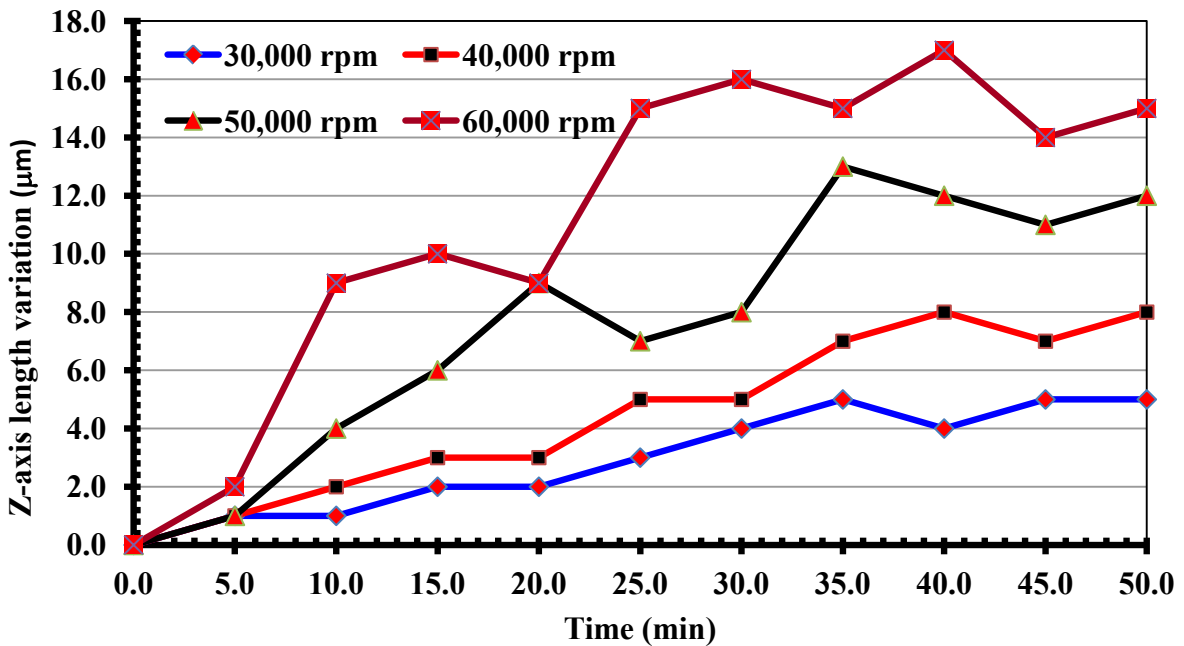


Figure 4.14: The z-axis length variation measured using NC3 when spindle operating at 30,000rpm, 40,000rpm, 50,000rpm and 60,000rpm.

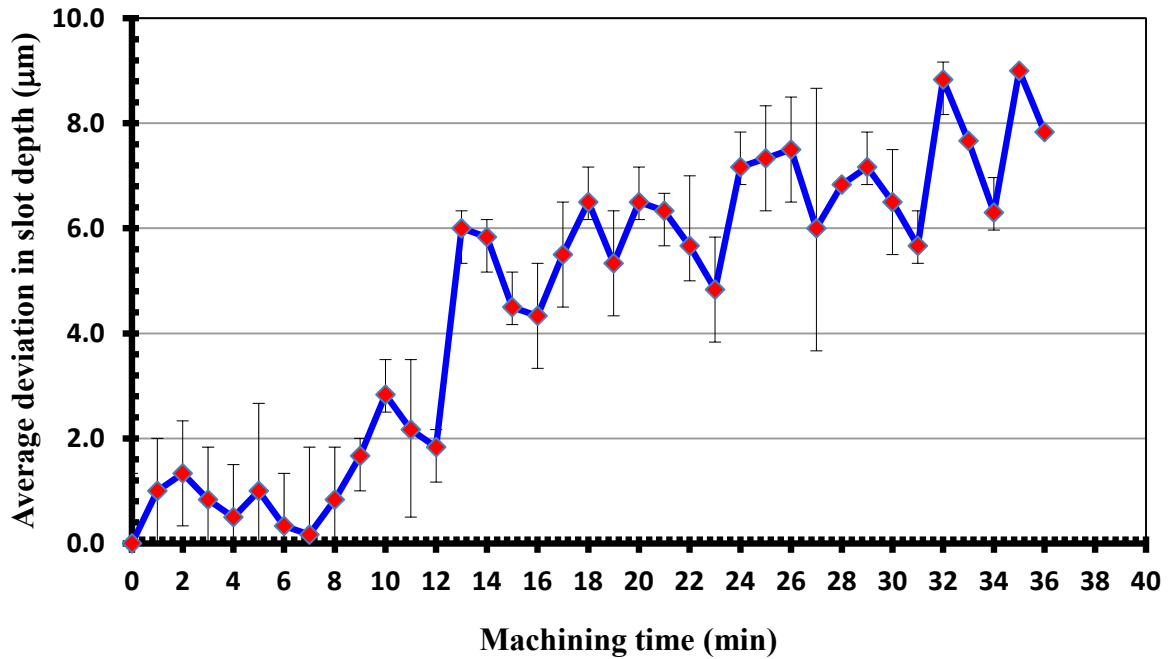


Figure 4.15: Slot depths measured using the OMP 40 during machining of graphite following modification of spindle acceleration-deceleration rate

### 4.3 Phase 3A: Preliminary micromilling trials

#### 4.3.1 Evaluation of tool wear/reduction in tool diameter

Figure 4.16 shows an example of wear progression on the rake face, flank face and end flute of a new micro end mill at cut lengths of 100mm, 520mm and 2500mm respectively. The cutting parameters employed were a cutting speed of 20m/min, feed per tooth of 1µm/tooth and 55µm depth of cut. The cutting edge corner of the tool was relatively sharp prior to machining, see Figure 4.16 (a-c). Following a 100mm cut length, the corner of the end mill began to radius and the sharp edge dulled due to wear (Figure 4.16 (d)). The coating layer was also seen to flake, particularly at the boundary between the flank and rake faces (cutting edge) with signs of chipping/fracture visible from the end of the flute, see Figure 4.16 (e) and (f). As machining proceeded, high stress concentration and impact due to the intermittent engagement/disengagement of the micro cutter with the workpiece, led to further fracture/chipping of the flank face and dulling of the cutting edges after 520mm cut length (26 slots). Abrasive wear was also apparent as the TiAlN coating delaminated, thereby exposing the carbide substrate in the machining zone, see Figure 4.16 (g) – (i). Severe fracture/rounding of the tool, removal of coating as well as significant loss of edge geometry was evident as the cut length reached 2500mm (125 slots).

The widths of the micro-milled slots/channels were used to quantify tool wear. From preliminary tests, it was observed that there was a correlation between tool diameter and slot width, as shown in Figure 4.17 with a difference of ~9% for the first slot (after 20mm cutting length) and 8.4% for the last slot (slot 26). The discrepancy in the values between tool diameter and corresponding slot width was attributed to measurement errors and the difficulties in determining the actual location of channel walls when viewed from the top. The difference however did not exceed 10% for all cases.

The corresponding reduction in tool diameter (based on slot widths with details of measurement given in Section 3.3.4) as the cut length increased, is illustrated in Figure 4.18. The wear of the microtool appears to progress according to three distinct stages: the initial, steady-stage and failure stage. In the initial stage, wear developed rapidly with a 12.4% reduction of tool diameter (~ 60 $\mu$ m) after only 520mm cut length. This period was characterised by fracture/rounding of the cutting edges together with flaking of the coating. As cutting proceeded to the steady-state region, the rate of wear slowed dramatically with a very gradual reduction in end mill diameter (10 $\mu$ m over a distance of 2000mm machined). While chipping/abrasion of the tool was still prevalent, radiusing of the cutting edges probably improved its strength (compared to a sharp corner) and resistance to impact, thereby providing a relatively stable cutting configuration. When the cut length progressed beyond ~2500mm (125 slots) however, the failure stage was initiated as tool wear began to increase drastically similar to that observed in the initial phase. The intense level of damage suffered by the end mill eventually led to sudden failure/breakage of the tool after ~3100mm cut length.

Figure 4.19 shows an example of mean static forces,  $F_x$ ,  $F_y$  and  $F_z$  in Slot 1 and Slot 26 respectively. The  $F_x$  and  $F_y$  forces showed similar magnitudes in Slot 1 while  $F_z$  was generally lower. As cutting progressed, all force components increased substantially as a result of tool wear, with  $F_z$  showing the highest magnitude due to rubbing, while  $F_x$  was typically twice the level of  $F_y$ .

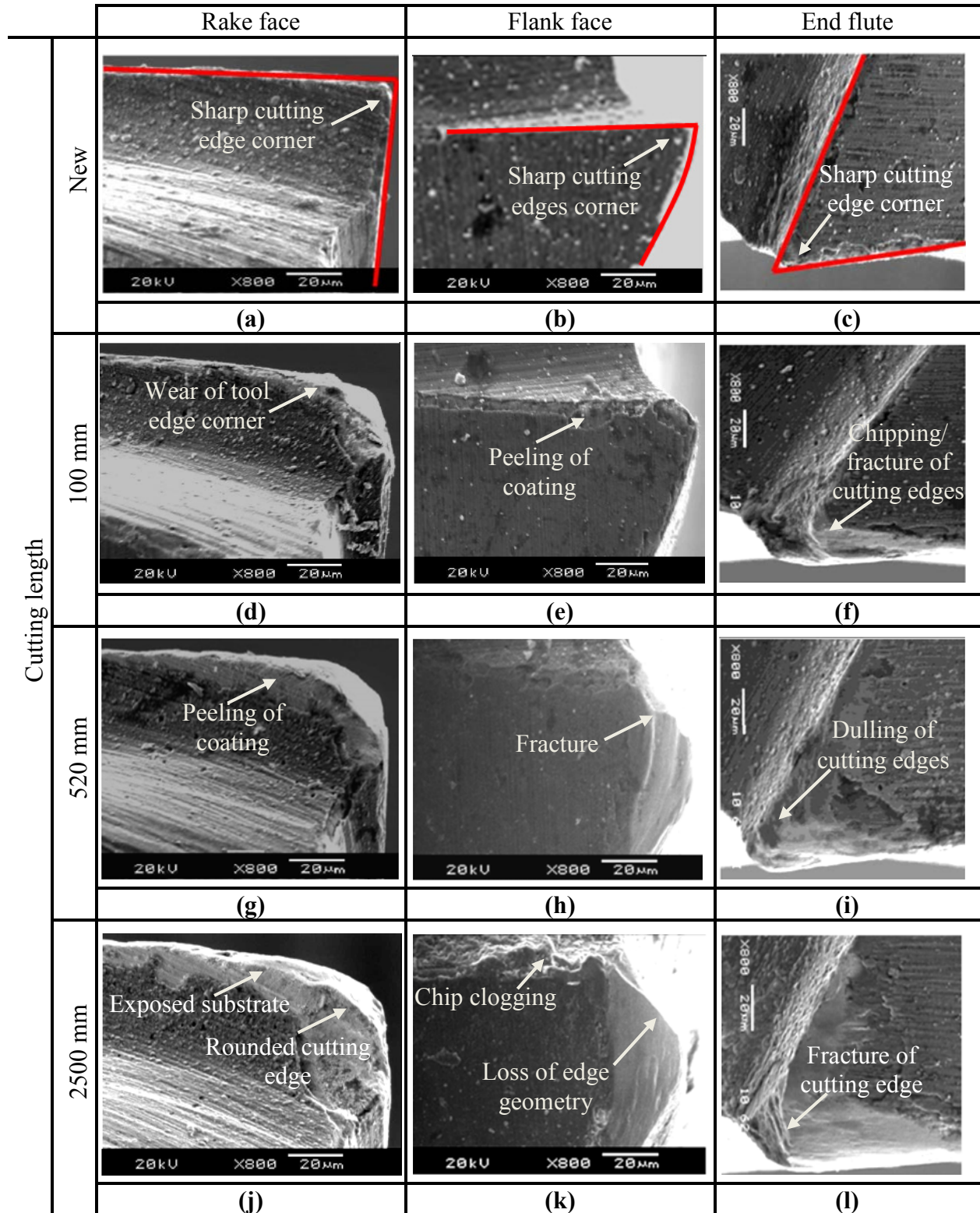


Figure 4.16: Microtool wear progression during micromilling

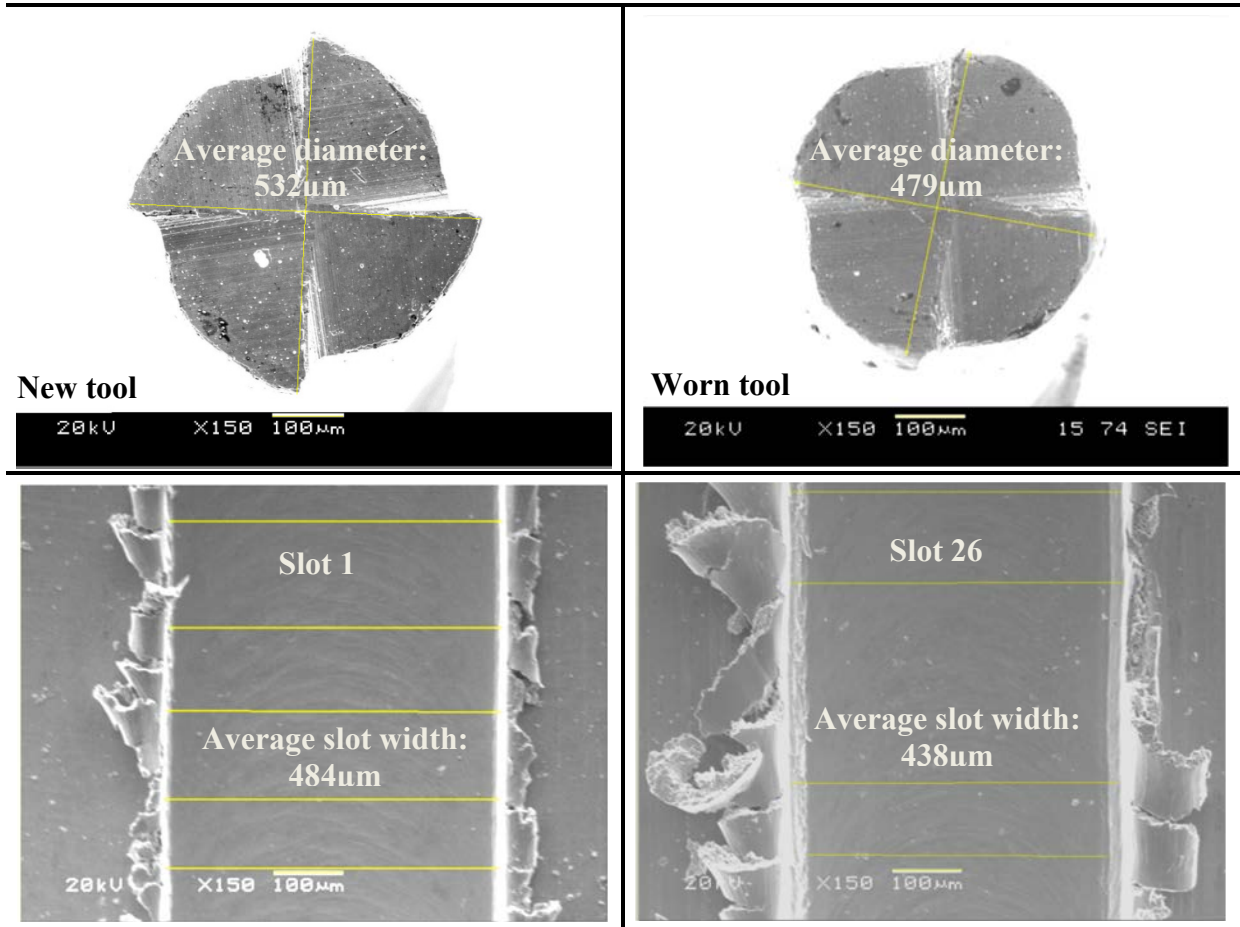


Figure 4.17: Correlation between tool diameter and slot width

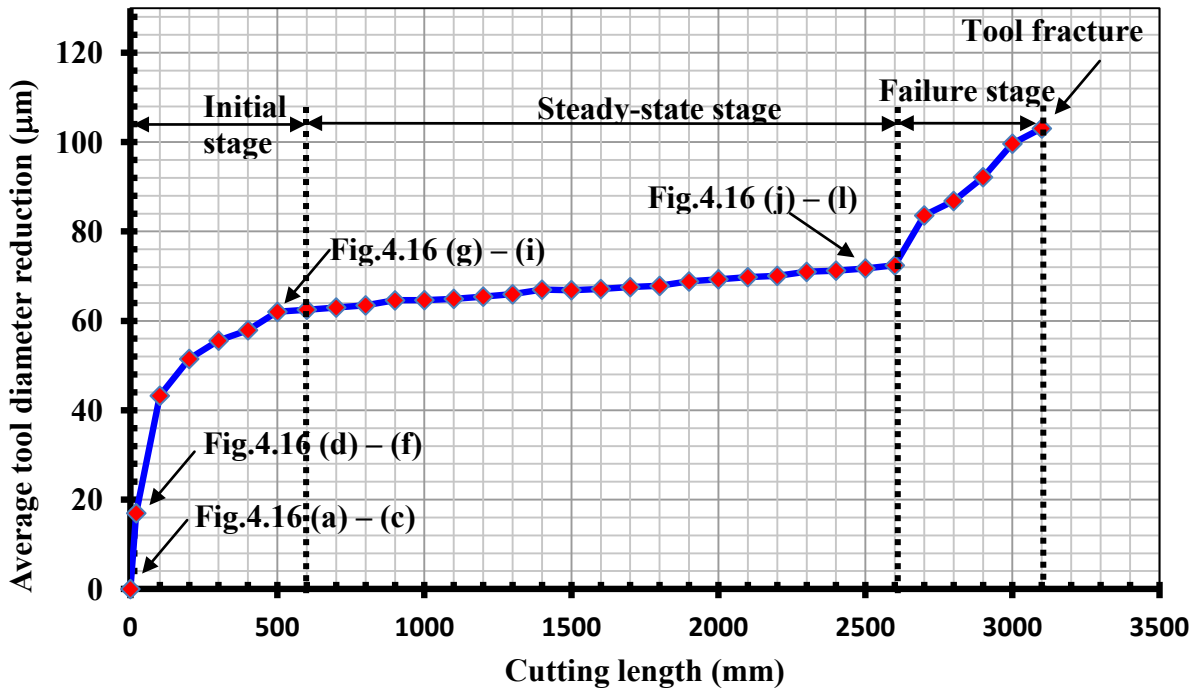


Figure 4.18: Microtool wear progression

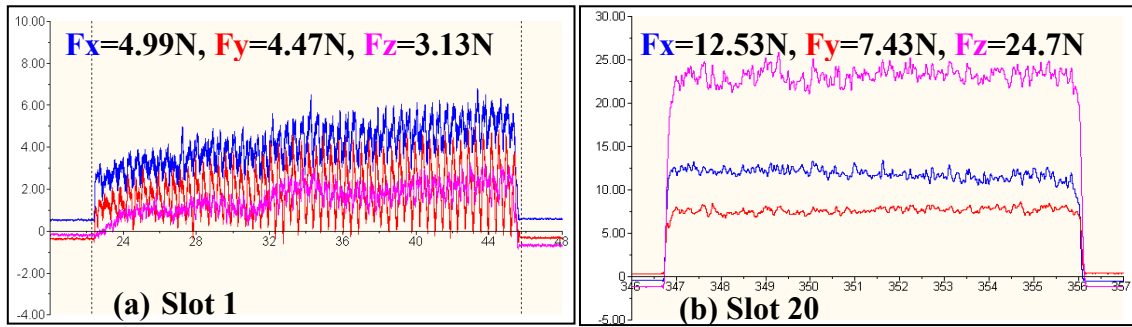


Figure 4.19: Cutting forces (a) new tool vs (b) worn tool

### 4.3.2 Workpiece surface roughness assessment

Workpiece roughness ( $R_a$ ) of the machined surface was measured along the centre line of the slots in the feed direction, see Figure 4.20(a). This represented the highest roughness value across the slot surface as it corresponds to the position of maximum undeformed chip thickness and the longest distance between feed marks per revolution of the tool. When using a new cutter, the surface roughness of the slot produced was  $\sim 0.2\mu\text{m}$   $R_a$ , with no obvious/major sign of flaws or defects, even up to a cut length of 520mm, see Figure 4.20(b). The surface topography of the slots however deteriorated/became irregular as tool wear increased with cut length. Workpiece smearing/adhered material and rounding of the slot corner was evident as shown in Figure 4.20(c) and Figure 4.20(d), while Figure 4.21 details 3D topography plots of surfaces generated with new and worn end mills. In addition to the fracture/abrasion of the end mills, material adhesion also contributed towards dulling of the cutting edges and subsequent transfer/re-deposition onto the slot surfaces, see Figure 4.22. The associated change in surface roughness with respect to cut length is illustrated in Figure 4.23. In general, only a marginal increase in  $R_a$  was detected following the first 520mm cut ( $\sim 0.2\mu\text{m}$ ), while surface roughness was almost 70% higher ( $0.33\mu\text{m}$   $R_a$ ) prior to tool failure.

The influence of the minimum chip thickness criterion on surface roughness and burr formation (details in Section 2.4.1) can be observed from Figure 4.20. Although not directly measured, visual inspection clearly showed that wear of the end mills and hence cutting edge radius, increased as machining progressed (see Figure 4.16). The corresponding decrease in the ratio of chip thickness to tool edge radius most likely led to greater ploughing (rather than shearing) and caused the decline in micro milling performance, particularly in relation to workpiece surface roughness (Figure 4.23), burr size (Figure 4.20), cutting forces (Figure 4.19) and overall process stability.

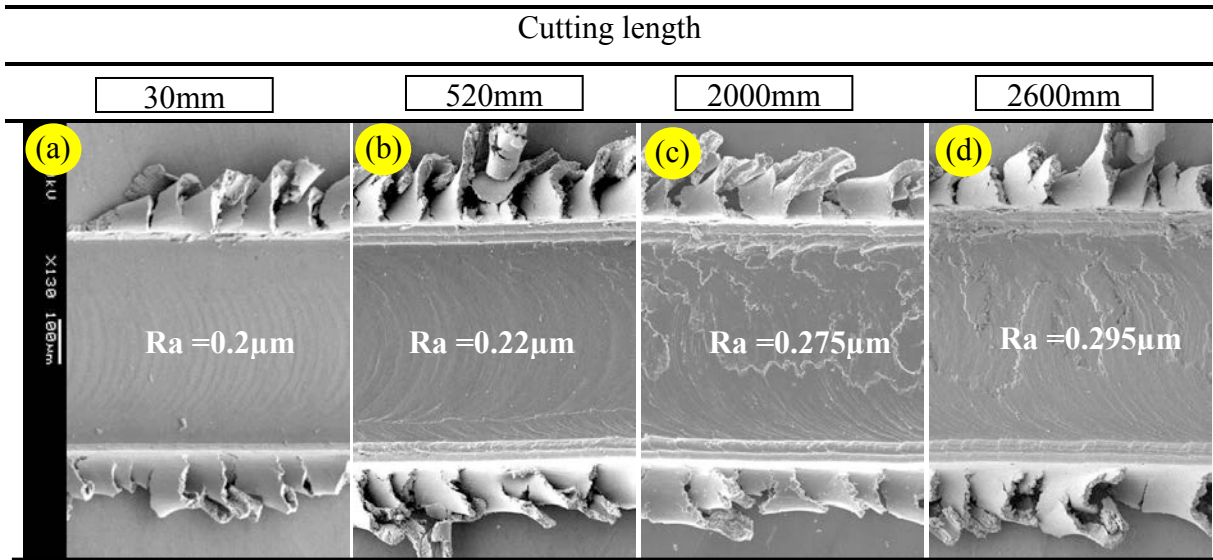


Figure 4.20: Slot surface roughness progression

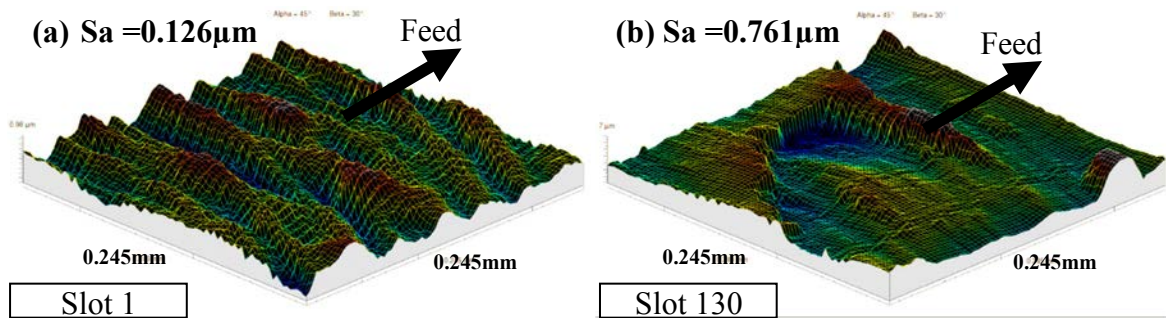


Figure 4.21: 3D topography plots of surface (a) new tool (b) worn tool

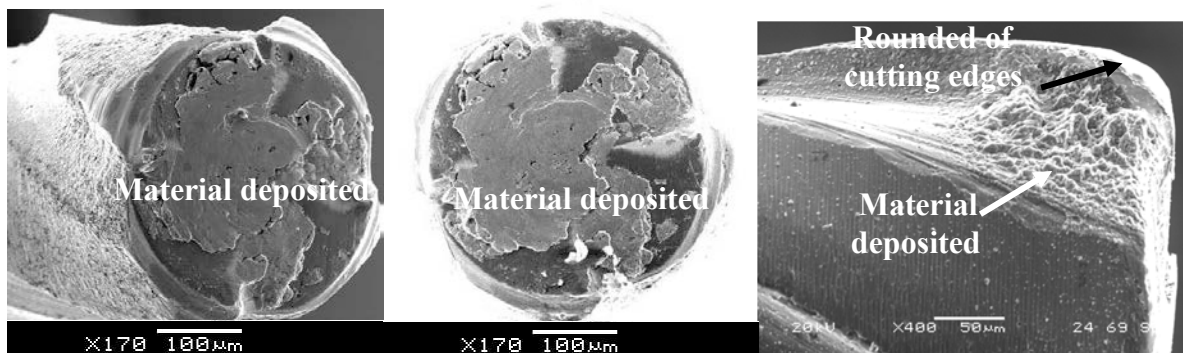


Figure 4.22: Worn tool with adhered material

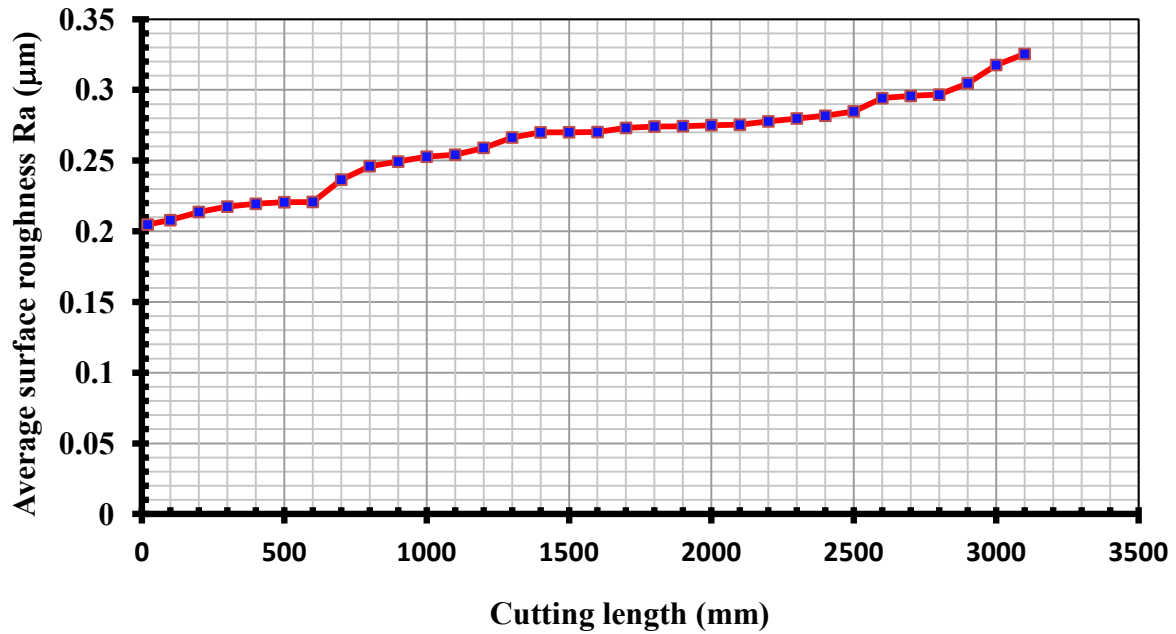


Figure 4.23: Cutting length versus surface roughness (Ra)

### 4.3.3 Determination of end of test criterion

Tests conducted at various operating parameter levels showed similar trends in terms of tool wear and surface roughness to that discussed in Sections 4.3.1 and 4.3.2, see Figure 4.24 for a summary/compilation of the data. Typically, all the trials (Trials 8, 9 & 10) conducted at the highest feed per tooth ( $3\mu\text{m}/\text{tooth}$ ) fractured before achieving a cut length of 500mm, which would suggest a limiting feed rate level when machining this workpiece material in the hardened state. The only exception was in Trial 11 where the tool achieved a cut length of  $\sim 2100\text{mm}$ , albeit at a comparatively lower cutting speed ( $10\text{m}/\text{min}$ ) and depth of cut ( $5\mu\text{m}$ ). For Trials 1 to 6, tool wear progression appeared to follow a similar trend to that observed previously in Figure 4.18 (discussed in Section 4.3.1) but with failure stage initiation only occurring after about 3000mm cut length involving rapid progression of wear and eventual fracture of the tool. Based on results in the preliminary tests, a cut length of 520mm was defined as the end of test criterion (prior to initiation of steady –state region) for subsequent mainstream experiments. However for tool life evaluation, a  $30\mu\text{m}$  tool diameter reduction was specified in order to accommodate limitations relating to the response range (RSM analysis) in the statistical calculations.

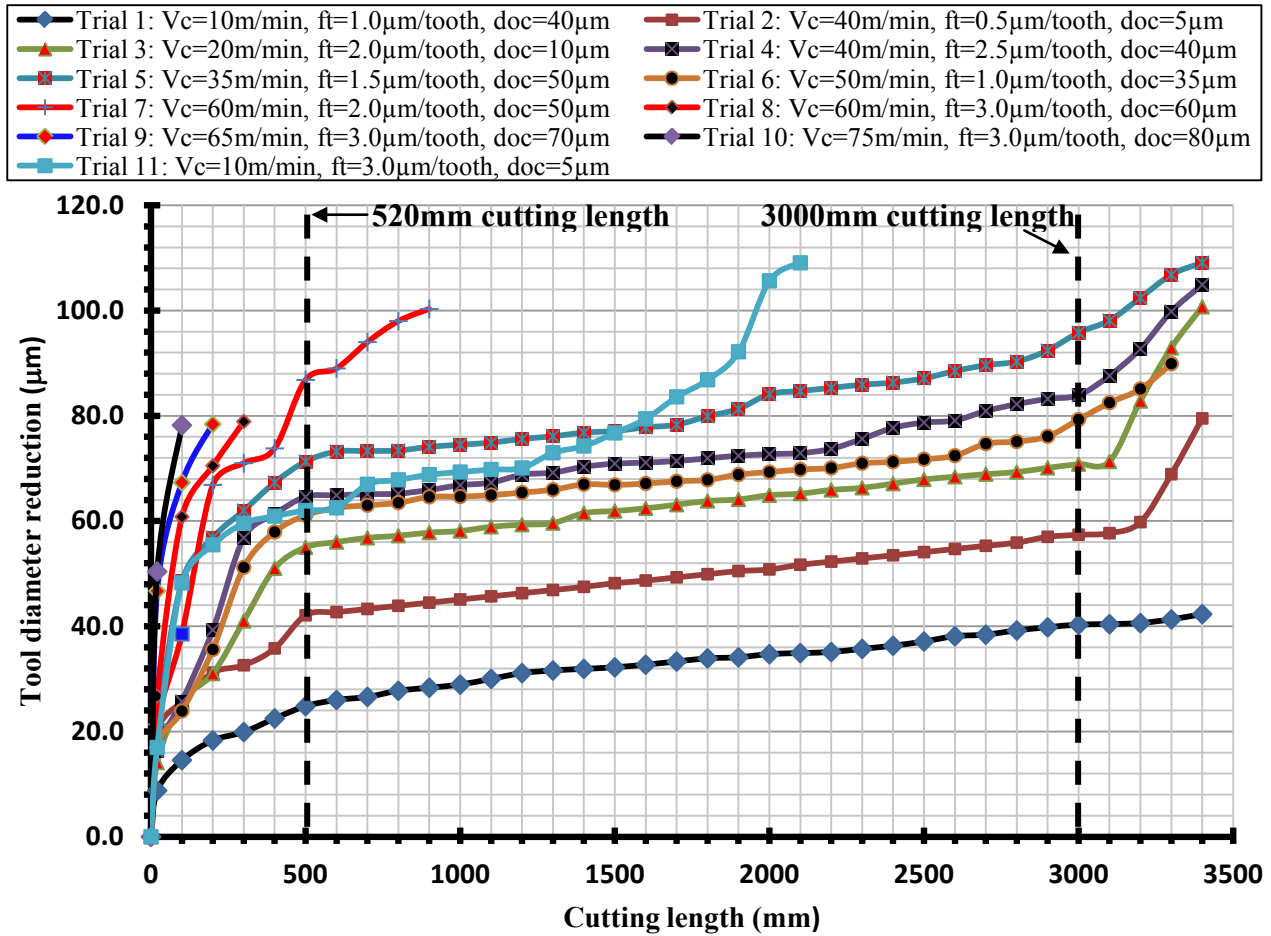


Figure 4.24: Compilation of trials for various operating parameters

### 4.3.4 Microtool wear/failure modes

#### 4.3.4.1 Coating delamination

Tool coatings are generally applied to enhance wear resistance (predominantly solution wear), improve lubrication/reduce friction and act as a thermal barrier [201]. Areas of the micro end mill which appear to have suffered from chipping and delamination of the coating layer following the initial machining pass were further analysed using high magnification SEM. Figure 4.25(a) & 4.25(b) shows the surface of the tool close to the cutting edge radius on the flank and rake faces respectively. A rough and wavy surface was observed with some carbide grains visible, suggesting the coating detached initially from the sub-surface layer beneath the coating/substrate interface. Energy dispersive X-ray spectroscopy (EDX) analysis was subsequently carried out on the region indicated in Figure 4.25(b). Results from EDX maps of the rake face showed large amounts of tungsten around the cutting edge periphery

and nose area, thereby confirming the absence of the coating and exposure of the tool substrate at this location, see Figure 4.25(c). Similar observations were found from EDX scans on the flank face, see Figure 4.26. No major deposition of workpiece material on the tool surfaces however was detected at this stage of cutting.

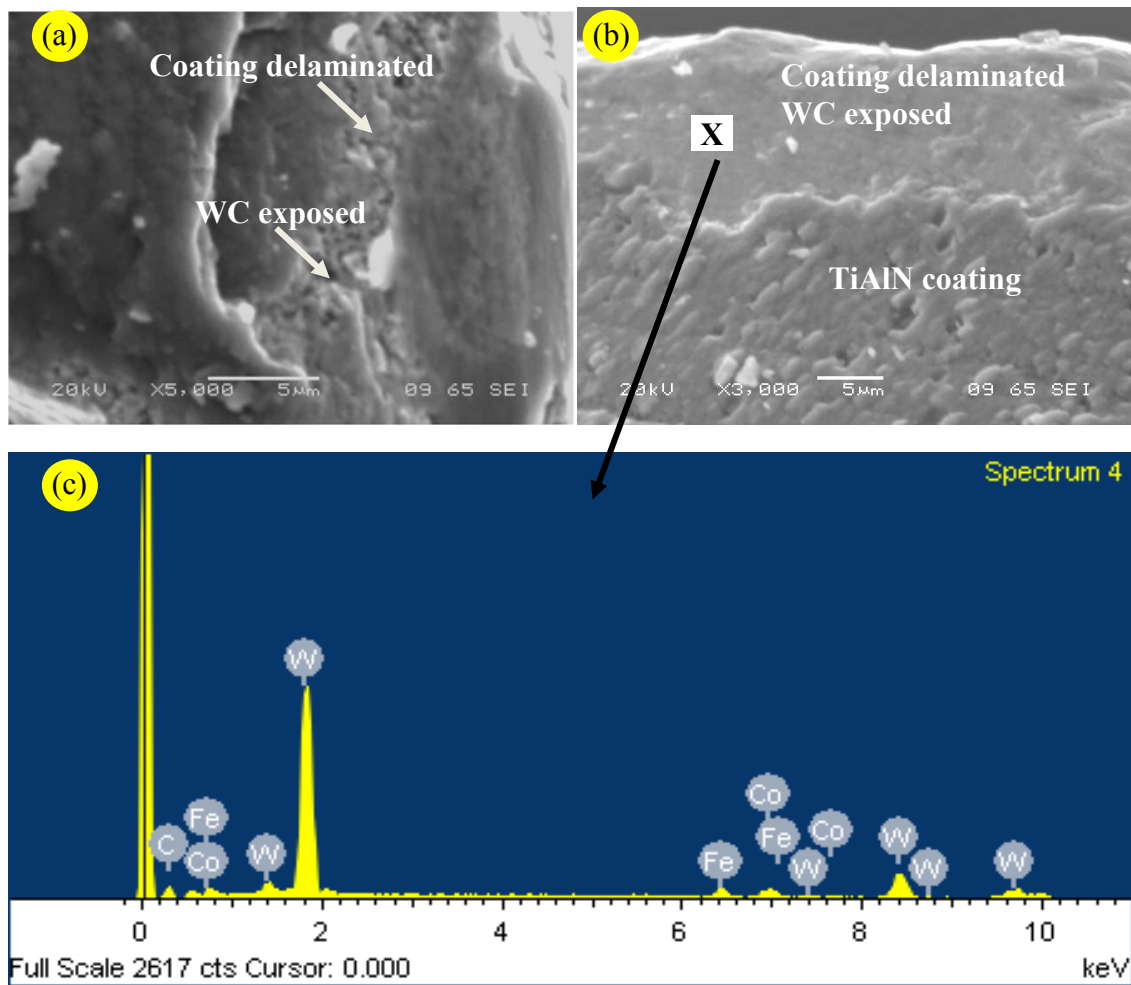


Figure 4.25: Delamination of the coating from (a) flank face (b) rake face (c) EDX analysis on site X

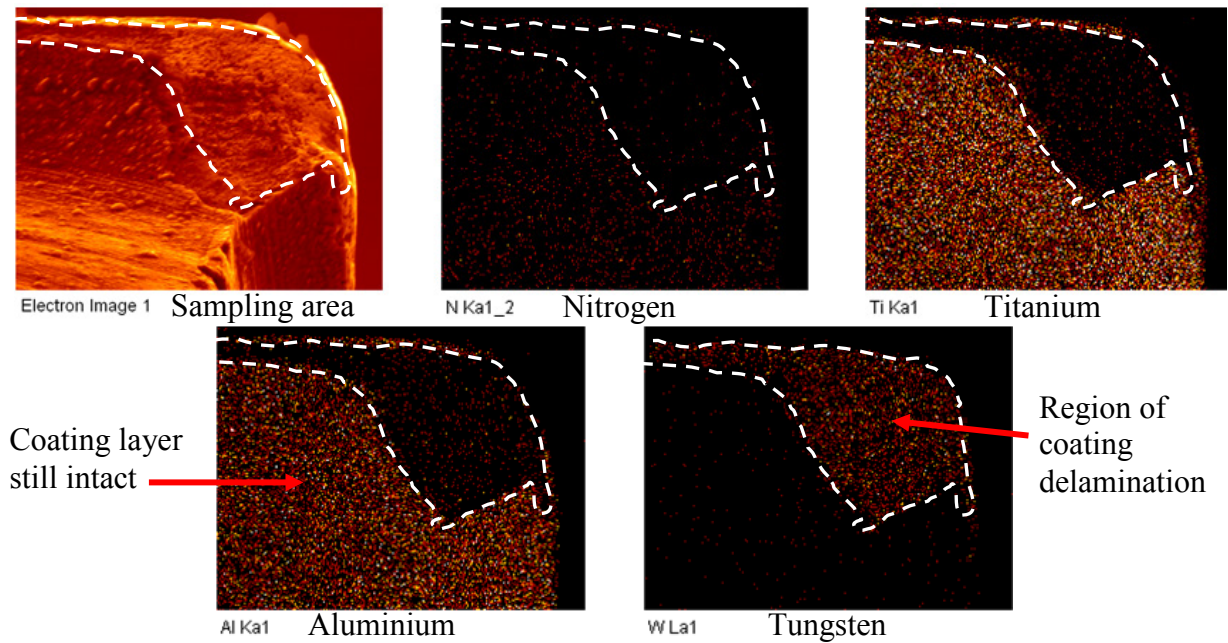


Figure 4.26: EDX area mapping of flank face.

#### 4.3.4.2 Fracture of cutting edge

Following delamination/peeling of the coating layer, the cyclic impact due to the micromilling operation initiated small cracks on the tool surface. As cutting proceeded, the microscale chipping on the exposed substrate along the cutting edge changed to fracture of the tool tip as shown in Figure 4.27, which reduced the effective diameter of the end mill. This generally occurs at a very early stage of the machining process, which was reported by Li et al. [150]. Apart from the influence of cutting forces, the formation of built-up edges (BUE) can also lead to fracture of the tool cutting edge during removal/brake off of the BUE. In addition, tools with a positive rake angle and sharper corner radii are more prone to edge failures compared to cutters with relatively large angles between the tool flank and rake face.

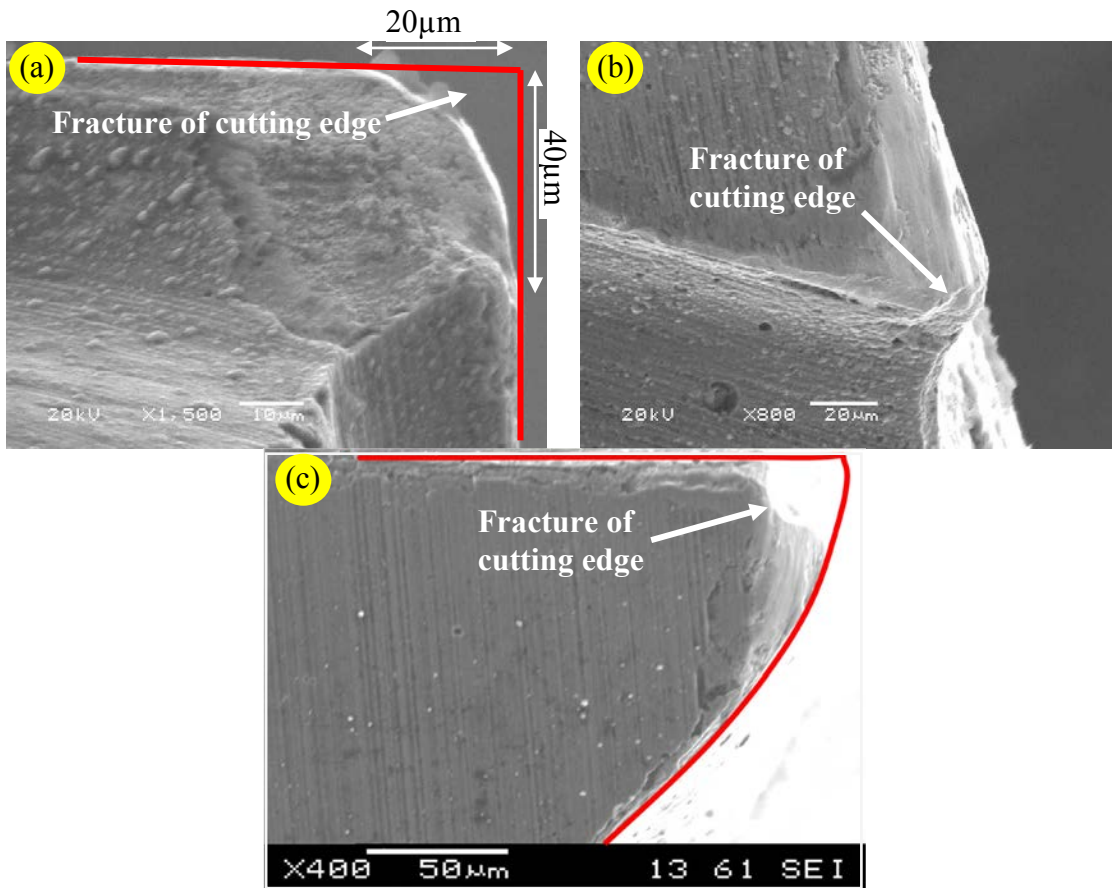


Figure 4.27: Fracture of cutting edge viewed from; (a) rake face (b) end flute (c) flank face

#### 4.3.4.3 Abrasive wear

Wear on the rake, flank and end flute surfaces typically characterised by grooving marks are shown in Figure 4.28(a), (b) and (c) respectively, and are indicative of an abrasive mechanism. This generally led to rounding of the tool following initial fracture of the sharp cutting edges. The increased cutting edge radius as shown in Figure 4.28(a) contributed to a change in the tool geometry, with rubbing more dominant during machining rather than shearing. Abrasion was also seen as the principal wear mode causing the gradual reduction in cutter diameter during the steady-state stage of tool wear progression.

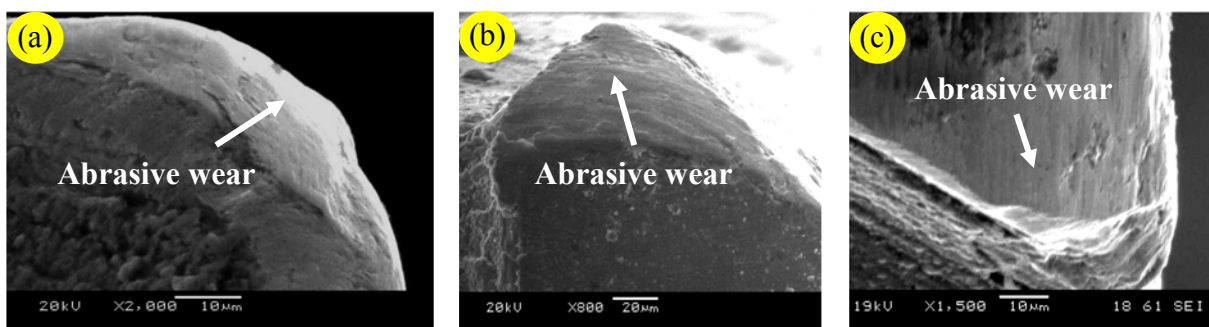


Figure 4.28: Abrasive wear (a) rake face (b) flank face and (c) end flute

#### 4.3.4.4 Workpiece material deposition

In addition to BUE on tool cutting edges, adhered workpiece material was also commonly observed on the tool flank and rake face as shown in Figure 4.29, particularly after the steady-state stage. In addition to reducing tool sharpness and limiting cutting/shearing efficiency, adhered material is also usually re-deposited/transferred back onto the machined slot during subsequent passes, as illustrated by the smeared surface detailed in Figure 4.30. An EDX spot analysis and associated element mapping of the machined surface showed no traces of coating or tool material, see Figure 4.31, which suggests the smeared material was not due to BUE from the cutter. Similar results were seen with EDX scans of the chips produced, see Figure 4.32.

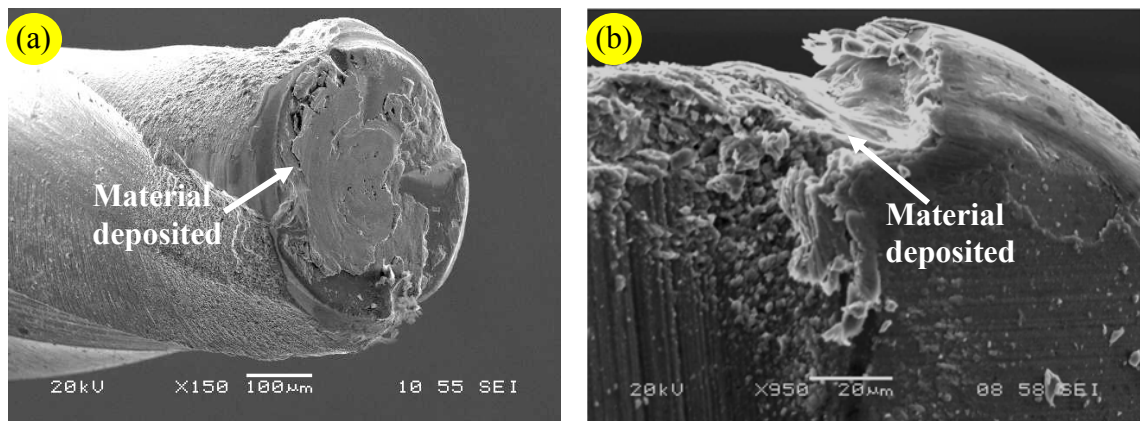


Figure 4.29: Adhered material on tool; (a) rake face (b) flank face,  
( $V_c=20\text{m/min}$ ,  $f_t=2\mu\text{m/tooth}$ ,  $d=55\mu\text{m}$ )

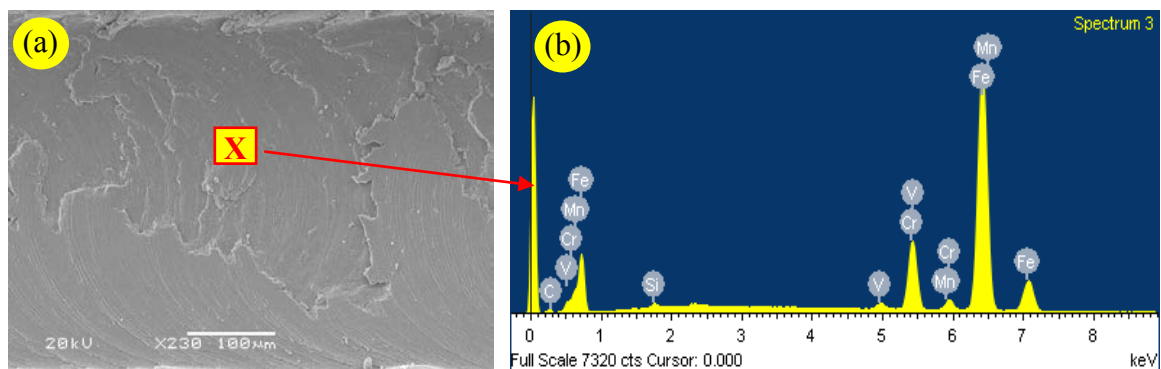


Figure 4.30: EDX of machined surface

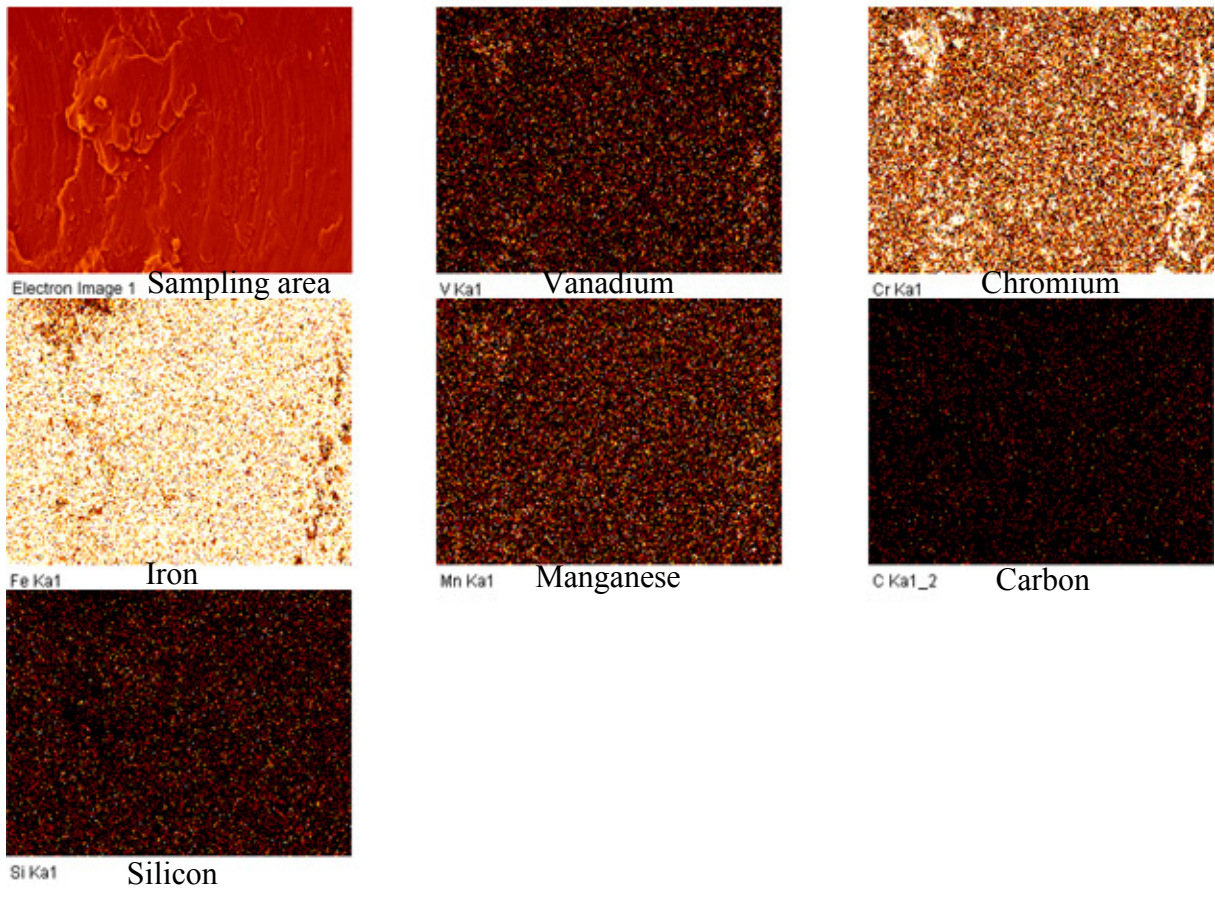


Figure 4.31: EDX area mapping of slot machined surface

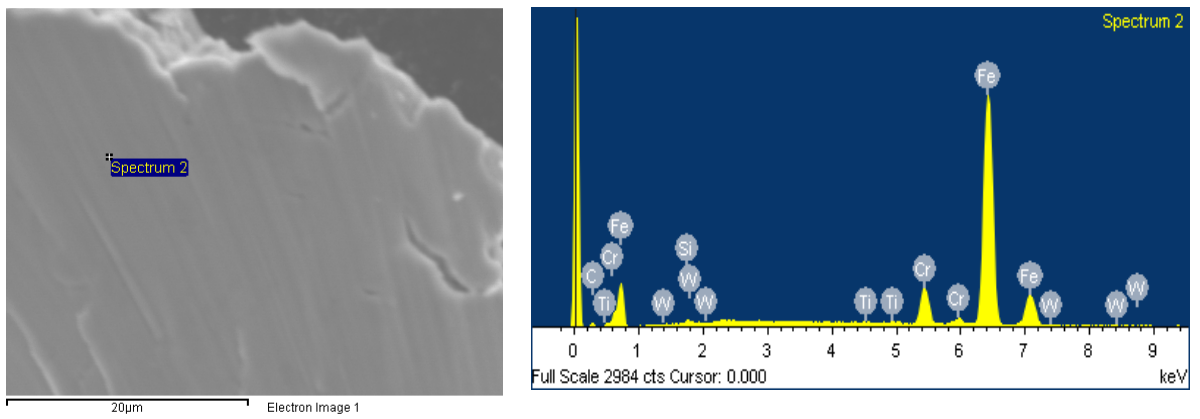


Figure 4.32: EDX spot analysis of microchip surface

#### 4.3.4.5 Tool breakage

Figure 4.33 shows breakage of the cutting tool which can occur upon initial contact with the workpiece due to inappropriate selection of cutting parameters (excessively high depth of cut, feed per tooth etc.). Such failure also occurs when the tool is no longer able to withstand the applied load due to dulling of the cutting edges from chipping/fracture or clogging as a result of adhered workpiece material/chips [14].

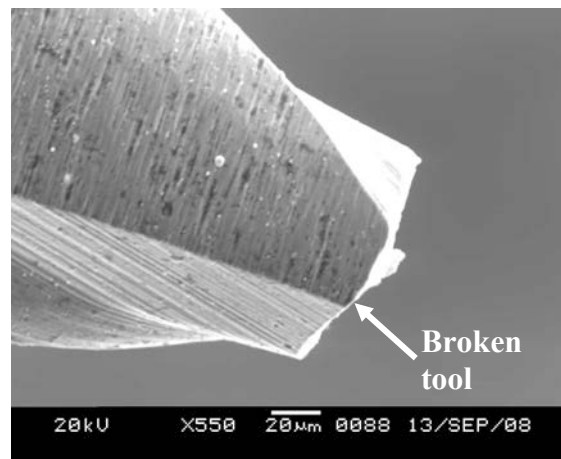


Figure 4.33: Broken microtool

### 4.4 Phase 3B: Influence of operating parameters

The effect of varying cutting speeds, feed per tooth/feed rates and depth of cut when micromilling hardened AISI D2 steel was investigated. Response measures evaluated include tool life, surface roughness, burr formation and cutting forces together with slot quality, cutting temperature and surface integrity (microstructure, microhardness and residual stress). Statistical analysis including main effects plots and ANOVA were employed to identify key process variables and preferred operating conditions for micromilling.

#### 4.4.1 Tool life

The reduction in tool diameter against cutting time for each test is shown in Figure 4.34, with a tool life criteria corresponding to a 30µm tool diameter reduction. In general, tool life ranged between 0.5 to 4.7 minutes, with the latter figure obtained when operating at the lowest parameter levels (Test 1) and vice versa for the former (Test 8).

Table 4.1 details the ANOVA results with respect to tool life. All 3 variable factors were found to be statistically significant with cutting speed having an overwhelming influence on

tool life with a percentage contribution ratio (PCR) of 53%. This was followed by feed per tooth and depth of cut at reduced PCR's of 19% and 15% respectively. Two level interactions between cutting speed x feed per tooth and cutting speed x depth of cut were also found to have a significant effect, albeit with correspondingly low contributions of 9% and 4% respectively, see Appendix C for interaction plot.

The associated main effects plot for mean tool life shown in Figure 4.35 confirmed that the longest tool life was achieved when using a cutting speed of 20m/min, feed rate of 1 $\mu$ m/tooth and 15 $\mu$ m depth of cut. Similar results were reported by several other researchers [17, 139, 202] who concluded that cutting velocity generally had a large influence on tool wear.

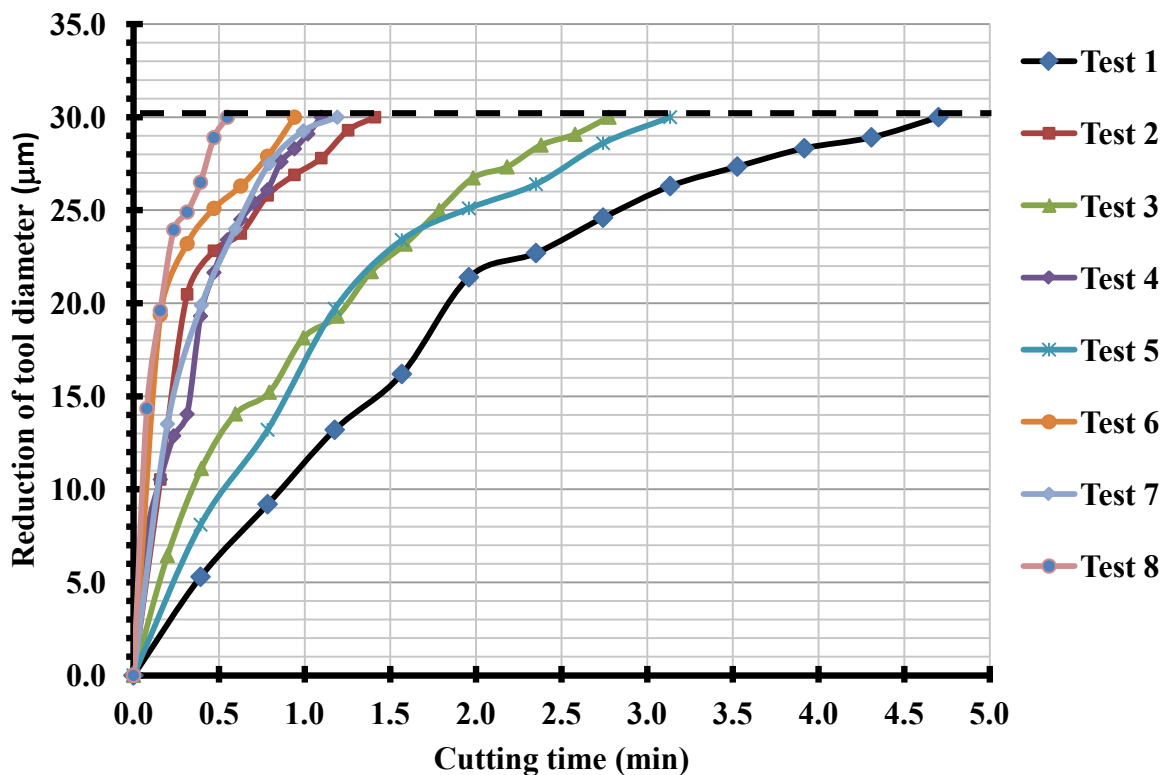


Figure 4.34: The cutting time versus reduction of tool diameter

\*Refer to Table 3.6 for test parameters

Table 4.1: ANOVA results for tool life

Source	Sum of Squares	DF	Mean Square	F Value	Prob > F	% PCR
Cutting speed (A)	7.585512	1	7.585512	12384.51	0.0057*	53%
Feed per tooth (B)	2.656513	1	2.656513	4337.163	0.0097*	19%
Depth of cut (C)	2.173612	1	2.173612	3548.755	0.0107*	15%
AB	1.256113	1	1.256113	2050.796	0.0141*	9%
AC	0.567112	1	0.567112	925.898	0.0209*	4%
BC	0.001013	1	0.001013	1.653061	0.4208	0%
Residual	0.000612	1	0.000612			
Total	14.24049	7				

\*Significant at 5% level

Std. Dev.	0.024749	R-Squared	0.999957
Mean	1.97875	Adjusted R-Squared	0.999699

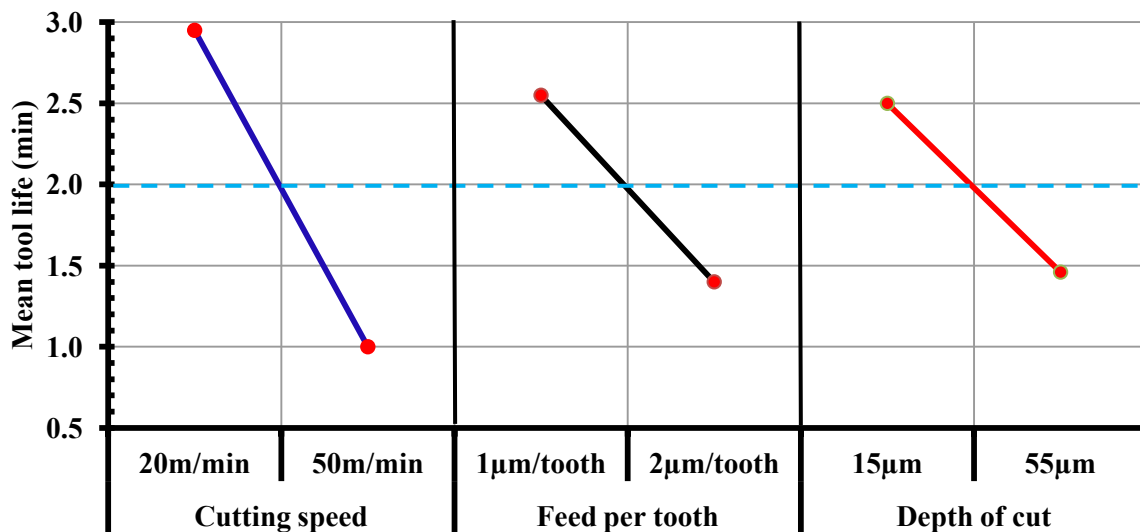


Figure 4.35: Main effects plot, means for tool life

#### 4.4.2 Surface roughness

The mean surface roughness response for each trial at Slot 26 (end of test criteria as detailed in Section 4.3.3) is shown in Figure 4.36. In general, surface roughness ranged between 0.15 to 0.31µm Ra. Test 2 (cutting speed 50m/min, feed per tooth 1µm/flute and depth of cut 15µm) exhibited the lowest surface roughness value (Ra=0.15µm) among all the tests while the highest value (Ra=0.31µm) was obtained in Test 7 (cutting speed 20m/min, feed per tooth 2µm/flute and depth of cut 55µm). Despite utilising higher cutting parameters (cutting speed 50m/min, feed per tooth 2µm/flute and depth of cut 55µm) in Test 8 (resulting in greater tool wear rate and short tool life), the surface roughness (Ra=0.23µm) was lower compared to Test 7, which suggests that tool wear was not the only factor determining slot surface

roughness. A possible explanation for this observation was the formation of BUE/adhered material being more prevalent at low cutting speeds, which influenced the effective tool geometry and reduced sharpness, see Figure 4.37 and Figure 4.38. While the use of cutting fluid/lubrication would have reduced the incidence of BUE formation, this could also have resulted in thermal shock or possibly cutter vibration/chatter and hence lower tool life.

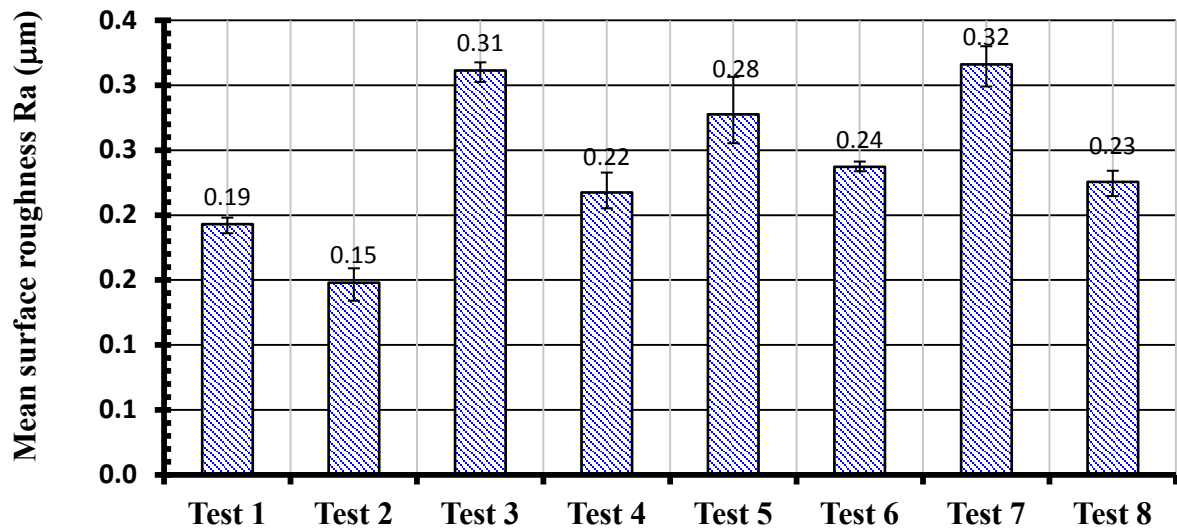


Figure 4.36: Mean surface roughness

\*Refer to Table 3.6 for test parameters

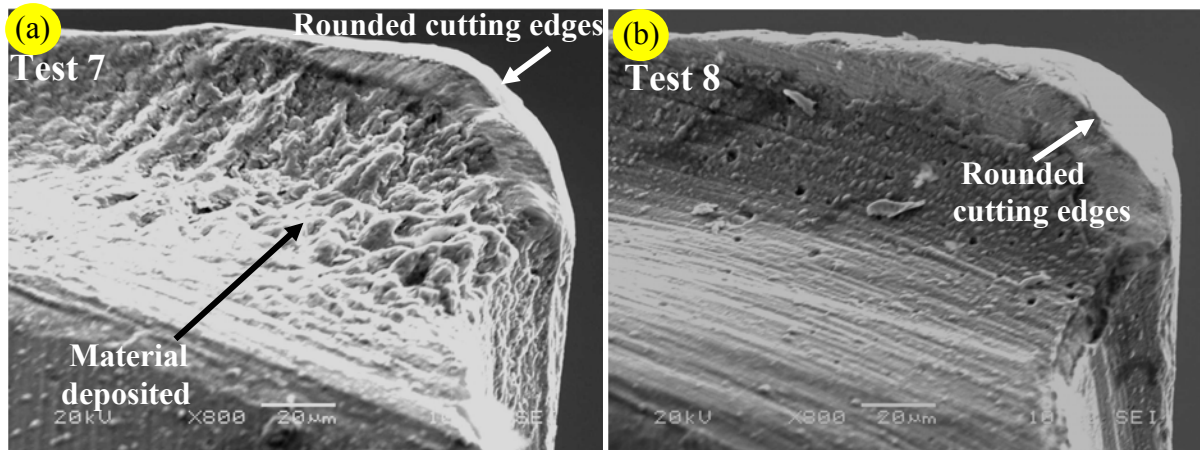


Figure 4.37: Tool wear for Test 7 vs Test 8

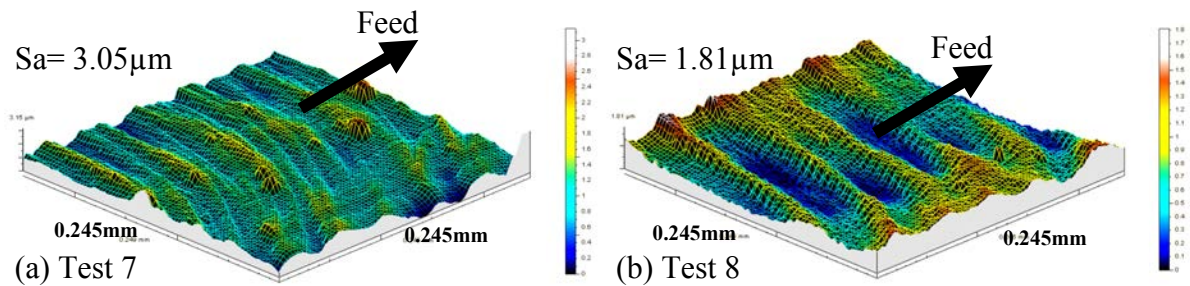


Figure 4.38: 3D topography plot of surface in (a) Test 7 vs (b) Test 8

As with tool life, all 3 parameters were found to have a statistically significant influence on workpiece surface roughness highlighted in the ANOVA in Table 4.2. Cutting speed had the greatest effect on surface roughness with a PCR of 38% followed by feed per tooth (24%) and depth of cut (18%). In terms of factor interactions, only feed per tooth x depth of cut was significant at the 5% level with a contribution of 14%, although cutting speed x feed per tooth demonstrated a PCR of 5%, see Appendix C for interaction plot. Figure 4.39 shows the main effects plot for mean surface roughness, which suggests that minimum roughness would be obtained by employing high cutting speed (50m/min) and both low feed rate (1 $\mu$ m/tooth) and depth of cut (15 $\mu$ m) conditions. These findings agreed with previous work reported on the micromilling of copper and H13 tool steel [11, 17] where surface roughness typically increased with feed rate.

Table 4.2: ANOVA results for surface roughness

Source	Sum of Squares	DF	Mean Square	F Value	Prob > F	% PCR
Cutting speed (A)	0.008965	1	0.008965	71716.84	0.0024*	38%
Feed per tooth (B)	0.00565	1	0.00565	45198.76	0.0030*	24%
Depth of cut (C)	0.00426	1	0.00426	34077.16	0.0034*	18%
AB	0.001171	1	0.001171	9370.24	0.0066	5%
AC	1.25E-05	1	1.25E-05	100	0.0635	0%
BC	0.003313	1	0.003313	26503.84	0.0039*	14%
Residual	1.25E-07	1	1.25E-07			
Total	0.023371	7				
<b>*Significant at 5% level</b>						
Std. Dev.	0.000354		R-Squared	0.999995		
Mean	0.2405		Adjusted R-Squared	0.999963		

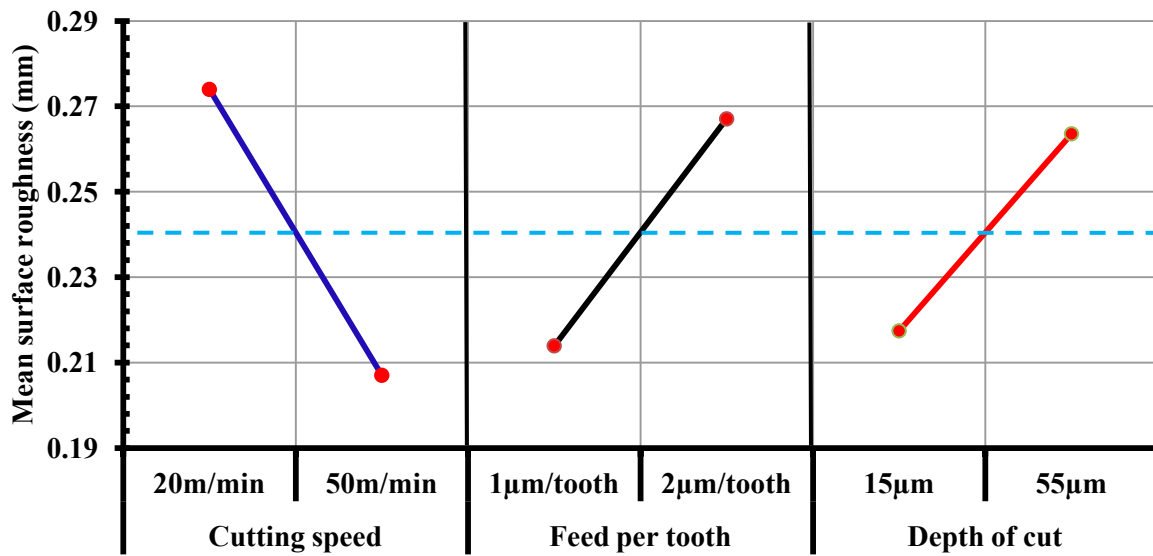


Figure 4.39: Main effects plot, means for surface roughness

A confirmation test was performed using the above conditions ( $V_c=50\text{m/min}$ ,  $ft=1.0\mu\text{m/tooth}$  and  $d=15\mu\text{m}$ ) in order to validate results from the statistical analysis  $L_8$ . The confidence interval (95%) for surface roughness results of the confirmation test was calculated using the following equation;

$$\text{Confidence interval} = \sqrt{F_{\alpha}(1, \nu_e) V_e [(1/n_{eff}) + (1/r)]}$$

$F_{\alpha}$  = tabulated F value for a 95% confidence interval

$\nu_e$  = degrees of freedom associated with the error/residual

$V_e$  = mean sum of square associated with the error/residual

$r$  = sample size for the confirmation experiment

$$n_{eff} = \frac{\text{Total number of observations}}{1 + [\text{total degrees of freedom associated with items used in estimating mean}]}$$

$$F_{\alpha} = 161.4, V_e = 1.25 \times 10^{-7} \text{ and } r = 1$$

$$n_{eff} = \frac{8}{1+3} = 2$$

The predicted value from optimum surface roughness (A2,B1,C1) is 0.1573 (Ra)

$$\text{Confidence interval} = \sqrt{161.4 \times 1.25 \times 10^{-7} [(1/2) + (1/1)]}$$

$$\text{Confidence interval} = \pm 0.0055$$

Confidence limits are  $0.1573 \pm 0.0055$ ; between 0.1518 to 0.1629 (Ra)

Following the confirmation test, the surface roughness obtained was  $Ra = 0.1591\mu\text{m}$ , which was within the confidence interval calculated, indicating that the experiment was statistically acceptable.

### 4.4.3 Burr formation

Burr formation at the top of the slot was investigated, which is considered to be the most difficult to remove. Average burr width was selected as the measurement criteria [11] and varied from 23 to 228 $\mu\text{m}$  depending on the cutting parameters used. Ploughing generally occurs when the ratio of feed per tooth to cutting edge radius is less than one, leading to elastic recovery of the material instead of shearing. Indeed, Lee and Dornfeld [165] observed that tool rake angle at the cutting edge is effectively negative in such cases, with the condition being further exacerbated as tool wear increases. In the current work, the ratio ranged from 0.14 to 0.4. All tests showed some degree of burr formation with rubbing and compression of the material instead of cutting. Furthermore, the trials were performed under full immersion slot milling where one side of the slot experienced up-milling and the other side down-milling. The reasons for the difference between down-milling and up-milling burr width can be due to the amount of material that is pushed in front of the cutting edge in the direction of the cutting force component ( $F_x$ ). Typically, the direction of material deformation follows the effective direction of the largest force component (in this case  $F_x$ ), which is away from the up-milling side and towards the down milling side [168]. In terms of the effect of milling direction, down-milling burrs were larger and wavy while up-milling burrs were smaller and ragged, see Figure 4.40. Similar features have been reported by other researchers [11, 165, 170].

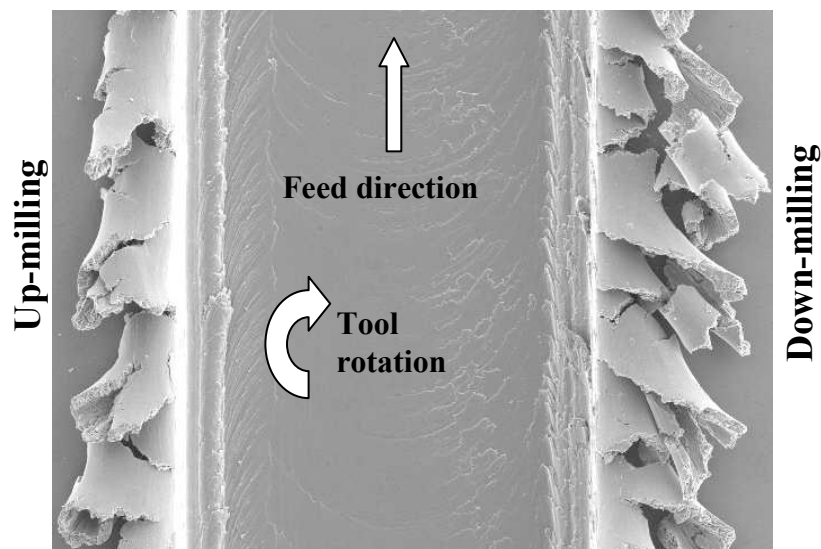


Figure 4.40: Effect of milling direction on burr formation

Figure 4.41 shows the width of burrs generated under different operating conditions after 520mm cut length. The mean burr width for each test at Slot 26 (down-milling side) is shown in Figure 4.42, which ranged between 92 $\mu$ m to 228 $\mu$ m, depending on the cutting parameters used. Even when machining the first slot with a new tool, burrs were observed on the top of the side walls, albeit the average widths being less than 30 $\mu$ m.

The main effects plot and corresponding ANOVA for mean burr width is shown in Figure 4.43 and Table 4.3 respectively. The former suggests that burr size is smaller when utilising low feed rate and depth of cut, which increased (burr size) at higher parameters levels, due to greater levels of tool wear under these conditions. Conversely, burr widths tended to be larger when cutting speed was decreased with associated ANOVA calculations indicating this parameter to be a statistically significant factor with respect to burr size (46% PCR). A possible explanation for this phenomenon is the greater likelihood of built up edge (BUE)/adhered material (see Figure 4.37(a)) being more prevalent at low cutting speeds (low temperature pressure welding), which influenced the tool geometry and reduced tool sharpness. While feed rate and depth of cut were also significant in affecting burr size at PCR's of 24% and 26% respectively, none of the 2 level interactions were found to influence burr formation, see Appendix C for interaction plot. Furthermore, there appeared to be a correlation between burr width and cutting forces (detailed later in Section 4.4.4), where larger burrs resulted in higher forces (Test 7) and vice versa (Test 2).

DOC = 15 $\mu$ m

		$f = 1\mu\text{m/tooth}$	$f = 2\mu\text{m/tooth}$
$V_c = 20\text{m/min}$	<p><b>Test 1</b> Feed direction</p> <p><b>Test 3</b> Up-milling Down-milling</p>		
		Avg burr width: UM: 135 $\mu$ m DM: 162 $\mu$ m	Avg burr width: UM: 161 $\mu$ m DM: 189 $\mu$ m
$V_c = 50\text{m/min}$	<p><b>Test 2</b> Tool rotation</p> <p><b>Test 4</b></p>		
		Avg burr width: UM: 64.7 $\mu$ m DM: 92 $\mu$ m	Avg burr width: UM: 119 $\mu$ m DM: 147 $\mu$ m

DOC = 55 $\mu$ m

		$f = 1\mu\text{m/tooth}$	$f = 2\mu\text{m/tooth}$
$V_c = 20\text{m/min}$	<p><b>Test 5</b></p> <p><b>Test 7</b></p>		
		Avg burr width: UM: 178 $\mu$ m DM: 206 $\mu$ m	Avg burr width: UM: 201 $\mu$ m DM: 228 $\mu$ m
$V_c = 50\text{m/min}$	<p><b>Test 6</b></p> <p><b>Test 8</b></p>		
		Avg burr width: UM: 105 $\mu$ m DM: 134 $\mu$ m	Avg burr width: UM: 164 $\mu$ m DM: 191 $\mu$ m

UM = Up-milling , DM = Down-milling

\*Orientation of slots with respect to tool rotation and feed direction was constant for all tests

\*\*Burr width was measured at 3points: start, middle and end of slot

Figure 4.41: Burr widths after 520mm cut length

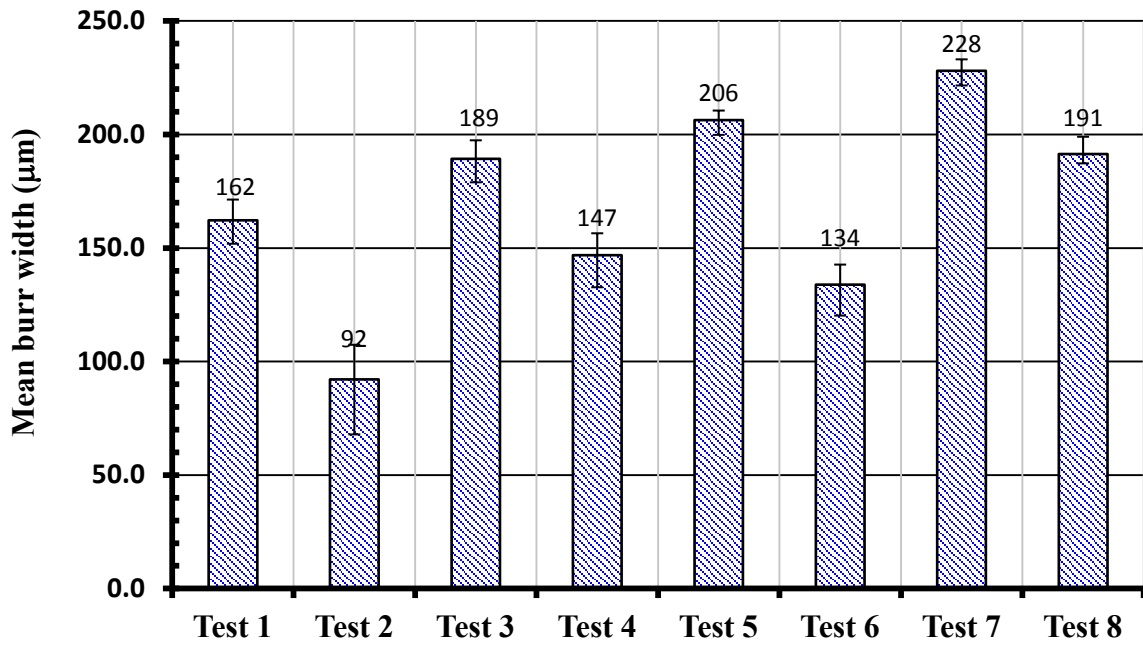


Figure 4.42: Mean burr width

\*Refer to Table 3.6 for test parameters

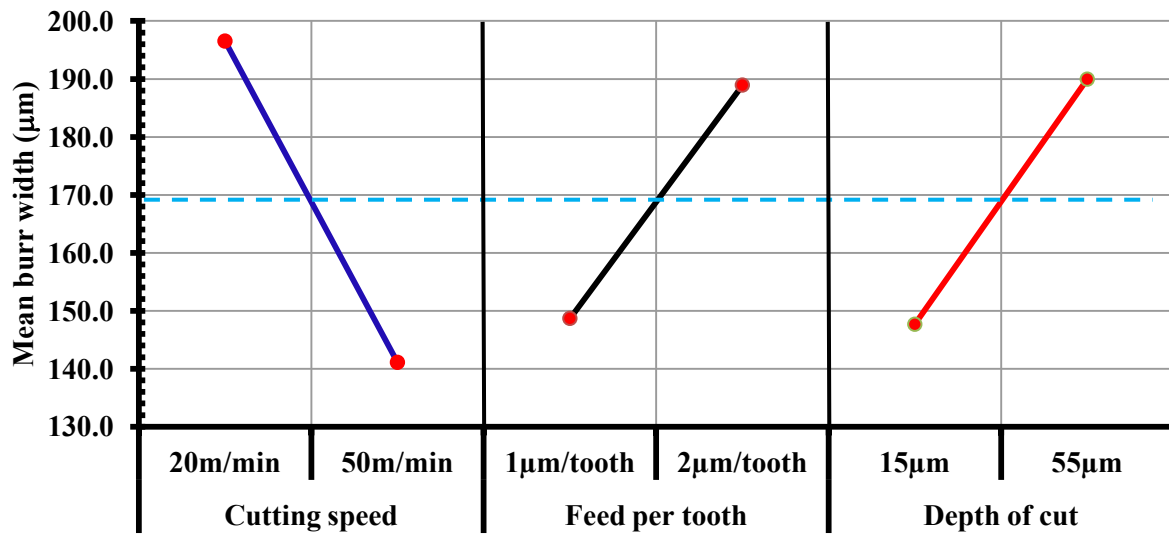


Figure 4.43: Main effects plot, means for burr width

Table 4.3: ANOVA results for burr width

Source	Sum of Squares	DF	Mean Square	F Value	Prob > F	% PCR
Cutting speed (A)	6145.524	1	6145.524	705.141	0.0240*	46%
Feed per tooth (B)	3241.333	1	3241.333	371.912	0.0330*	24%
Depth of cut (C)	3576.465	1	3576.465	410.366	0.0314*	26%
AB	503.555	1	503.555	57.778	0.0833	4%
AC	1.471	1	1.471	0.169	0.7519	0%
BC	0.726	1	0.726	0.083	0.8211	0%
Residual	8.715	1	8.715			
Total	13477.789	7				
<b>*Significant at 5% level</b>						
Std. Dev.	2.9522		R-Squared	0.9994		
Mean	168.8088		Adjusted R-Squared	0.9955		

#### 4.4.4 Cutting force

The mean static forces,  $F_x$ ,  $F_y$  and  $F_z$  over the full factorial test range following Slot 1 (new tool) are detailed in Figure 4.44. None of the force components exceeded 4.5N at this point, with levels as low as 0.4N recorded. In Tests 5 to 8, the  $F_x$  and  $F_y$  forces showed similar magnitudes while  $F_z$  was generally lower. At small depths of cut (Tests 1 – 4) the  $F_z$  component tended to be comparable or larger than the feed ( $F_x$ ) and normal forces ( $F_y$ ). This can be attributed to the fact that in hard machining, a pronounced increase in the thrust force component is generally observed particularly when cutting at low feed rates and depth of cut, as ploughing rather than shearing is dominant [201].

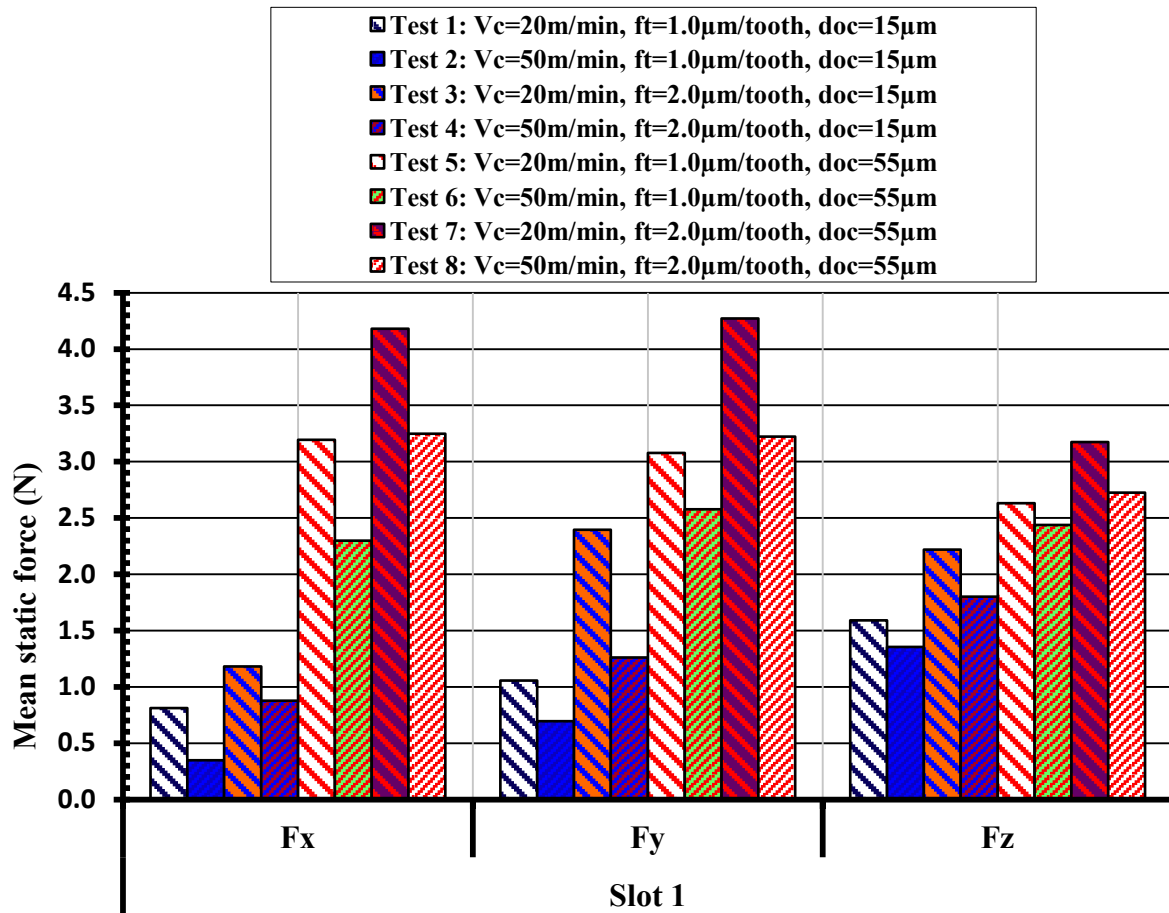


Figure 4.44: Mean static force at Slot 1- new tool

The corresponding force levels obtained when the tool was worn (Slot 26) for each test is shown in Figure 4.45. The magnitudes ranged from 1.8N ( $F_y$  - Test 2) to 20.7N ( $F_z$  – Test 7). The forces increased as expected with tool wear but in contrast to results seen with new cutters, the thrust force ( $F_z$ ) was the largest component (due to ploughing/rubbing) with  $F_x$  typically twice the level of  $F_y$ . Similar trends were also detailed by Rahman et al. [141] when micromilling copper workpiece material.

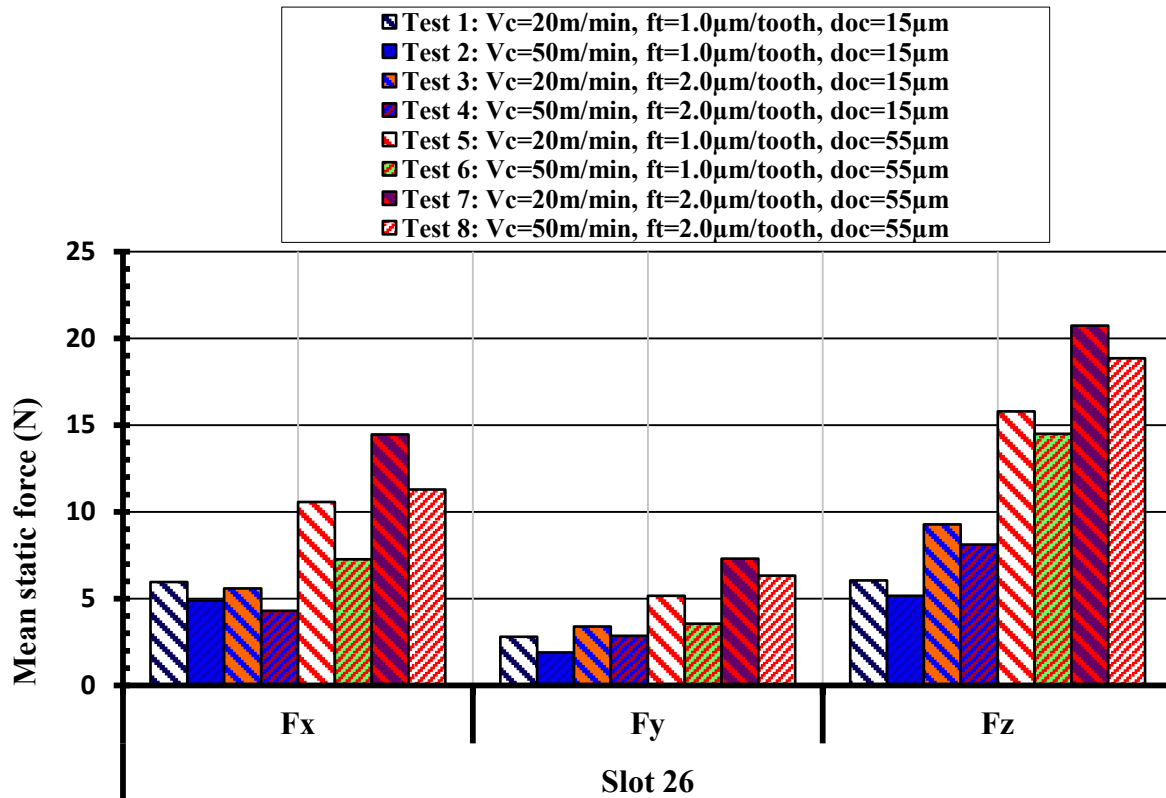


Figure 4.45: Mean static force at Slot 26 – worn tool

Figure 4.46 shows the comparison in cutting forces between Test 1 conducted using low level machining parameters and Test 8 carried out with high level parameters. The data relates to forces after cutting 520mm slot length. All forces increased with cut length due to tool wear progression. The feed force ( $F_x$ ) in Test 8 rose from 3.2N (first slot) to 11.3N (slot 26), which was twice that of the normal force ( $F_y$ ) component. Tool wear micrographs for new and worn tools are given in Figure 4.47 and show that the cutting edge corners were fractured or rounded and the coating partially removed from the rake and flank faces. As a result, cutting edges in contact with the slot side wall were subjected to higher cutting forces leading to tool deflection in the radial direction. This was more dominant in Test 8, where there was an increase in thrust force from 2.7N to 18.8N over the test cycle. Use of the larger depth of cut and feed rate increased the chip cross-sectional area, resulting in higher cutting forces. No obvious vibration or chatter was detected in any of the tests based on analysis of the respective force signatures and inspection of resulting slot surfaces. Additionally, the magnitude of milling forces recorded was above the intrinsic background / machine noise level, which was typically  $\leq 1$ N for the experimental arrangement employed [203].

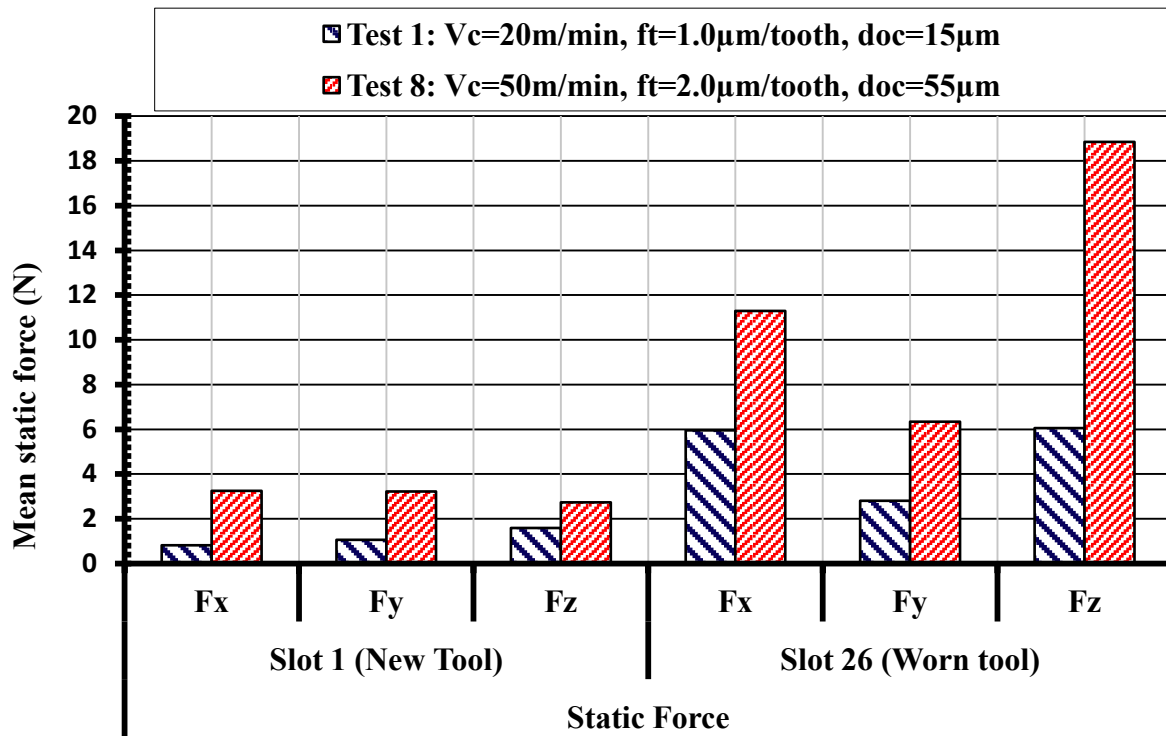


Figure 4.46: Comparison of static forces generated in Test 1 and Test 8 with new and worn tools

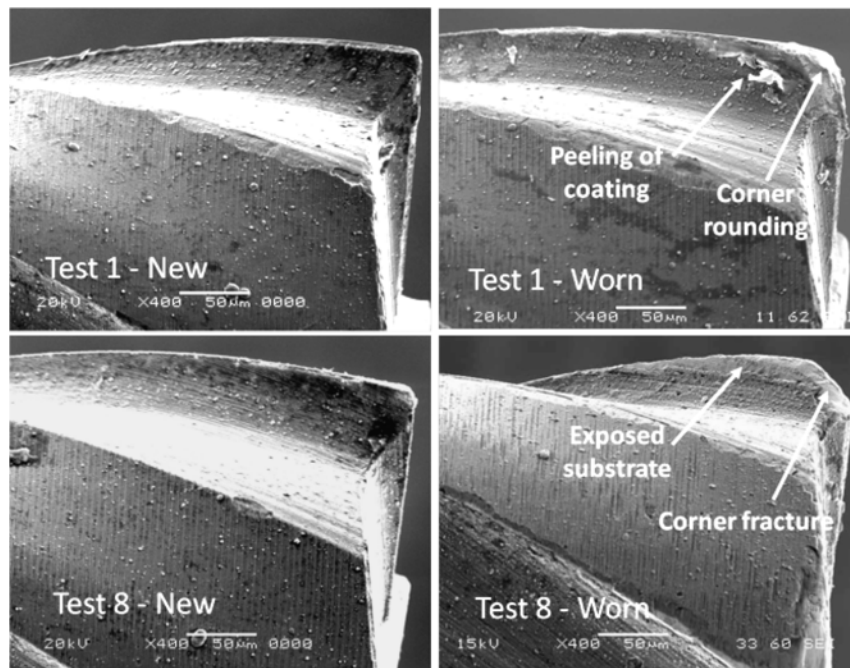


Figure 4.47: Micrographs of tool wear for low vs. high parameters

Table 4.4 shows the ANOVA details for mean feed force ( $F_x$ ) at Slot 26 while Figure 4.48 highlights the corresponding main effects plot. All 3 factors were statically significant with depth of cut having the largest effect with a PCR of 70% followed by cutting speed, and feed per tooth at 10% and 6% respectively. Furthermore, the interaction between feed per tooth and depth of cut was also significant at the 5% level with an 11% contribution, see Appendix C for interaction plot.

Table 4.4: ANOVA results for  $F_x$  worn tool – Slot 26

Source	Sum of Squares	DF	Mean Square	F Value	Prob > F	% PCR
Cutting speed (A)	9.768	1	9.768	541.628	0.0273*	10%
Feed per tooth (B)	6.011	1	6.011	333.314	0.0348*	6%
Depth of cut (C)	65.197	1	65.197	3615.041	0.0106*	70%
AB	0.001	1	0.001	0.063	0.8433	0%
AC	2.124	1	2.124	117.766	0.0585	2%
BC	9.835	1	9.835	545.325	0.0272*	11%
Residual	0.018	1	0.018			
Total	92.954	7				

\*Significant at 5% level

Std. Dev.	0.13429	R-Squared	0.99981
Mean	8.04016	Adjusted R-Squared	0.99864

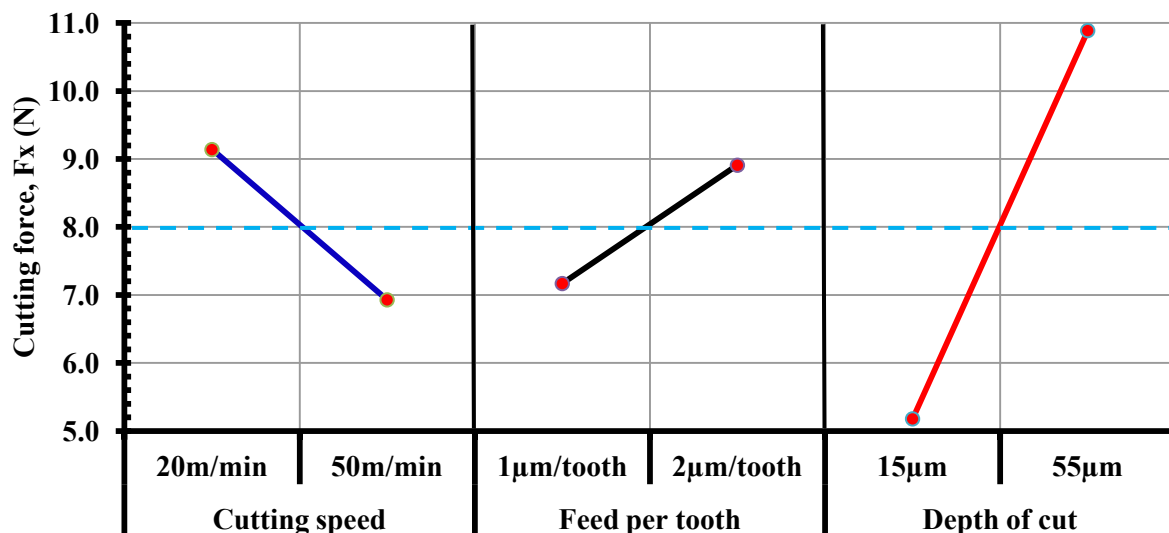


Figure 4.48: Main effects plot, means for  $F_x$  worn tool – Slot 26

Similar trends were observed with the mean normal force,  $F_y$  where all 3 variables were significant with depth of cut again having the biggest influence at a PCR of 65%, see Table 4.5. Feed per tooth had a greater effect at 21% PCR compared to cutting speed (8%), while none of the interactions analysed were significant at 5% significant level, see Appendix C for interaction plot. The main effects plot in Figure 4.49 showed that minimum force was obtained with high cutting speed and low feed per tooth and depth of cut.

Table 4.5: ANOVA results for  $F_y$  worn tool – Slot 26

Source	Sum of Squares	DF	Mean Square	F Value	Prob > F	% PCR
Cutting speed (A)	2.023	1	2.023	211.346	0.0437*	8%
Feed per tooth (B)	5.182	1	5.182	541.261	0.0273*	21%
Depth of cut (C)	16.318	1	16.318	1704.398	0.0154*	65%
AB	0.126	1	0.126	13.186	0.1711	0%
AC	0.156	1	0.156	16.283	0.1547	1%
BC	1.404	1	1.404	146.632	0.0525	6%
Residual	0.010	1	0.010			
Total	25.219	7				

**\*Significant at 5% level**

Std. Dev.	0.0978	R-Squared	0.9996
Mean	4.1659	Adjusted R-Squared	0.9973

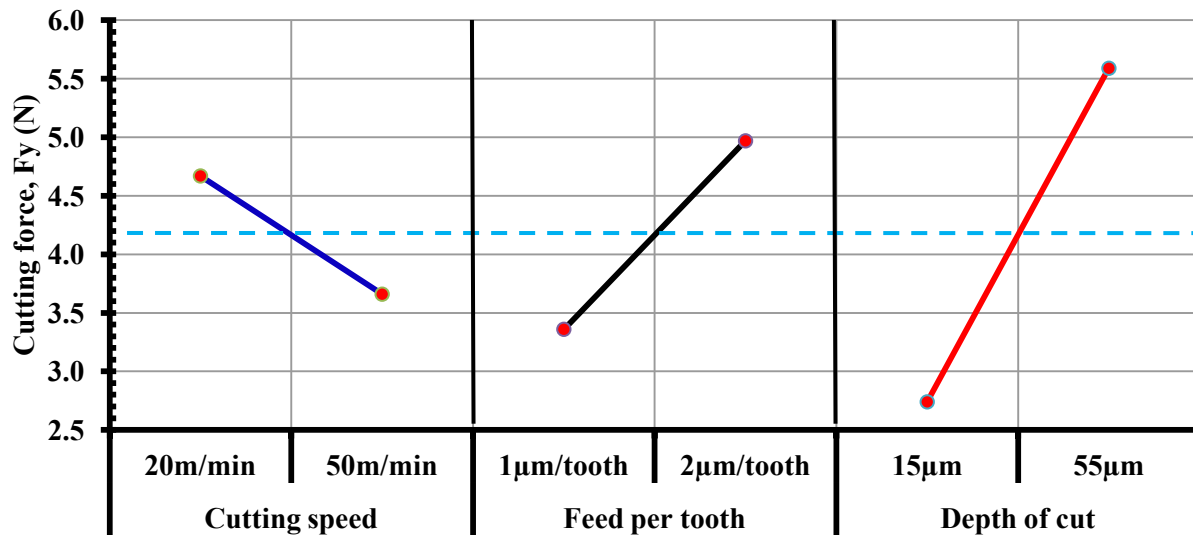


Figure 4.49: Main effects plot, means for  $F_y$  worn tool – Slot 26

Table 4.6 and Figure 4.50 show the ANOVA and main effects plot for mean thrust force ( $F_z$ ) respectively. Once again force, depth of cut had a dominant effect with a PCR of 86%. Despite having low PCR values, both feed per tooth (12%) and cutting speed (1%) were also found to be statistically significant factors affecting the thrust force.

Table 4.6: ANOVA results for  $F_z$  worn tool – Slot 26

Source	Sum of Squares	DF	Mean Square	F Value	Prob > F	% PCR
Cutting speed (A)	3.393	1	3.393	259.331	0.0395*	1%
Feed per tooth (B)	29.891	1	29.891	2284.432	0.0133*	12%
Depth of cut (C)	212.855	1	212.855	16267.390	0.0050*	86%
AB	0.093	1	0.093	7.085	0.2288	0%
AC	0.158	1	0.158	12.111	0.1781	0%
BC	1.198	1	1.198	91.537	0.0663	0%
Residual	0.013	1	0.013			
Total	247.601	7				
<b>*Significant at 5% level</b>						
Std. Dev.	0.16699		R-Squared	0.99989		
Mean	12.29020		Adjusted R-Squared	0.99926		

\*See Appendix C for interaction plot.

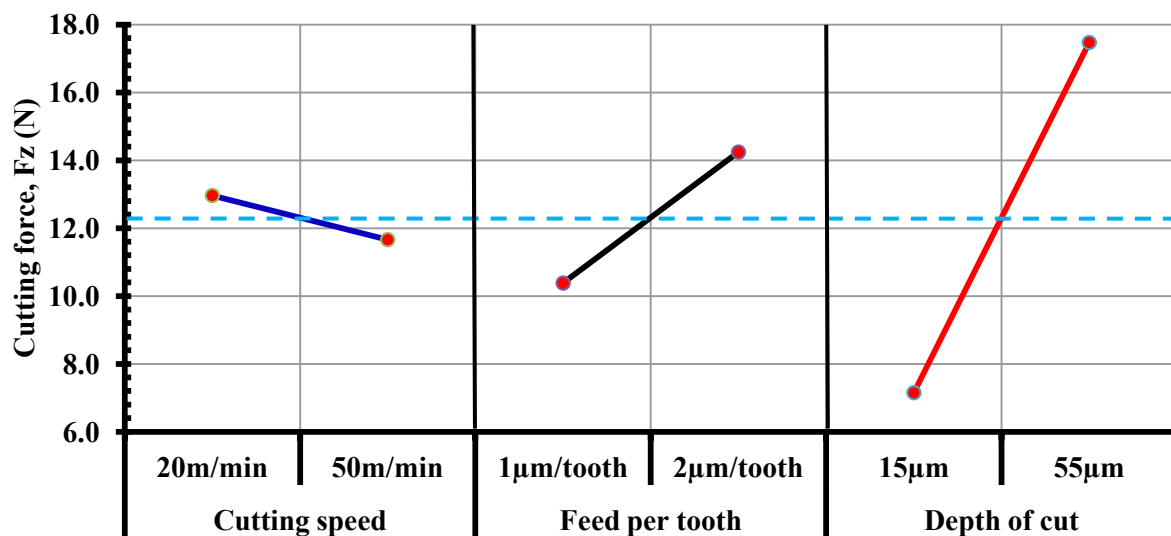


Figure 4.50: Main effects plot, means for  $F_z$  worn tool– Slot 26

#### 4.4.5 Slot quality/geometry

As detailed previously, the primary tool wear mode in micromilling is fracture/chipping of cutting edges rather than traditional flank wear as in conventional macromilling. The change in cutter edge geometry due to the wear has a direct effect on the resulting slot quality/dimensions. Figure 4.51 (a) & (b) details an example of slots produced (viewed from the exit location) using a new and worn (after 520mm cut length) tool respectively. Sharp corners at the interface between the base and side walls of the slot together with near burr-free surfaces were obtained for Slot 1, see Figure 4.51(a). This was in stark contrast to Slot 26 where highly radiused corners and heavy burr formation, especially on the top surfaces, were prevalent. Similar trends were observed in all the other tests, with results shown in Appendix D. The deterioration in slot quality progressed gradually with length cut, where burr size and the extent of corner rounding increased with tool wear, see Figure 4.52 and Figure 4.53 showing SEM micrographs of machined slots at various cut lengths for Test 1 and Test 8 respectively.

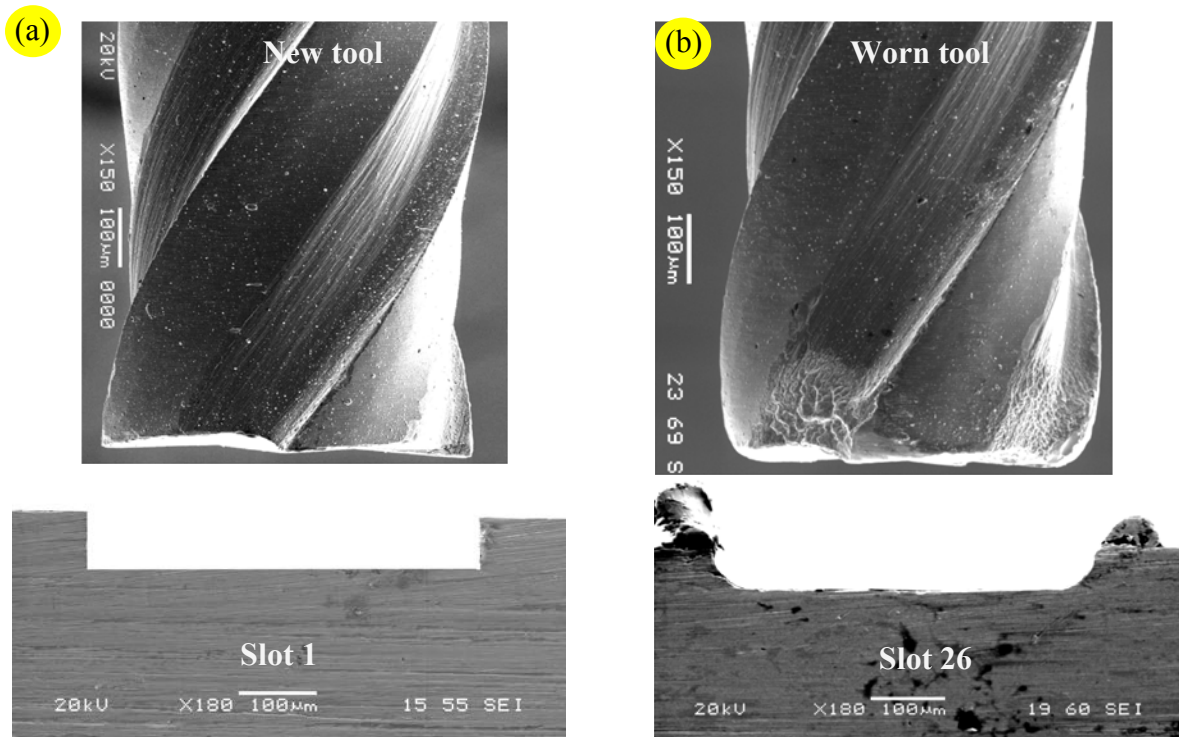


Figure 4.51: Comparison of slot quality in Test 6 (a) New tool / Slot 1 (b) Worn tool / Slot 26

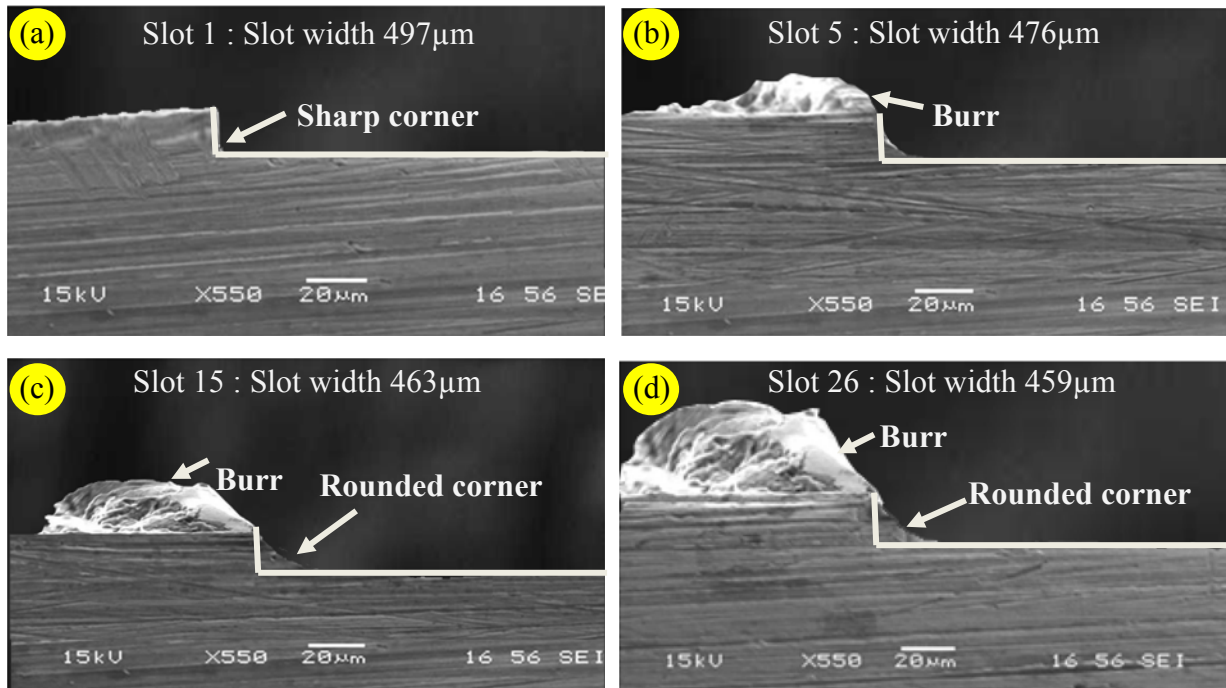


Figure 4.52: Slot quality at different cut lengths for Test 1: (a) First slot (b) 100mm (c) 300mm (d) 520mm

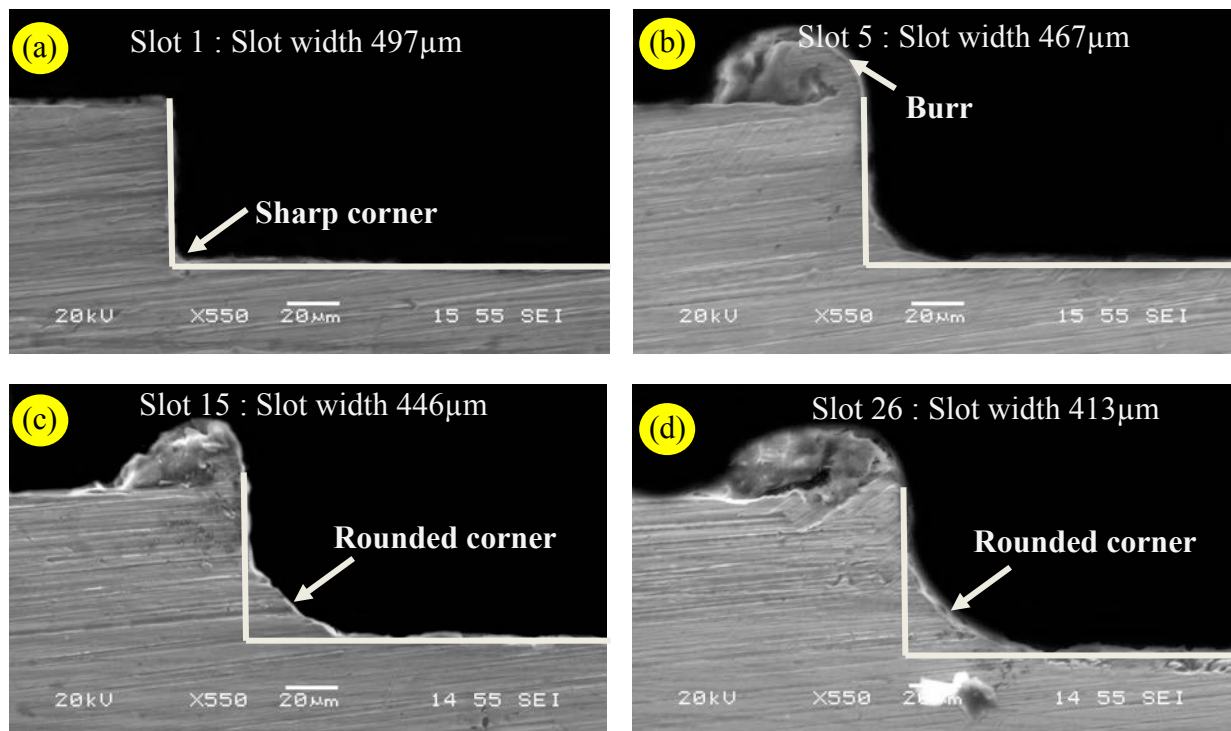


Figure 4.53: Slot quality at different cut lengths for Test 8: (a) First slot (b) 100mm (c) 300mm (d) 520mm

#### 4.4.6 Cutting temperature

Cutting temperature Figure 4.54 shows infrared thermal micrographs during micro slotting using both new and worn tools (after 520mm cut length) at parameters utilised in Test 8 ( $V_c=50\text{m/min}$ ,  $f_t=2\mu\text{m/tooth}$ ,  $d=55\mu\text{m}$ ). The highest cutting temperature was located at the tool-workpiece interface, with a value of  $47.5^\circ\text{C}$  and  $54.1^\circ\text{C}$  for Slot 1 and 26 respectively. This was somewhat lower than previously reported temperatures of  $\sim 92^\circ\text{C}$  measured using an equivalent IR camera (Phoenix ThermalCAM Midwave) when micromilling 1018 steel at operating parameters of  $V_c=37.7\text{m/min}$ ,  $f_t=2.5\mu\text{m/tooth}$ ,  $d=75\mu\text{m}$  [159]. Apart from the different cutting parameters and workpiece material used, a further reason for the discrepancy in the results was thought to be due to the insufficient close focus capability of the thermal imaging camera (leading to lower average values) employed in the present work.

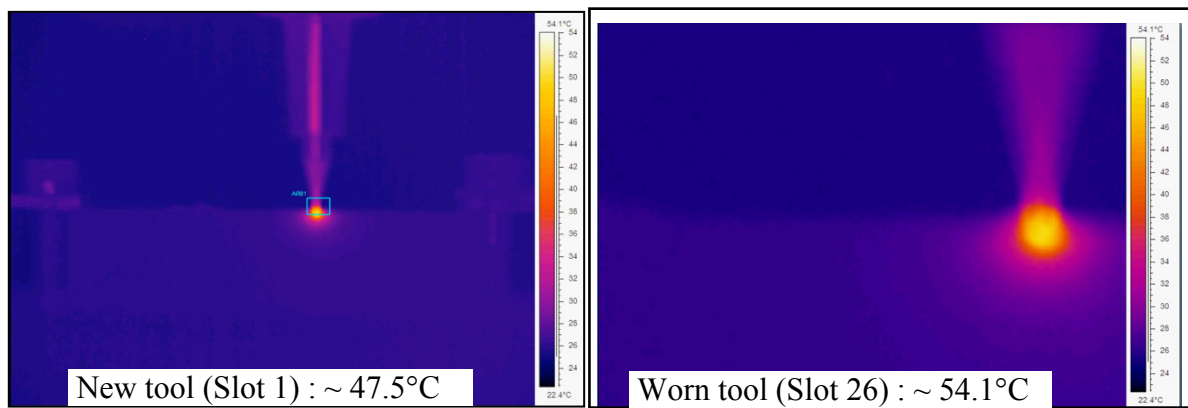


Figure 4.54: Micromilling temperature measurement

#### 4.4.7 Microstructure

SEM micrographs of etched cross-sectional slot samples machined using new (Slot 1) and worn (Slot 26) end mills for each test is shown in Figure 4.55 and Figure 4.56 respectively. No evidence of major surface/subsurface damage such as microcracks, un-tempered/over-tempered martensite, phase transformations or white layer formation was detected in any of the specimens analysed. A further assessment at higher magnification (3000x) of Slot 26 in Test 8 (highest parameters) at 2 different positions (see Figure 4.57) also revealed no discernible deformation of the material grain structure beneath the machined surface. Sample cross-sections on the top of the side walls of Slot 26 in Test 8 (X-Y plane) as well as parallel (X-Z) and perpendicular to the feed (Y-Z) also showed no evidence of any surface/subsurface damage, see Figure 4.58 and Figure 4.59. Reasons for the lack of surface integrity damage was likely due to the relatively low cutting forces (maximum resultant force = 25.3N) and temperatures ( $\sim 54.1^\circ\text{C}$ ) experienced during micromilling, as previously discussed.

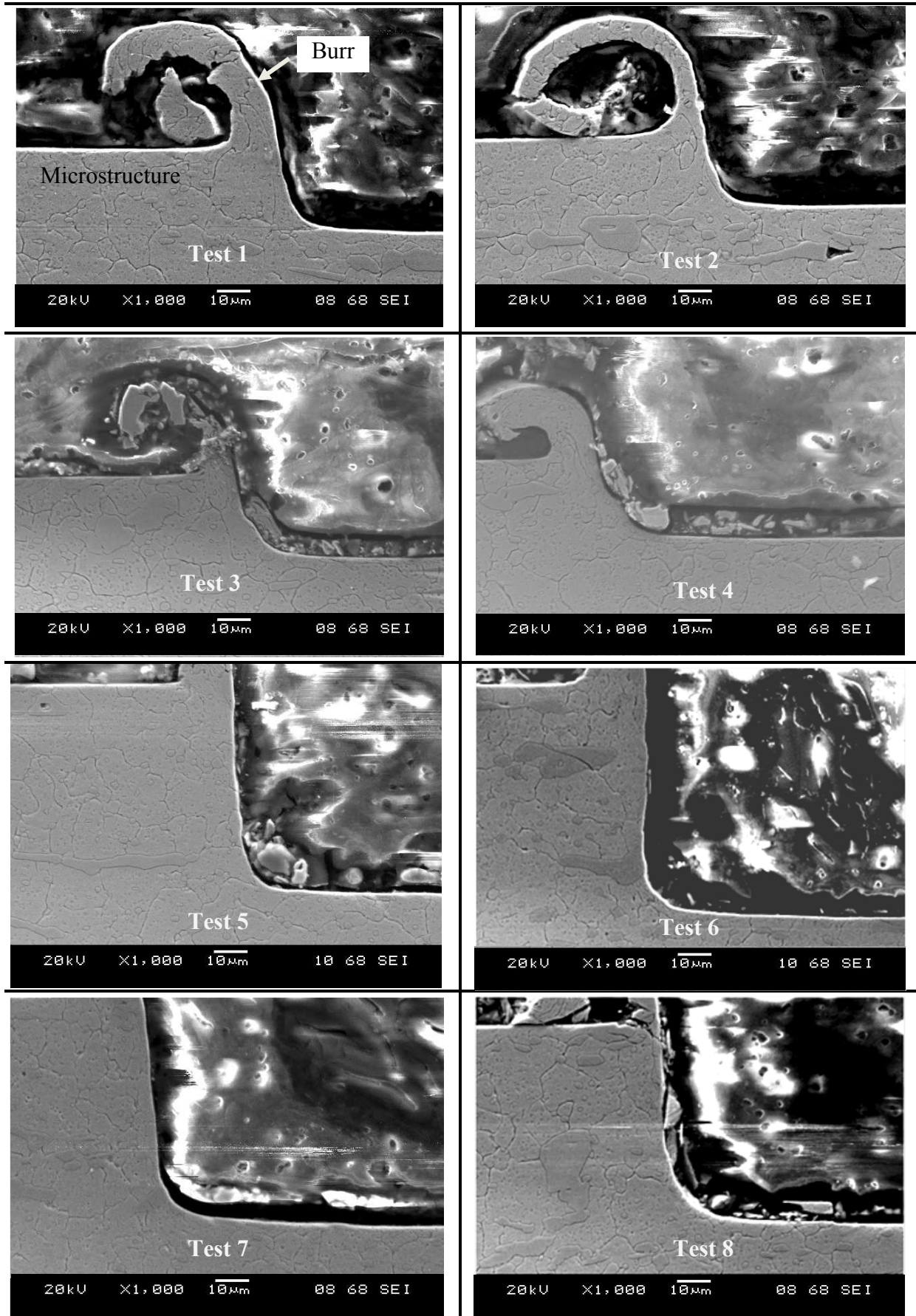


Figure 4.55: Cross sectional micrograph of slots machined using new tools (Slot 1)

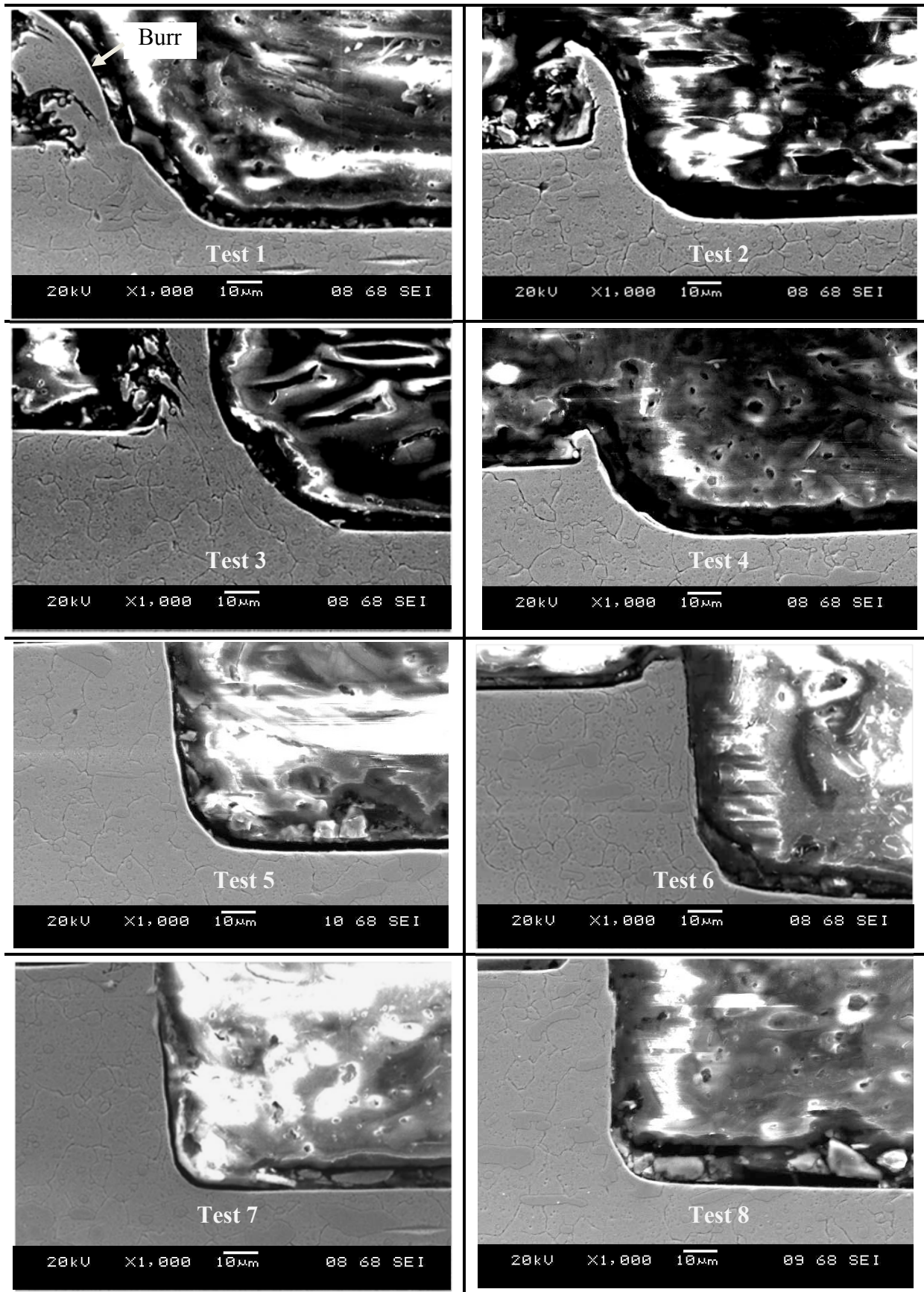


Figure 4.56: Cross sectional micrograph of slots machined using worn tools (Slot 26)

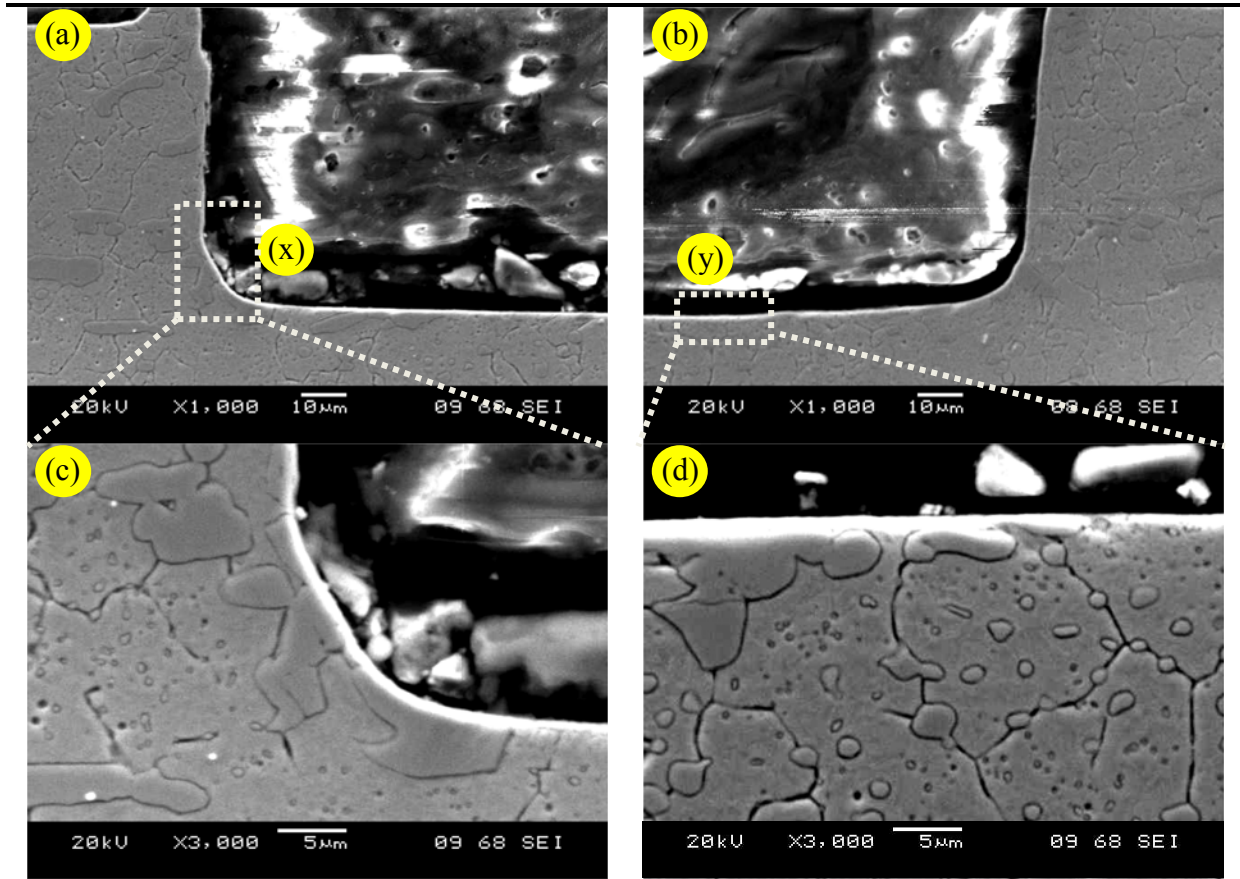


Figure 4.57: Cross sectional (Y-Z plane) microstructure of a micromilled specimen from Test 8-Slot 26 (a) left side (b) right side (c) 3000x magnification of Section x (d) 3000x magnification of Section y

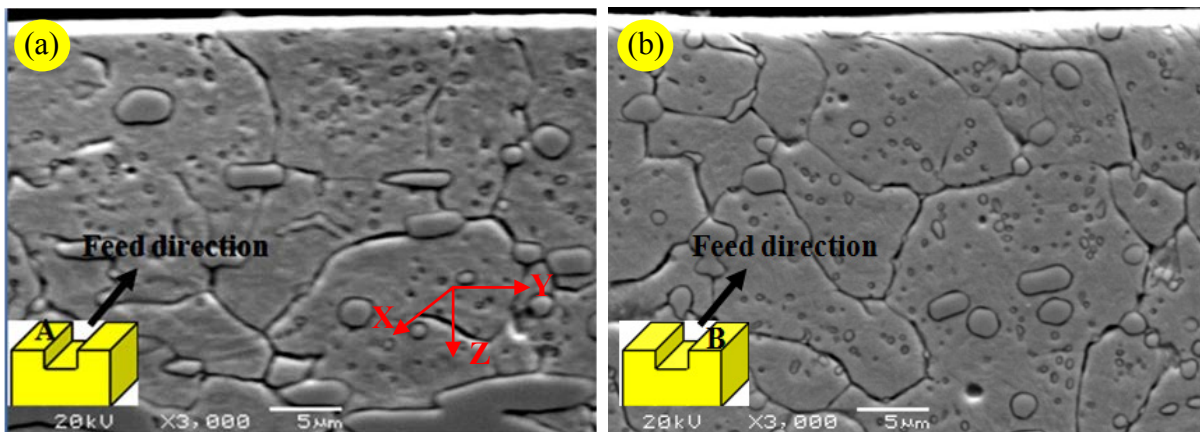


Figure 4.58: Cross sectional (X-Y plane) microstructure of a micromilled specimen from Test 8-Slot 26 (a) A-up milling side (b) B-down milling side

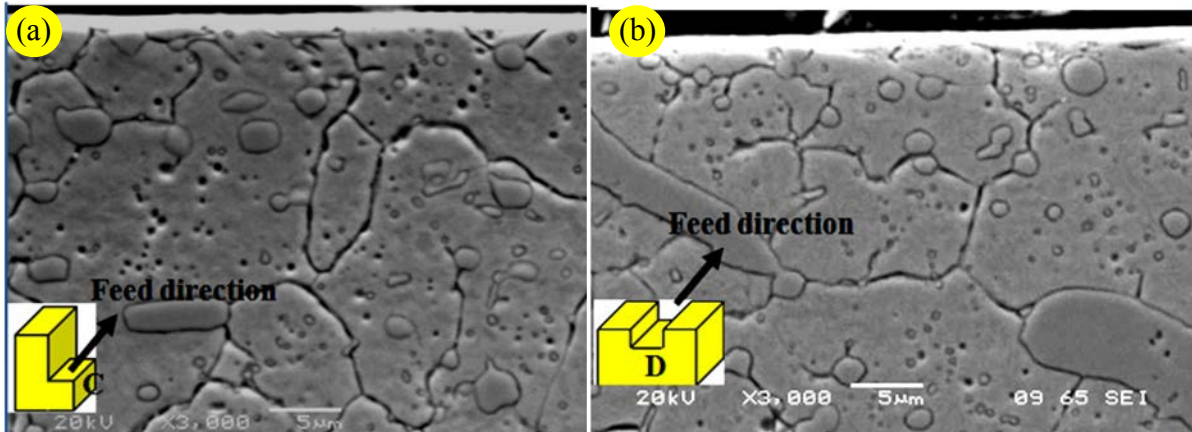


Figure 4.59: Cross sectional microstructure of a micromilled specimen from Test 8-Slot 26  
 (a) X-Z plane, C- cross section (parallel to feed direction) (b) Y-Z plane, D- cross section  
 (perpendicular to feed direction)

#### 4.4.8 Microhardness

Microhardness depth profile measurements were taken at the bottom of the slot for all tests from samples sectioned perpendicular to the feed direction (near the middle position along the length). Figure 4.60 shows the results compared against the material bulk hardness. The variation in measurement values highlighted by the range bars were due to the inhomogeneity of the workpiece material and indentation of different sized carbide particles [204]. The data was found to converge into two distinct groups, which reflect the different depths of cut used. Trials at 15 $\mu\text{m}$  depth of cut (Test 1 – 4) showed a softened layer of up to  $\sim 130 \text{ HK}_{0.025}$  below the bulk hardness for a distance of  $\sim 20\mu\text{m}$  from the machined surface. Conversely, tests at the higher depth of cut (55 $\mu\text{m}$ ) unexpectedly showed only marginal softening to a maximum of  $\sim 35 \text{ HK}_{0.025}$  below the bulk and which recovered after  $\sim 10\mu\text{m}$  beneath the slot surface. In general, a reduction in workpiece hardness is caused by thermal softening (assuming the absence of heavy workpiece deformation/strain hardening), typically associated with severe operating parameters. The unusual response recorded in the current work (in the absence of measureable deformation and the relatively low temperature detected) was thought to be due to the previous face milling operation used in preparing the workpiece material for micromilling trials. The influence of the face milling process on the workpiece microhardness was subsequently evaluated.

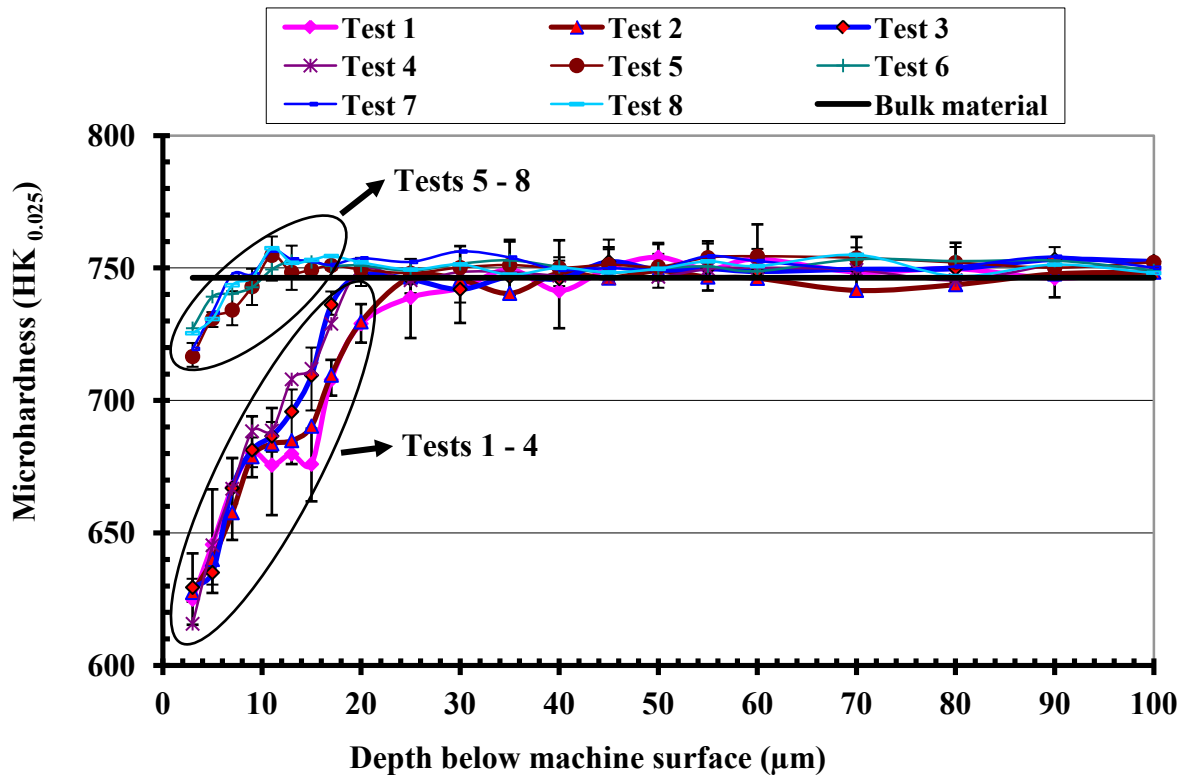


Figure 4.60: Microhardness depth profiles of all tests compared to the bulk material – New tools

\*Refer to Table 3.6 for test parameters

Figure 4.61 shows the microhardness depth profile for a sample which was face milled according to the conditions employed during preparation of the workpiece blocks for micromilling. A softened layer up to  $\sim 200$   $\text{HK}_{0.025}$  below the bulk hardness of  $\sim 750$   $\text{HK}_{0.025}$  to a depth of  $\sim 60\mu\text{m}$  from the machined surface was found. The decrease in microhardness was expected due to the relatively high temperatures generated during the face milling process. A similar observation was reported by Axinte and Dewes [205] when milling AISI H13 steel. With the face milled profile as a reference, results from the 8 micromilling trials were superimposed onto the same plot while adjusting for the respective depths of cut, see Figure 4.62. The near surface microhardness of all the slots were clearly in line with the corresponding value on the face milling graph. This strongly suggests that the softening observed was due entirely to the face milling operation with the micro slotting process having little or no effect on workpiece microhardness. The influence of tool wear on workpiece microhardness was subsequently investigated involving Test 1 and Test 8, see Figure 4.63. The difference in the average microhardness between new and worn tools was negligible (up to  $\sim 15\text{HK}_{0.025}$ ), with the limits of the range bars generally overlapping at the majority of measured points.

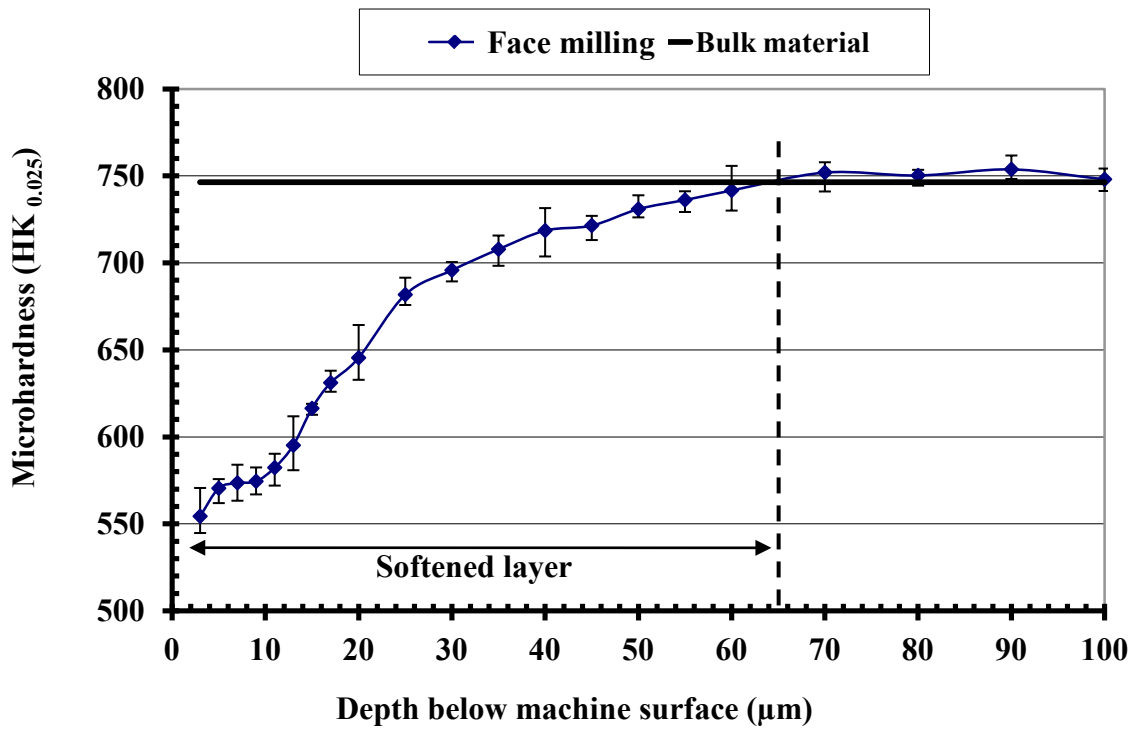


Figure 4.61: Microhardness depth profiles for face milling and bulk material

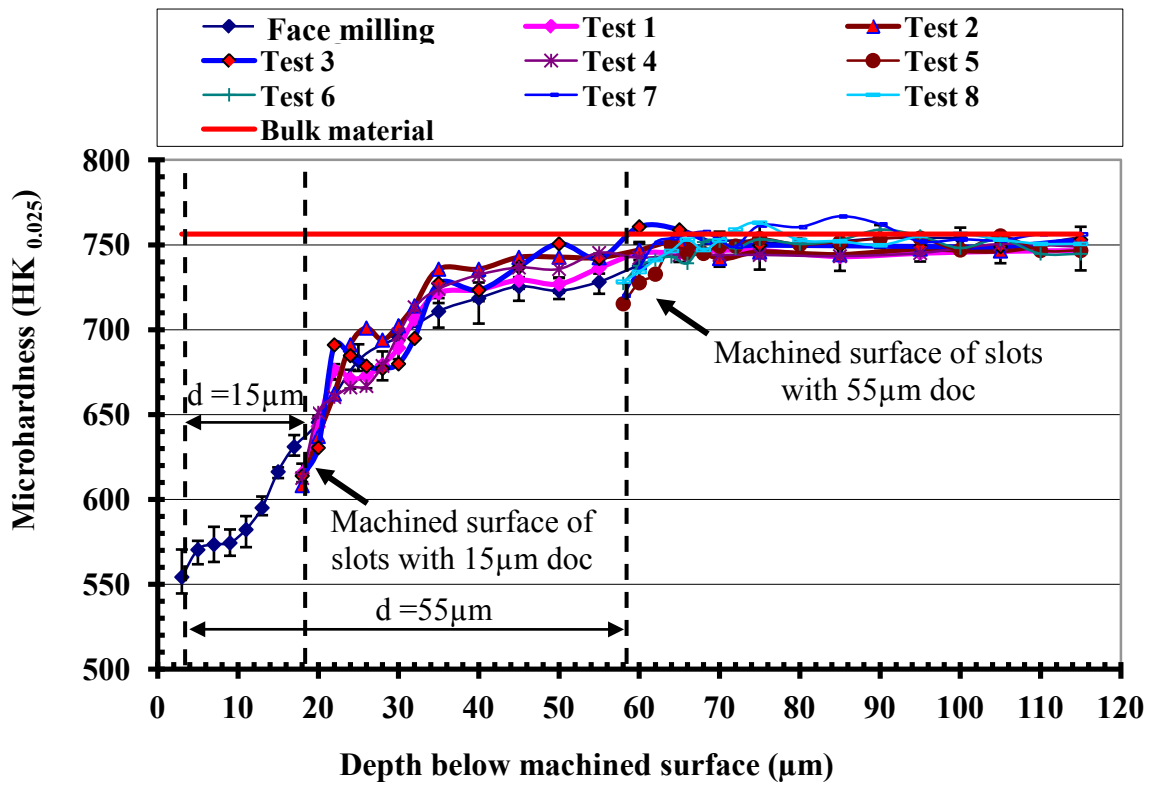


Figure 4.62: Combined microhardness depth profiles - worn tools

\*Refer to Table 3.6 for test parameters

Additionally, a t-test between the gradients of the two best fit lines between 3 and 20 $\mu\text{m}$  depth below the machined surface for Test 1 in Figure 4.63 showed no significant difference.

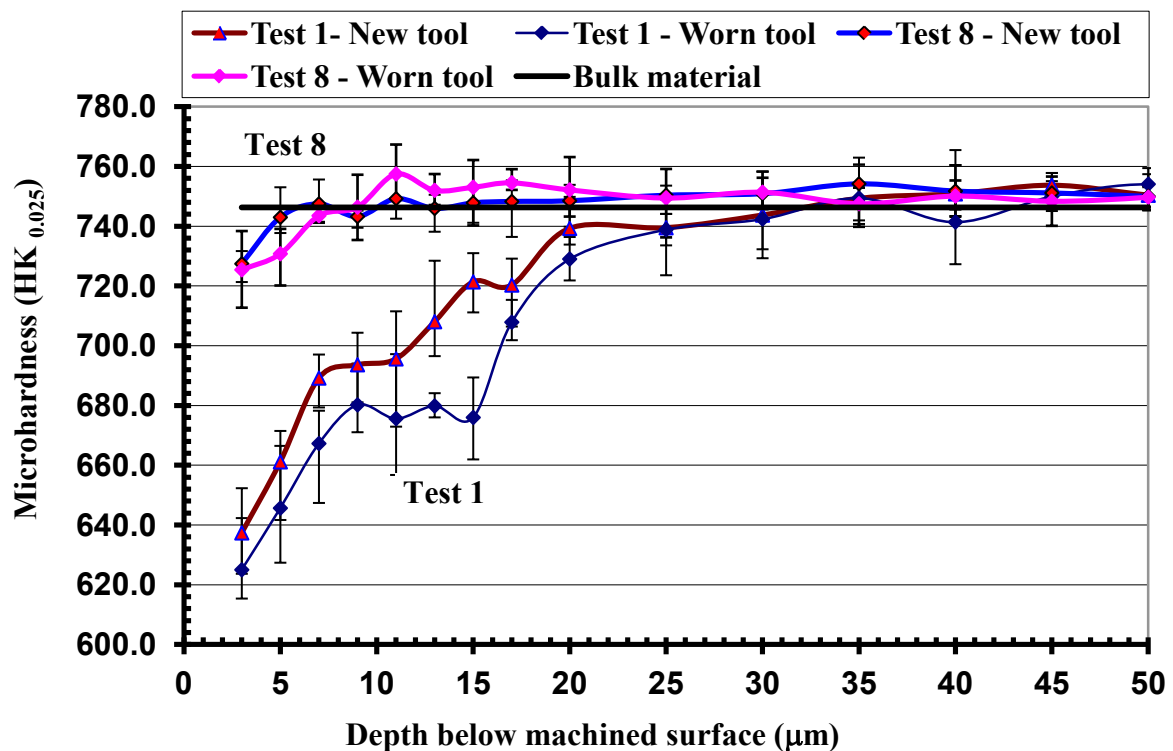


Figure 4.63: Microhardness depth profiles for Test 1 and Test 8 with new and worn tools  
*\*Refer to Table 3.6 for test parameters*

Testing involved depths of cuts of 15-55 $\mu\text{m}$  (mainstream) and while there is evidence to suggest that trials at the lower value (15 $\mu\text{m}$ ) did occur within the slightly reduced hardness band (55HRC equivalent – 630HK) due to the previous face milling operation, this did not occur to any great extent when the depth of cut was 55 $\mu\text{m}$  as the depth of softening although extending to ~60 $\mu\text{m}$  deep, was subject to relatively shallow degradation after 25 $\mu\text{m}$ . It was not possible to substantiate this with further testing on etched surfaces or similar (to remove the softened layer), however it is likely that the difference between 62HRC and 55HRC had only a marginal effect on machinability as the workpiece is still classified as a hardened steel (> 45HRC) with equivalent microstructural/physical/mechanical properties.

#### 4.4.9 Residual stress

An evaluation of workpiece surface residual stress (see Section 3.3.7 for measurement technique/procedure) after face milling followed by a micro slotting (using Test 8 parameters with a worn cutter) operation was performed with 2 replications. The results detailed in

Figure 4.64 show that surface residual stress was compressive with a maximum recorded magnitude of -104.8MPa. More importantly, there was essentially no difference in measured surface residual stresses after micro slotting compared to the face milled surface in all 3 trials. This implies that the micromilling operation had no effect on workpiece residual stresses, which reflects the low cutting forces and temperatures (detailed in Section 4.4.5 and 4.4.6) typical of micro machining processes (depths of cut of 15 - 55 $\mu$ m). Taken in tandem with other surface integrity measurements (microhardness, temperature etc.), it is highly likely there was no discernible effect on bulk workpiece properties due to micro milling.

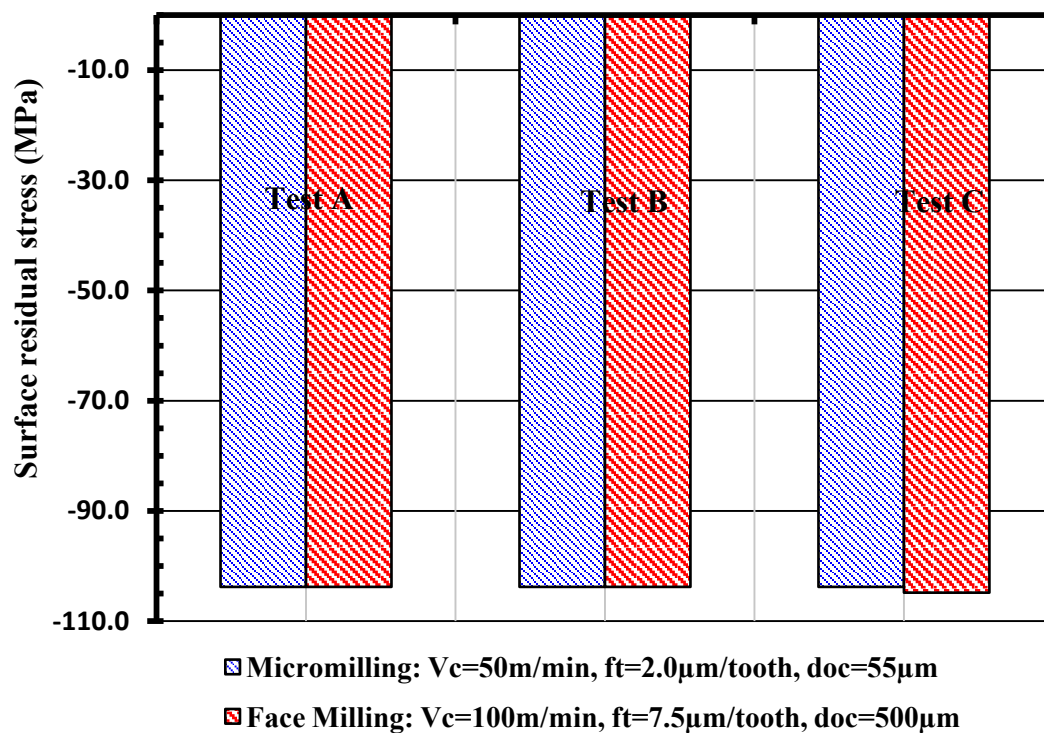


Figure 4.64: Surface residual stress

## 4.5 Phase 4: Optimisation of tool life and surface roughness

### 4.5.1 Tool life and material removal rate

A comparison between tool life (mins), material removed ( $\text{mm}^3$ ) and material removal rate ( $\text{mm}^3/\text{min}$ ) following the extended central composite design (CCD) testing is shown in Figure 4.65, based on a tool life criterion of 30 $\mu$ m cutter diameter reduction. In general tool life ranged from 0.5 to 4.7 minutes, with Test 1 ( $V_c=20\text{m/min}$ ,  $ft=1\mu\text{m/tooth}$ ,  $d=15\mu\text{m}$ ) showing the longest tool life (4.7 minutes) and correspondingly Test 8 ( $V_c=50\text{m/min}$ ,  $ft=2\mu\text{m/tooth}$ ,

$d=55\mu\text{m}$ ) giving the shortest (0.5 minutes). Understandably, the highest operating parameters led to the shortest tool life (Test 8) due to the greater tool wear, albeit with the highest material removal rate. In contrast, Test 18 which employed the ‘preferred’ combination of cutting parameters ( $V_c=35\text{m/min}$ ,  $f_t=1.5\mu\text{m/tooth}$ ,  $d=68.6\mu\text{m}$ ), achieved the highest volume of material removed ( $7.3\text{mm}^3$ ).

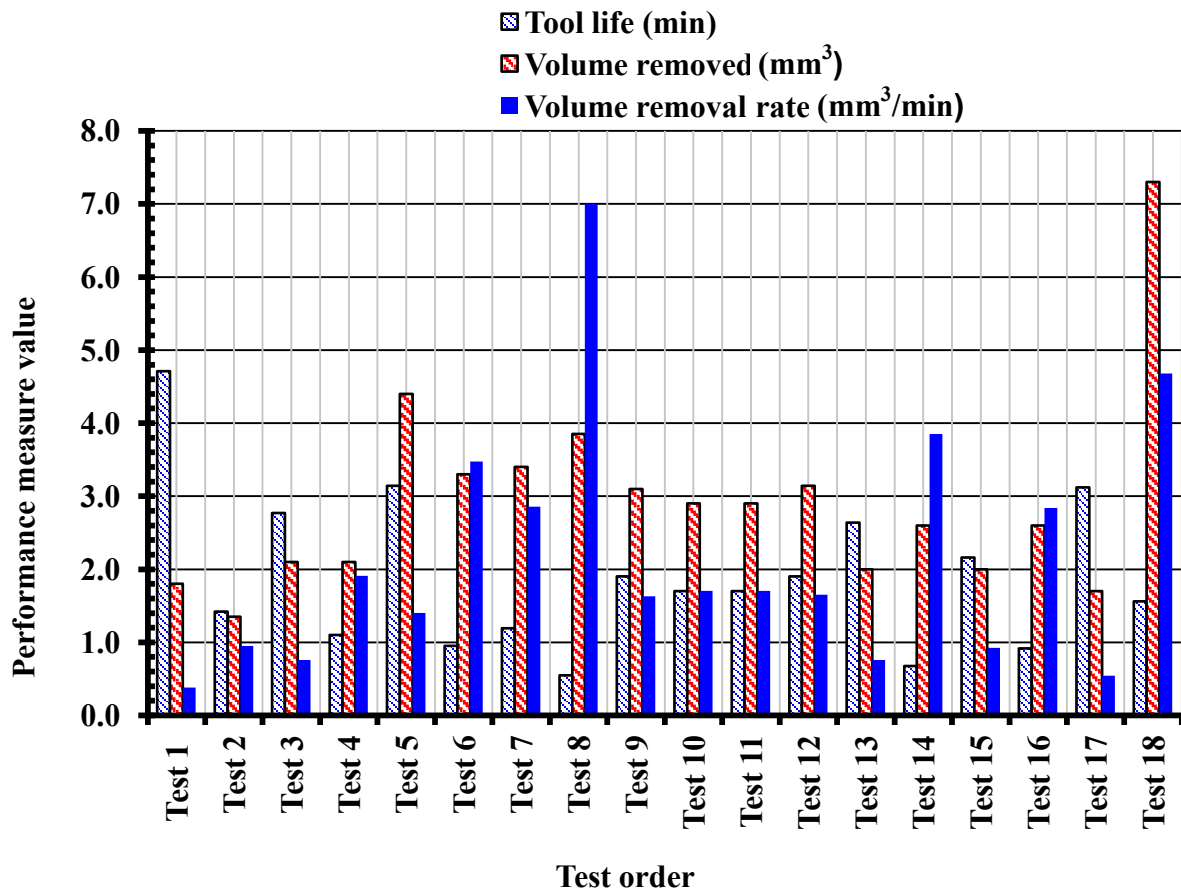


Figure 4.65: Tool life, volume removed and volume removal rate at test citation

\*Refer Table 3.6 for test parameter

#### 4.5.2 First order model of tool life

Table 4.7 shows ANOVA results for tool life based on the linear model ( $L_{12}$  array – 12 tests) with estimated effects of each parameter, along with their interactions and standard error. It can be seen that cutting speed, feed per tooth, depth of cut and the interactions between cutting speed  $\times$  feed per tooth, as well as feed per tooth  $\times$  depth of cut were significant factors in terms of tool life. Among the variable factors, cutting speed had the largest influence with a contribution of 58%, while feed per tooth and depth of cut showed similar levels at 18% and 20% respectively. The two statistically significant interactions each had very low percentage contributions of 2%.

Table 4.7: ANOVA results for tool life of linear model (based on L<sub>12</sub>)

Factor	Sum of Squares	DF	Mean of Squares	F Value	Prob > F	PCR
Cutting speed (A)	2.0457	1	2.0457	1773.6961	< 0.0001*	58%
Feed per tooth (B)	0.6376	1	0.6376	552.8538	< 0.0001*	18%
Depth of cut (C)	0.7140	1	0.7140	619.0330	< 0.0001*	20%
AB	0.0691	1	0.0691	59.9396	0.0015*	2%
AC	0.0015	1	0.0015	1.3308	0.3129	
BC	0.0751	1	0.0751	65.1091	0.0013*	2%
Curvature	0.0232	1	0.0232	20.0868	0.0110*	Significant
Residual	0.0046	4	0.0012	* Significant		
Lack of Fit	0.0013	1	0.0013	1.2362	0.3473	Not significant
Pure error	0.0033	3	0.0011			
Total	3.5476	11	*Significant at 5% level			
Std. Dev	0.0034		R-Squared	0.9987		
Mean	0.5		Adjusted R-Squared	0.9967		
C.V	6.83		Predicted R-Squared	0.9742		

From the regression analysis, the predicted first-order tool life model based on the first 12 experiments in a coded form is given as;

$$\hat{y} = 0.460 - 0.511x_1 - 0.288x_2 - 0.293x_3 \text{ -----Eq. 8}$$

with  $x_1$ ,  $x_2$  and  $x_3$  representing the associated transformation equations for cutting speed, feed rate and depth of cut respectively, see Section 3.5.5.

A mathematical relationship for tool life, T (min) as a function of the cutting speed,  $V_c$ , (m/min), feed per tooth,  $ft$ , ( $\mu\text{m tooth}^{-1}$ ) and depth of cut,  $d$ , ( $\mu\text{m}$ ) can be further formulated by substituting Equations 4 - 6 (detailed in Section 3.4.5) into Equation 8. The model can therefore be expressed as;

$$\ln T = 6.241 - 1.145 \ln V_c - 0.807 \ln ft - 0.458 \ln d \text{ -----Eq. 9}$$

and by applying inverse logarithms,

$$T = 513.6 V_c^{-1.145} ft^{-0.807} d^{-0.458} \text{ -----Eq. 10}$$

It can be seen from Equation 10 that tool life is inversely proportional to cutting speed, feed per tooth and depth of cut. The equation is valid when micromilling hardened AISI D2 (62HRC) cold work tool steel under dry cutting conditions within the range of experimental conditions assessed; cutting speed ( $20 \leq V_c \leq 50$  m/min), feed per tooth ( $1.0 \leq ft \leq 2.0$   $\mu\text{m/tooth}$ ), and depth of cut ( $15 \leq d \leq 55$   $\mu\text{m}$ ).

#### 4.5.2.1 Adequacy of the linear model

From the ANOVA results in Table 4.7, the regression analysis of the linear model was found to be significant, as both the predicted ‘R-Squared’ and adjusted ‘R-Squared’ values were comparable (0.9987 and 0.9967 respectively). This indicates that the model/prediction fits well with the experimental data, with only a 0.01% probability that the results observed were due to noise. Curvature however was highlighted as being significant and hence additional tests were required (6 axial points) to account for the non-linearity present in the model. These were subsequently performed with the results used to develop a second order predictive model for tool life, which is discussed later in Section 4.5.3.

#### 4.5.2.2 Utilisation of the first order tool life model

A range of variables levels (cutting speed and feed per tooth) were substituted into Equation 8 with the axial depth of cut kept constant at 35 $\mu$ m to produce a contour plot for tool life, see Figure 4.66. The response surface shows the possible combinations of cutting speed and feed per tooth to achieve a specific tool life level. In a production environment, productivity is also a key concern, which generally entails higher operating parameters, but at the expense of tool life or part quality.

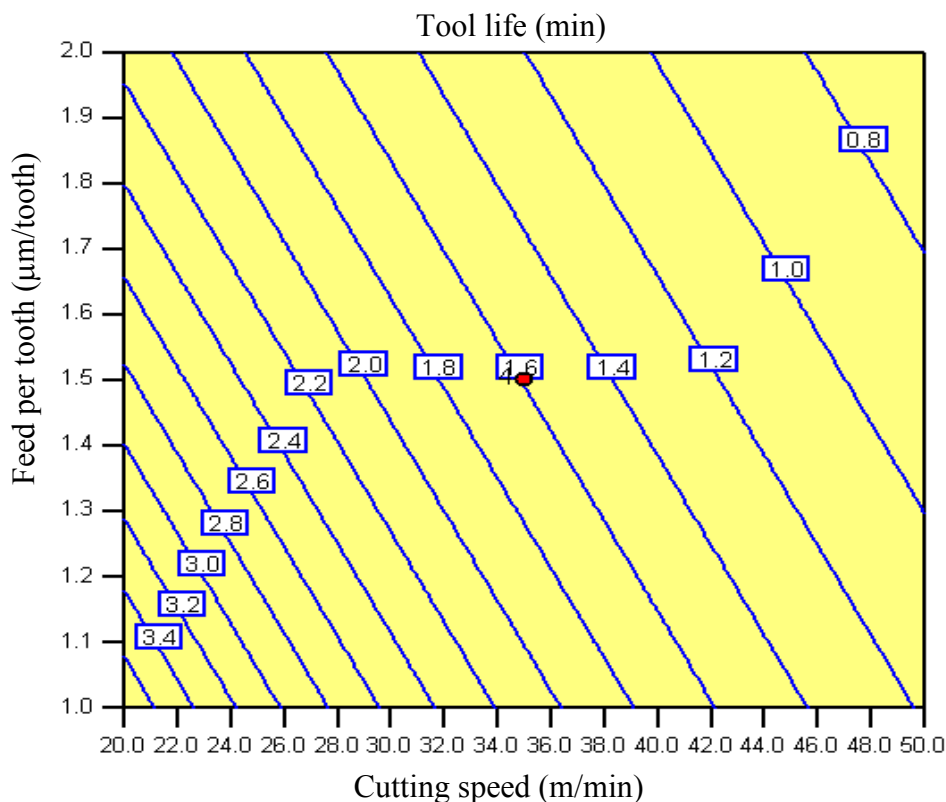


Figure 4.66: First order tool life contours at 35 $\mu$ m doc

Further investigation on productivity was therefore carried out by considering the relationship between cutting parameters and material removal rates. The material removal rate,  $Q$  ( $\text{mm}^3 \text{min}^{-1}$ ) is given by Equation 11:

$$Q = ft \times n \times N_s \times a_a \times a_r \text{ -----Eq. 11}$$

where  $ft$  is the feed per tooth (mm/tooth),  $n$  is the number of cutter flutes,  $N_s$  is the rotational speed of the microtool (rpm),  $a_a$  is the axial depth of cut (mm) and  $a_r$  is the diameter of the microtool (mm). By taking logarithms of each term, Equation 11 can be rewritten as;

$$\ln Q = \ln ft + \ln n + \ln N_s + \ln a_a + \ln a_r \text{ -----Eq. 12}$$

For the specified axial depth of cut of  $35\mu\text{m}$  in a slot milling operation using a 4 flute, 0.5mm diameter end mill, and by employing the transformation functions in Equation 4 and Equation 5, thus, Equation 12 becomes;

$$\ln Q = 0.5019 + 0.447x_1 + 0.357x_2 \text{ -----Eq. 13}$$

For a given rate of material removal, Equation 13 can be represented by a straight lines which can then be superimposed onto the cutting speed – feed per tooth response surface plot shown previously in Figure 4.66. This can then be used to maximise tool life for a required/desired material metal removal rate (MRR). An example is detailed in Figure 4.67 where the operating parameters at both point A and B, produce equivalent MRR is  $1.5 \text{ mm}^3/\text{min}$ , but with the latter giving a 22.2% higher tool life.

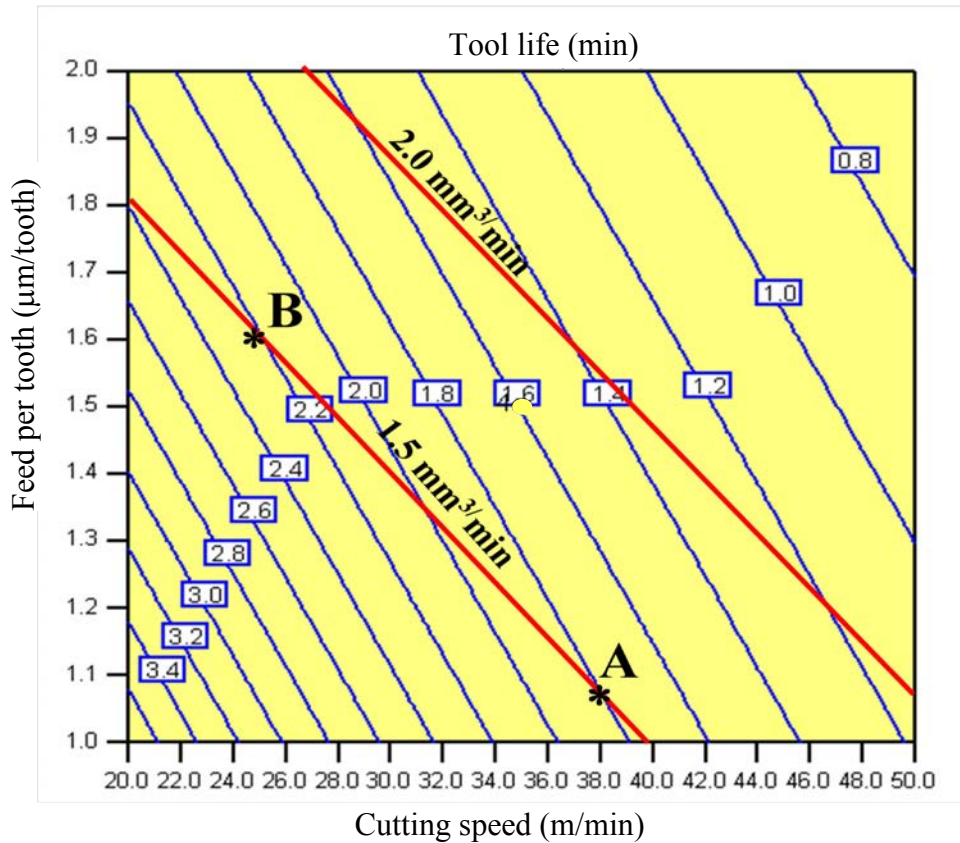


Figure 4.67: First order tool life contours and material removal rates

### 4.5.3 Second order model of tool life

A second-order relationship was considered to improve the correlation and hence accuracy of the predicted tool life with respect to the independent variables investigated. The model was developed utilising the CCD array ( $L_{18}$ ) as detailed in Section 3.4.5. The coefficients of the quadratic model were derived using the least squares method. Following the regression analysis, the second-order tool life equation in coded form can be expressed as;

$$\hat{y} = 0.5866 - 0.4660x_1 - 0.2737x_2 - 0.2571x_3 - 0.1062x_1^2 - 0.0875x_2^2 + 0.0708x_3^2 + 0.0874x_1x_2 + 0.0194x_1x_3 - 0.0913x_2x_3 \quad \text{-----Eq. 14}$$

Here, the sign of the coefficients indicates the positive or negative influence of the respective input variables on tool life. However the identification of the specific effect/importance of individual input variables is complicated by their interaction ( $x_1x_2$ ,  $x_1x_3$ ,  $x_2x_3$ ) and quadratic terms ( $x_1^2$ ,  $x_2^2$ ,  $x_3^2$ ). Therefore, only significant terms (at the 5% level) were considered in developing the second order tool life model.

Table 4.8 shows the percentage error of the predicted tool life using the various models (linear, analytical and quadratic) compared to the experimental data. It was found that the predicted tool life values (calculated using Design Expert simulation, see Appendix E) obtained with the first order linear model showed close agreement to experimental data with percentage errors ranging between  $\pm 3\%$ . Conversely, tool life predicted by the mathematical/analytical model detailed in Equation 10, highlighted relatively large deviations of between  $-21\%$  and  $20\%$ . This was likely due to the fact that only the main variable parameters (cutting speed, feed rate & depth of cut) were considered, with interactions between factors neglected. Predictions using the second order quadratic model were shown to be similar to first order relationship with percentage errors within  $\pm 4\%$  of the respective experimental values. A graphical comparison of predicted tool lives using the various analytical models versus the experimental results is shown in Figure 4.68.

Table 4.8: Percentage error of the tool life models

		Tool life model					
		First order model & predicted value				Second order model – predicted value	
	Experimental value (min)	Linear model (Eq. 8)	% error	Analytical (Eq. 10)	% error	Quadratic model (Eq.14)	% error
Test 1	4.71	4.77	-1%	4.81	-2%	4.60	2%
Test 2	1.42	1.40	1%	1.68	-15%	1.42	0%
Test 3	2.77	2.73	1%	2.75	1%	2.66	4%
Test 4	1.15	1.17	-1%	0.96	20%	1.19	-4%
Test 5	3.14	3.10	1%	2.65	18%	3.12	1%
Test 6	0.95	0.96	-1%	0.93	2%	0.96	-2%
Test 7	1.19	1.21	-1%	1.51	-21%	1.22	-3%
Test 8	0.55	0.54	1%	0.53	4%	0.55	0%
Test 9	1.80	1.75	3%	1.56	15%	1.75	3%
Test 10	1.70	1.75	-3%	1.56	9%	1.75	-3%
Test 11	1.70	1.75	-3%	1.56	9%	1.75	-3%
Test 12	1.80	1.75	3%	1.56	15%	1.75	3%
Test 13	3.03					3.11	-3%
Test 14	0.61					0.59	3%
Test 15	2.22					2.24	-1%
Test 16	0.89					0.88	1%
Test 17	3.48					3.53	-2%
Test 18	1.35					1.33	2%

\*Refer Table 3.6 for test parameter

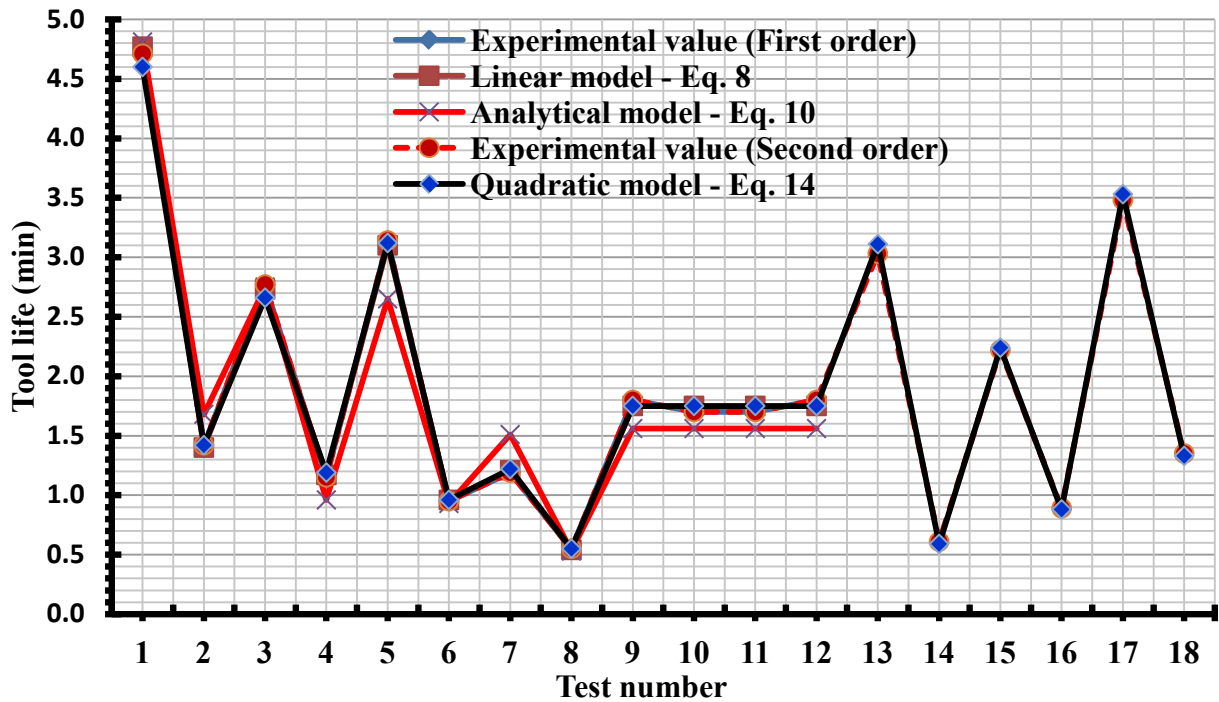


Figure 4.68: Comparison between experimental and predicted values for tool life

#### 4.5.3.1 Adequacy of the quadratic model

Summary statistics of the various R-Squared measures (R-Squared, Adjusted R-Squared and Predicted R-Squared) from the different possible tool life models which can be generated from the L<sub>18</sub> design/array (performed using Design Expert), are shown in Table 4.9. This was used to identify the best model for use in future analysis/predictions. A cubic relationship was initially considered in the assessment however aliasing (confounding) between the factors/interactions was found to be significant and was thus disregarded. The results showed that the quadratic model was preferred based on the larger R-Squared value (0.9985) obtained, which suggests that 99.85% of the total variations are explained by the model. The Adjusted R-Squared is a modified R-Squared value which considers the size of the model as a result of the number of variables/terms considered (always smaller or equal to R-Squared). Correspondingly, the value of the Adjusted R-Squared (0.9968) indicates that 99.68% of the total variability is accounted for by the model after considering the significant factors. Similarly, the Predicted R-Squared value of 0.9916 (which is in close agreement with the Adjusted R-Squared term) implies that 99.16% of any variability when introducing new/future data would be covered in the model. Here, a value of 0.8 or higher is generally considered to be of an acceptable level.

Table 4.10 shows the ANOVA calculations for tool life based on the ‘recommended’ quadratic model, but which only takes into account statistically significant factors and interactions. It was found that all variable factors and interactions considered were found to be significant at the 5% level, except for the interaction between cutting speed and depth of cut (AC). This was therefore removed from the calculations which resulted in a marginally higher Predicted R-Squared value compared to that detailed in Table 4.9 (0.99266 vs. 0.99166)

Table 4.9: Summary statistics of the tool life models (based on L<sub>18</sub> array)

Model	Std. Dev.	R-Squared	Adjusted R-Squared	Predicted R-Squared	Remarks
Linear	0.17943	0.92481	0.9087	0.86279	
Interaction	0.1665	0.94913	0.92138	0.90133	
<b>Quadratic</b>	<b>0.03317</b>	<b>0.99853</b>	<b>0.99688</b>	<b>0.99166</b>	<b>Recommended</b>

Table 4.10: ANOVA results for tool life of quadratic model (L<sub>18</sub>)

Factor	Sum of Squares	DF	Mean of Squares	F Value	Prob > F	PCR
Cutting speed (A)	3.32744	1	3.32744	2897.31	< 0.0001*	56%
Feed per tooth (B)	1.055	1	1.055	918.618	< 0.0001*	18%
Depth of cut (C)	1.16131	1	1.16131	1011.19	< 0.0001*	19%
A <sup>2</sup>	0.10171	1	0.10171	88.5658	< 0.0001*	2%
B <sup>2</sup>	0.07672	1	0.07672	66.804	< 0.0001*	1%
C <sup>2</sup>	0.0716	1	0.0716	62.3464	< 0.0001*	1%
AB	0.06913	1	0.06913	60.1945	< 0.0001*	1%
BC	0.07509	1	0.07509	65.386	< 0.0001*	1%
Residual	0.01034	9	0.00115			
Lack of Fit	0.00707	6	0.00118	1.08186	0.5159	Not significant
Pure error	0.00327	3	0.00109			
Total	5.99446	17	*Significant at 5% level			
Std. Dev	0.03389			R-Squared	0.99828	
Mean	0.48929			Adjusted R-Squared	0.99674	
C.V	6.92615			Predicted R-Squared	0.99266	

#### 4.5.3.2 Utilisation of the second order tool life model

As with the first order relationship, Equation 14 comprising significant terms was plotted in the form of response surfaces for tool life at a depth of cut of 35 $\mu$ m as shown in Figure 4.69. By overlaying specific MRR values calculated using Equation 11 onto Figure 4.69, the best combination of operating parameters can be selected which optimises productivity without decreasing the tool life. As an example, the 3 points (A, B & C) highlighted in Figure 4.69 are all predicted to provide a tool life of 1 minute but with A giving a lower MRR of 1.5mm<sup>3</sup>/min. While the parameters at both points B and C gave equivalent MRR's (2.0mm<sup>3</sup>/min), the latter was preferred due to the superior surface finish obtained as a result of the lower feed rate.

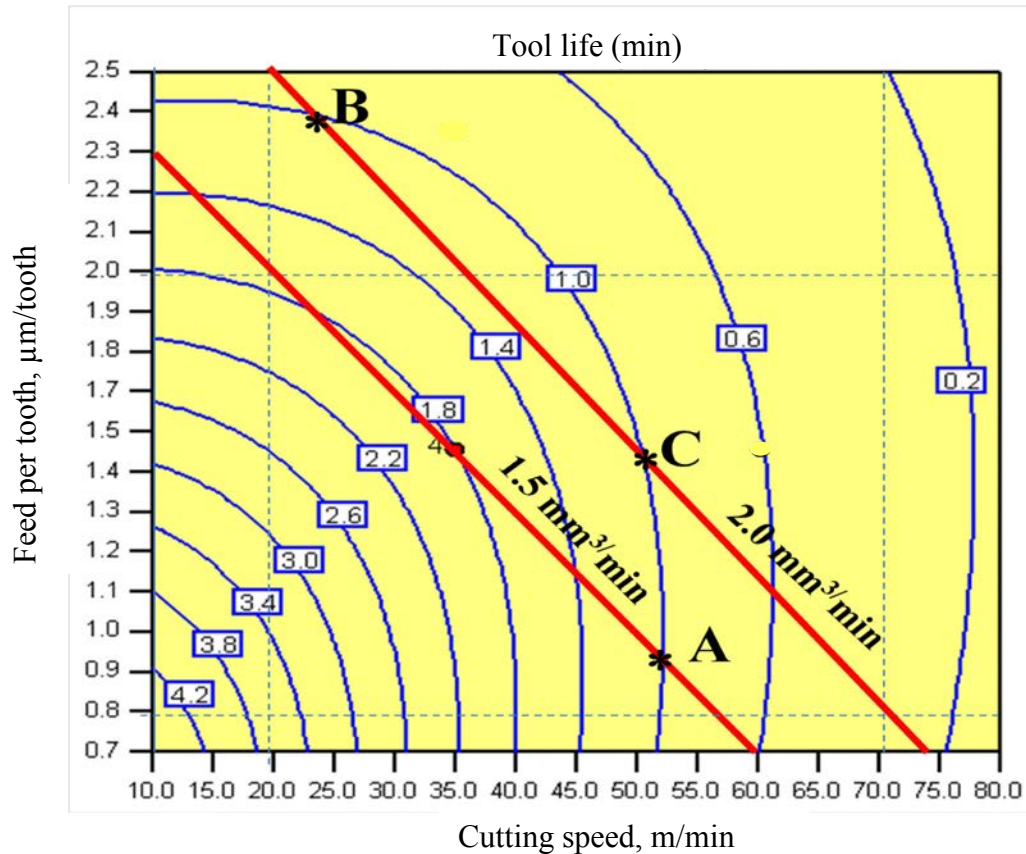


Figure 4.69: Second order tool life contours and material removal rates

#### 4.5.4 First order model of surface roughness

Table 4.11 shows ANOVA results for surface roughness based on a linear model with the estimated effects of each parameter, along with their interactions and standard error. All main factors and their interactions were found to have a significant effect on resulting surface roughness, despite the interactions between cutting speed  $\times$  feed per tooth and cutting speed  $\times$  depth of cut having very low percentage contributions of 2% and 0.3% respectively. The influence of all 3 primary variables exceeded 20% with cutting speed showing the highest PCR at 33%.

Table 4.11: Linear model ANOVA results for surface roughness (based on L<sub>12</sub>)

Factor	Sum of Squares	DF	Mean of Squares	F Value	Prob > F	PCR
Cutting Speed (A)	0.15479	1	0.154797	572.9352	< 0.0001*	33%
Feed per tooth (B)	0.10953	1	0.109532	405.4005	< 0.0001*	23%
Depth of cut (C)	0.09689	1	0.096893	358.6187	< 0.0001*	21%
AB	0.00887	1	0.008876	32.85111	0.0046*	2%
AC	0.00231	1	0.002318	8.578231	0.0429*	0.3%
BC	0.07783	1	0.077835	288.0822	< 0.0001*	17%
Curvature	0.01351	1	0.013516	50.02606	0.0021	Significant
Residual	0.00108	4	0.00027			
Lack of Fit	0.00078	1	0.000788	8.069874	0.0656	Not significant
Pure error	0.00029	3	9.76E-05			
Total	0.46484	11			*Significant at 5% level	
Std. Dev	0.016437			R-Squared	0.997605	
Mean	-1.47583			Adjusted R-Squared	0.994014	
C.V	-1.11376			Predicted R-Squared	0.890409	

From the regression analysis, the predicted first-order surface roughness model based on the first 12 experiments in coded form is shown in Equation 15;

$$\hat{y} = -1.452 - 0.139x_1 + 0.117x_2 + 0.110x_3 \text{ -----Eq. 15}$$

The analytical relationship to describe workpiece surface roughness (Ra) as a function of the cutting speed,  $V_c$ , (m/min), feed per tooth,  $ft$ , ( $\mu\text{m}/\text{tooth}$ ) and depth of cut,  $d$ , ( $\mu\text{m}$ ) was then obtained by substituting Equations 4 - 6 (Section 3.4.5) into Equation 15. The model can therefore be expressed as;

$$\ln(\text{Ra}) = -1.061 - 0.312 \ln V + 0.328 \ln f + 0.172 \ln d \text{ -----Eq.16}$$

and by taking inverse logarithms,

$$\text{Ra} = 0.346 V_c^{-0.312} ft^{0.328} d^{0.172} \text{ -----Eq. 17}$$

From the mathematical function in Equation 17, surface roughness improves with higher cutting speeds but deteriorates as the feed per tooth and depth of cut are similarly increased. This corresponds to the results detailed in Section 4.4.2.

#### 4.5.4.1 Adequacy of the linear model

Table 4.11 shows that the linear regression model correlates well to the experimental data, with only a 0.01% probability that the results were due to noise or random events. As with the tool life response, curvature was found to be significant from the ANOVA calculations, which points to the presence of non-linearity within the model. Additional tests were therefore performed to expand the experimental design (6 additional axial points) to account for the non-linear elements and formulate a second order surface roughness predictive equation, which is further detailed later in Section 4.5.5.

#### 4.5.4.2 Utilisation of the first order surface roughness model

Figure 4.70 details the response surfaces based on Equation 15 for surface roughness at an axial depth of cut of 35  $\mu\text{m}$ . Material removal rate calculations as described in Section 4.5.2.2, can be employed in conjunction with the contour plot to determine preferred operating parameters to achieve a specific surface roughness while maximising productivity.

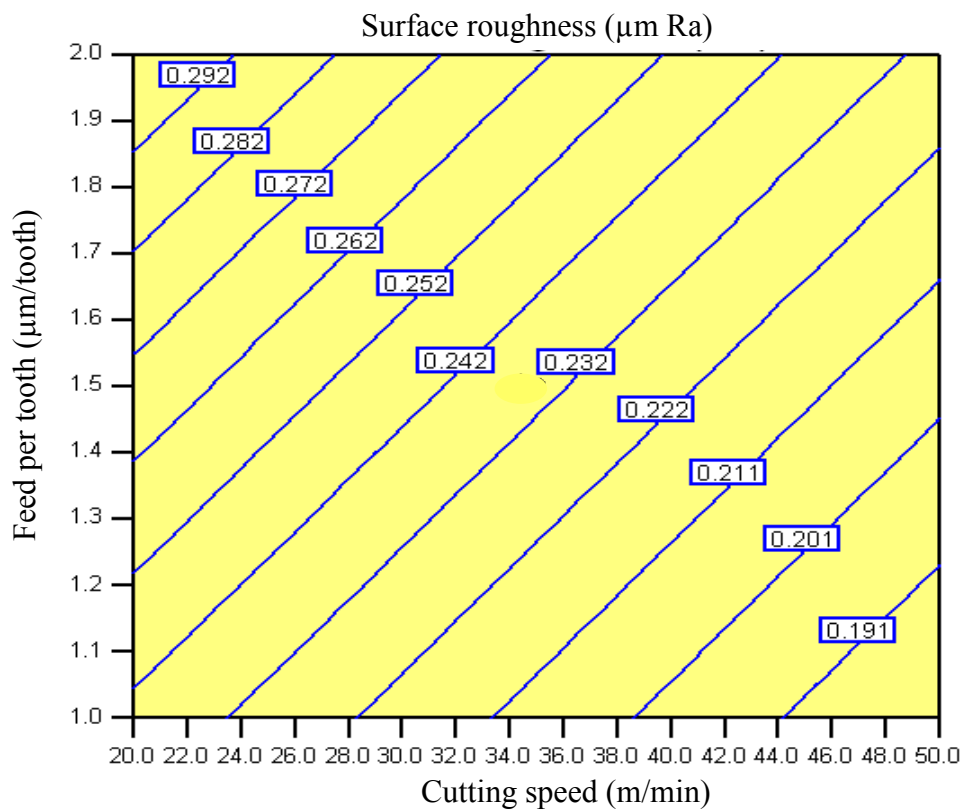


Figure 4.70: First order surface roughness contours at 35 $\mu\text{m}$  depth of cut.

Lines representing different values of MRR ( $Q$ ) were calculated using Equation 11 and superimposed over the first order surface roughness contour plot, detailed in Figure 4.70 in order to identify the best combination of cutting speed and feed rate (within the boundaries of the experimental tests) to obtain the lowest possible surface roughness for a given metal removal rate. Figure 4.71 shows an example where the operating conditions at point A and B both result in a MRR of  $1.5\text{mm}^3/\text{min}$ , but the former (cutting speed  $40\text{m}/\text{min}$ , feed per tooth  $1.05\mu\text{m}/\text{tooth}$  and depth of cut  $35\mu\text{m}$ ) is recommended due to the lower/superior surface roughness predicted ( $0.2\mu\text{m}$  vs.  $0.28\mu\text{m}$  Ra).

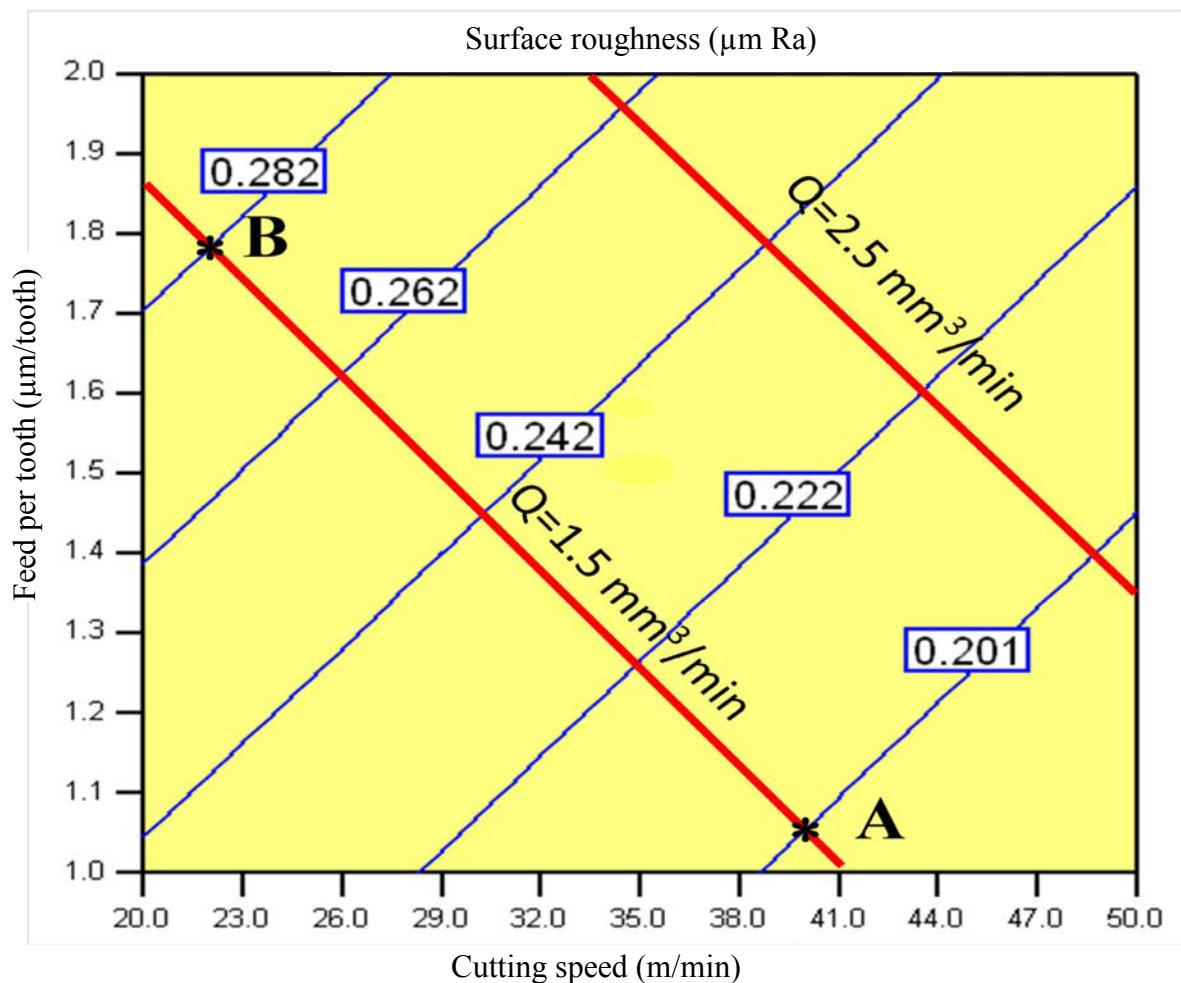


Figure 4.71: First order surface roughness contours and material removal rates

#### 4.5.5 Second order model of surface roughness

A second-order model was developed to extend the variable range as well as to account for non-linearity between workpiece surface roughness and the independent variables investigated. Based on the techniques adopted in Section 4.5.3 with regard to tool life assessment, the predicted second-order surface roughness model in a coded form can be written as;

$$\hat{y} = -1.526 - 0.125x_1 + 0.1159x_2 - 0.1038x_3 - 0.0374x_1^2 - 0.0116x_2^2 + 0.0458x_3^2 - 0.0333x_1x_2 + 0.0170x_1x_3 - 0.0986x_2x_3 \quad \text{-----Eq. 18}$$

As outlined previously, the sign of the coefficients show the positive or negative effect of the input variable on surface roughness. While the influence of input parameters are complicated by their interaction and quadratic terms, only statistically significant main factors and interactions were considered in developing the second order model for surface roughness.

Table 4.12 details the percentage error of the predicted surface roughness using the various models (linear, analytical and quadratic) compared to the experimental data. It was observed that the predicted values using the first order model closely matched the experimental results with errors of  $\pm 1\%$ . However for the mathematical model, errors of between  $-12\%$  to  $16\%$  was observed. This was mainly because the interactions between factors were neglected, particularly where the interaction of feed per tooth and depth of cut was significant with a relatively high PCR of  $17\%$  (detailed in Table 4.11). The errors recorded for the second order relationship with respect to the experimental results were also relatively low, ranging from  $-4\%$  to  $3\%$ . Figure 4.72 shows a comparison of the predicted and experimental surface roughness values. Here, the general trend in Ra variation appeared to be well described by both the linear and quadratic models.

Table 4.12: Percentage error of the surface roughness models

Surface roughness model							
Experimental value ( $\mu\text{m}$ )	First order model & predicted value				Second order model-predicted value		
	Linear model (Eq. 15)	% error	Analytical (Eq. 17)	% error	Quadratic model (Eq.18)	% error	
Test 1	0.1930	0.1911	1%	0.2167	-11%	0.1894	2%
Test 2	0.1480	0.1495	-1%	0.1628	-9%	0.1524	-3%
Test 3	0.3113	0.3144	-1%	0.2720	14%	0.3110	0%
Test 4	0.2174	0.2153	1%	0.2044	6%	0.2190	-1%
Test 5	0.2776	0.2804	-1%	0.2709	2%	0.2745	1%
Test 6	0.2371	0.2348	1%	0.2036	16%	0.2364	0%
Test 7	0.3140	0.3109	1%	0.3401	-8%	0.3037	3%
Test 8	0.2256	0.2278	-1%	0.2556	-12%	0.2289	-1%
Test 9	0.2180	0.2180	0%	0.2341	-7%	0.2174	0%
Test 10	0.2150	0.2180	0%	0.2341	-7%	0.2174	-1%
Test 11	0.2160	0.2180	-1%	0.2341	-8%	0.2174	-1%
Test 12	0.2210	0.2180	1%	0.2341	-6%	0.2174	2%
Test 13	0.2877					0.2983	-4%
Test 14	0.2019					0.1959	3%
Test 15	0.1731					0.1732	0%
Test 16	0.2543					0.2557	-1%
Test 17	0.2103					0.2079	1%
Test 18	0.2896					0.2947	-2%

\*Refer to Table 3.6 for test parameters

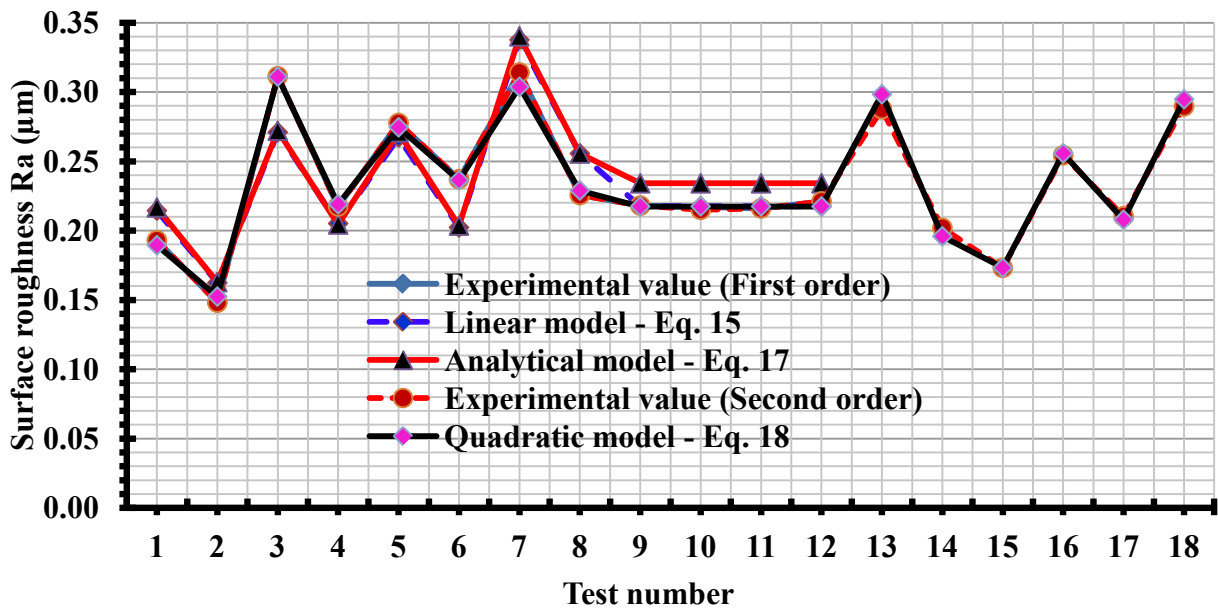


Figure 4.72: Comparison between experiment results, mathematical equation, prediction first and second order model for surface roughness

#### 4.5.5.1 Adequacy of the quadratic model

Following augmentation of the experimental design with 6 axial points, summary statistics of the various/possible models (based on  $L_{18}$  design) are shown in Table 4.13. The quadratic model was found to be the best model for predicting surface roughness due to the larger R-Squared value (0.9914).

Table 4.14 shows the ANOVA results for surface roughness based on the quadratic model. All main factors, their quadratic terms and interactions between the primary variables were found to be significant at the 95% confidence interval, with the exception of  $B^2$  and AC. The value of the Adjusted R-Squared (0.9817) indicates that 98.17% of the total variability is accounted for by the model after considering the significant factors, with reasonably good agreement found when compared against the Predicted R-Squared calculation of 0.9366 (model will accommodate for 93.66% of the variability when used with new data).

Table 4.13: Summary statistics of surface roughness models

Model	Std. Dev.	R-Squared	Adjusted R-Squared	Predicted R-Squared	Remarks
Linear	0.10	0.7943	0.7503	0.6256	
Interaction	0.069	0.9243	0.8829	0.8208	
<b>Quadratic</b>	<b>0.027</b>	<b>0.9914</b>	<b>0.9817</b>	<b>0.9366</b>	<b>Recommended</b>

Table 4.14: ANOVA results for surface roughness of quadratic model

Factor	Sum of Squares	DF	Mean of Squares	F Value	Prob > F	PCR
Cutting speed (A)	0.213585	1	0.213585	289.9064	< 0.0001*	31%
Feed per tooth (B)	0.1835	1	0.1835	249.0711	< 0.0001*	27%
Depth of cut (C)	0.147274	1	0.147274	199.9004	< 0.0001*	21%
$A^2$	0.017729	1	0.017729	24.06467	0.0012*	2%
$B^2$	0.001694	1	0.001694	2.299501	0.1679	0%
$C^2$	0.026548	1	0.026548	36.03511	0.0003*	4%
AB	0.008876	1	0.008876	12.04744	0.0084*	1%
AC	0.002318	1	0.002318	3.145882	0.1140	0%
BC	0.077835	1	0.077835	105.648	< 0.0001*	11%
Residual	0.001289	8	0.000737			
Lack of Fit	0.005452	5	0.00109	7.407119	0.0650	Not significant
Pure error	0.000442	3	0.000147			
Total	0.680648	17				
				*Significant at 5% level		
Std. Dev	0.027143			R-Squared	0.9914	
Mean	-1.47148			Adjusted R-Squared	0.981724	
C.V	-1.8446			Predicted R-Squared	0.936591	

#### 4.5.5.2 Utilisation of the second order surface roughness model

Figure 4.73 details a contour plot of the predicted surface roughness when using the second order model (Equation 18) at a depth of cut of  $35\mu\text{m}$  and which is overlaid with lines corresponding to MRR's of  $1.0$  and  $2.0\text{mm}^3/\text{min}$  respectively. Here, operating parameters can be selected to increase productivity without sacrificing surface roughness/quality. In Figure 4.73, the parameters at both point A and B are predicted to produce surfaces with identical roughness values of  $0.2\mu\text{m Ra}$ , however with the former resulting in a two fold increase in material removal rate.

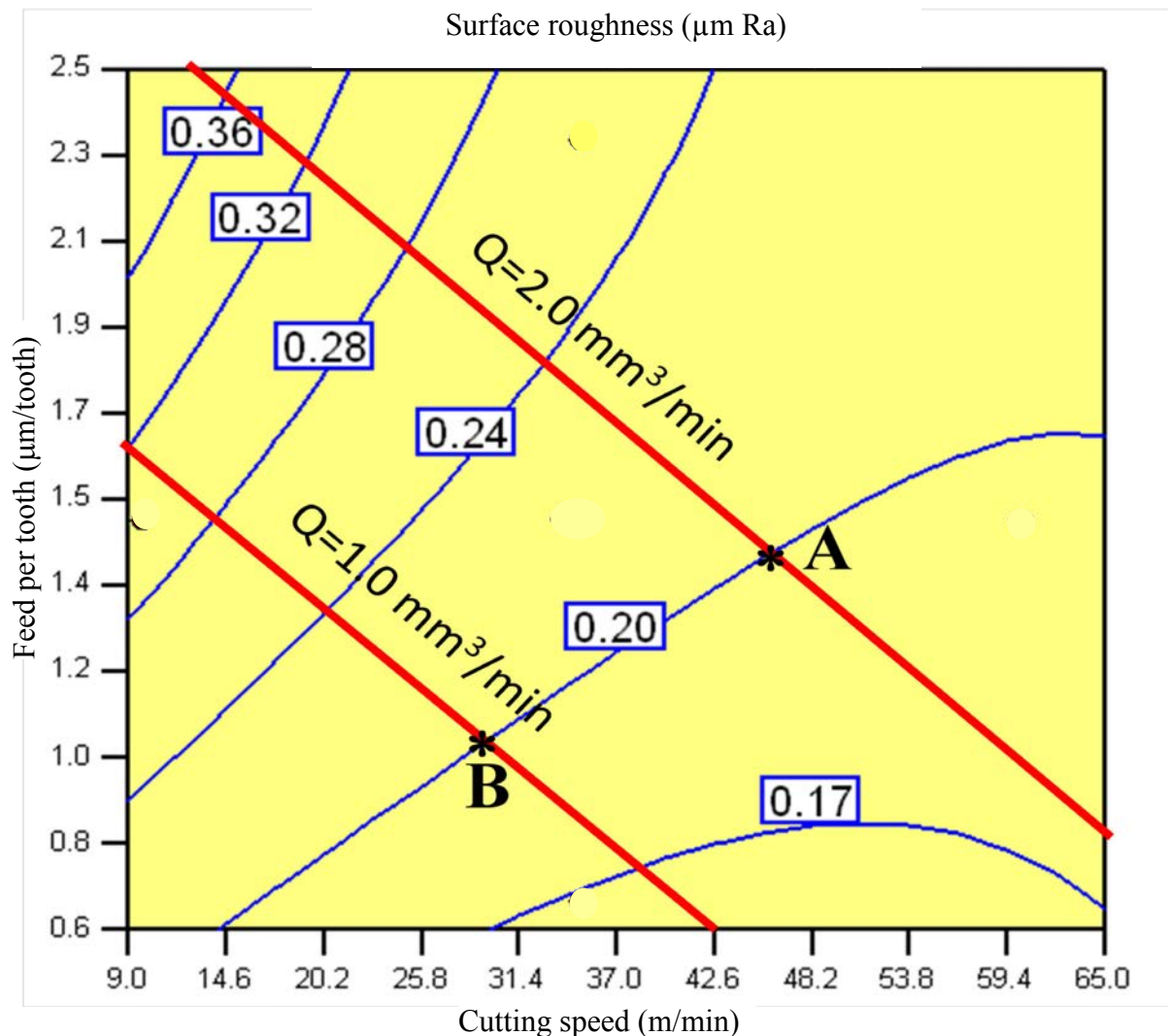


Figure 4.73: Second order surface roughness contours and material removal rates

## **4.6 Phase 5: Effect of tool coating and geometry on tool life and surface roughness**

### **4.6.1 Influence of tool coating**

#### **4.6.1.1 Tool wear progression**

Both uncoated and coated tools in the new and worn condition were examined under the SEM in order to study the wear progression and corresponding failure mechanisms. The micro slotting trials were all conducted at a cutting speed of 50m/min, a feed per tooth of 1 $\mu$ m/tooth and depth of cut of 55 $\mu$ m.

Micrographs showing the rake, flank and end flute face of a new uncoated microtool and following various cut lengths of 20mm, 60mm and 160mm respectively, are presented in Figure 4.74. Rounding/fracture of the cutting edge corner together with damage of the chip breaker feature was evident after only the first slot (20mm cut length). This was primarily due to the intermittent/cyclic forces acting on the tool as it repeatedly entered and exited the workpiece. Limited amounts of workpiece material adhering to the end mill were also observed. As machining progressed, tool wear increased gradually via abrasion up to a cut length of ~80mm, although the cutter was also prone to high levels of smeared/adhered material, particularly on the rake face as shown in Figure 4.74(j-l), prior to tool breakage at 180mm cut length (9 slots). The large concentration of deposited material on the rake face led to ‘clogging’ as well as greater resistance to chip evacuation along the tool helix, resulting in higher levels of forces/stress on the microtool. The ‘trapped’ material/chips were either pressed between the tool and workpiece thus increasing the amount of material stuck to the tool (similar to a pressure welding action), or forced to flow round the cutting edge and therefore cause abrasive wear, which was confirmed by the scratches shown in Figure 4.74(j).

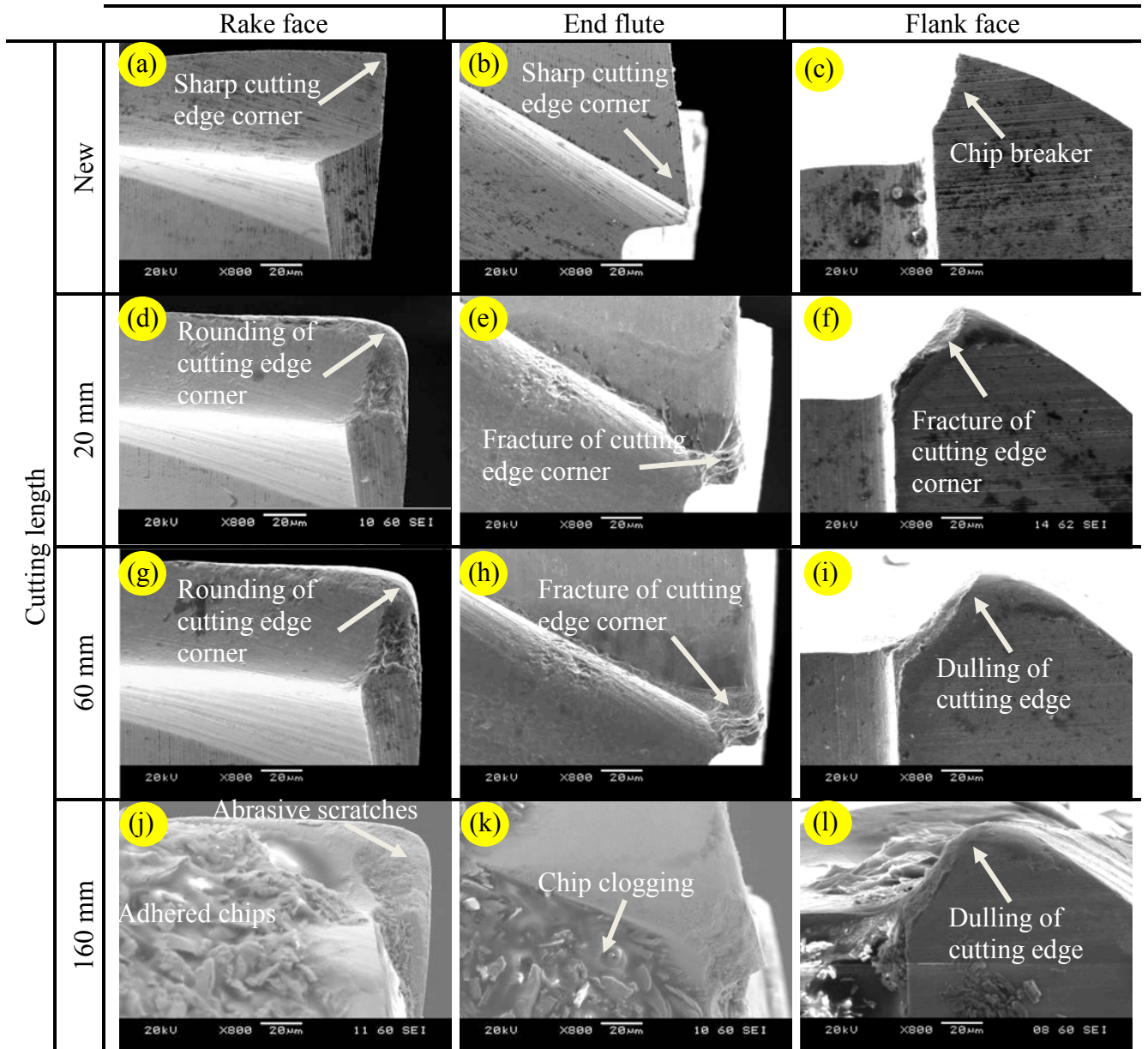


Figure 4.74: SEM micrographs of uncoated tool wear progression.

SEM micrographs viewed at the rake face, flank face and end flute of an equivalent coated microtool when new and after cut lengths of 100mm, 200mm, 300mm, 400mm and 500mm respectively are detailed in Figure 4.75. Fracture and rounding of the cutting edge was observed as with the uncoated tools, as early as the first slot. Unlike the uncoated cutters however, there was coating delamination/peeling due to abrasion from the workpiece material. The regions where the underlying carbide substrate had been exposed were subsequently seen to experience greater wear. Significantly reduced adhered material was seen on the coated tool surfaces however, with no obvious chips sticking to the rake face.

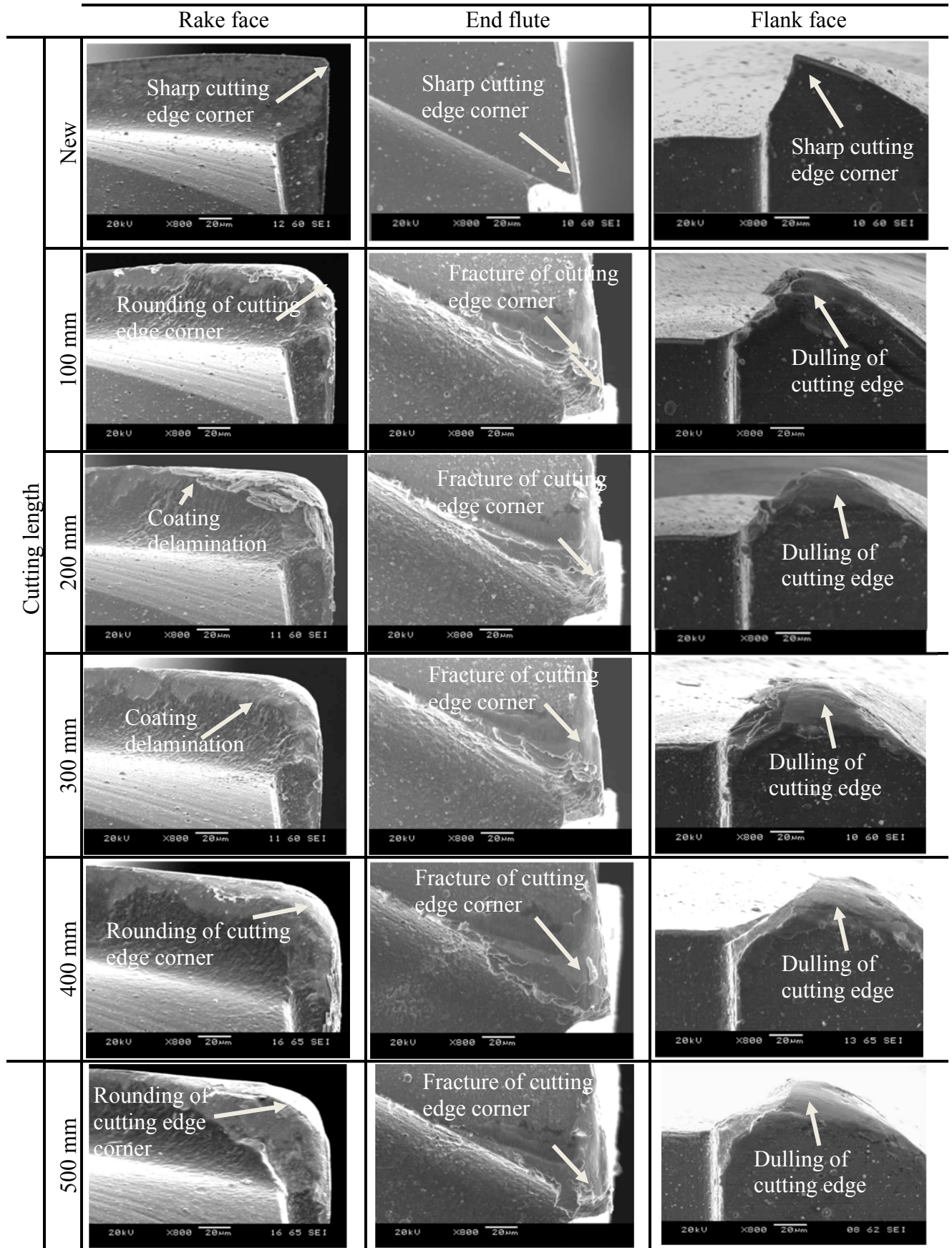


Figure 4.75: SEM micrographs of coated tool with chip breaker wear progression.

The reduction in tool diameter versus cut length (measured in the same way as in Phase 3 work) for both the uncoated and coated tools are illustrated Figure 4.76. In general, the wear progression of the coated cutter was in accordance with the trend described in Section 4.3.1. At the initial stage of machining, the rate of tool diameter reduction with the uncoated end mill was marginally higher in comparison to the coated version. This was most likely due to the greater wear resistance afforded by the coating and the varying degree of tool sharpness, where the measured cutting edge radius for uncoated and coated cutters was  $2.4\mu\text{m}$  and  $3.6\mu\text{m}$  respectively, see Figure 4.77.

The uncoated end mill failed/broke after a cut length of only 180mm ( $\sim 9$  slots) which was over ten times less than its coated counterpart, which had a tool life of 2040mm. This corresponded to results reported by Mativenga et al. [174] when micromilling AISI H13 using uncoated and coated (TiN) tools, the latter tooling showing nearly a 6 fold (580%) increase in tool life over the former. Apart from its superior hardness, the coating was also thought to decrease friction at the tool-chip interface and reduce the tendency for workpiece material sticking to the tool [206]. Indeed, no significant adhered material/chips were visible on the rake face of the coated end mill at the cutting parameters employed.

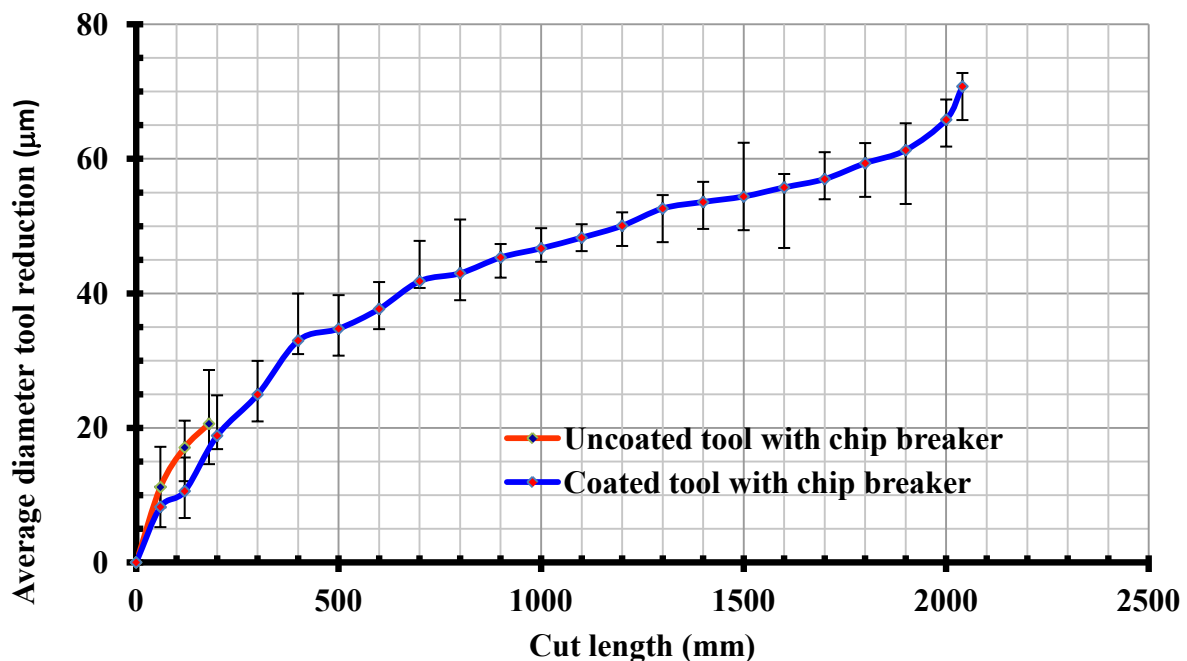


Figure 4.76: Tool wear progression versus cutting length for uncoated and coated tools ( $V_c=50$  m/min,  $f_t=1$   $\mu\text{m}/\text{tooth}$ ,  $a_p=55$   $\mu\text{m}$ )

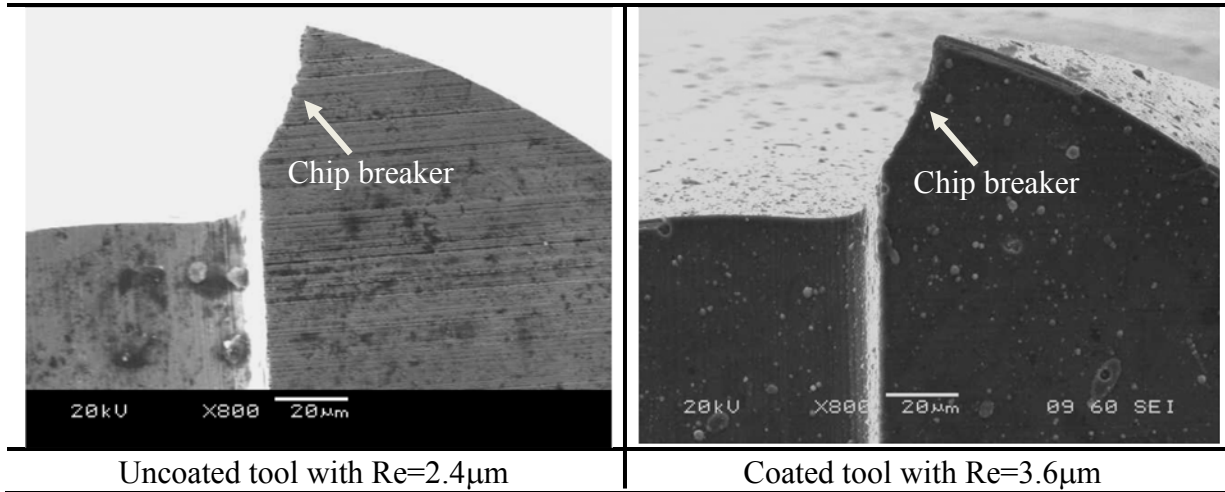


Figure 4.77: Uncoated and coated microtool with cutting edge radius

Figure 4.78 shows the average cutting forces recorded when machining the first slot using uncoated and coated tools. In general, the force components when utilising the coated tool were up to ~40% lower than the uncoated end mill. This is due to the positive effects (lower coefficient of friction, greater wear resistance etc.) of the coating in reducing cutting forces [207]. While the magnitude of the individual force components was similar when using the coated tool, the feed force ( $F_x$ ) was the largest when operating with the uncoated cutter. The resultant force when utilising the coated and uncoated end mills were 10.2 and 14.8N respectively.

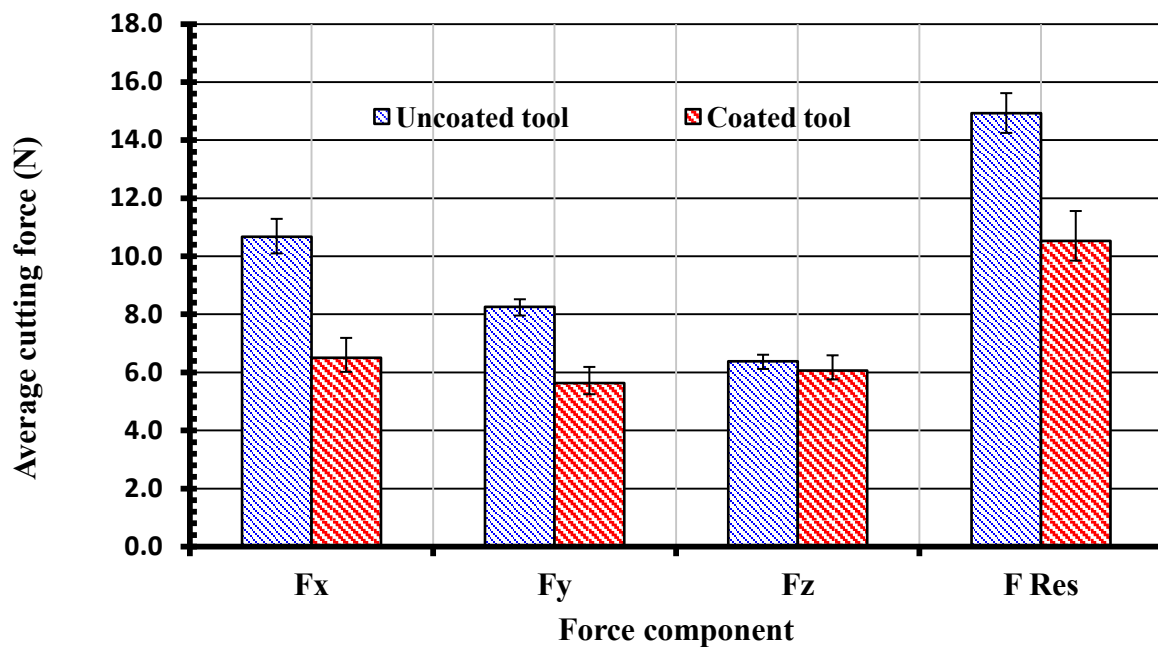


Figure 4.78: Average cutting forces for uncoated and coated tool during Slot 1

The corresponding average force levels at the point prior to tool breakage are detailed in Figure 4.79. While a two-fold increase in force magnitude (all 3 components) was sufficient to initiate catastrophic failure of the uncoated end mill, the coated variant only failed after a significantly longer cut length with recorded forces of up to ~33N ( $F_z$ ). Furthermore, the resultant force with the coated tool was ~60% greater than the uncoated end mill at the point of failure, which was attributed to the higher levels of tool wear in the former.

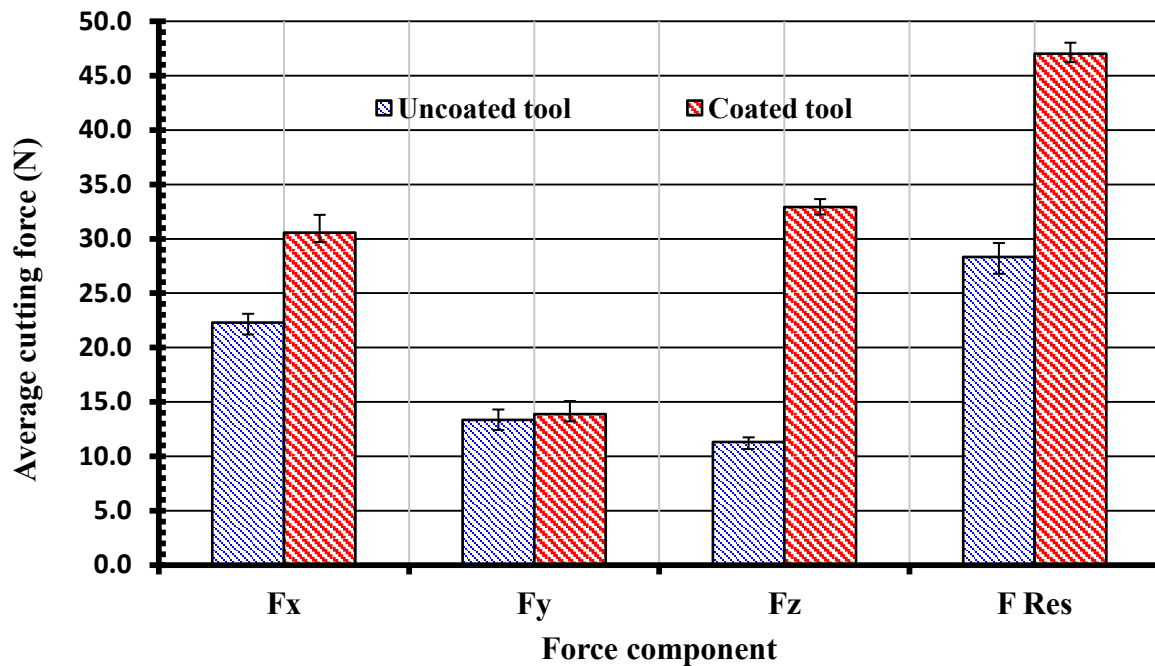


Figure 4.79: Average cutting forces for coated and uncoated tool at the point of tool failure

#### 4.6.1.2 3D surface topography

Figure 4.80 shows 3D surface topography plots taken of the slot base which were machined using uncoated and coated tools following the first and the last slot prior to cutter failure. The workpiece surface roughness obtained was lower using the uncoated tool, which was  $1.3\mu\text{m Sa}$  compared to  $\sim 1.6\mu\text{m Sa}$  with the coated end mill for Slot 1. This was most likely due to the sharper cutting edge present on the uncoated tool (edge radius of  $2.4\mu\text{m}$ ). As cutting length increased, the surface roughness ( $Sa$ ) produced using the uncoated tool increased from  $1.3\mu\text{m}$  to  $1.7\mu\text{m}$  after 9 slots (180mm cut length). Similarly, wear of the coated tool led to a deterioration of the surface roughness from  $1.6\mu\text{m Sa}$  to  $2.3\mu\text{m Sa}$ , albeit after a significantly longer cut length of 2040mm (102 slots).

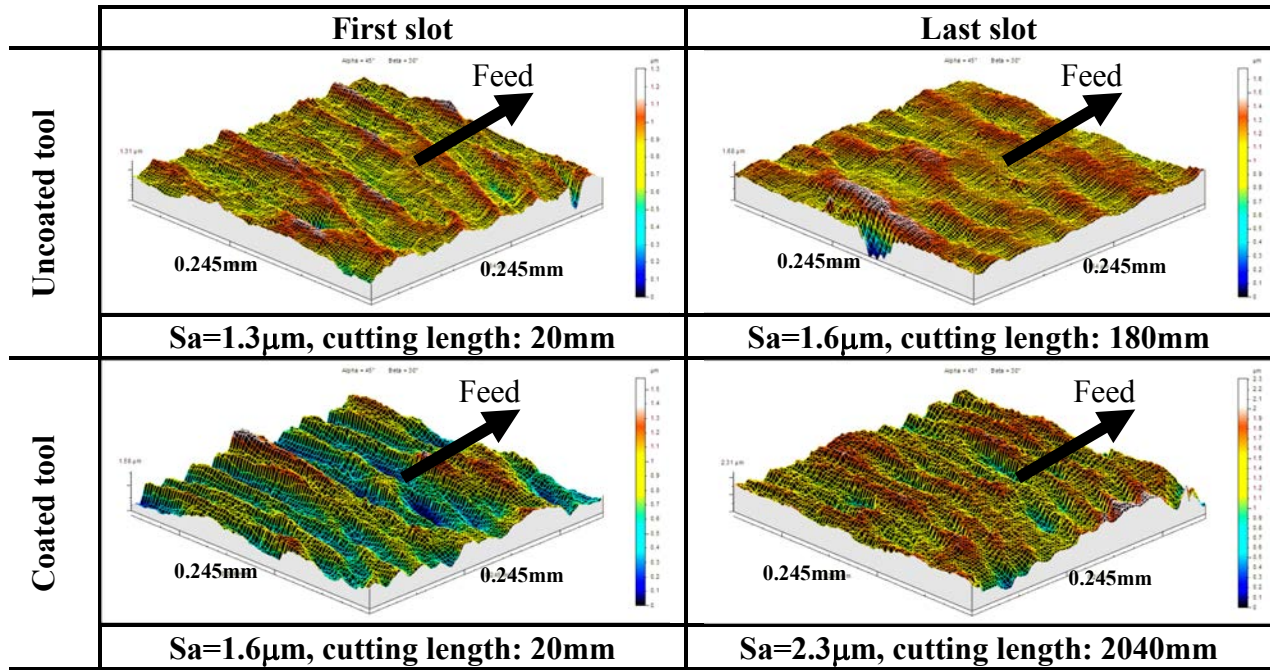


Figure 4.80: 3D surface topography plots when using new and worn tools

## 4.6.2 Effect of tool geometry

### 4.6.2.1 Tool wear progression

Figure 4.81 shows the different coated micro end mills employed with and without chip breaker geometry together with their respective cutting edge radius values. The performance of the latter (without chip breaker) when slotting hardened AISI D2 steel was evaluated and compared against results obtained using a corresponding tool with the chip breaker feature, which was detailed in Section 4.6.1.

The change in tool diameter with respect to cut length is shown in Figure 4.82 for the coated cutters with and without chip breakers. The wear rate of the tool without the chip breaker was up to twice that of the chip breaker end mill, particularly within the first 300mm of cut / initial stage. The level of tool diameter reduction for both cutters was similar during the steady-state region (> 520mm cut length) up to the point of breakage of the end mill with the chip breaker, which occurred after a machined distance of 2040mm.

SEM micrographs of a new coated microtool (without chip breaker) and its condition after cut lengths of 100mm, 200mm, 300mm, 400mm and 500mm respectively, are presented in Figure 4.83. Wear progression was generally in line with trends observed when utilising end mills designed with a chip breaker.

The cutting force levels were comparable during Slot 1, with the exception of the thrust component ( $F_z$ ) where the chip breaker tool was ~35% higher, see Figure 4.84. Despite a ~30% longer tool life when using the standard/plain geometry end mill (2640mm cut length), the force magnitudes recorded for both tools at the end of the tests were essentially the same, see Figure 4.85. This suggests that the chip breaker feature had completely worn away following the initial stage of machining as its influence clearly diminished after a cut length of ~520mm.

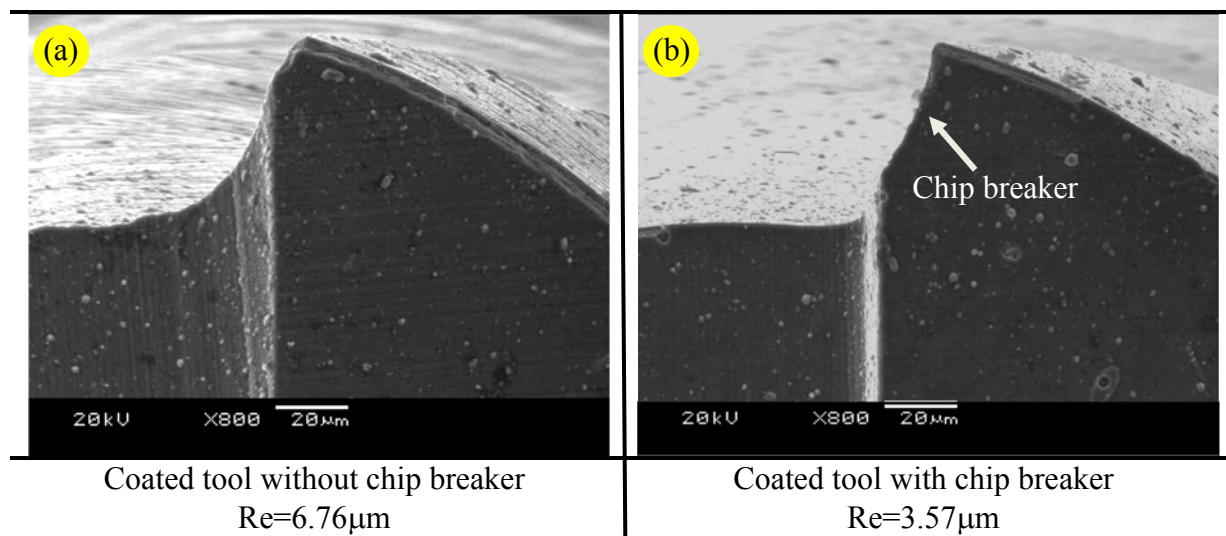


Figure 4.81: Coated micro end mill; (a) without chip breaker (b) with chip breaker

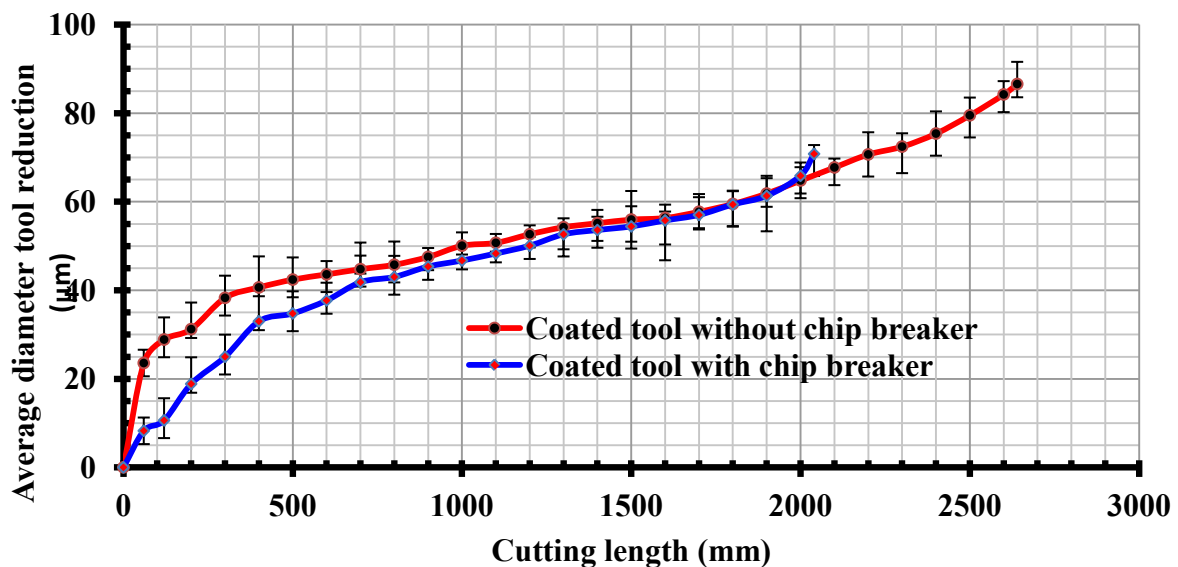


Figure 4.82: Tool wear progression versus cut length for different tool geometry ( $V_c=50m/min$ ,  $f_t=1\mu m/tooth$ ,  $a_p=55\mu m$ )

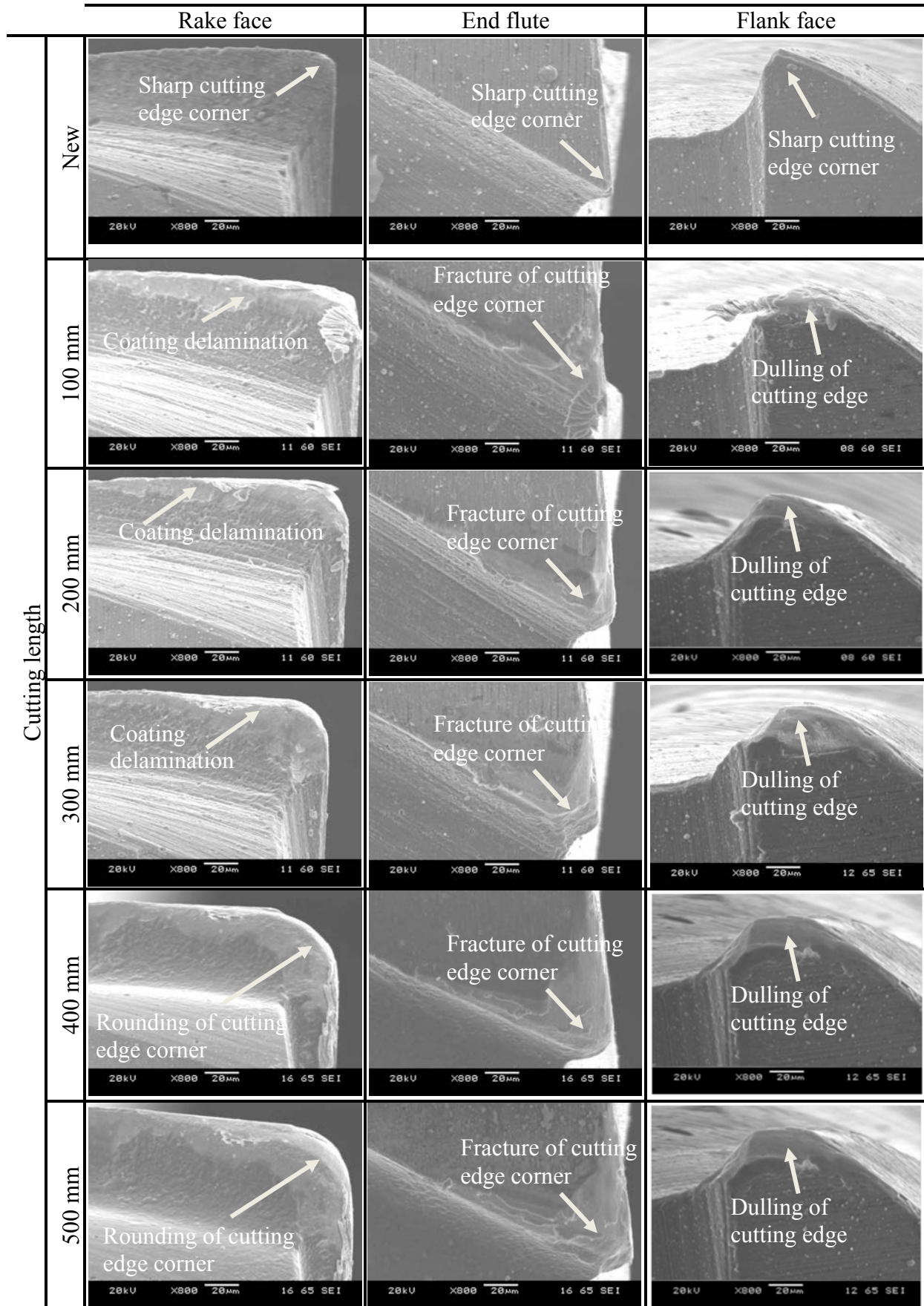


Figure 4.83: Wear progression of the coated tool without chip breaker geometry

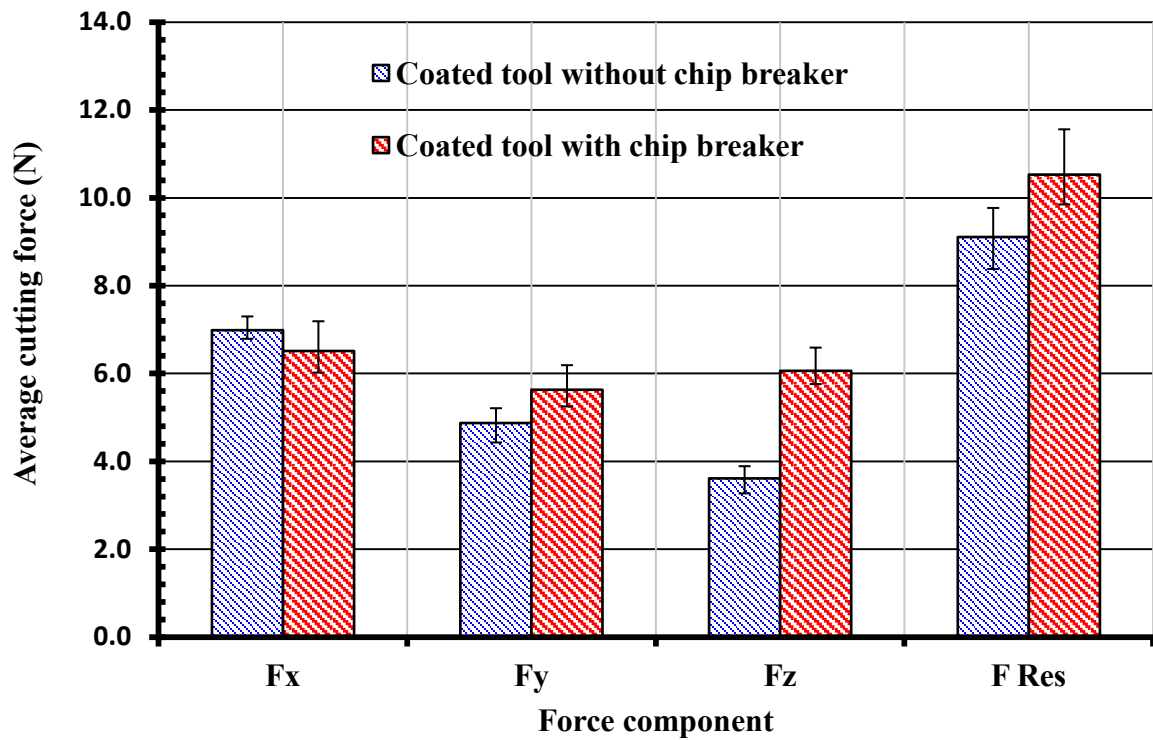


Figure 4.84: Average cutting forces for tools with and without chip breaker during Slot 1

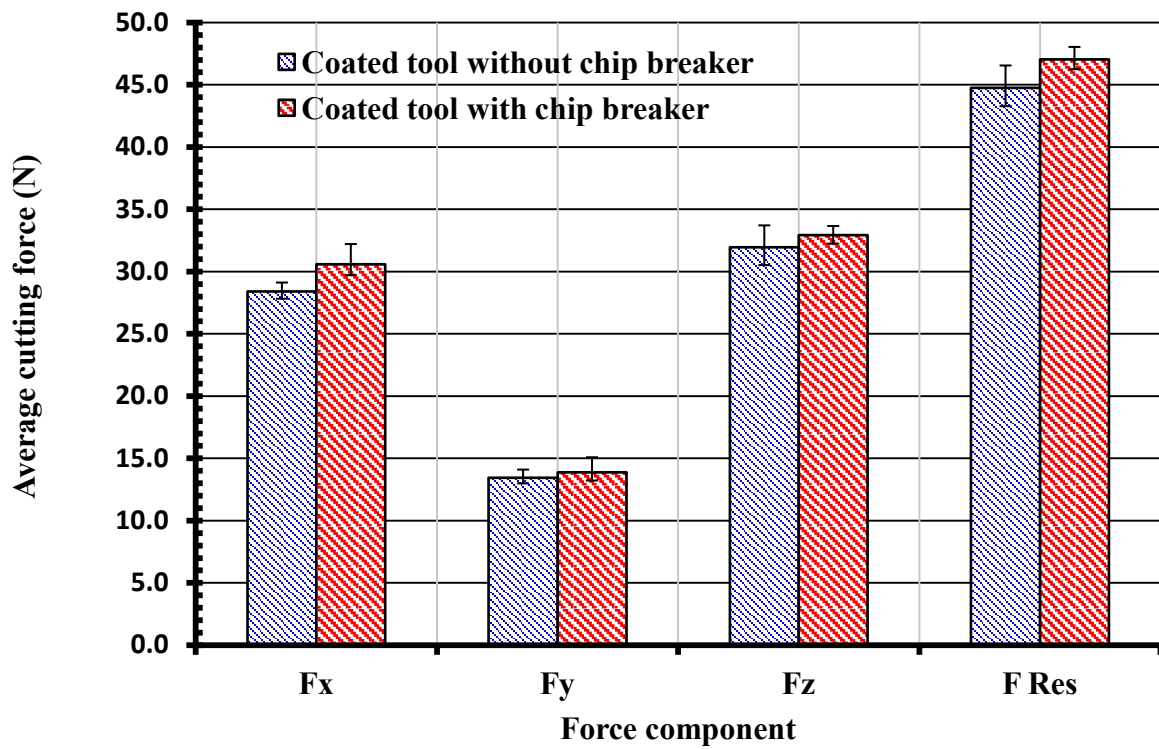


Figure 4.85: Average cutting forces for tools with and without chip breaker at the point of failure

#### 4.6.2.2 3D surface topography

Figure 4.86 shows 3D surface topography plots of the slot bottom produced using tools with and without the chip breaker in the new and worn condition. The roughness for both slots were comparable when employing new tools ( $1.5\mu\text{m Sa}$  vs  $1.6\mu\text{m Sa}$ ), despite the significantly smaller cutting edge radius of the tool with the chip breaker. While the Sa of the last slot was  $\sim 20\%$  higher when using the plain geometry end mills, this was achieved after a  $\sim 600\text{mm}$  longer cut length.

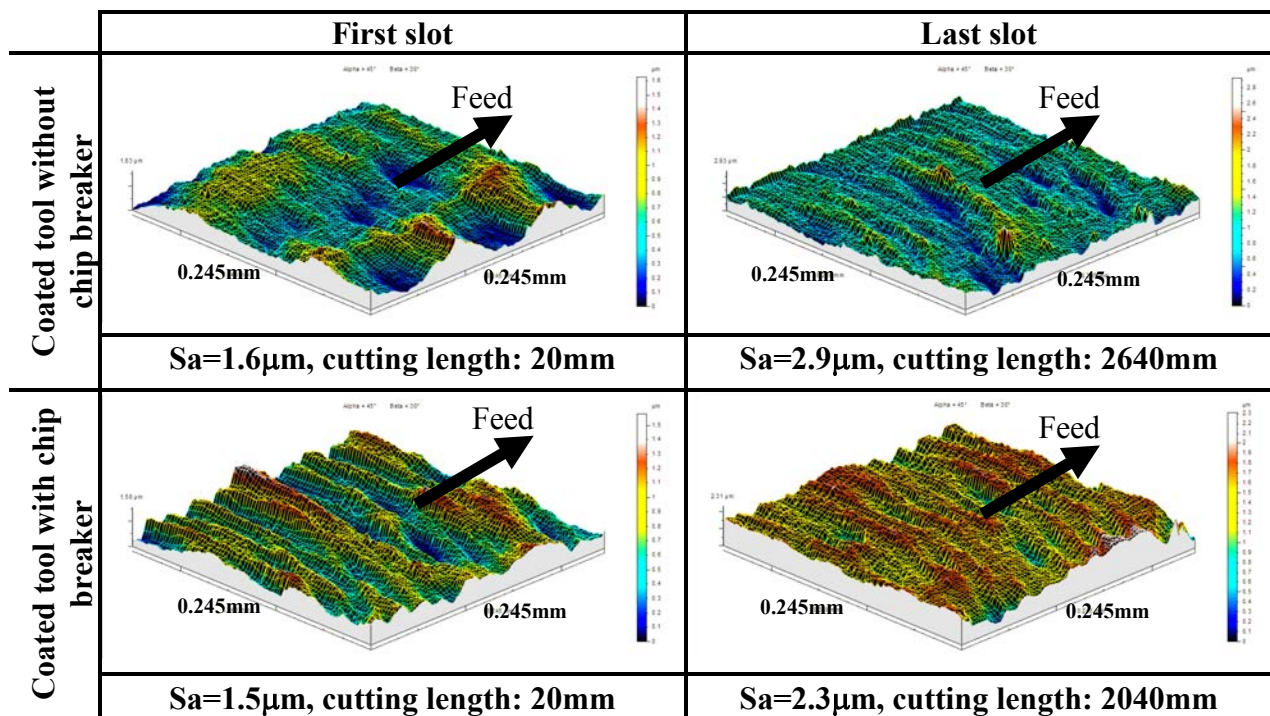


Figure 4.86: 3D surface topography plots when using new and worn tools with and without chip breaker geometry

## Chapter 5: CONCLUSIONS

### 5.1 Literature review on micro-milling technologies

- The last decade has seen a rapid expansion in the production of micro components manufactured from conventional workpiece materials (Fe, Cu, etc.) as opposed to silicon, which requires alternative fabrication technologies other than MEMS techniques.
- Micromilling is gaining popularity as a viable method for the manufacture of miniature parts particularly in hardened steel workpiece materials for miniature moulds and tooling inserts, for use in micro replication technologies such as micro injection moulding, hot embossing and micro stamping. This is further reinforced by the advancements in miniature/ultraprecision machine tools and micro cutters.
- Machine tools used for micromilling operations can broadly be classified into 3 categories. The first encompasses large-scale conventional ultraprecision machines with high speed spindle speed capability (above 50,000rpm) while the second involves small meso-scale machine tools (mMT), which have generally been developed on a bespoke basis at academic/research institutes. The third type of machine tool is generally referred to as bench-top precision units which offer a good trade-off between conventional ultraprecision machines and mMT systems.
- The ratio between the minimum chip thickness to cutting edge radius typically reported in the literature is between 0.1–0.45, depending on cutting conditions/operations.
- The fundamental mechanisms of microscale cutting has been investigated and reported by various researchers generally via the study of micro orthogonal cutting. Issues relating to the influence of process parameters and machinability of workpiece materials with hardness  $\geq 60\text{HRC}$  (such as AISI D2 62HRC cold work tool steel) however, have not previously been evaluated.

- Based on the literature survey and initial micromilling tests, the general goals of the research have been defined in order to develop preferred micromilling process parameters for AISI D2 ~62HRC cold work tool steel together with evaluation of corresponding workpiece surface integrity.

## **5.2 Experimental work**

### **5.2.1 Phase 1**

*The aim was to evaluate the quality of 'off the shelf' commercial micro endmill tools produced by a range of manufacturers.*

- Defects were typically observed with the majority of tools supplied, which involved either grinding/formatting based flaws or coating deficiencies. The former comprised chipping of cutting edges, grinding scratches and poor geometrical accuracy due to limitations of the grinding process during fabrication of the microtool geometry. Poor coating quality with aspects such as droplets and non-uniform tool surfaces was regularly seen.
- The deviation from the nominal tool diameter varied between  $-19.5\mu\text{m}$  (undersized) and  $+27.4\mu\text{m}$  (oversized) in magnitude (3.9% to 5.5% in percentage terms) over the range of tools analysed. There were considerable differences in terms of manufacturing process capability and quality control procedures between the different tool suppliers.
- In general, the measured cutting edge radii of the different micro end mills were between  $3.6\mu\text{m}$  and  $\sim 9\mu\text{m}$ .

### **5.2.2 Phase 2**

*The objective of this phase was to quantify and minimise spindle thermal growth errors of the Matsuura LX-1 machine tool.*

- Analysis of a commercial micro/mesoscale (Matsuura LX-1) high speed machining centre operating at up to 60,000rpm identified significant z-axis spindle variation of up to  $\sim 16\mu\text{m}$  following a standard warm-up cycle, despite the unit employing an active spindle cooling system and coordinate compensation algorithms.

- Improved accuracy (~50%) was obtained through manipulation of spindle acceleration and deceleration rates with consequent effects on the rate of thermal loading and cooling.

### **5.2.3 Phase 3A**

*The objective of this phase was to perform exploratory tests to gain a preliminary insight into key operating parameters and their effect on tool performance in slot micromilling of hardened AISI D2 steel.*

- The wear progression of the micro end mills involved three distinct stages: an initial, steady-stage and failure stage.
- A cut length of 520mm was defined as the end of test criterion (due to initiation of steady-state region) for subsequent mainstream experiments. However for evaluating tool life response, a 30µm tool diameter reduction was specified to accommodate the limitations in response ranges (in RSM analysis) in the statistical analysis.
- It was observed that there was a difference in the nature of primary wear modes between macro and micro end milling, with flank wear being the main wear mechanism in the former while fracture of the cutting edge was prevalent in the latter.
- Five types of tool wear were observed including fracture of cutting edge corner, coating delamination, abrasive wear, material deposition and tool breakage. The results showed that the microtool generally suffered severe fracture of the cutting edge corners. Furthermore, use of inappropriate/excessive cutting parameters usually resulted in instantaneous tool breakage.

### **5.2.4 Phase 3B**

*The objective of this phase was to evaluate the effect of cutting speed, feed per tooth and depth of cut on the machinability of hardened AISI D2 steel. The effect of increased wear on tool life, surface roughness, burr formation and cutting forces was analysed. The use of statistical analysis facilitated the identification of key process variables and establishing the best process performance for micromilling.*

- All three main operating variables (cutting speed, feed per tooth and depth of cut) had a significant effect on tool life/wear. From ANOVA results, cutting speed had the

highest influence on tool life with a PCR of 53% followed by the feed per tooth (19%) and the depth of cut (15%). The optimal cutting parameters in order to maximise tool life was a cutting speed of 20m/min, a feed per tooth of 1 $\mu$ m/tooth and a depth of cut of 15 $\mu$ m. Tool life under these operating conditions was 4.71 minutes.

- The effect of cutting parameters on the surface roughness was found to be significant. ANOVA calculations showed cutting speed had the greatest effect on surface roughness with a PCR of 38% followed by feed per tooth (24%) and depth of cut (18%). It was further observed that the interaction between feed per tooth and depth of cut exhibited a significant contribution of 14%. However, there was no significant interaction between the other factors at the 5% level. The preferred cutting parameter combination in order to obtain the minimum surface roughness was a cutting speed of 50m/min, a feed per tooth of 1 $\mu$ m/tooth and a depth of cut of 15 $\mu$ m. Surface roughness under these conditions was  $R_a = 0.148\mu\text{m}$ .
- Burrs were evident on top of the slot walls irrespective of operating parameters at the end of tool life (520mm length of cut). The size/width of the burrs increased with the progression of tool wear as anticipated, but decreased at higher cutting speeds. This was attributed to increased BUE or adhered workpiece material on the micro tools at lower speeds, which would have affected cutter geometry/sharpness.
- Cutting speed had the greatest effect on burr width with a PCR of 46% followed by the depth of cut 26% and the feed per tooth 24%. However, there was no significant interaction between factors at the 5% significance level. The minimum burr width was achieved by utilising a cutting speed of 50m/min, a feed per tooth of 1 $\mu$ m/tooth and a depth of cut of 15 $\mu$ m. Burr width for these operating conditions was 92.2 $\mu$ m.
- A summary of the PCR's of each factor and their associated interactions on performance measures (tool life, surface roughness and burr formation) together with the recommended cutting parameters are detailed in Table 5.1 and Table 5.2 respectively. Note that the ratio between the high and low levels of the cutting speed, feed rate and depth of cut factor is 2.5, 2.0 and 3.67 respectively.
- Cutting forces increased alongside cutting length due to tool wear progression. This involved cutting edge corner fracture, tool edge rounding and peeling of the coating at the rake and flank face.
- A summary of the PCR's of each factor and interactions on cutting forces ( $F_x$ ,  $F_y$  and  $F_z$ ) is shown in Table 5.3.

- The average maximum cutting temperature when micromilling hardened AISI D2 at cutting speed of 50m/min, a feed per tooth of 2 $\mu$ m/tooth and a depth of cut of 55 $\mu$ m was 54.1°C.
- The deterioration in slot quality progressed gradually with length cut, as burr size and the extent of corner rounding increased with tool wear.
- No evidence of major surface damage such as microcracks, untempered/overtempered martensite, phase transformations or white layer formation was detected in any of the specimens analysed. Furthermore no discernible deformation of the material grain structure beneath the machined surface was observed, which was attributed to the low cutting forces and temperatures generated.
- The micro slotting process had little or no effect on workpiece microhardness. The changes observed were due to the previous face milling operation used to prepare the workpiece specimen.
- The micromilling operation had no influence on workpiece surface residual stresses, which reflected the relatively low cutting forces and temperatures generated in the micro-machining processes.
- Wet machining was not expected to improve performance as no evidence of thermal damage was seen on any of the slot surfaces. Furthermore, the use of high pressure fluid would most likely cause vibration or deflection of the micro end mills, despite the likelihood for reducing BUE and adhered/smear material.
- The results presented here suggests that micro milling of hardened steel is feasible for applications such as micro mould manufacture, however further research is necessary in order to improve characterisation of tool wear, productivity and reduce/eliminate flaws such as burr formation.

Table 5.1: Summary of percentage contribution of each factor relative to response measures

Performance measure	PCR of cutting parameter factors			Interaction factors
	Cutting speed (20 & 50m/min)	Feed per tooth (1 & 2 $\mu$ m/tooth)	Depth of cut (15 & 55 $\mu$ m)	
Tool life	53%	19%	15%	1. Cutting speed and feed per tooth (9%) 2. Cutting speed and depth of cut (4%)
Surface roughness	38%	24%	18%	Feed per tooth and depth of cut (14%)
Burr width	46%	26%	24%	

Table 5.2: Summary of optimum cutting parameters with respect to response measures.

	Cutting speed (m/min)	Feed per tooth ( $\mu\text{m}/\text{tooth}$ )	Depth of cut ( $\mu\text{m}$ )	Best results
Tool life	20	1	15	4.71 minutes
Surface roughness	50	1	15	$R_a=0.148\mu\text{m}$
Burr width	50	1	15	$92.2\mu\text{m}$

Table 5.3: Summary of percentage contribution of each factor for cutting force components

Cutting force	Contribution of cutting parameters			Interaction factors
	Cutting speed (m/min)	Feed per tooth ( $\mu\text{m}/\text{tooth}$ )	Depth of cut ( $\mu\text{m}$ )	
$F_x$	10%	6%	70%	Feed per tooth and depth of cut (11%)
$F_y$	21%	8%	65%	
$F_z$	1%	12%	86%	
$F_{Res}$	4%	13%	82%	

### 5.2.5 Phase 4

*The objective of this phase was to optimise the tool life and surface roughness using RSM.*

- First and second order models for tool life and surface roughness were developed for micro end milling of hardened steel. Adequacy of the models was evaluated by ANOVA which indicated that both models were significant at the 5% level. This suggests that the models can be reliably used to predict tool life and surface roughness when micromilling hardened (62HRC) AISI D2 cold work tool steel under the specified cutting conditions. The second order model is valid under dry cutting conditions over the following range of cutting speed ( $9.77 \leq V_c \leq 60.23\text{m/min}$ ), feed per tooth ( $0.66 \leq ft \leq 2.34\mu\text{m}$ ), and depth of cut ( $1.36 \leq d \leq 68.64\mu\text{m}$ ).
- Both models (first and second order) showed similar predictive trends indicating that cutting speed had the most significant influence on tool life followed by feed per tooth and depth of cut. The average percentage error between the predicted and experimental values of tool life for first order model was not more than 3% while for second order model, this was within 4%.
- In terms of workpiece surface roughness, cutting speed had the greatest influence followed by feed per tooth and depth of cut. The absolute average percentage error between the predicted and experimental value of surface roughness for first order

linear model did not exceed 1% while for second order quadratic model, the value was 4%.

- Dual-response contour plots of metal removal rate and tool life contours were generated based on the model equations formulated based on the RSM technique. The response surfaces can be employed to select the appropriate/optimum combination of cutting speed and feed per tooth at a specified depth of cut in order to increase the material removal rate without reducing tool life.
- A contour plot involving both workpiece surface roughness and MRR with respect to the two independent variables (cutting speed and feed per tooth) allows selection of operating parameters to maximise material removal rate without sacrificing the quality of surface roughness produced.

### **5.2.6 Phase 5**

*The objective of this phase was to benchmark the performance of uncoated tools as well as coated end mills incorporating a chip breaker feature against conventional coated micro cutters.*

- The uncoated tools showed a relatively short tool life of 180mm cut length compared to equivalent coated cutters which machined a length of 2040mm prior to tool breakage (over a 10 fold increase in material removed).
- The force components when utilising the coated tool were up to ~40% lower than the uncoated end mill. The coating was also shown to provide greater wear resistance and the maximum resultant force recorded prior to tool failure for the uncoated and coated end mills was 28.6N and 45.8N respectively.
- The coating also reduced the tendency for the workpiece material to adhere onto the micro end mill surface. The uncoated tool however suffered severe ‘clogging’ of the flute helix and cutting edges due to ‘sticking’ of the chips.
- The machined surface roughness (Ra) was generally higher when employing the conventional/plain geometry end mills, probably due to the larger cutting edge radius compared to the chip breaker tool (~6.8 $\mu$ m vs. ~3.6 $\mu$ m).

- The rate of tool diameter reduction was greater when using the standard geometry tool, particularly in the initial stage of cutting. This however converged with the chip breaker tool as machining progressed.
- Despite similar levels of cutting forces, the tool without the chip breaker showed a ~ 30% increase in distance cut (2640mm vs. 2040mm) compared to the cutter incorporating a chip breaker.

## **Chapter 6: RECOMMENDATIONS FOR FUTURE WORK**

While mechanical micromilling has been shown to provide significant benefits such as higher material removal rates (for small batch production), together with greater process flexibility/scope (wider range of workpiece materials, part complexity etc.) compared to MEMS techniques, further research is required to improve the process capability (tool life, productivity, accuracy etc.) for widespread industrial application and particularly for micro machining of hardened steels and similarly difficult to cut materials (titanium/nickel alloys, CFRP etc.). A list of publications stemming from the current project is shown in Appendix F however, the following are relevant topics which warrant additional work/investigation:

- Further in-depth temperature measurement work possibly using implanted thermocouples or other techniques such as a two/three colour micro fibre optic infrared system.
- Development of an on-line system for real time monitoring of tool wear and detection of tool breakage possibly based on force signals.
- Development of a knowledge based system to help selection of preferred micro machining parameters which maximises productivity and also accounts for other performance measures such as tool life, surface roughness, burr formation and tool wear.
- Simulation and prediction of process performance and workpiece surface integrity using finite element modelling.
- Development of a more sensitive/higher resolution force measurement transducer/system to distinguish between background noise and forces, particularly at magnitudes of  $< 1\text{N}$ .
- Quantitative characterisation of tool quality (e.g. geometry accuracy etc.) and its subsequent effect on machining performance.

## REFERENCES

1. Woon, K.S., et al., *Investigations of tool edge radius effect in micromachining: A FEM simulation approach*. Journal of Materials Processing Technology, 2008. 195(1-3): p. 204-211, ISSN: 0924-0136.
2. Weck, S., Fischer, S., and Vos, M., *Fabrication of microcomponents using ultraprecision machine tools*. Nanotechnology, 1997. 8: p. 145–148.
3. Aramcharoen, A. and Mativenga, P.T., *Tool wear modes in micro/mesoscale milling of hardened die steel*. Proceedings of the 3rd International CIRP High Performance Cutting Conference, 2008. 1: p. 179-188, ISBN 978-1-905254-32-3.
4. Jun, M.B.G., et al., *Experimental investigation of machinability and tool wear in micro-endmilling*. Transactions of the North American Manufacturing Research Institution of SME 2008., 2008. NAMRC 36: p. 201-208.
5. Malekian, M., Park, S.S., and Jun, M.B.G., *Modeling of dynamic micro-milling cutting forces*. International Journal of Machine Tools and Manufacture, 2009. 49(7-8): p. 586-598, ISSN: 0890-6955.
6. Chae, J., Park, S.S., and Freiheit, T., *Investigation of micro-cutting operations*. International Journal of Machine Tools and Manufacture, 2006. 46(3-4): p. 313-332, ISSN: 0890-6955.
7. Salomon, P., *Micro Sensors and Microsystems –World Wide Markets and Economic Impact*. Microtechnology Management Marketing Media Communication Consulting, 2006, 2006: p. 1-29.
8. Liu, X., et al., *The mechanics of machining at the micro scale: assessment of the current state of the science*. Journal of Manufacturing Science and Engineering, 2004. 126: p. 666–678, ISSN: 1087-1357.
9. Bissacco, G., Hansen, H.N., and De Chiffre, L., *Micromilling of hardened tool steel for mould making applications*. Journal of Materials Processing Technology, 2005. 167: p. 201-207, ISSN:0924-0136.
10. Dornfeld, D., Min, S., and Takeuchi, Y., *Recent Advances in Mechanical Micromachining*. CIRP Annals - Manufacturing Technology, 2006. 55(2): p. 745-768, ISSN: 0007-8506.
11. Aramcharoen, A. and Mativenga, P.T., *Size effect and tool geometry in micromilling of tool steel*. Precision Engineering, 2009. 33(4): p. 402-407, ISSN: 0141-6359
12. Vogler, M.P., DeVor, R.E., and Kapoor, S.G., *On the Modeling and Analysis of Machining Performance in Micro-Endmilling, Part I: Surface Generation*. Journal of Manufacturing Science and Engineering, Transactions of the ASME, 2004. 126: p. 685-694, ISSN: 1087-1357.
13. Rajurkar, K.P., et al., *Micro and Nano Machining by Electro-Physical and Chemical Processes*. CIRP Annals - Manufacturing Technology, 2006. 55(2): p. 643-666, ISSN: 0007-8506.
14. Tansel, I., et al., *Micro-end-milling - I. Wear and breakage*. International Journal of Machine Tools and Manufacture, 1998. 38(12): p. 1419-1436, ISSN: 0890-6955.
15. Li, P., et al., *Experimental validation of micro endmill design for hard milling application*. Proceedings of the 3rd International CIRP High Performance Cutting Conference, 2008. 1: p. 69-78, ISBN 978-1-905254-32-3.

16. Li, P., et al., *A study of factors affecting the performance of micro square endmills in milling of hardened tool steels*. Proceedings of the 4th International Conference on Multi-Material Micro Manufacture, 2008: p. 1-4, ISBN 978-1904445-76-0.
17. Filiz, S., et al., *An experimental investigation of micro-machinability of copper 101 using tungsten carbide micro-endmills*. International Journal of Machine Tools and Manufacture, 2007. 47(7): p. 1088-1100, ISSN: 0890-6955.
18. Aramcharoen, A. and Mativenga, P.T., *Evaluation of critical parameters in micro machining of hardened tool steel*. International Journal Nanomanufacturing, 2009. 3(1/2): p. 100-111, ISSN: 1746-9406.
19. Kang, I.S., et al., *A mechanistic model of cutting force in the micro end milling process*. Journal of Materials Processing Technology 2007. 187: p. 250-255, ISSN: 0924-0136.
20. Tönshoff, H.K., Arendt, C., and Amor, R.B., *Cutting of Hardened Steel*. CIRP Annals - Manufacturing Technology, 2000. 49(2): p. 547-566, ISSN: 0007-8506.
21. Bissacco, G., Hansen, H.N., and De Chiffre, L., *Size Effects on Surface Generation in Micro Milling of Hardened Tool Steel*. CIRP Annals-Manufacturing Technology, 2006. 55(1): p. 1-4, ISSN: 0007-8506.
22. Weule, H., Hüntrup, V., and Tritschler, H., *Micro-Cutting of Steel to Meet New Requirements in Miniaturization*. CIRP Annals - Manufacturing Technology, 2001. 50(1): p. 61-64, ISSN: 0007-8506.
23. Liu, X., Devor, R.E., and Kapoor, S.G., *Model-Based Analysis of the Structure Generation in Microendmilling—Part II: Experimental Validation and Analysis*. ASME Journal of Manufacturing Science Engineering, 2007. 129(3): p. 461-469, ISSN: 10871357.
24. Robinson, G.M., Jackson, M.J., and Whitfield, M.D., *A review of machining theory and tool wear with a view to developing micro and nano machining processes*. Journal of Material Science, 2007. 42: p. 2002–2015, ISSN: 1573-4803.
25. Malekian, M., Park, S.S., and Jun, M.B.G., *Tool wear monitoring of micro-milling operations*. Journal of Materials Processing Technology, 2009. 209(10): p. 4903-4914, ISSN: 0924-0136.
26. Vogler, M.P., Devor, R.E., and Kapoor, S.G., *Microstructure-level force prediction model for micro-milling of multi-phase materials*. Journal of Manufacturing Science and Engineering, Transaction of the ASME, 2003. 125(2): p. 202–209, ISSN: 1087-1357.
27. Gowri, S., et al., *Micromachining: technology for the future*. International Journal of Materials and Structural Integrity, 2007. 1: p. 161-179, ISSN: 1745-0063.
28. Uriarte, L., et al., *Error budget and stiffness chain assessment in a micromilling machine equipped with tools less than 0.3mm in diameter*. Precision Engineering, 2007. 31(1): p. 1-12, ISSN: 0141-6359
29. Saedon, J., Soo, S.L., and Aspinwall, D.K., *Measurement of Spindle Thermal Growth on a Machine Intended for Micro / Meso Scale Milling*. Key Engineering Materials, 2010. 447-448: p. 55-60, ISSN: 1013-9826.
30. Nor, M.K.M., *Development of the UMAC-based control system with application to 5-axis ultraprecision micromilling machines*. PhD, Thesis, Brunel University, 2010.
31. Okazaki, Y., Mishima, N., and Ashida, K., *Microfactory—concept, history, and developments*. Journal of Manufacturing Science and Engineering, 2004. 126: p. 837–844, ISSN: 1087-1357.
32. Huo, D., Cheng, K., and Wardle, F., *Design of a five-axis ultra-precision micro-milling machine—UltraMill. Part 1: holistic design approach, design considerations*

- and specifications*. The International Journal of Advanced Manufacturing Technology, 2010. 47(9): p. 867-877, ISSN: 1433-3015.
33. *Nanotech 350 UPL Brochure, Moore Nanotechnology Systems Ltd.* <http://www.nanotechsys.com> (accessed on 1st November 2010).
  34. *Hyper2J, Makino.* <http://www.makino.com/machines/HYPER2J/> (accessed on 1st November 2010).
  35. *Sodick AZ250L.* <http://www.sodick.com/index.php?t=products/az150l&> (accessed on 1st November 2010).
  36. *KERN Micro.* [http://www.kern-microtechnic.com/upload/media/kern\\_micro\\_e.pdf](http://www.kern-microtechnic.com/upload/media/kern_micro_e.pdf) (accessed on 1st November 2010).
  37. *Robonano alpha-0iB, Japan* <http://www.fanuc.co.jp/en/product/robonano/index.htm#test>, (accessed on 1st November 2010).
  38. *Micromaster 5X, Kugler.* <http://www.kugler-precision.com/> (accessed on 1st November 2010).
  39. *Matsuura LX-1, Japan.* [http://www.matsuura.co.jp/english/products/lx\\_series.shtm](http://www.matsuura.co.jp/english/products/lx_series.shtm) (accessed on 1st November 2010).
  40. Vogler, M., et al., *Development of Meso-scale Machine Tool (MMT) Systems*. Society of Manufacturing Engineers, 2002: p. 1-9, ISSN: 0361-0853.
  41. Li, H., et al., *Development of meso-scale milling machine tool and its performance analysis*. Front. Mech. Eng. China, 2008. 3(1): p. 59–65, ISSN: 1673-3592.
  42. Lee, S.W., Mayor, R., and Ni, J., *Dynamic Analysis of a Mesoscale Machine Tool*. Journal of Manufacturing Science and Engineering, 2006. 128(1): p. 194-203, ISSN: 1087-1357.
  43. Bang, Y.B., Lee, K.M., and Oh, S., *5-axis micro milling machine for machining micro parts*. The International Journal of Advanced Manufacturing Technology, 2005. 25(9): p. 888-894, ISSN: 1433-3015.
  44. Li, K.-M. and Chou, S.-Y., *Experimental evaluation of minimum quantity lubrication in near micro-milling*. Journal of Materials Processing Technology, 2010. 210(15): p. 2163-2170, ISSN: 0924-0136.
  45. Filiz, S., et al., *Micromilling of microbarbs for medical implants*. International Journal of Machine Tools and Manufacture, 2008. 48(3-4): p. 459-472, ISSN: 0890-6955.
  46. Yang, K., et al., *Tool edge radius effect on cutting temperature in micro-end-milling process*. The International Journal of Advanced Manufacturing Technology, 2011. 52(9): p. 905-912, ISSN: 1433-3015.
  47. Ciurana, J., Quintana, G., and Campa, F.J., *Machine tool spindles*, in *Machine tools for high performance machining*. 2009, Springer London. p. 75-127, ISBN 978-1-84800-380-4.
  48. Lin, C.W., Tu, J.F., and Kamman, J., *An integrated thermo-mechanical-dynamic model to characterize motorized machine tool spindles during very high speed rotation*. International Journal of Machine Tools and Manufacture, 2003. 43(10): p. 1035-1050, ISSN: 0890-6955.
  49. Lin, C.W. and Tu, J.F., *Model-Based Design of Motorized Spindle Systems to Improve Dynamic Performance at High Speeds*. Journal of Manufacturing Processes, 2007. 9(2): p. 94-108, ISSN: 1526-6125.
  50. Chang, C.-F. and Chen, J.-J., *Thermal growth control techniques for motorized spindles*. Mechatronics, 2009. 19(8): p. 1313-1320, ISSN 0957-4158
  51. Abele, E., Altintas, Y., and Brecher, C., *Machine tool spindle units*. CIRP Annals - Manufacturing Technology, 2010. 59(2): p. 781-802, ISSN: 0007-8506.

52. Borisavljevic, A., et al. *Motor drive for a novel high-speed micro-milling spindle*. 2009. The Institution of Engineering and Technology,; IEEE, 1492-1497, ISBN: 978-1-4244-2852-6
53. Creighton, E., et al., *Analysis of thermal errors in a high-speed micro-milling spindle*. International Journal of Machine Tools and Manufacture, 2010. 50(4): p. 386-393, ISSN: 0890-6955.
54. Mou, J. and Richard Liu, C., *A method for enhancing the accuracy of CNC machine tools for on-machine inspection*. Journal of Manufacturing Systems, 1992. 11(4): p. 229-237, ISSN: 0278-6125.
55. Kreng, V.B., Liu, C.R., and Chu, C.N., *A kinematic model for machine tool accuracy characterisation*. The International Journal of Advanced Manufacturing Technology, 1994. 9(2): p. 79-86, ISSN: 1433-3015.
56. Bryan, J., *International Status of Thermal Error Research (1990)*. CIRP Annals - Manufacturing Technology, 1990. 39(2): p. 645-656, ISSN: 0007-8506.
57. Zhao, H., Yang, J., and Shen, J., *Simulation of thermal behavior of a CNC machine tool spindle*. International Journal of Machine Tools and Manufacture, 2007. 47(6): p. 1003-1010, ISSN: 0890-6955.
58. Weck, M., et al., *Reduction and Compensation of Thermal Errors in Machine Tools*. CIRP Annals - Manufacturing Technology, 1995. 44(2): p. 589-598, ISSN: 0007-8506.
59. Mou, J., *A method of using neural networks and inverse kinematics for machine tools error estimation and correction*. Journal of Manufacturing Science and Engineering, Transaction of the ASME, 1997. 119(2): p. 247-54, ISSN: 10871357.
60. Donmez, M.A., et al., *A general methodology for machine tool accuracy enhancement by error compensation*. Precision Engineering, 1986. 8(4): p. 187-196, ISSN: 0141-6359.
61. Pahk, H.J. and Lee, S.W., *Thermal error measurement and real time compensation system for the CNC machine tools incorporating the spindle thermal error and the feed axis thermal error*. The International Journal of Advanced Manufacturing Technology, 2002. 20(7): p. 487-494, ISSN: 1433-3015.
62. Ramesh, R., Mannan, M.A., and Poo, A.N., *Error compensation in machine tools -- a review: Part II: thermal errors*. International Journal of Machine Tools and Manufacture, 2000. 40(9): p. 1257-1284, ISSN: 0890-6955.
63. Postlethwaite, S.R., Allen, J.P., and Ford, D.G., *Machine tool thermal error reduction—an appraisal*. Proceedings of the Institution of Mechanical Engineers, Part B: Journal of Engineering Manufacture, 1999. 213: p. 1-9, ISSN: 0954-4054.
64. Holkup, T., et al., *Thermo-mechanical model of spindles*. CIRP Annals - Manufacturing Technology, 2010. 59(1): p. 365-368, ISSN: 0007-8506.
65. Jedrzejewski, J., et al., *High-speed precise machine tools spindle units improving*. Journal of Materials Processing Technology, 2005. 162-163: p. 615-621, ISSN: 0924-0136.
66. Chen, J.-S. and Hsu, W.-Y., *Characterizations and models for the thermal growth of a motorized high speed spindle*. International Journal of Machine Tools and Manufacture, 2003. 43(11): p. 1163-1170, ISSN: 0890-6955.
67. Lin, Z.C. and Chang, J.S., *The building of spindle thermal displacement model of high speed machine center*. The International Journal of Advanced Manufacturing Technology, 2007. 34(5): p. 556-566, ISSN: 1433-3015.

68. Bissacco, G., Hansen, H.N., and De Chiffre, L., *Improving axial depth of cut accuracy in micro milling*. Proc. of 4th euspen International Conference- Glasgow, Scotland (UK), 2004.
69. Vasile, M.J., et al., *Micrometer-scale machining: Tool fabrication and initial results*. Precision Engineering, 1996. 19(2-3): p. 180-186, ISSN: 0141-6359.
70. Friedrich, C.R. and Vasile, M.J., *Development of the Micromilling Process for High-Aspect-Ratio Microstructures*. Journal of Microelectromechanical Systems, 1996. 5: p. 33-38, ISSN: 1057-7157.
71. Adams, D.P., et al., *Micromilling of metal alloys with focused ion beam-fabricated tools*. Precision Engineering, 2001. 25(2): p. 107-113, ISSN: 0141-6359.
72. Fleischer, J., et al., *New applications for micro-EDM*. Journal of Materials Processing Technology, 2004. 149(1-3): p. 246-249, ISSN: 0924-0136.
73. Masuzawa, T., et al., *Wire Electro-Discharge Grinding for Micro-Machining*. CIRP Annals - Manufacturing Technology, 1985. 34(1): p. 431-434, ISSN: 0007-8506.
74. Chern, G., et al., *Study on burr formation in micro-machining using micro-tools fabricated by micro-EDM*. Precision Engineering, 2007. 31: p. 122-129, ISSN: 0141-6359.
75. Schaller, T., et al., *Microstructure grooves with a width of less than 50  $\mu\text{m}$  cut with ground hard metal micro end mills*. Precision Engineering, 1999. 23(4): p. 229-235, ISSN: 0141-6359.
76. Onikura, H., et al., *Fabrication of Micro Carbide Tools by Ultrasonic Vibration Grinding*. CIRP Annals - Manufacturing Technology, 2000. 49(1): p. 257-260, ISSN: 0007-8506.
77. Ohmori, H., et al., *Improvement of Mechanical Strength of Micro Tools by Controlling Surface Characteristics*. CIRP Annals - Manufacturing Technology, 2003. 52(1): p. 467-470, ISSN: 0007-8506.
78. Schmidt, J., Kotschenreuther, J., and Knoll, M., *Alternative methods for manufacturing milling tools*. Euspen, ISBN: 92-990035-0-5, 2005.
79. Yan, J., et al., *Fabrication of micro end mills by wire EDM and some micro cutting tests*. Journal of Micromechanics and Microengineering, 2009. 19: p. 1-9, ISSN: 1361-6439.
80. *Mitsubishi materials general catalogue*. Mitsubishi carbide. 2007-2009.
81. Ezugwu, E.O. and Wang, Z.M., *Titanium alloys and their machinability - A review*. Journal of Materials Processing Technology, 1997. 68(3): p. 262-274, ISSN: 0924-0136.
82. Kalpakjian, S. and Schmid, S.R., *Manufacturing processes for engineering materials*. Prentice Hall, 2008. Fifth edition, ISBN-13 978-981-067953-8.
83. Sandvik, *Modern metal cutting*. A practical handbook, 1994. First edition, ISBN: 91-97 22 99 -0-3.
84. Byrne, G., Dornfeld, D., and Denkena, B., *Advancing cutting technology* CIRP Annals-Manufacturing Technology, 2003. 52(2): p. 483-507, ISSN: 0007-8506.
85. Brookes, K., *World dictionary and handbook of hardmetals and hard materials*. Hertfordshire: International carbide data, 1996. 6th edition, p. 83-94, ISBN: 0950899542.
86. Fleischer, J., et al., *Geometry Optimization of Micro Milling Tools*. Proceedings of the 4th International Conference on Multi-Material Micro Manufacture, 2008. p.1-4, ISBN 978-1904445-76-0.
87. Fang, F.Z., et al., *Tool geometry study in micromachining*. Journal of Micromechanics and Microengineering, 2003. 13: p. 726-731, ISSN 1361-6439.

88. Li, P., et al., *Improvement of micro endmill geometry for micro hard milling application*. Proceedings of the euspen International Conference – Zurich - May 2008, 2008. 1: p. 157-160, ISBN: 13 978-0-9553082-5-3.
89. Aramcharoen, A., et al., *Evaluation and selection of hard coatings for micro milling of hardened tool steel*. International Journal of Machine Tools and Manufacture, 2008. 48(14): p. 1578-1584, ISSN: 0890-6955.
90. Takács, M., Verő, B., and Mészáros, I., *Micromilling of metallic materials*. Journal of Materials Processing Technology, 2003. 138(1-3): p. 152-155, ISSN: 0924-0136.
91. Guo, Z., et al., *Characterization and properties of MTCVD Ti(C,N) coated cemented carbide substrates with Fe/Ni binder*. International Journal of Refractory Metals and Hard Materials, 2010. 28(2): p. 238-242, ISSN: 0263-4368.
92. Aramcharoen, A., Mativenga, P.T., and Yang, S., *The Effect of AlCrTiN Coatings on Product Quality in Micro-milling of 45 HRC Hardened H13 Die Steel*. Proceedings of the 35th International MATADOR Conference, 2007: p. 203-206, ISBN: 978-1-84628-987-3.
93. Yang, K., et al., *Tool edge radius effect on cutting temperature in micro-end-milling process*. The International Journal of Advanced Manufacturing Technology, 2010. 52: p. 905-912, ISSN: 1433-3015.
94. Fleischer, J., et al., *Design and manufacturing of micro milling tools*. Microsystem Technologies, 2008. 14: p. 1771–1775, ISSN: 1432-1858.
95. Uriarte, L., et al., *Comparison between microfabrication technologies for metal tooling*. Proceedings of the Institution of Mechanical Engineers, Part C: Journal of Mechanical Engineering Science, 2006. 220: p. 1665-1676, ISSN: 2041-2983.
96. Kahnis, P. and Weinert, K., *Analysis of tool influences on high precision-micromilling of steel workpieces*. Proceedings of the 6th euspen International Conference – Baden bei Wien - May 2006, 2006: p. 128–131, ISBN 13: 978-0-9553082-0-8.
97. Weinert, K., Kahnis, P., and Koehler, W., *Investigation of scaling effects on modelling and simulation of scaled milling processes*. 1st Colloquium Process scaling, Bremen, 2003: p. 1-6, ISBN 3-933762-14-6.
98. Ikawa, N., et al., *Atomistic Analysis of Nanometric Chip Removal as Affected by Tool-Work Interaction in Diamond Turning*. CIRP Annals-Manufacturing Technology, 1991. 40(1): p. 551-554, ISSN: 0007-8506.
99. Özel, T., Lui, X., and Dhanorker, A., *Modelling and simulation of micro-milling process*. Proceedings of the 4th International Conference and Exhibition on Design and Production of Machines and Dies/Molds, Turkey., 2007: p. 1-8.
100. Yuan, Z.J., Zhou, M., and Dong, S., *Effect of diamond tool sharpness on minimum cutting thickness and cutting surface integrity in ultraprecision machining*. Journal of Materials Processing Technology, 1996. 62(4): p. 327-330, ISSN: 0924-0136.
101. Shimada, S., et al., *Feasibility Study on Ultimate Accuracy in Microcutting Using Molecular Dynamics Simulation*. CIRP Annals-Manufacturing Technology, 1993. 42(1): p. 91-94, ISSN: 0007-8506.
102. Vogler, M.P., Kapoor, S.G., and DeVor, R.E., *On the Modeling and Analysis of Machining Performance in Micro-Endmilling, Part II: Cutting Force Prediction*. Journal of Manufacturing Science and Engineering, Transactions of the ASME 2004. 126(4): p. 695–705, ISSN: 1087-1357.
103. Jun, M.B.G., et al., *Investigation of the dynamics of microend milling - Part I: Model development*. Journal of Manufacturing Science and Engineering, Transactions of the ASME, 2006. 128(4): p. 893-900, ISSN: 10871357.

104. Kim, C.J., Bono, M., and Ni, J., *Experimental analysis of chip formation in micro-milling*. Technical Paper - Society of Manufacturing Engineers, 2002. 159: p. 1-8.
105. Mian, A.J., Driver, N., and Mativenga, P.T., *Estimation of minimum chip thickness for multi-phase steel using acoustic emission signals*. Proceedings of the 36th International MATADOR Conference, 2010. 6: p. 197-200, ISBN: 978-1-84996-431-9.
106. Kim, C.J., Mayor, J.R., and Ni, J., *A Static Model of Chip Formation in Microscale Milling*. Journal of Manufacturing Science and Engineering, Transaction of the ASME, 2004. 126: p. 710-718, ISSN: 1087-1357.
107. Son, S.M., Lim, H.S., and Ahn, J.H., *Effects of the friction coefficient on the minimum cutting thickness in micro cutting*. International Journal of Machine Tools and Manufacture 2005. 45: p. 529–535, ISSN: 0890-6955.
108. Liu, X., DeVor, R.E., and Kapoor, S.G., *An Analytical Model for Prediction of Minimum Chip Thickness in Micro-Machining*. Journal of Manufacturing Science and Engineering, Transaction of the ASME, 2006. 128(2): p. 474-481, ISSN: 1087-1357.
109. Lai, X., et al., *Modelling and analysis of micro scale milling considering size effect, micro cutter edge radius and minimum chip thickness*. International Journal of Machine Tools and Manufacture, 2008. 48: p. 1-14, ISSN: 0890-6955.
110. Jaffery, S.I., Driver, N., and Mativenga, P.T., *Analysis of process parameters in the micromachining of Ti-6Al-4V alloy*. Proceedings of the 36th International MATADOR Conference, 2010. 6: p. 239-242, ISBN: 978-1-84996-431-9.
111. Sun, Y., Meng, Q., and Liu, H. *Experiment and simulation of micro-milling process for plastic material*. in *Proceedings of SPIE - The International Society for Optical Engineering*. 2009. V 7206, p 1-6, ISSN 0277-786X.
112. Jun, M.B.G., DeVor, R.E., and Kapoor, S.G., *Investigation of the dynamics of microend milling - Part II: Model validation and interpretation*. Journal of Manufacturing Science and Engineering, Transaction of the ASME, 2006. 128(4): p. 901-912, ISSN: 10871357.
113. Biermann, D. and Baschin, A., *Influence of cutting edge geometry and cutting edge radius on the stability of micromilling processes*. Production Engineering, 2009. 3(4-5): p. 375-380, ISSN: 1433-3015.
114. Özel, T., *Modeling Based Micro-Milling Process Planning For Machining Mold Cavities*. Proceedings of the 3rd International CIRP High Performance Cutting Conference, 2008. 2: p. 805-817, ISBN 978-1-905254-32-3.
115. Liu, K. and Melkote, S.N., *Finite element analysis of the influence of tool edge radius on size effect in orthogonal micro-cutting process*. International Journal of Mechanical Sciences, 2007. 49(5): p. 650-660, ISSN: 0020-7403.
116. Woon, K.S., et al., *The effect of tool edge radius on the contact phenomenon of tool-based micromachining*. International Journal of Machine Tools and Manufacture, 2008. 48(12-13): p. 1395-1407, ISSN: 0890-6955.
117. Woon, K.S. and Rahman, M., *The effect of tool edge radius on the chip formation behavior of tool-based micromachining*. The International Journal of Advanced Manufacturing Technology, 2010: p. 1-17, ISSN: 1433-3015.
118. Liang, Y., et al., *Modeling and experimental analysis of microburr formation considering tool edge radius and tool-tip breakage in microend milling*. Journal of Vacuum Science & Technology B 2009: p. 1531–1535, ISSN 0734-211X.
119. Mian, A.J., Driver, N., and Mativenga, P.T., *Micromachining of coarse-grained multi-phase material*. Proceedings of the Institution of Mechanical Engineers, Part B: Journal of Engineering Manufacture, 2009. 223(4): p. 377-385, ISSN: 0954-4054.

120. Mian, A.J., Driver, N., and Mativenga, P.T., *A comparative study of material phase effects on micro-machinability of multiphase materials*. The International Journal of Advanced Manufacturing Technology, 2010. 50(1-4): p. 163-174, ISSN: 1433-3015.
121. Wyen, C.F. and Wegener, K., *Influence of cutting edge radius on cutting forces in machining titanium*. CIRP Annals - Manufacturing Technology, 2010. 59(1): p. 93-96, ISSN: 0007-8506.
122. Miao, J.C., et al., *Review of dynamic issues in micro-end-milling*. The International Journal of Advanced Manufacturing Technology, 2007. 31(9-10): p. 897-904, ISSN: 1433-3015.
123. Chuzhoy, L., DeVor, R. E., Kapoor, S. G., and Bammann, D. J., *Machining Simulation of Ductile Iron and Its Constituents, Part 1: Estimation of Material Model Parameters and Their Validation*. Journal of Manufacturing Science and Engineering, Transaction of the ASME, 2003. 125: p. 181-191, ISSN: 10871357.
124. Chuzhoy, L., DeVor, R. E., Kapoor, S. G., and Bammann, D. J., *Machining Simulation of Ductile Iron and Its Constituents, Part 2: Numerical Simulation and Experimental Validation of Machining*. Journal of Manufacturing Science and Engineering, Transaction of the ASME, 2003. 125: p. 192-201, ISSN: 10871357.
125. Simoneau, A., Ng, E., and Elbestawi, M.A., *Chip formation during microscale cutting of a medium carbon steel*. International Journal of Machine Tools and Manufacture, 2006. 46(5): p. 467-481, ISSN: 0890-6955.
126. Simoneau, A., Ng, E., and Elbestawi, M.A., *Surface defects during microcutting*. International Journal of Machine Tools and Manufacture, 2006. 46: p. 1378-1387, ISSN: 0890-6955.
127. Zhou, M. and Ngoi, B., *Effect of tool and workpiece anisotropy on microcutting processes*. Proceedings of the Institution of Mechanical Engineers, Part B: Journal of Engineering Manufacture, 2001. 215: p. 13-19, ISSN: 0954-4054.
128. Wang, J., et al., *Surface generation analysis in micro end-milling considering the influences of grain*. Microsystem Technologies, 2008. 14: p. 937-942, ISSN: 1432-1858.
129. Popov, K., et al., *Micromilling: material microstructure effects* Proceedings of the Institution of Mechanical Engineers, Part B: Journal of Engineering Manufacture, 2006. 220: p. 1807-1813, ISSN: 0954-4054.
130. Arsecularatne, J.A., et al., *On machining of hardened AISI D2 steel with PCBN tools*. Journal of Materials Processing Technology, 2006. 171(2): p. 244-252, ISSN: 0924-0136.
131. Iqbal, A., et al., *Modeling the effects of cutting parameters in MQL-employed finish hard-milling process using D-optimal method*. Journal of Materials Processing Technology, 2008. 199: p. 379-390, ISSN: 0924-0136.
132. *ASM Metals Reference Book*. 1993. Third edition.
133. Coane, P.J. and Friedrich, C.R. *Fabrication of composite x-ray masks by micromilling*. in *The Society of Photo-Optical Instrumentation Engineers (SPIE)*. 1996.
134. Friedrich, C.R., Coane, P.J., and Vasile, M.J., *Micromilling development and applications for microfabrication*. Microelectronic Engineering, 1997. 35(1-4): p. 367-372, ISSN: 0167-9317
135. Tansel, I., et al., *Micro-end-milling - II. Extending tool life with a Smart Workpiece Holder (SWH)*. International Journal of Machine Tools and Manufacture, 1998. 38(12): p. 1437-1448, ISSN: 0890-6955.

136. Tansel, I., et al., *Micro-end-milling - III. Wear estimation and tool breakage detection using acoustic emission signals*. International Journal of Machine Tools and Manufacture, 1998. 38(12): p. 1449-1466, ISSN: 0890-6955.
137. Denkena, B., et al., *Micromachining processes for microsystem technology*. Microsystem Technologies, 2006. 12: p. 659-664, ISSN: 1432-1858.
138. Dhanorker, A. and Özel, T., *An experimental and modeling study on meso/micro end milling process*. Proceedings of 2006 ASME International Conference on manufacturing Science and Engineering, 2006: p. 1-8, ISBN: 0791837868.
139. Hangtao, L., et al., *Modelling and experimental analysis of the effects of tool wear, minimum chip thickness and micro tool geometry on the surface roughness in micro-end-milling*. Journal of Micromechanics and Microengineering, 2008. 18: p. 1-12, ISSN 1361-6439.
140. Li, C., et al., *Modeling of three-dimensional cutting forces in micro-end-milling*. Journal of Micromechanics and Microengineering, 2007. 17: p. 671-678, ISSN 1361-6439.
141. Rahman, M., A. S. Kumar, and J.R.S.Prakash, *Micro milling of pure copper*. Journal of Materials Processing Technology, 2001. 116(1): p. 39-43, ISSN: 0924-0136.
142. Dow, T.A., Miller, E.L., and Garrard, K., *Tool force and deflection compensation for small milling tools*. Precision Engineering, 2004. 28: p. 31-45, ISSN: 0141-6359.
143. Uhlmann, E., Piltz, S., and Schauer, K., *Micro milling of sintered tungsten-copper composite materials*. Journal of Materials Processing Technology, 2005. 167: p. 402-407, ISSN: 0924-0136.
144. Weinert, K. and Petzoldt, V., *Machining of NiTi based shape memory alloys* Materials Science and Engineering A 2004. 278: p. 180-184, ISSN: 0921-5093.
145. Weinert, K. and Petzoldt, V., *Machining NiTi micro-parts by micro-milling*. Materials Science and Engineering: A, 2008. 481-482: p. 672-675, ISSN: 0921-5093.
146. Rusnaldy, Ko, T.J., and Kim, H.S., *Micro-end-milling of single-crystal silicon*. International Journal of Machine Tools and Manufacture, 2007. 47(14): p. 2111-2119, ISSN: 0890-6955.
147. Foy, K., et al., *Effect of tilt angle on cutting regime transition in glass micromilling*. International Journal of Machine Tools and Manufacture, 2009. 49(3-4): p. 315-324, ISSN: 0890-6955.
148. *AISI Type D2 Tool Steel, air quenched at 1010°C, tempered at 200°C*. Materials Handbook, 2nd Ed, Francois Cardarelli, Springer-Verlag, London, 2008.
149. Klocke, F., et al. *A Study of the influence of cutting parameters on micro milling of steel with cubic boron nitride (CBN) tools*. in *Proceedings of SPIE - The International Society for Optical Engineering*. 2009. 7204, p. 1-10, ISSN 0277-786X.
150. Li, P., Oosterling, J.A.J., and Hoogstrate, A.M. *Performance evaluation of micromilling of hardened tool steel*. Proceedings of the 2nd International Conference on Micromanufacturing, Greenville, USA. 2007, p. 219-224, ISBN: 0-080-45263-9.
151. Dimov, S., et al., *Micromilling strategies: optimization issues*. Proceedings of the Institution of Mechanical Engineers, Part B: Journal of Engineering Manufacture, 2004. 218: p. 731-736, ISSN: 0954-4054.
152. Afazov, S.M., Ratchev, S.M., and Segal, J., *Modelling and simulation of micro-milling cutting forces*. Journal of Materials Processing Technology, 2010. 210(15): p. 2154-2162, ISSN: 0924-0136.
153. Newby, G., Venkatachalam, S., and Liang, S.Y., *Empirical analysis of cutting force constants in micro-end-milling operations*. Journal of Materials Processing Technology 2007. 192-193: p. 41-47, ISSN: 0924-0136.

154. Torres, C.D., et al., *Analyzing the performance of diamond coated micro end mills*. International Journal of Machine Tools and Manufacture, 2009. 49: p. 599-612, ISSN: 0890-6955.
155. Zhou, L., Wang, C.Y., and Qin, Z., *Tool wear characteristics in high-speed milling of graphite using a coated carbide micro endmill*. Proceedings of the Institution of Mechanical Engineers, Part B: Journal of Engineering Manufacture, 2009. 223: p. 267-277, ISSN: 0954-4054.
156. Zhu, K., Wong, Y.S., and Hong, G.S., *Multi-category micro-milling tool wear monitoring with continuous hidden Markov models*. Mechanical Systems and Signal Processing, 2009. 23(2): p. 547-560, ISSN: 0888-3270.
157. Ding, H., et al., *Experimental study on machinability improvement of hardened tool steel using two dimensional vibration-assisted micro-end-milling*. International Journal of Machine Tools and Manufacture, 2010. 50(12): p. 1115-1118, ISSN: 0890-6955.
158. Aurich, J.C., et al., *Burrs-Analysis, control and removal*. CIRP Annals - Manufacturing Technology, 2009. 58(2): p. 519-542, ISSN: 0007-8506.
159. Wissmiller, D.L. and Pfefferkorn, F.E., *Micro end mill tool temperature measurement and prediction*. Journal of Manufacturing Processes, 2009. 11(1): p. 45-53, ISSN: 1526-6125.
160. Liu, X., Devor, R.E., and Kapoor, S.G., *Model-Based Analysis of the Structure Generation in Microendmilling—Part I: Model Development* Journal of Manufacturing Science and Engineering, Transaction of the ASME, 2007. 129(3): p. 453–460, ISSN: 1087-1357.
161. Uriarte, L., et al., *Mechanistic modelling of the micro end milling operation*. Proceedings of the Institution of Mechanical Engineers, Part B: Journal of Engineering Manufacture, 2008. 222: p. 23-33, ISSN: 0954-4054.
162. Bissacco, G., Hansen, H.N., and De Chiffre, L., *Wear of micro end mills*. Proceedings of 5<sup>th</sup> Euspen International Conference - Montpellier – France - May 2005, 2005: p. 561-564, ISSN 0954-4054.
163. Wang, W., Kweon, S.H., and Yang, S.H., *A study on roughness of the micro-end-milled surface produced by a miniaturized machine tool*. Journal of Materials Processing Technology, 2005. 162-163: p. 702-708, ISSN: 0924-0136.
164. Wang, J., et al., *Surface roughness prediction in micromilling using neural networks and Taguchi's design of experiments*. IEEE International Conference, Australia, 2009: p. 1-6, ISBN: 978-1-4244-3506-7
165. Lee, K. and Dornfeld, D.A., *Micro-burr formation and minimization through process control*. Precision Engineering, 2005. 29(2): p. 246-252, ISSN: 0141-6359.
166. Wang, J., et al., *Chip formation analysis in micromilling operation*. The International Journal of Advanced Manufacturing Technology, 2009. 45(5-6): p. 430-447, ISSN: 1433-3015.
167. Schueler, G.M., et al., *Burr Formation and Surface Characteristics in Micro-End Milling of Titanium Alloys* Springer Berlin Heidelberg, 2010: p. 129-138, ISBN 978-3-642-00567-1
168. Lee, K. and Dornfeld, D.A., *An experimental study on burr formation in micro milling aluminum and copper*. Transactions of the North American Manufacturing Research Institute of SME, 2002: p. 255-262, ISSN: 1047-3025.
169. Schmidt, J. and Tritschler, H., *Micro cutting of steel*. Microsystem Technologies, 2004. 10(3): p. 167-174, ISSN: 1432-1858.

170. Cheng, Z.J., et al., *The characteristics of cutting forces in the micro-milling of AISI D2 steel*. Journal of Mechanical Science and Technology 2009. 23(10): p. 2823-2829, ISSN: 1976-3824.
171. Bissacco, G., Gietzelt, T., and Hansen, H.N., *Force analysis in micro milling Al 6082 T6 in various engagement conditions*. Proceedings of the 4th International Conference on Multi-Material Micro Manufacture, 2008: p. 1-4, ISBN 978-1904445-76-0.
172. Abukhshim, N.A., Mativenga, P.T., and Sheikh, M.A., *Heat generation and temperature prediction in metal cutting: A review and implications for high speed machining*. International Journal of Machine Tools and Manufacture, 2006. 46: p. 782-800, ISSN: 0890-6955.
173. Dhanorker, A. and Özel, T., *Meso/Micro Scale Milling for Micromanufacturing*. International Journal of Mechatronics and Manufacturing Systems, 2008. 1(1): p. 22-43, ISSN: 1753-1047
174. Mativenga, P.T., et al., *Knowledge driven micro machining science and technology an overview*. Extended life microtooling by advanced coating technology (ELMACT), Dissemination seminar, 19 November 2010, Coventry, 2010.
175. Dewes, R.C., et al., *Temperature measurement when high speed machining hardened mould/die steel*. Journal of Materials Processing Technology, 1999. 92-93: p. 293-301.
176. *Machining data handbook*. 3rd edition, Machinability data centre, 1980. 2: p. 39-136, ISBN 0-936974-02-8.
177. El-Wardany, T.I., Kishawy, H.A., and Elbestawi, M.A., *Surface Integrity of Die Material in High Speed Hard Machining, Part I Micrographical Analysis*. Journal of Manufacturing Science and Engineering, Transaction of the ASME, 2000. 122(4): p. 620-631, ISSN: 10871357.
178. Lin, Z.C., Lin, Y.Y., and Liu, C.R., *Effect of thermal load and mechanical load on the residual stress of a machined workpiece*. International Journal of Mechanical Sciences, 1991. 33(4): p. 263-278, ISSN: 0020-7403.
179. Field, M., Kahles, J.F., and Cammett, J.N.T., *Review of Measuring Methods for Surface Integrity*. CIRP Annals - Manufacturing Technology, 1972. 21(2): p. 219-238, ISSN: 0007-8506.
180. Kahles, J.F. and Field, M., *Surface integrity guidelines for machining*. Paper Number: IQ71-240, Society of Manufacturing Engineers, 1971.
181. Umbrello, D., *Influence of material microstructure changes on surface integrity in hard machining of AISI 52100 steel*, in *The International Journal of Advanced Manufacturing Technology*. 2010: p. 1-12, ISSN: 1433-3015.
182. Choi, Y. and Liu, C.R., *Effects of machining parameters on surface integrity of hard machined surfaces*. Proceedings of the Institution of Mechanical Engineers, Part B: Journal of Engineering Manufacture, 2010. 224: p. 699-708, ISSN: 0890-6955.
183. Sun, J. and Guo, Y.B., *A comprehensive experimental study on surface integrity by end milling Ti-6Al-4V*. Journal of Materials Processing Technology, 2009. 209(8): p. 4036-4042, ISSN: 0924-0136.
184. Pawade, R.S., Joshi, S.S., and Brahmankar, P.K., *Effect of machining parameters and cutting edge geometry on surface integrity of high-speed turned Inconel 718*. International Journal of Machine Tools and Manufacture, 2008. 48: p. 15-28, ISSN: 0890-6955.
185. Guo, Y.B., Li, W., and Jawahir, I.S., *Surface integrity characterization and prediction in machining of hardened and difficult-to-machine alloys: a state-of-art research*

- review and analysis*. Machining Science and Technology, 2009. 13: p. 437-470, ISSN 1091-0344
186. M'Saoubi, R., et al., *A review of surface integrity in machining and its impact on functional performance and life of machined products*. International Journal of Sustainable Manufacturing, 2008. 1(1-2): p. 203 - 236, ISSN: 1742-7231.
  187. Montgomery, D.C., *Design and Analysis of Experiments*. 7th edition, John Wiley & Sons, Inc: New York, 2009: p. 417-480, ISBN: 978-0-470-39882-1.
  188. Ross, P.J., *Taguchi Techniques for quality Engineering*. New York: McGraw-Hill, 1996. 2nd edition ISBN: 0070539588.
  189. Vivancos, J., et al., *Optimal machining parameters selection in high speed milling of hardened steels for injection moulds*. Journal of Materials Processing Technology, 2004. 155-156: p. 1505-1512, ISSN: 0924-0136.
  190. Lajis, M.A., et al., *Prediction of Tool Life in End Milling of Hardened Steel AISI D2*. European Journal of Scientific Research, 2008. 21(4): p. 592-602, ISSN 1450-216X.
  191. Alauddin, M., El Baradie, M.A., and Hashmi, M.S.J., *Prediction of tool life in end milling by response surface methodology*. Journal of Materials Processing Technology, 1997. 71(3): p. 456-465, ISSN: 0924-0136.
  192. Routara, B.C., Bandyopadhyay, A., and Sahoo, P., *Roughness modeling and optimization in CNC end milling using response surface method: effect of workpiece material variation*. The International Journal of Advanced Manufacturing Technology, 2009. 40(11-12): p. 1166-1180, ISSN: 1433-3015.
  193. Palanisamy, P., Rajendran, I., and Shanmugasundaram, S., *Prediction of tool wear using regression and ANN models in end-milling operation*. The Journal of Advanced Manufacturing Technology, 2008. 37: p. 29-41, ISSN: 1433-3015.
  194. Ginta, T.L., et al., *Tool life prediction by response surface methodology for end milling titanium alloy Ti-6Al-4V using uncoated carbide inserts*. European Journal of Scientific Research, 2009. 28(4): p. 533-541, ISSN 1450-216X.
  195. Quiza, R., Figueira, L., and Davim, J.P., *Comparing statistical models and artificial networks on predicting the tool wear in hard machining D2 AISI steel*. The International Journal of Advanced Manufacturing Technology, 2008. 37: p. 641-648, ISSN: 1433-3015.
  196. Pradhan, M.K. and Biswas, C.K., *Modeling and Analysis of process parameters on Surface Roughness in EDM of AISI D2 tool Steel by RSM Approach*. International Journal of Mathematical, Physical and Engineering Sciences, 2009. 3: p. 66-71, ISSN 1307-7465.
  197. Masuzawa, T. and Tönshoff, H.K., *Three-Dimensional Micromachining by Machine Tools*. CIRP Annals - Manufacturing Technology, 1997. 46(2): p. 621-628, ISSN: 0007-8506.
  198. *BS ISO 230-3, 2007 Test code for machine tools —Part 3: Determination of thermal effects*.
  199. *Matsuura L-Tech 15i, Instruction manual, Matsuura machinery corporation, Japan. 2000.*
  200. *ISO 8688-2 : Tool life testing in milling - Part 2 : End milling. 1989.*
  201. Elbestawi, M.A., et al., *High-Speed Milling of Dies and Molds in Their Hardened State*. CIRP Annals - Manufacturing Technology, 1997. 46(1): p. 57-62, ISSN: 0007-8506.
  202. Rodriguez, P., *Research on tool life in micro end milling as related to workpiece quality criteria*. Proceedings of ECTC 2008, ASME Early Career Technical Conference., 2008: p. 1-5.

203. Lawrenson, T., Undergraduate Project Report, University of Birmingham, 2008.
204. El-Wardany, T.I., Kishawy, H.A., and Elbestawi, M.A., *Surface integrity of die material in high speed hard machining, Part 2: Microhardness variations and residual stresses*. Journal of Manufacturing Science and Engineering, Transaction of the ASME, 2000. 122(4): p. 632-641, ISSN: 10871357.
205. Axinte, D.A. and Dewes, R.C., *Surface integrity of hot work tool steel after high speed milling-experimental data and empirical models*. Journal of Materials Processing Technology, 2002. 127(3): p. 325-335, ISSN: 0924-0136.
206. Klocke, F. and Krieg, T., *Coated Tools for Metal Cutting - Features and Applications*. CIRP Annals - Manufacturing Technology, 1999. 48(2): p. 515-525, ISSN: 0007-8506.
207. Trent, E.M. and Wright, P.K., *Metal Cutting*. Butterworth–Heinemann, 2000. 4th edition.

# APPENDICES

## 6.1.1 Appendix A: CNC programme

### CNC programme for NC3

N600  
(USED NC3)(60K RPM)  
G65P9862B3T33D49Z3.0

S60000M3  
G4X600.0  
G65P9862B3T34D50Z3.0

S60000M3  
G4X300.0  
G65P9862B3T35D51Z3.0

S60000M3  
G4X300.0  
G65P9862B3T36D52Z3.0

S60000M3  
G4X300.0  
G65P9862B3T37D53Z3.0

S60000M3  
G4X300.0  
G65P9862B3T38D54Z3.0

S60000M3  
G4X300.0

G65P9862B3T39D55Z3.0

S60000M3  
G4X300.0  
G65P9862B3T40D56Z3.0

S60000M3

G4X300.0  
G65P9862B3T41D57Z3.0

S60000M3  
G4X300.0  
G65P9862B3T42D58Z3.0

S60000M3  
G4X300.0  
G65P9862B3T43D59Z3.0  
GOTO100  
M30  
M99

N800  
G0Z30.0  
G0G90X0.0Y0.0  
M30  
M99

## CNC programme for DTI

N800  
(MACHINE WARM)  
(USING DTI)

G90G80G40G21

G55G1F1000X0.Y0.S60000M3  
G55G43H6G1F1000Z2.  
G1M5F50Z0.  
G4X5.0

G1Z1.  
M3  
G1F200Z50.  
G4X300.  
G1Z1.  
M05  
G1F50Z0.  
G4X5.0

G1Z1.  
M3  
G1F200Z50.  
G4X300.0  
G1Z1.  
M05  
G1F50Z0.  
G4X5.0

G1Z1.  
M3  
G1F200Z50.  
G4X300.0

G1Z1.  
M05  
G1F50Z0.  
G4X5.0

G1Z1.  
M3  
G1F200Z50.  
G4X300.  
G1Z1.  
M05

G1F50Z0.  
G4X5.0

G1Z1.  
M3  
G1F200Z50.  
G4X300.  
G1Z1.  
M05  
G1F50Z0.  
G4X5.0

G1Z1.  
M3  
G1F200Z50.  
G4X300.  
G1Z1.  
M05  
G1F50Z0.  
G4X5.0

G1Z1.  
M3  
G1F200Z50.  
G4X300.  
G1Z1.  
M05  
G1F50Z0.  
G4X5.0

G1Z1.  
M3  
G1F200Z50.  
G4X300.  
G1Z1.  
M05  
G1F50Z0.  
G4X5.0

G1Z1.  
M3  
G1F200Z50.  
G4X300.  
G1Z1.  
M05

G1F50Z0.  
G4X5.0

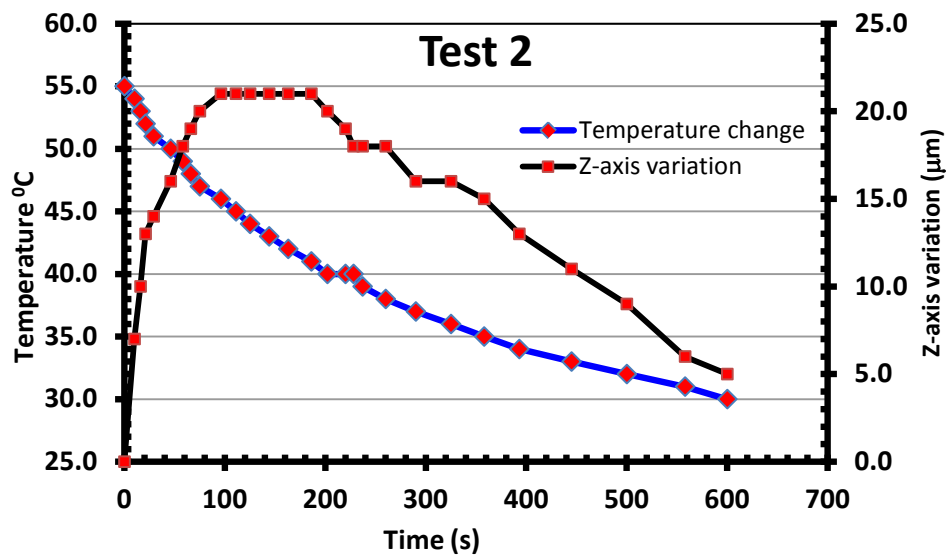
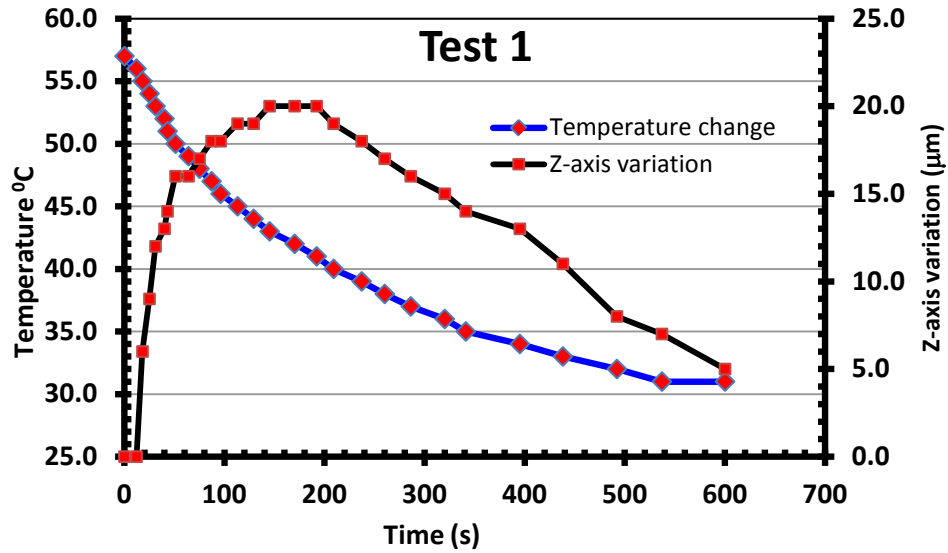
G1Z1.  
M3  
G1F200Z50.  
G4X300.  
G1Z1.  
M05  
G1F50Z0.  
G4X5.0  
G1Z1.

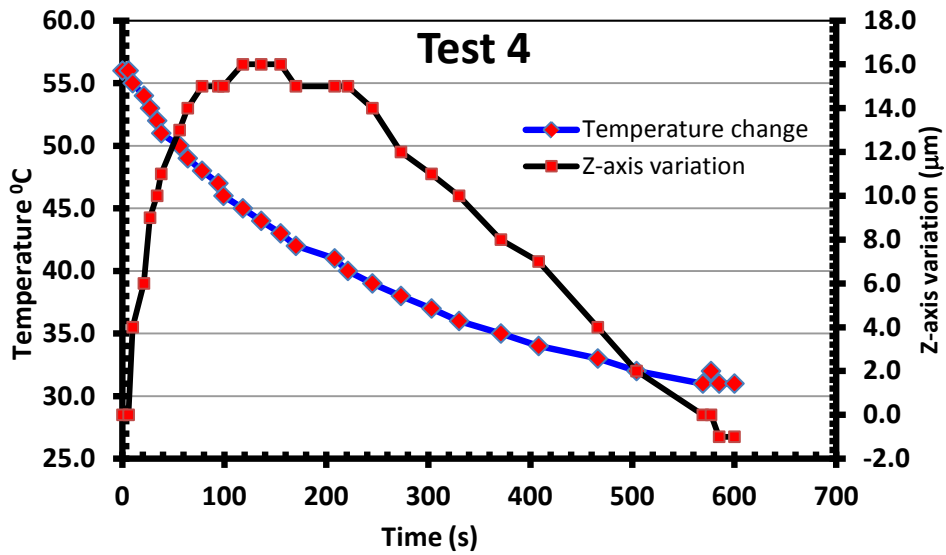
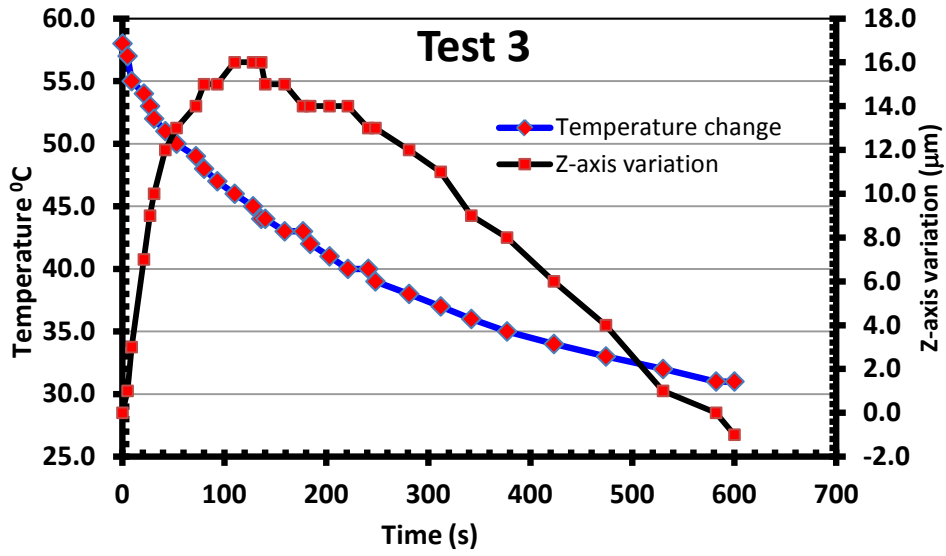
M3  
G1F200Z50.  
G4X300.  
G1Z1.  
M05  
G1F50Z0.  
G4X5.0

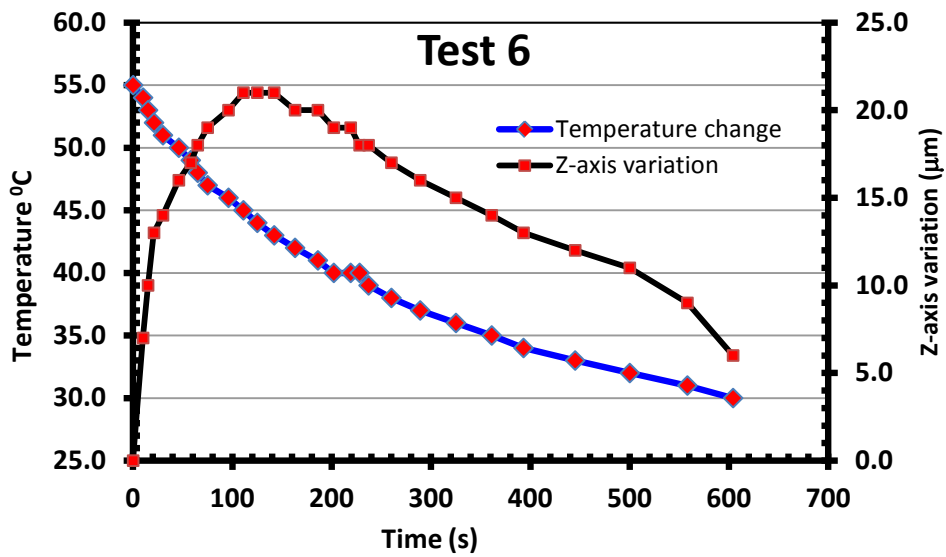
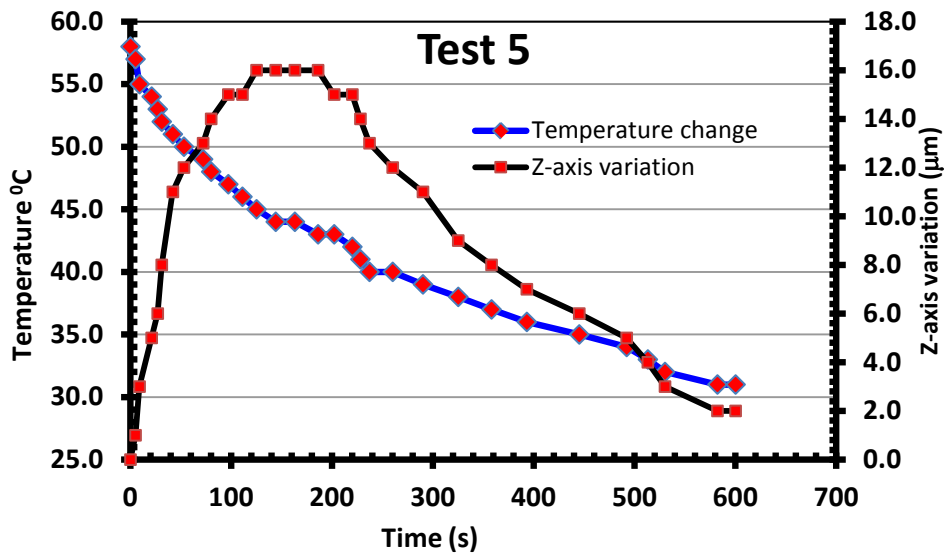
G0Z50.  
M5G0X0.Y0  
M30  
M99

## 6.1.2 Appendix B: Spindle cool down cycles

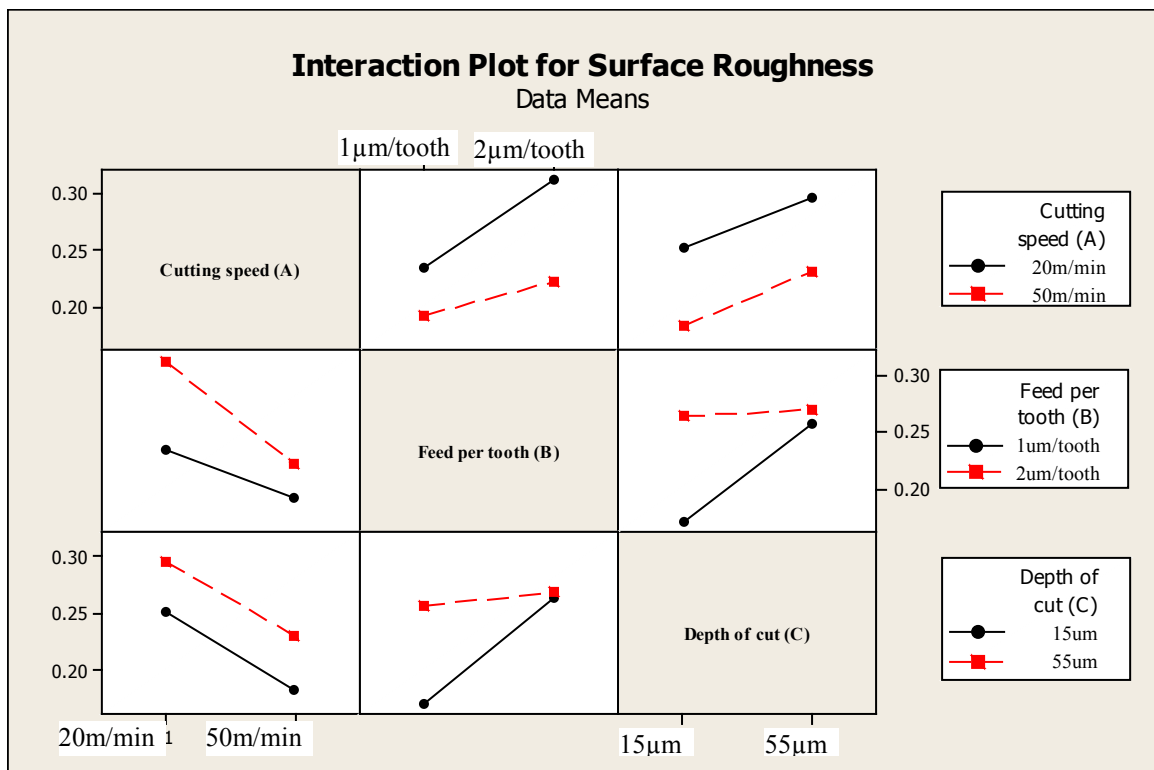
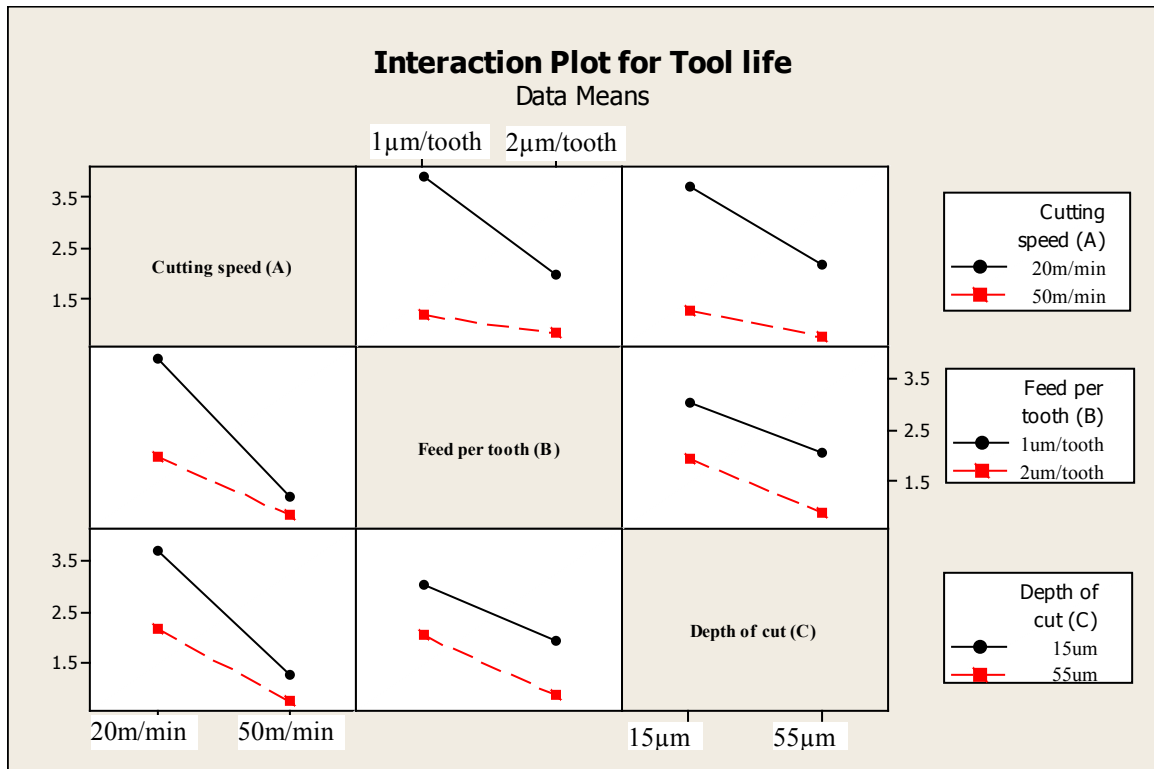
Cycles cool down spindle in Phase 2.

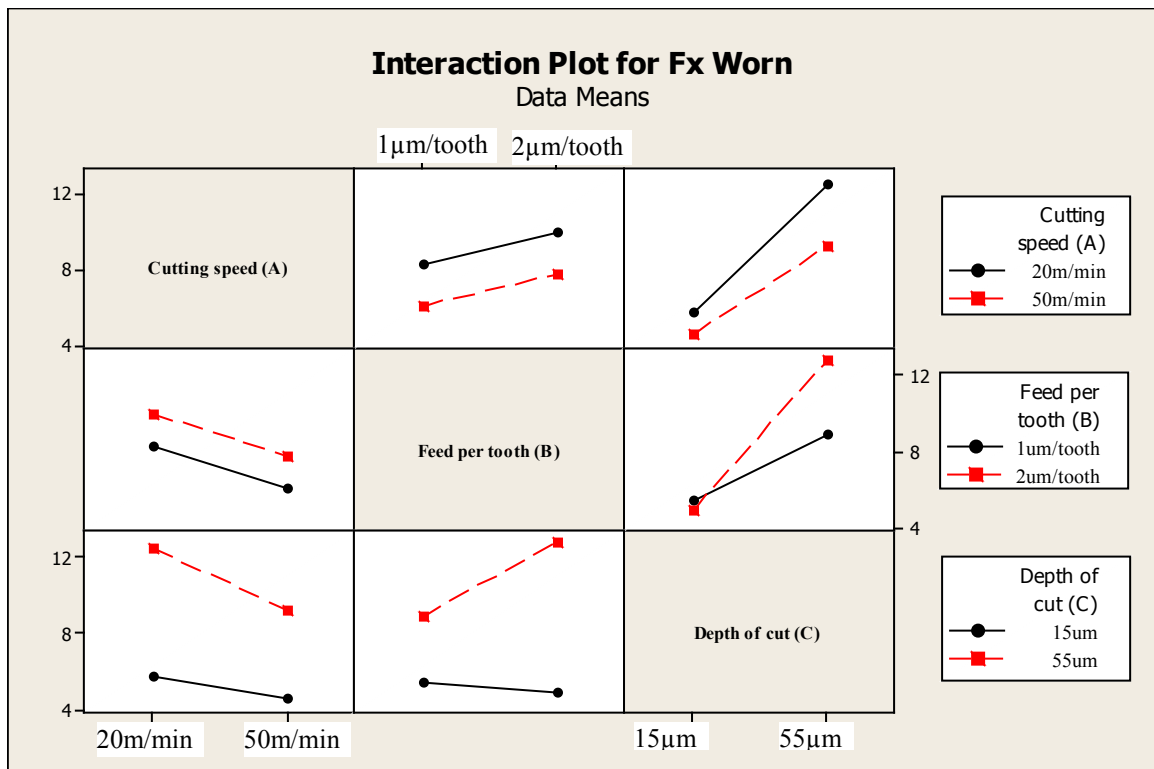
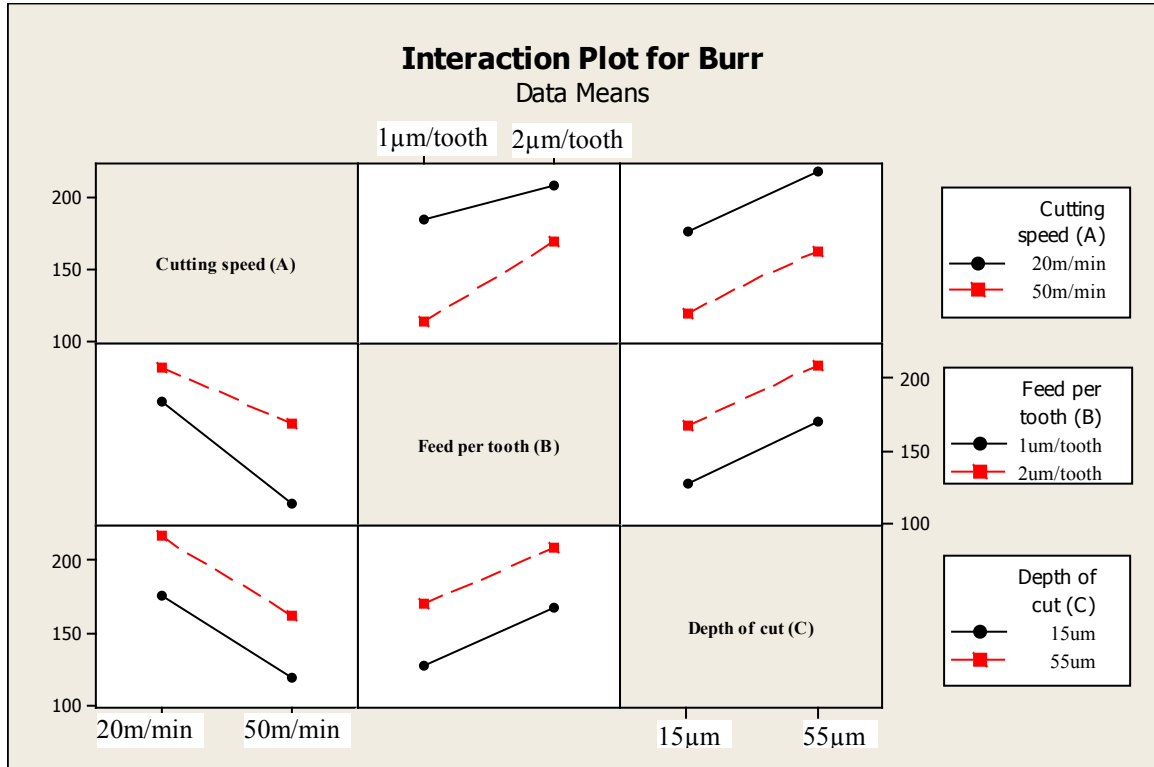


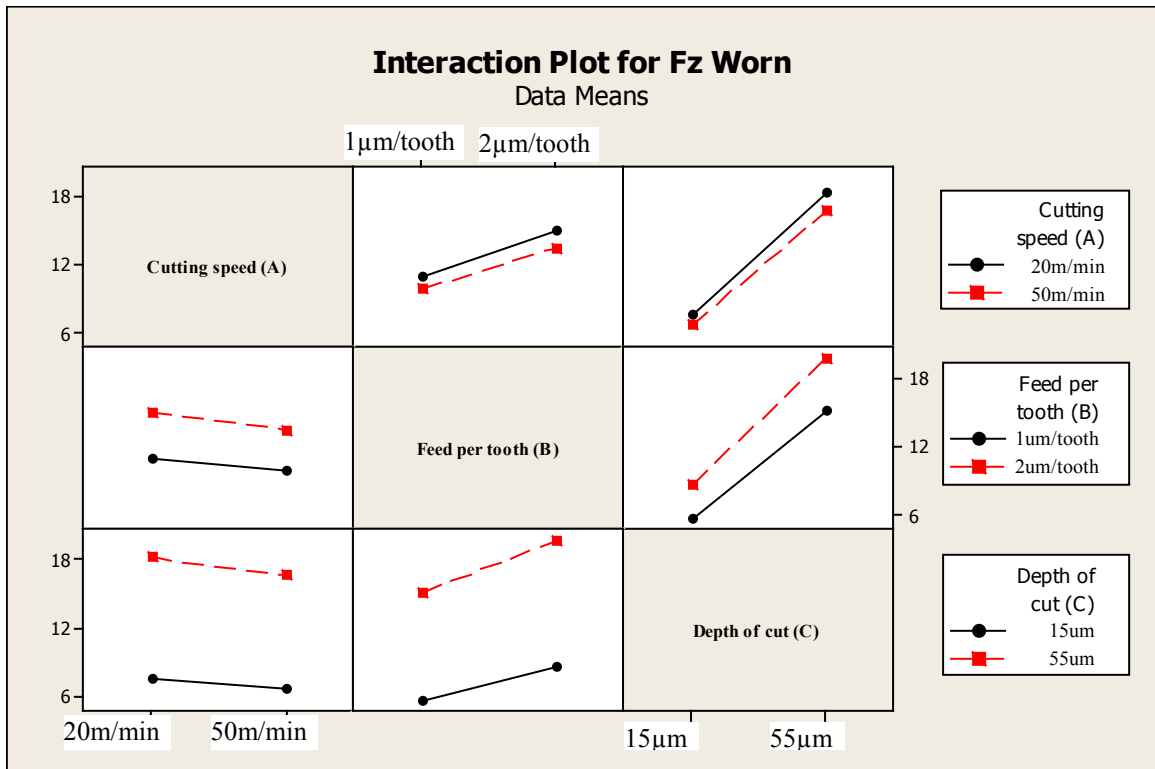
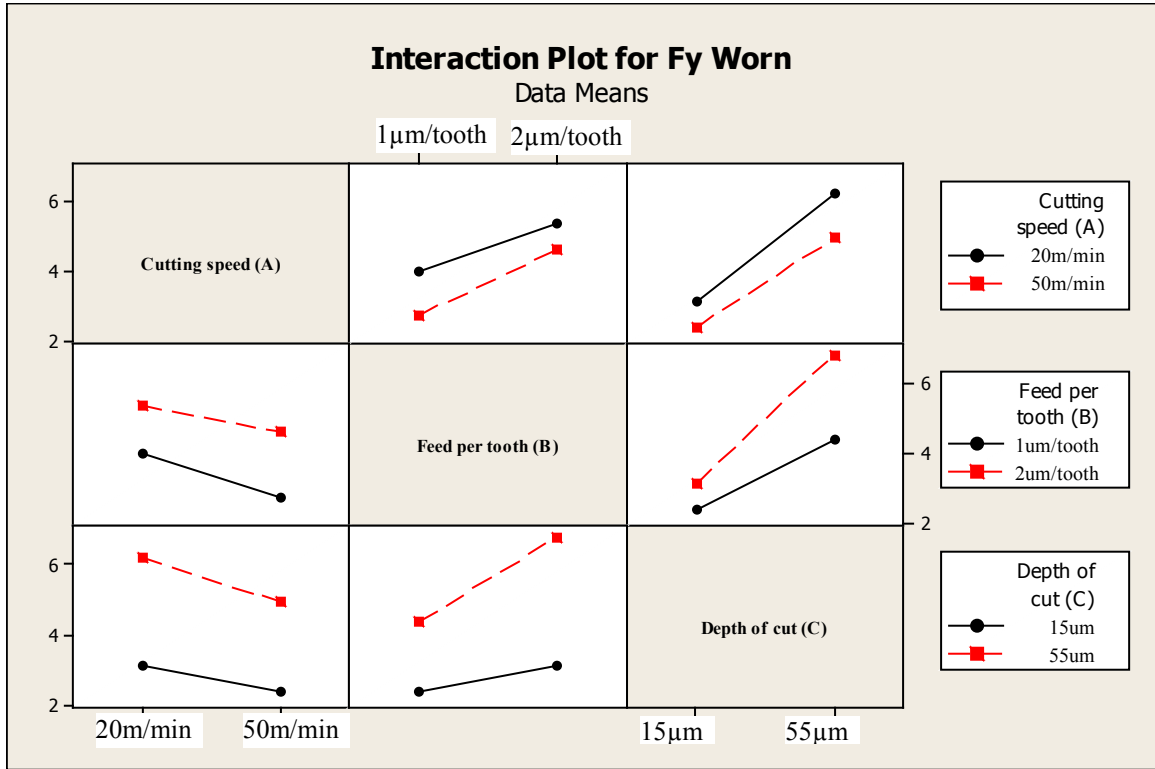




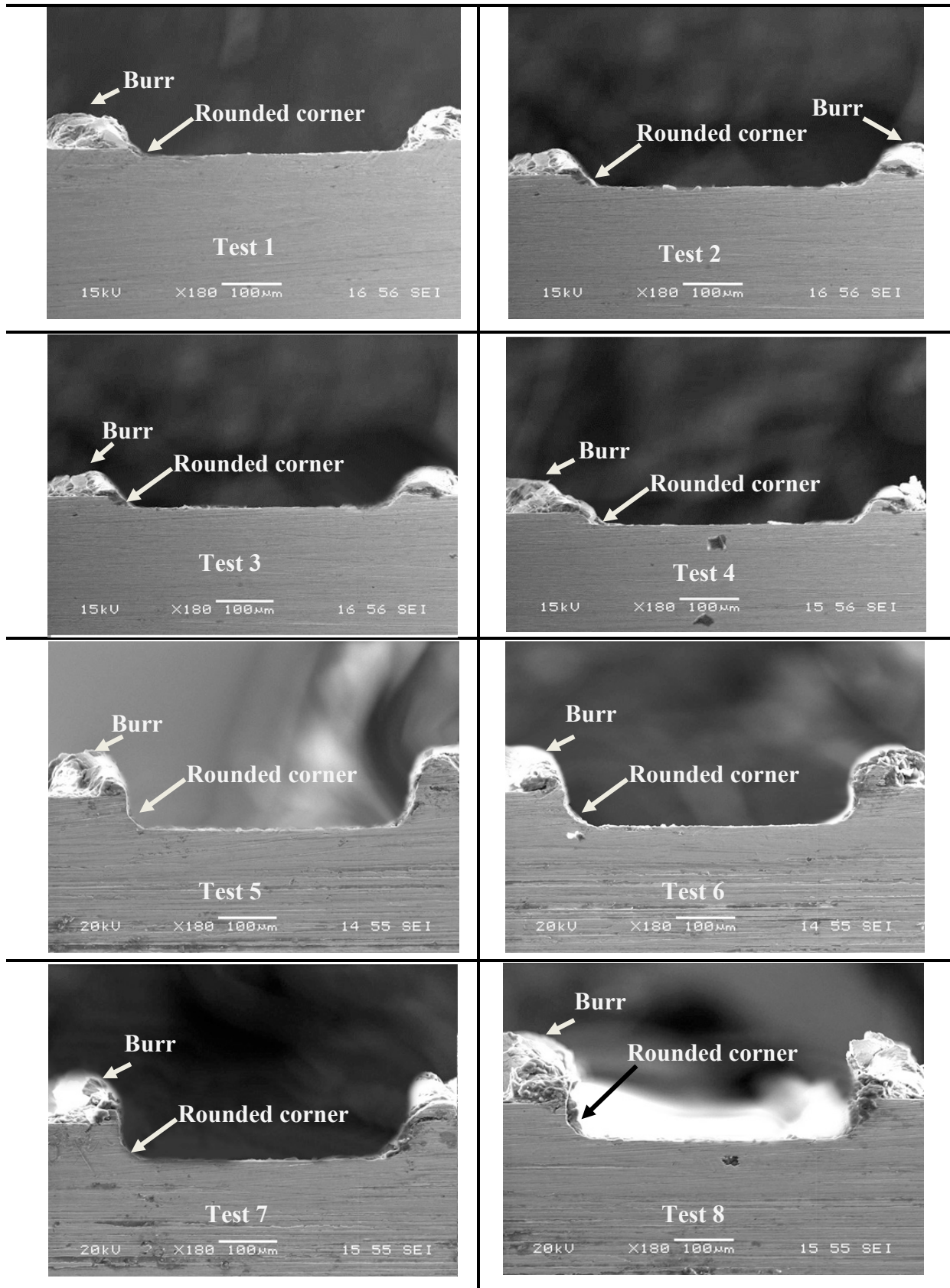
### 6.1.3 Appendix C: Interaction Plots







### 6.1.4 Appendix D: Micrograph of slots machining using worn tools (Slot 26)



### 6.1.5 Appendix E: Sample statistical calculations using Design Expert

Use your mouse to right click on individual cells for definitions.

Response  
 Response: 1      Transform: Natural log      Constant: 0

ANOVA for Selected Factorial Model

Analysis of variance table [Partial sum of squares]

Source	Sum of Squares	DF	Mean Square	F Value	Prob > F
Model	3.57236	6	0.595393	157.5351	0.0001
A	2.090884	1	2.090884	553.2271	< 0.0001
B	0.662976	1	0.662976	175.4169	0.0002
C	0.687646	1	0.687646	181.9442	0.0002
AB	0.061114	1	0.061114	16.17003	0.0158
AC	0.003013	1	0.003013	0.797283	0.4224
BC	0.066727	1	0.066727	17.65524	0.0137
Curvature	0.0422	1	0.0422	11.16572	0.0288
Residual	0.015118	4	0.003779		
Lack of Fit	0.002747	1	0.002747	0.666047	0.4742
Pure Error	0.012371	3	0.004124		
Cor Total	3.629678	11			

Std. Dev.	0.061477	R-Squared	0.995786
Mean	0.502376	Adj R-Squared	0.989465
C.V.	12.23727	Pred R-Squared	0.945512
PRESS	0.197775	Adeq Precision	43.5212

Factor	Coefficient Estimate	DF	Standard Error	95% CI Low	95% CI High	VIF
Intercept	0.460444	1	0.021735	0.400096	0.520791	
A-A	-0.51123	1	0.021735	-0.57158	-0.45089	1
B-B	-0.28788	1	0.021735	-0.34822	-0.22753	1
C-C	-0.29318	1	0.021735	-0.35353	-0.23283	1
AB	0.087402	1	0.021735	0.027055	0.14775	1
AC	0.019408	1	0.021735	-0.04094	0.079755	1
BC	-0.09133	1	0.021735	-0.15168	-0.03098	1
Center Point	0.125798	1	0.037647	0.021273	0.230322	1

Final Equation in Terms of Coded Factors:

$$\begin{aligned} \text{Ln(Response 1)} &= \\ &0.460444 \\ &-0.51123 \quad * A \\ &-0.28788 \quad * B \\ &-0.29318 \quad * C \\ &0.087402 \quad * A * B \\ &0.019408 \quad * A * C \\ &-0.09133 \quad * B * C \end{aligned}$$

Final Equation in Terms of Actual Factors:

$$\begin{aligned} \text{Ln(Response 1)} &= \\ &0.460444 \\ &-0.51123 \quad * A \\ &-0.28788 \quad * B \\ &-0.29318 \quad * C \\ &0.087402 \quad * A * B \\ &0.019408 \quad * A * C \\ &-0.09133 \quad * B * C \end{aligned}$$

Diagnostics Case Statistics								
Standard Order	Actual Value	Predicted Value	Residual	Leverage	Student Residual	Cook's Distance	Outlier t	Run Order
1	1.550	1.568	-0.019	0.875	-0.852	0.636	-0.816	2
2	0.351	0.332	0.019	0.875	0.852	0.636	0.816	5
3	1.019	1.000	0.019	0.875	0.852	0.636	0.816	9
4	0.095	0.114	-0.019	0.875	-0.852	0.636	-0.816	11
5	1.144	1.126	0.019	0.875	0.852	0.636	0.816	10
6	-0.051	-0.033	-0.019	0.875	-0.852	0.636	-0.816	12
7	0.174	0.192	-0.019	0.875	-0.852	0.636	-0.816	6
8	-0.598	-0.616	0.019	0.875	0.852	0.636	0.816	7
9	0.642	0.586	0.056	0.250	1.045	0.045	1.061	8
10	0.531	0.586	-0.056	0.250	-1.045	0.045	-1.061	1
11	0.531	0.586	-0.056	0.250	-1.045	0.045	-1.061	3
12	0.642	0.586	0.056	0.250	1.045	0.045	1.061	4

Note: Predicted values of center points include center point coefficient.

Proceed to Diagnostic Plots (the next icon in progression). Be sure to look at the:

- 1) Normal probability plot of the studentized residuals to check for normality of residuals.
- 2) Studentized residuals versus predicted values to check for constant error.
- 3) Outlier t versus run order to look for outliers, i.e., influential values.
- 4) Box-Cox plot for power transformations.

## 6.1.6 Appendix F: List of publications

### Papers published

1. J. Saedon, S.L. Soo and D.K. Aspinwall, 2011. *Measurement of Spindle Thermal Growth on a Machine Intended for Micro / Meso Scale Milling*. Key Engineering Materials, 447-448: p. 55-60.
2. J. Saedon, S.L. Soo, D.K. Aspinwall and A. Barnacle, 2012. *Micromilling of Hardened AISI D2 Tool Steel*. Advanced Materials Research, 445: p. 62-67.

### Papers submitted

1. J. Saedon, S.L. Soo, D.K. Aspinwall and A. Barnacle. *Investigation of workpiece surface roughness when micromilling hardened AISI D2 steel*. Submitted to the 1<sup>st</sup> Joint International Symposium on System-Integrated Intelligence 2012

### Papers under preparation

1. J. Saedon, S.L. Soo, and D.K. Aspinwall, *Wear characteristics and tool life evaluation in micromilling of hardened AISI D2 tool steel using coated micro-endmill*, to be submitted to Precision Engineering.
2. J. Saedon, S.L. Soo, and D.K. Aspinwall, *Tool life prediction in micromilling AISI D2 (~62 HRC) hardened steel by Response Surface Methodology*, to be submitted to Proceedings of the Institution of Mechanical Engineers, Part B: Journal of Engineering Manufacture.
3. J. Saedon, S.L. Soo, and D.K. Aspinwall, *Investigation of micro end mill tool quality and workpiece roughness when machining micro slots in hardened AISI D2 steel*, to be submitted to International Journal of Machine Tools and Manufacture.